Pressure-dependent dielectric spectroscopy measurements on organic spin liquid compounds

Von der Fakultät Mathematik und Physik der Universität Stuttgart
zur Erlangung der Würde eines Doktors der Naturwissenschaften
(Dr. rer. nat.) genehmigte Abhandlung

Vorgelegt von

Roland Felix Ludwig Rösslhuber

aus Rum

Hauptberichter: Prof. Dr. Martin Dressel
Mitberichter: Prof. Dr. Hidenori Takagi

Tag der mündlichen Prüfung: 22.11.2019
Prüfungsvorsitzende: Prof. Dr. Maria Daghofer

1. Physikalisches Institut der Universität Stuttgart

2019

Non quia difficilia sunt non audemus,
sed quia non audemus difficilia sunt.

Seneca, Epistuale Morales 104.26

It is not because things are difficult that we do not dare;
but it is because we do not dare that things are difficult.

To my family and friends.

List of Abbreviations

HT high-temperature (peak)
LT low-temperature (peak)
IMT insulator-metal transition
TMTTF tetramethyltetrathiafulvalene
BEDT-TTF, ET bis(ethylenedithio)-tetrathiafulvalene
BEDT-STF, STF bis(ethylenedithio)diselenadithiafulvalene
(dmit) 1,3-dithiole-2-thione-4,5-dithiolate
κ-CuCN κ-(BEDT-TTF)$_2$Cu$_2$(CN)$_3$
κ-STF$_x$-CuCN κ-[(BEDT-STF)$_x$-(BEDT-TTF)$_{1-x}$]$_2$Cu$_2$(CN)$_3$
κ-AgCN κ-(BEDT-TTF)$_2$Ag$_2$(CN)$_3$
κ-CuCl κ-(BEDT-TTF)$_2$Cu[N(CN)$_2$]Cl
ac alternating current
dc direct current
ADR anomalous dielectric response
AFM antiferromagnetic (order)
ARPES angle-resolved photoemission spectroscopy
BEMA Bruggemans's effective medium approximation
CO charge order, charge ordered or charge ordering
DMFT dynamical mean field theory
EEG ethylene end groups
ESR electron spin resonance
FTIR Fourier-transform infrared spectroscopy
HOMO highest occupied molecular orbital
LUMO lowest occupied molecular orbital
NMR nuclear magnetic resonance
QSL quantum spin liquid
QWL quantum Widom line
RVB resonating valence bond
μSR muyon spin resonance
SQUID superconducting quantum interference device
VBS valence bond state
VBG valence bond glass

Abstract

Understanding the mutual interaction of electrons in a solid and their impact on its materials properties is one of the central topics of contemporary condensed matter research [1–5]. In Mott insulators, the strong Coulomb repulsion among electrons leads to insulating behavior, which is usually accompanied with anti-ferromagnetic ordering, although simple band structure calculations would infer metallic transport behavior [6–8]. In proximity to the Mott transition, many unconventional phenomena are revealed ranging from bad-metal behavior, quantum criticality to high-temperature superconductivity [9–11]. From a theoretical point of view, it is hard to capture all relevant aspects of this many body system and a stringent treatment of the Mott transition is complicated by the various ordering phenomena next to it [10, 12, 13].

In Mott insulators hosting a quantum spin liquid (QSL) state [14–16], magnetic ordering is impeded by a combination of geometrical frustration, inherent disorder and quantum fluctuations, despite a considerable high exchange coupling. They provide the unique opportunity to investigate the genuine Mott transition [17–20], which is solely mediated by Coulomb interactions without breaking any symmetry. However, the presence of spinons - the fermionic spin exciations of the QSL - at the Mott transition and their possible interference with it is vividly discussed [17, 19, 21, 22]. In that sense, the scenario of a smooth transformation of a spinon Fermi surface to a charge Fermi surface upon crossing the phase boundary, eventually resulting in a continuous phase transition was put forward recently [17, 21, 23]. In contrast, dynamical mean field theory (DMFT) predicts a first order scenario and negates a coherent merging of the two Fermi surfaces at the Mott transition [22, 24–26].

The investigations carried out in this thesis unveil a percolating phase coexistence at the bandwidth-tuned Mott insulator-metal transition (IMT) of the organic spin liquid compound κ-(BEDT-TTF)$_2$Cu$_2$(CN)$_3$[14–16, 27–30] and unequivocally proof the first oder nature of the genuine Mott transition. Our findings are in remarkable agreement with DMFT and finally rebut the controversy of spinons interfering with the Mott transition. In addition, we shed light onto the anomalous dielectric response (ADR) observed in the insulating phase of many organic charge transfer salts subject to electronic correlations, which puzzled the community for a decade.

More specifically, we performed comprehensive dielectric spectroscopy measurements on the organic dimer Mott insulators κ-(BEDT-TTF)$_2$Cu$_2$(CN)$_3$ (κ-CuCN), κ-[(BEDT-STF)$_x$-(BEDT-TTF)$_{1-x}$]$_2$Cu$_2$(CN)$_3$ (κ-STF$_x$-CuCN) and κ-(BEDT-TTF)$_2$Ag$_2$(CN)$_3$ (κ-AgCN). In addition to varying temperature and frequency as experimental parameters, we

applied hydrostatic pressure to tune κ-CuCN across the Mott IMT and to scrutinize the dielectric response in the entire phase diagram. These investigations are complemented by measuring a set of κ-STF$_x$-CuCN crystals, wherein varying the substitution level x is used to tune the compound across the Mott IMT. Additional pressure-dependent measurements of κ-AgCN extend our investigations further into the insulating state of the organic spin liquid compounds allowing us to thoroughly inspect the ADR.

The dielectric response $\varepsilon_1(T)$ in the insulating state of the investigated compounds contains two main dielectric contributions, a high-temperature (HT) peak, showing relaxor ferroelectric characteristics, and a low-temperature (LT) peak. The HT peak corresponds to the dielectric response of the Mott insulating fraction. In contrast, the LT peak emerges due to a small metallic filling fraction already on the insulating side of the phase diagram and is a precursor feature of the phase coexistence enveloping the IMT.

We identify the HT peak with the ADR previously observed at ambient pressure in various organic charge transfer salts. The corresponding activation energy Δ_{HT} diminishes upon intensifying pressure while the relaxation time τ_{HT} in the high-temperature limit increases. In the framework of domain walls, the former indicates that domains are easier to move and the latter that their size increases upon approaching the IMT. Despite comprehensive considerations, however, the microscopic origin of the domain walls remains yet unclear while we only can discard quantum electric dipoles or disorder in the anion network as a possible origin, which were put forward previously in literature [31–34].

The ADR shifts towards lower temperature upon increasing pressure p or the substitution x, showing that it is sensitive to modifying the correlations strength W/U. An elaborate comparison of our findings with other organic dimer Mott insulators indicates, that the intriguing ADR is common to organics with correlated electrons. Thereby we also exclude a purely phononic origin of the ADR. However, we can not rule out a connection of the ADR to details of the crystal lattice yet, such as the packing motif or a structural degrees of freedom related to hydrogen atoms.

For both investigated systems, κ-CuCN under increasing pressure p and κ-STF$_x$-CuCN with rising the substitution x, the observed signature of ε_1 and σ_1 for temperatures $T < T_{\mathrm{crit}}$ below the critical endpoint of the Mott IMT agrees very well with the expectations for a percolating system. Upon approaching the Mott IMT from the insulating side, metallic puddles start to nucleate and grow upon decreasing the interaction strength U/W. In contrast to conventional dc-transport, our measurements of the complex dielectric permittivity are sensitive to polarization effects at the interface between finite metallic clusters in the insulting host fraction, which lead to the drastic enhancement of ε_1 up to 10^5 for 7.5 kHz. The percolative behavior is strongly suppressed for higher

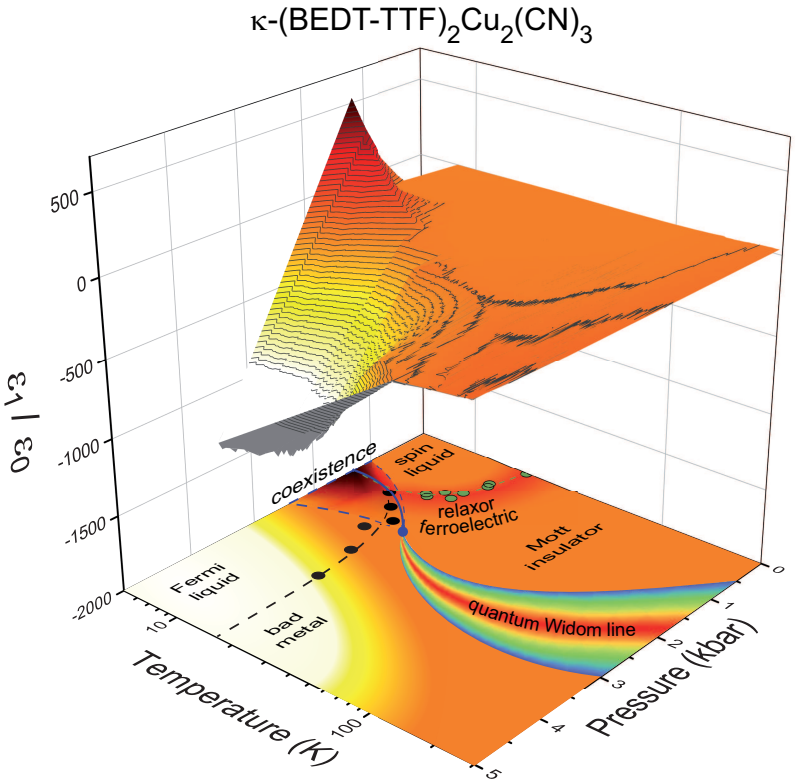

Figure 1: 3D plot of $\varepsilon_1(p,T)$ probed at 380 kHz and the phase diagram of κ-(BEDT-TTF)$_2$Cu$_2$(CN)$_3$. Most importantly, we observe a strong increase of ε_1 up to 500, centered around 1.8 kbar and below 20 K, close to the first-order Mott transition (blue line). We ascribe this to a coexistence phase hosting spatially separated metallic and insulating regions, as predicted by theory [25]. For temperatures above 16 K, the first-order insulator-to-metal transition becomes a gradual crossover which is indicated by the quantum Widom line [17, 20, 35]. The Mott insulating phase for $p < 1.5$ kbar reveals a relaxor ferroelectric response in $\varepsilon_1(T)$ wherein T_B (green circles) is the bifurcation temperature indicating a change in the relaxation mechanism.

temperatures where the first-order Mott insulator-to-metal transition becomes a smooth crossover featuring quantum critical scaling.

These findings confirm the DMFT picture and discard a smooth transformation of a spin Fermi surface to a conventional charge Fermi surface upon crossing the IMT. Moreover, we establish pressure-dependent dielectric spectroscopy as a powerful tool to scrutinize the whole phase diagram of correlated electron systems, revealing relevant physical regimes. Among them are the presence of phase coexistence or the Brinkman-Rice line, the latter separating incoherent conduction from bad metal behavior, besides the easily detectable insulating and metallic regimes.

We apply Bruggeman's effective medium approximation (BEMA) to determine the metallic filling fraction m and obtain the critical exponent $q \approx 1$ upon approaching the threshold from the insulating side. The LT-peak emerges due to a small metallic filling fraction already on the insulating side of the phase diagram. A drop of Δ_{LT} close to the IMT indicates an increased coupling between the metallic inclusions. τ_{LT} decreasing from 10^{-6} to 10^{-8} s upon increasing m. The origin of this intriguing behavior has yet to be clarified, i.e. whether this can be assigned to changes in size and/or shape of the metallic inclusions.

In the coexistence phase, we observed an unexpected strong power-law decrease of $\varepsilon_1(f)$ with increasing frequency, which does not match standard percolation theory. Testing our data with theory [36, 37] ascribing the peculiar behavior to phonon assisted tunneling of charge carriers between the metallic inclusions yields rather unrealistic results. Very recent DMFT calculations [38] with particular emphasis on low frequencies reveal a peculiar frequency-dependence of the spectral function $A(\omega)$ in proximity to the Mott IMT. Whether this can be connected to the intriguing dielectric response observed here has yet to be clarified, but might provide a route to place the various features in $\varepsilon_1(p, T, f)$ on the same footing.

The main results of our pressure- and temperature-dependent dielectric spectroscopy on κ-CuCN are summarized in Fig. 1, where a three-dimensional plot of $\varepsilon_1(p, T)$ is produced from the data taken at $f = 380$ kHz. The bottom area contains a sketch of the phase diagram constructed on the projection of the $\varepsilon_1(p, T)$ values with the corresponding color code; the intense dark red area indicates the enhanced values in the coexistence phase when spatially separated metallic regions grow in the insulating matrix. The percolative behavior softens as temperature increases: the maximum diminishes and eventually a gradual crossover remains above T_{crit}. Additionally, we include the quantum Widom line reproduced after Ref. [39], the bifurcation temperature T_{B} marking the change from the HT to the LT peak and the concomitant change in the relaxation dynamics, and the Fermi-liquid temperature T_{FL}.

Zusammenfassung

Die gegenseitige Beeinflussung von Elektronen und deren Auswirkung auf die Materialeigenschaften ist eines der zentralen Themen der heutigen Festkörperforschung [1–5]. Die starke Coulomb-Abstoßung zwischen Elektronen in Mott-Isolatoren führt zu nicht leitenden Eigenschaften, die für gewöhnlich mit Antiferromagnetismus einhergehen, obwohl einfache Bandstrukturrechnungen metallisches Transportverhalten vorhersagen würden [6–8]. Der Mott-Isolator-Metall-Phasenübergang (*engl.* insulator-metal transition, IMT) ist von diversen unkonventionellen Phänomenen umgeben, die von schlechten metallischen (*engl.* bad metal) und quanten-kritischen Skalierungsverhalten bis zur Hochtemperatursupraleitung reichen [9–11]. Aus der theoretischen Perspektive betrachtet ist es kompliziert, alle relevanten Aspekte dieses Vielteilchensystems in einen stringente Rahmen zu fassen, was durch die verschiedenartigen Ordnungsphänomene in der Umgebung des Mott-Übergangs zusätzlich erschwert wird [10, 12, 13].

In Mott-Isolatoren mit einem Quanten-Spin-Flussigkeit-Zustand (*engl.* quantum spin liquid, QSL) [14–16] wird die magnetische Ordnung durch eine Kombination von geometrischer Frustration, inhärenter struktureller Unordnung und Quantenfluktuationen unterdrückt, ungeachtet einer hohen Austauschwechselwirkung. Diese Systeme bieten die einzigartige Möglichkeit den ursprüngliche Mott-Übergang zu untersuchen [17–20], der ausschließlich durch Coulomb-Wechselwirkung und ohne Symmetriebrechung herbeigeführt wird. Allerdings wird eine Beinflussung des Mott-Übergangs durch die Anwesenheit von Spinonen - den fermionischen Spinanregungen einer Quanten-Spin-Flüssigkeit - kontrovers diskutiert [17, 19, 21, 22]. Insofern wird das Scenario einer reibungslosen Transformation von einer Spinon-Fermi-Fläche zu einer Ladungs-Fermi-Fläche beim Durchqueren der Phasengrenze vorgeschlagen [17, 21, 23]. Im Gegensatz dazu prognostiziert dynamische Molekularfeld-Theorie (*engl.* dynamical mean field theory, DMFT) einen Übergang erster Ordnung und negiert ein kohärentes Zusammenwachsen der zwei Fermi-Flächen am Mott-Übergang [22, 24–26].

Die in dieser Arbeit durchgeführten Untersuchungen enthüllen eine perkolationsartige Phasenkoexistenz des bandbreitenveränderten Mott-Übergangs in dem organischen Quanten-Spin-Flussigkeit-Kandidaten κ-(BEDT-TTF)$_2$Cu$_2$(CN)$_3$ [14–16, 27–30] und belegen eindeutig die erste Ordnung des ursprünglichen Mott-Übergangs. Die Ergebnisse stimmen in bemerkenswerter Weise mit DMFT-Berechnungen überein und schließen eine Beeinflussung des Mott-Übergangs durch Spinonen aus. Darüber hinaus werden die ungewöhnlichen dielektrischen Eigenschaften (*engl.* anomalous dielectric response, ADR) im

isolierenden Zustand vieler organischer Ladungstransfersalze mit korrelierten Elektronensystemen behandelt, die seit einer Decade die Wissenschaftswelt verblüffen.

Insbesondere führte ich umfassende dielektrische Spektroskopiemessungen der organischen Mott-Isolatoren κ-(BEDT-TTF)$_2$Cu$_2$(CN)$_3$ (κ-CuCN), κ-[(BEDT-STF)$_x$-(BEDT--TTF)$_{1-x}$]$_2$Cu$_2$(CN)$_3$ (κ-STF$_x$-CuCN) und κ-(BEDT-TTF)$_2$Ag$_2$(CN)$_3$ (κ-AgCN) durch. Neben dem Variieren von Temperatur und Frequenz wird hydrostatischer Druck als experimenteller Parameter verändert um in κ-CuCN den Mott-Übergang herbeizuführen und die dielektrischen Eigenschaften im gesamten Phasendiagram genau zu untersuchen. Diese Untersuchungen werden durch Messungen einer Reihe von κ-STF$_x$-CuCN Kristallen komplementiert, wobei ein Erhöhen der chemische Substitution x den Mott-Übergang einleitet. Zusätzliche druckabhängige Messungen an κ-AgCN ergänzen diese Studie weiter in den isolierenden Zustand der untersuchten organischen Quanten-Spin-Flussigkeit-Kandidaten.

Die Permittivität $\varepsilon_1(T)$ im isolierenden Zustand der untersuchten Materialien beinhaltet zwei dielektrische Beiträge, einen Peak bei höheren Temperaturen (HT) mit realxorferroelektrischen Merkmalen, und einen Peak bei niedrigeren Temperaturen (LT). Der HT-Peak entspricht der dielektrischen Antwort des Mott-Isolators. Im Gegensatz dazu tritt der LT-Peak aufgrund eines geringen metallischen Anteils auf, der bereits auf der isolierenden Seite des Phasendiagrams vorhanden und eine Vorläufererscheinung der Phasenkoexistenz am Mott-Übergang ist.

Wir identifizieren den HT-Peak mit der ADR, die zuvor bei Umgebungsdruck in verschiedenen organischen Ladungstransfersalzen beobachtet wurde. Die dazugehörige Aktivierungsenergie Δ_{HT} schwindet mit zunehmenden Druck während die Relaxationszeit im Hochtemperaturlimit τ_{HT} ansteigt. Für Domänenwänden zeigt ersteres an, dass diese leichter zu bewegen sind und letzteres, dass deren Ausmaß mit dem Annähern an den Phasenübergang zunimmt. Jedoch gelang es trotz weitreichender Betrachtungen nicht, den mikroskopischen Ursprung von dielektrischen Domänen zu bestimmen während ich quanten-elektrische Dipole und strukturelle Unordnung in den Anionenschichten, wie bisher vermutet [31–34], als möglische Ursache ausschließen konnten.

Die ADR schiebt zu niedrigeren Temperaturen wenn der Druck p oder die Substitution x erhöht wird und reagiert somit sensitiv auf eine Modulierung der Korrelationssträrke U/W. Eine ausführliche Gegenüberstellung meiner Ergebnisse mit der Literatur zeigt, dass die faszinierende ADR in verschiednen organischen Ladungstransfersalzen mit korrelierten Elektronensystemen auftritt. Dabei wird auch ein rein phononischer Ursprung der ADR verneint, während ein Zusammenhang mit Details in der Kristallstruktur, etwa der Dimer-Anordnung oder strukturelle Freiheitsgrade der Wasserstoffatome in den BEDT-TTF-Molekülen, nicht ausgeschlossen werden konnten.

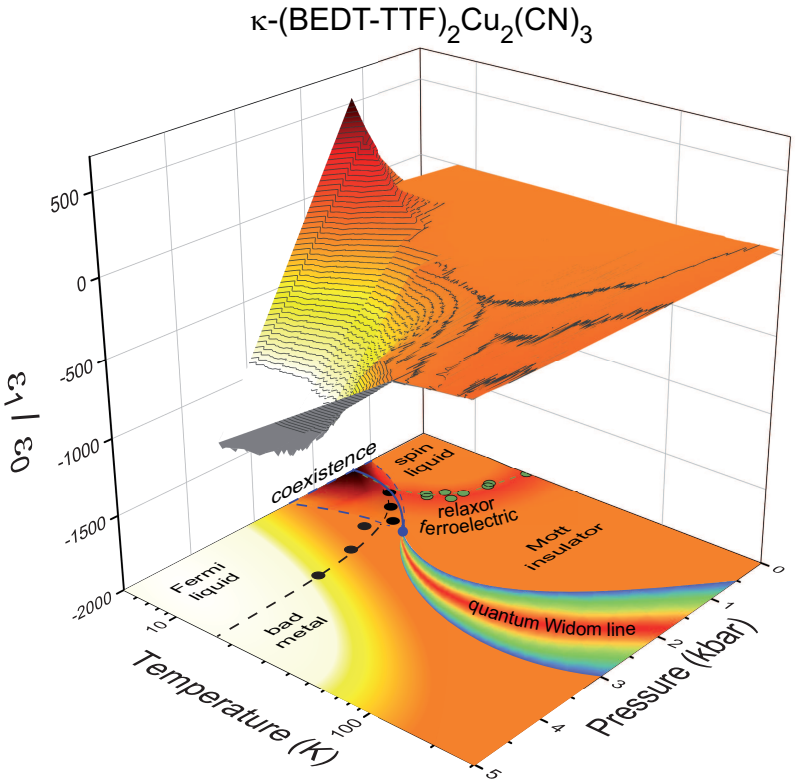

Abbildung 2: 3D Plot von $\varepsilon_1(p, T)$, gemessen bei $f = 380$ kHz, zusammen mit dem Phasediagramm von κ-(BEDT-TTF)$_2$Cu$_2$(CN)$_3$. Am bedeutsamesten ist der starke Anstieg von ε_1 bis zu 500, der bei 1.8 kbar und unter 20 K in der Nähe zum Übergang erster Ordnung (blaue Linie) liegt. Wir führen diesen auf eine Phasenkoexistenz zurück, die metallische und isolierende Regionen separiert aufweist und bereits theoretisch vorhergesagt wurde [25]. Für Temperaturen über 16 K wird der Übergang erster Ordnung zu einem graduellen Wechsel von isolierenden zu metallischen Eigenschaften, der durch die Quantum-Widom-Linie (QWL) angezeigt wird [17, 20, 35]. Die Mott-isolierende Phase für $p < 1.5$ kbar offenbart eine relaxor-ferroelektrische Antwort in $\varepsilon_1(T)$ wobei T_B (grüne Kreise) die Bifurcationstemperatur ist, die eine Änderung des Relaxationsmechanismus anzeigt.

In beiden untersuchten Systemen, κ-CuCN unter wachsendem Druck p und κ-STF$_x$--CuCN mit steigender Substitution x, entspricht das beobachtete Verhalten in ε_1 und σ_1 für Temperaturen $T < T_{\mathrm{crit}}$ unter dem kritischen Punkt den Erwartungen für ein perkolierendes System. Führt man das Sysmens von der isolierenden Seite an den Mott-Übergang heran, so bilden sich metallische Regionen die sich mit ansteigender Korrelationsstärke U/W vergrößern. Im Gegensatz zu konventionellen DC-Transportmessungen sind unsere der komplexen Permittivität empfindlich für Polarisationseffekte die an der Grenzfläche zwischen meatllischen Regionen in der isolierenden Phase entstehen und letztendlich zu einer drastischen Steigerung in ε_1 führen, bis zu 10^5 für $f = 7.5$ kHz. Das charakteristische perkolative Verhalten wird für $T > T_{\mathrm{crit}}$ stark unterdrückt, bei denen der Mott-Übergang erster Ordnung zu einem graduellen Crossover wird der quantenkritisches Verhalten aufweist.

Diese Ergebnisse bestätigen die Vorhersagen von DMFT und negieren eine kohärente Transformation einer Spinon-Fermi-Fläche zu einer kanonischen Ladungs-Fermi-Fläche beim Durchqueren der Phasengrenze. Darüber hinaus etablieren wir druckabhängige dielektische Spektroskopie als eine wertvolle Messmethode um das gesamte Phasendiagramm von korrelierten Elektronensystemen zu untersuchen, die alle relevanten Bereiche aufdeckt. Neben den leicht zu detektierenden isolierenden und metallisch leitenden Bereichen, fallen darunter das Vorhandensein einer Phasenkoexistenz und die Brinkman-Rice-Linie, welche den Bereich inkohärenten Leitvermögens vom schlechten metallischen Eigenschaften trennt.

Wir benutzen Bruggeman's Effektiv-Medium-Theorie (*eng.* Bruggeman's effective medium approximation, BEMA) um den metallischen Füllanteil m zu bestimmen und ermittlen $q \approx 1$ als kritischen Exponenten wenn man sich der Perkolationsschwelle von der isolierenden Seite nähert. Der LT-Peak bildet sich aufgrund eines kleinen metallischen Füllanteils der bereits auf der isolierenden Seite des Phasendiagramms besteht. Ein Abfallen von Δ_{LT} nahe des Phasenübergangs zeigt eine verstärkte Kopplung der Polarisationseffekte an metallischen Einschlüssen an. τ_{LT} verkürtzt sich von 10^{-6} zu 10^{-8} s mit steigendem m. Der Ursprung dieses Verhaltens muss noch erklärt werden, eine mögliche Ursache wäre eine veränderte Größe und/oder From der metallischen Einschlüsse.

In der Phasenkoexistenz beobachten wir ein unerwartet startkes Abnehmen von $\varepsilon_1(f)$ mit steigender Frequenz, das einem Potenzgesetzt folgt und nicht mit den Erwartungen der Standardtheorie für perkolierende Systeme übereinstimmt. Beim testweise Anwenden einer Theorie [36, 37], die dieses Verhalten einem phononen-unterstützten Tunneleffekt von Ladungsträgern zwischen den metallischen Einschlüssen zuschreibt, liefert eher unrealistische Resultate. Neuerste DMFT-Berechnungen [38] mit besonderem Schwerpunkt auf niedrige Frequenzen offenbaren eine sonderliche Frequenzabhängigkeit der Spektralfunktion $A(\omega)$

in der Nähe zum Mott-Übergang. Ob diese die hier beobachteten verblüffenden dielektrischen Eigenschaften schlussendlich erklären können muss noch genauer untersucht werden, könnten aber eine gemeinsame Basis darstellen um die verschiedenen Besonderheiten in $\varepsilon_1(p, T, f)$ zu beschreiben.

Die Hauptergebnisse unserer druck- und temperaturabhängigen dielektrischen Spektroskopiemessungen an κ-CuCN sind in Fig. 2 zusammengefasst, die einen 3D-Plot von $\varepsilon_1(p, T)$ bei $f = 380$ kHz zeigt. Die Grundfläche zeigt eine Skizze des Phasendiagrams, das auf einer Projektion der Werte von $\varepsilon_1(p, T)$ mit entsprechendem Farbcode basiert; der Bereich in intensiven rot kennzeichnet die Phasenkoexistenz in der räumlich separierte metallische Regionen auftreten und wachsen. Mit steigender Temperatur schwindet dieses Perkolationsmerkmal; das Maximum nimmt ab und wird schließlich zu einem glatten Rückgang für T_{crit}. Zusätzlich is die Quantum-Widom-Linie nach Ref. [39], die Bifurkationstemperatur T_{B}, die die Änderung der Relaxationsdynamik beim Wechsel vom HT- zum LT-Peak markiert, und die Fermi-Flüssigkeitstemperatur T_{FL} eingezeichnet.

Publications

Some results of this work have been already published:

- **R. Rösslhuber**, E. Uykur and M. Dressel
  Pressure cell for radio-frequency dielectric measurements at low temperatures
  Rev. Sci. Instrum. **89**, 054708 (2018)

- **R. Rösslhuber**, A. Pustogow, E. Uykur, A. Böhme, A. Löhle, R. Hübner, J. Schlueter and M. Dressel
  Phase coexistence at the first-order Mott-transition revealed by pressure-dependent dielectric spectroscopy of κ-(BEDT-TTF)$_2$Cu$_2$(CN)$_3$
  submitted to Phys. Rev. B (2019)

- A. Pustogow*, **R. Rösslhuber***, Y. Tan*, E. Uykur, A. Böhme, A. Löhle, R. Hübner, Y. Saito, A. Kawamoto, J. Schlueter, M. Dressel and V. Dobrosavljević
  Complex dielectric response across the Mott insulator-metal transition
  to be submitted to Phys. Rev. Lett. (2019)

- Y. Saito, **R. Rösslhuber**, A. Löhle, M. Sanz-Alonso, A. Pustogow, Y. Tan, V. Dobrosavljević, A. Kawamoto, M. Dressel
  Bandwidth-tuning from the insulating Mott quantum spin liquid to the superconducting Fermi liquid via chemical substitution in κ-[(BEDT-STF)$_x$-(BEDT-TTF)$_{1-x}$]$_2$-Cu$_2$(CN)$_3$
  to be submitted to Phys. Rev. B (2019)

Additional scientific publications which are not presented in this thesis:

- **R. Rösslhuber***, E. Rose*, T. Ivek, A. Pustogow, T. Breier, M. Geiger, K. Schrem, G. Untereiner and M. Dressel
  Structural and electronic properties of (TMTTF)$_2X$ salts with tetrahedral anions
  Crystals **8**, 121 (2018)

- A. Pustogow, M. Bories, A. Löhle, **R. Rösslhuber**, E. Zhukova, B. Gorshunov, S. Tomić, J. Schlueter, R. Hübner, T. Hiramatsu, Y. Yoshida, G. Saito, R. Kato, T.-H. Lee, V. Dobrosavljević, S. Fratini and M. Dressel
  Quantum spin liquids unveil the genuine Mott state
  Nat. Mat. **17**, 773 (2018)

- M.H. Beutel, N.G. Ebensperger, M. Thiemann, G. Untereiner, V. Fritz, M. Javaheri, J. Nägele, **R. Rösslhuber**, M. Dressel and M. Scheffler
  Microwave study of superconducting Sn films above and below percolation
  Supercond. Sci. Technol. **29**, 085011 (2016)

- S.A. Sokolov, **R. Rösslhuber**, D.M. Zhigunov, N.V. Latukhina, V.Yu. Timoshenko
  Photoluminescence of rare earth ions (Er^{3+}, Yb^{3+}) in a porous silicon matrix
  Thin Solid Films **562**, 462 (2014)

- M.V. Shestakov, A.N. Baranov, V.K. Tikhomirov, Y.V. Zubavichus, A.S. Kuznetsov, A.A. Veligzhanin, A.Yu. Kharin, **R. Rösslhuber**, V.Yu. Timoshenko, V.V. Moshchalkov
  Energy-transfer luminescence of a Zinc oxide/Ytterbium oxide nanocomposite
  RSC Adv. **2**, 8783 (2012)

* These authors contributed equally to the work.

Contents

1 Introduction **1**

2 Physics of correlated electron systems **5**
2.1 The Hubbard model . . . 5
2.2 Anti-ferromagnetic and quantum spin liquid state in Mott insulators . . . 8
2.3 The Mott transition . . . 10
2.3.1 Spinons at the Mott-transition . . . 11
2.4 Dynamical mean field theory . . . 12

3 Organic charge transfer salts as model compounds to study electronic correlations **17**
3.1 Organic charge transfer salts . . . 17
3.2 Quasi-two dimensional (BEDT-TTF)$_2X$ . . . 21
3.2.1 Packing motifs . . . 21
3.2.2 Tuning electronic correlations by chemical substitution . . . 25
3.2.3 Tuning electronic correlations with pressure . . . 25
3.2.4 Disorder in the BEDT-TTF configuration . . . 26
3.3 Organic spin liquid compounds κ-(BEDT-TTF)$_2$Cu$_2$(CN)$_3$ and κ-(BEDT-TTF)$_2$Ag$_2$(CN)$_3$ . . . 28
3.3.1 κ-[(BEDT-STF)$_x$-(BEDT-TTF)$_{1-x}$]$_2$Cu$_2$(CN)$_3$ . . . 32
3.4 6 K anomaly . . . 32
3.5 Anomalous dielectric response in (BEDT-TTF)$_2X$ . . . 36

4 Polarization effects **39**
4.1 Basic definitions . . . 39
4.2 Polarization mechanisms . . . 43
4.2.1 Dielectric relaxation . . . 45
4.2.2 Curie-Weiss law . . . 50
4.2.3 Relaxor ferroelectricity . . . 51
4.3 Lorentz field approximation and Clausius-Mossotti relation . . . 53
4.4 Effective medium approximations . . . 56
4.4.1 Maxwell Garnett EMA . . . 57
4.4.2 Bruggeman EMA . . . 58
4.5 Percolation . . . 60

5 Experimental setup and data analysis **67**
5.1 Dielectric spectroscopy . . . 67
5.2 Setup . . . 70
5.2.1 Pressure cell and feedthrough . . . 72
5.2.2 Compensation measurements characterizing the setup . . . 76
5.2.3 Open compensation measurement . . . 77
5.2.4 Short compensation measurement . . . 80

5.2.5 Measured observables . . . 81
5.2.6 Comparison ambient pressure and pressure dependent setup . . . 84
5.2.7 Conclusion . . . 86
5.3 Extrinsic effects . . . 86
5.3.1 Contact contribution . . . 86
5.4 Investigated samples . . . 90

6 Overview of the results 93
6.1 κ-(BEDT-TTF)$_2$Cu$_2$(CN)$_3$ . . . 93
6.2 κ-[(BEDT-STF)$_x$-(BEDT-TTF)$_{1-x}$]$_2$Cu$_2$(CN)$_3$ . . . 100
6.3 κ-(BEDT-TTF)$_2$Ag$_2$(CN)$_3$ . . . 104
6.4 Contact contribution . . . 108

7 Dielectric response in the Mott insulating state 111
7.1 Dielectric response of κ-(BEDT-TTF)$_2$Cu$_2$(CN)$_3$ at ambient pressure . . . 111
7.1.1 Frequency-dependent analysis . . . 113
7.2 κ-(BEDT-TTF)$_2$Cu$_2$(CN)$_3$ pressure-dependent analysis . . . 115
7.2.1 Pressure evolution of mode 1 . . . 118
7.2.2 Pressure evolution of T_B . . . 122
7.2.3 Pressure evolution of mode 2 . . . 123
7.3 κ-[(BEDT-STF)$_x$-(BEDT-TTF)$_{1-x}$]$_2$Cu$_2$(CN)$_3$ substitution-dependent analysis . . . 125
7.3.1 Substitution-dependence of mode 1 and mode 2 . . . 128
7.4 κ-(BEDT-TTF)$_2$Ag$_2$(CN)$_3$ pressure-dependent analysis . . . 131
7.4.1 Pressure evolution of mode 1 . . . 134
7.4.2 Pressure evolution of mode 2 . . . 137
7.4.3 Pressure evolution of T_B . . . 140
7.5 Discussion . . . 140
7.5.1 High-temperature peak . . . 140
7.5.2 Low-temperature peak . . . 146
7.5.3 Anomaly . . . 147
7.5.4 Mode 2 . . . 148

8 Phase coexistence at the Mott insulator-metal transition 149
8.1 Phase coexistence in κ-(BEDT-TTF)$_2$Cu$_2$(CN)$_3$ . . . 149
8.1.1 Effective medium approach . . . 152
8.1.2 Divergent dielectric constant . . . 154
8.1.3 Resonance effects . . . 157
8.1.4 Frequency dependence at the percolation threshold . . . 160
8.2 Phase coexistence in κ-[(BEDT-STF)$_x$-(BEDT-TTF)$_{1-x}$]$_2$Cu$_2$(CN)$_3$ . . . 162
8.2.1 Resonance effects . . . 163
8.2.2 Frequency dependence at the percolation threshold . . . 165
8.3 Discussion . . . 169

9 Summary **173**
9.1 Outlook 177

A Appendix A **179**
A.1 Maxwell's equations 179
A.2 "+" or "-" in $\hat{\varepsilon}$ 181

B Achnowledgements **183**

Bibliography **187**

Curriculum Vitae **205**

1 Introduction

Electronic correlations - strong Coulomb repulsion among electrons - give rise to a wide range of fascinating and unconventional phenomena, which are at the forefront of condensed matter research. Outstanding among them is the Mott insulator, which is realized in materials with a 1/2-filled conduction band when strong Coulomb repulsion forces electrons to localize, eventually resulting in insulating behavior although simple band structure calculations would infer metallic properties. This failure of band theory triggered the pioneering works of Mott and Hubbard [6–8], which explicitly identify a delicate interplay of the Coulomb replusion among electrons and the bandwidth as the driving force for the insulating behavior.

In proximity to the Mott-insulting state, many unconventional phenomena are revealed ranging from bad-metal behavior, anti-ferromagnetic ordering and quantum criticality to high-temperature superconductivity [9]. Despite great efforts, however, some key features of the Mott insulator and its phase transition to a metallic state remain unresolved. The various ordering phenomena next to the transition pose the question whether they are associated with symmetry breaking [9], whereas however, their complex environment complicates the identification of the dominant degree of freedom and the corresponding order parameter. This view is in contrast to the early concept of Mott and Anderson that spin or charge ordering is not the driving force but the consequence of Mottness. Early theories based on this approach favor a robust first-order scenario [8, 12, 13] but it has proven difficult to provide conclusive experimental evidence for the related phase-coexistence region enveloping the Mott transition [9, 40, 41].

Today, heavy fermion systems [3], transition metal oxides [4, 5] and organic charge transfer salts [1, 2] are well established systems to study electronic correlations. While the former two often feature rather complex band structures, the conduction band in organic salts is solely formed by the overlapping π-orbitals such that the single band Mott-Hubbard model is truly realized. Besides that, their modular composition with different sets of donor molecules in combination with various atomic or molecular anions turns out to be extremely versatile when it comes to modifying the system towards desired properties. Moreover it makes them rather soft, such that pressure of a few kilobars

is sufficient to drastically change their bandwidth making them prime candidates to investigate the bandwidth-tuned Mott transition [42]. This not only enables the systematic study of phenomena originating from electronic correlations, but their interplay with low dimensionality, electron-phonon coupling, spin charge separation and Fermi-surface topology, as for instance impressively demonstrated in the (BEDT-TTF)$_2X$ or (TMTTF)$_2X$ [1, 43] organic charge transfer salts (where BEDT-TTF stands for bis(ethylenedithio)tetrathiafulvalene and TMTTF for tetramethyltetrathiafulvalene).

Recently, the dimer Mott insulators κ-(BEDT-TTF)$_2X$ with X=Cu$_2$(CN)$_3$ and Ag$_2$(CN)$_3$ draw a lot of attention. They feature a spin-1/2 system arranged on a triangular lattice close to geometrical frustration which, in combination with the inherent disorder in their anion network and quantum fluctuations, impedes magnetic ordering despite a considerable high exchange coupling [27–30]. This is interpreted as the realization of the quantum spin liquid state (QSL) [14–16]. Most importantly, the absence of long-range magnetic ordering provides the unique opportunity to investigate the genuine Mott transition [17–20], which is solely mediated by Coulomb interactions without breaking any symmetry. The nature of the highly degenerate QSL state and its exotic spin excitations - spinons - are subject of intense studies [44, 45] and controversial debate. In particular, the presence of spinons at the Mott transition and their possible interference with it is vividly discussed [17, 19, 21, 22]. In that sense, the scenario of a smooth transformation of a spinon Fermi surface to a charge Fermi surface upon crossing the phase boundary, eventually resulting in a continuous phase transition opposing a first-order scenario, was put forward recently [17, 21, 23].

Besides the progress in material synthesis and experiments, remarkably theoretical advances in studying the Mott transition were achieved by the development of dynamical mean field theory (DMFT). Its predictions of a strongly renormalized Fermi liquid, bad-metal behavior and quantum critical scaling at temperatures above its critical end point were experimentally confirmed in κ-(BEDT-TTF)$_2$Cu$_2$(CN)$_3$ with striking agreement [17, 20, 24–26, 39]. In addition, DMFT predicts a phase coexistence in proximity to the phase boundary in accordance to a first-order scenario while its extension with resonating valence bond theory negates a coherent merging of the two Fermi surfaces at the Mott transition [22]. In this framework, spinons are well defined only deep in the insulating state and are destroyed by charge fluctuations upon approaching the Mott transition.

Therefore, it is urgently required to finally settle whether a first-order scenario with an associated phase coexistence is realized for the Mott transition in κ-(BEDT-TTF)$_2$-Cu$_2$(CN)$_3$. In particular, it is a crucial point for the further examination of experimental results obtained by non-local probes, such as dc-resistivity measurements which previously

were interpreted in the framework of spinons interfering with the Mott transition [17], since they are in particular affected by phase coexistence.

In this thesis, I demonstrate that dielectric spectroscopy is a very sensitive tool not only to provide conclusive evidence for the phase coexistence at the Mott transition in κ-(BEDT-TTF)$_2$Cu$_2$(CN)$_3$, but also to determine its whole phase diagram and to distinguish relevant physical regimes. To that end, a setup to perform dielectric spectroscopy in dependence of temperature, pressure and frequency was built at our institute, which is perfectly suited for investigating the dielectric response of organic charge transfer salts over the whole phase diagram. A crucial point in achieving this was to design and manufacture of novel electrical feed though for a clamp type pressure cell [46]. The pressure-dependent investigations on κ-(BEDT-TTF)$_2$Cu$_2$(CN)$_3$ and κ-(BEDT-TTF)$_2$Ag$_2$(CN)$_3$ are complemented with ambient pressure measurements on κ-[(BEDT-STF)$_x$-(BEDT-TTF)$_{1-x}$]$_2$-Cu$_2$(CN)$_3$, wherein chemical substitution is used to tune the crystal across the phase transition. In addition, light is shed onto the anomalous dielectric response observed in the insulating state of many organic charge transfer salts which puzzled the community for a decade.

This thesis is organized as follows: In chapter 2, electronic correlations are introduced on a basic level with particular emphasize on the Mott transition. Also, the currently competing theoretical viewpoints on spinons interfering with the transition are briefly summarized. Chapter 3 gives an overview on organic charge transfer salts and why they are well established model compounds to study electronic correlations. The intension of the first two chapters is to give a pedagogical introduction rather than a comprehensive, detailed collection such that they might appear trivial for a reader more familiar with these topics. In chapter 4, we give the basic definition of the measured observables, review the mechanism of dielectric relaxation and provide various models necessary to analyze the obtained data. The experimental setup, technical details on the feed through and the analyzing procedure are discussed in chapter 5. Chapter 6 gives a first overview of the collected data which can be divided into the dielectric response observed in the Mott insulating part and the coexistence region of the phase diagram, which are both subsequently examined in detail in Chapters 7 and 8, respectively. Finally, chapter 9 summarized the most important findings and gives an outlook for future projects.

2

Physics of correlated electron systems

In band theory, just a single electron in the periodic potential of the lattice is considered and the presence of all other electrons is accounted by a modification of this potential while an explicit electron-electron interaction is neglected. In certain cases, however, these electronic correlations are the driving force for a variety of phenomena, ranging from the charged ordered and Mott insulating state, to quantum critical scaling, renormalized Fermi liquid and bad metal behavior.

In this chapter, we will first introduce electronic correlations in the framework of the Mott-Hubbard model and briefly discuss the phenomenology of the anti-ferromagnetic ordered Mott insulator and its counterpart without long-range magnetic ordering, the quantum spin liquid. Subsequently, we will tackle the Mott transition and briefly summarize the currently competing theoretical viewpoints on spinons interfering with the transition. Finally, we give a short overview on the prediction of the dynamical mean field theory for correlated systems with 1/2-filling.

2.1 The Hubbard model

It turned out, that in many cases the important physics of electronic correlations are very well described by the extended Hubbard model [47]. Starting from electrons localized on discrete lattice sites, it considers their hopping between nearest-neighbor sites via the transfer integral t, which is a measure for the increase in kinetic energy through the delocalization of the non-interacting electrons. Needles to mention, that in a single band system the Pauli principles allows only two electrons on each site. Electronic correlations are then introduced by considering the mutual Coulomb repulsion among electrons. First of all there is the Coulomb repulsion which has to be overcome to put two electrons on the same site, the on-site Coulomb repulsion U, and of course there is a considerable Coulomb repulsion between electrons on nearest-neighboring sites, taken into account by

the inter-site Coulomb repulsion V. In general we consider $U > V$. The corresponding Hamiltonian then reads

$$H = -t \sum_{<i,j>,\sigma} \left(c^{\dagger}_{i,\sigma} c_{j,\sigma} + c^{\dagger}_{j,\sigma} c_{i,\sigma} \right) + U \sum_{i} n_{i,\uparrow} n_{i,\downarrow} + V \sum_{<i,j>} n_i n_j \quad , \tag{2.1}$$

where $c^{\dagger}_{i,\sigma}$ denotes the creation operator for an electron with spin σ at the site i, $c_{i,\sigma}$ the corresponding annihilation operator and $n_{i,\sigma}$ the electron number operator. The first term corresponds to the kinetic energy, the second and third to the electronic correlations mediated by the on-site and inter-site Coulomb repulsion, respectively.

The resulting physics depends on the band-filling, which in experiment can be adjusted by charge carrier doping. In course of this very basic introduction, we will considered a two-dimensional square lattice with 1/4- and 1/2-filling to give a simple picture of the implication of electronic correlations on the physical properties of the system.

The case of a 1/4-filled system is shown on the left side of Fig. 2.1. The hopping of an electron to an unoccupied site lowers its energy by $-t$ while the inter-site Coulomb repulsion V has to be paid for every electron sitting on a nearest-neighbor of the target site. If the electron hops to an occupied site, then additionally the on-site Coulomb repulsion U has to be overcome. The transport properties depend on the proportion of t, or the bandwidth which in this case is $W = 4t$, relative to the strength of the electronic correlations represented by U and V.

In case W is much larger then U and V ($U, V \ll t$), the energy cost U, for putting two electrons on the same site, and V, for putting an electron on a site where one of its nearest-neighbors is occupied, are negligible small compared to the energy gain $-t$ for delocalizing an electron. As a result, the system is metallic, its density of states remains unaffected and only the Pauli principle limits the hopping of electrons.

On the other hand for sufficiently narrow bands, U and V become the dominant energy scales ($U > V \gg t$) and it is energetically very unfavorable to put two electrons on the same site. Moreover, the electrons avoid sitting next to each other on nearest-neighbor sites in order to reduce V, eventually leading to their localization in a checkerboard-like arrangement. Due to this charge ordering, the density of states splits into an completely occupied lower band and an unoccupied upper band which are separated by the energy $3V$, which is necessary to create a charge excitation by shifting one electron by one site such that it obtains three nearest-neighbors. An additional band represents the charge excitation by putting two electrons on one site which is located in a distance of U above the occupied band.

In case of a 1/2-filled system, the main physics is well captured by only considering the first two terms in Eq. (2.1) with an effective on-site Coulomb repulsion $U' = U - V$ and

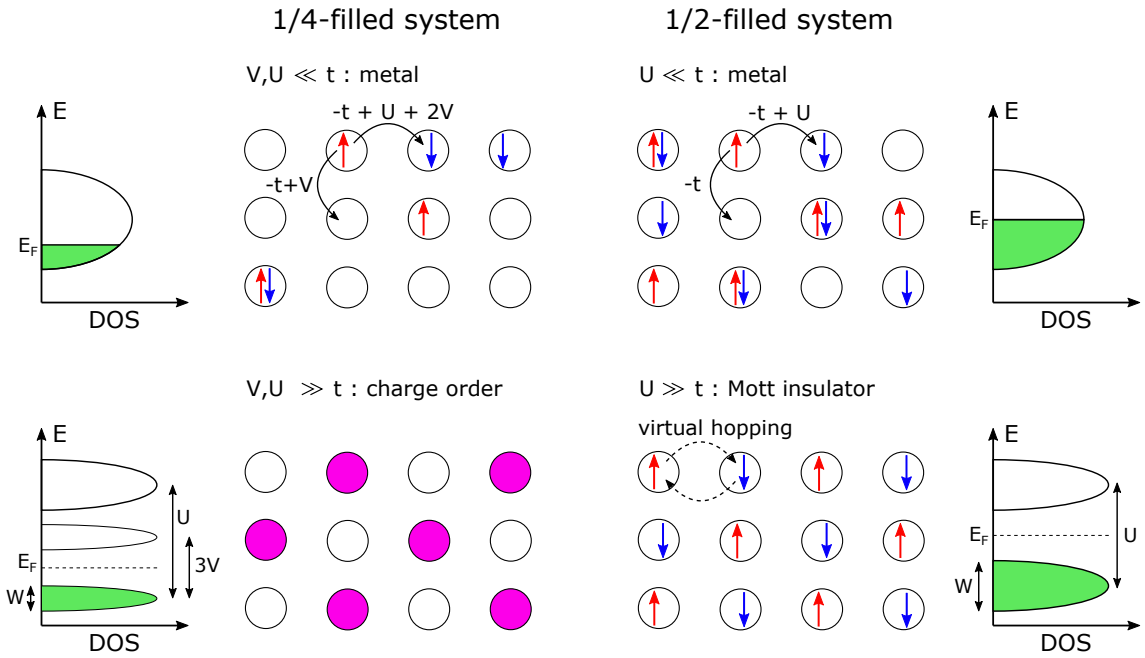

Figure 2.1: Illustration of the extended Hubbard model on a 1/4-filled and a 1/2-filled square lattice. Obeying the Pauli principle, a maximum of two electrons is allowed per site. The probability of an electron hopping to a neighboring site is given by the transfer integral t. If an electron hops to an unoccupied site, the delocalization lowers its energy by $-t$ whereas if it hops to an occupied site, it additionally has to overcome the on-site Coulomb repulsion U. For a 1/4-filled, also the inter-site Coulomb repulsion V has to be considered. For $U, V \ll t$ both systems are metallic, since the cost for putting two electrons on the same site or neighboring sites is negligible small compared to the kinetic energy. For both fillings, the corresponding density of states remains unaffected. For $U, V \gg t$ in a 1/4-filled system, it is energetically very unfavorable to put two electrons on the same site as well as on neighboring sites, such that the electrons arrange in a checkerboard pattern in order to minimize U and V. For $U, V \gg t$ at 1/2 filling, U impedes double-occupied sites and the electrons are forced to localize, eventually resulting in insulating behavior. In both cases, the density of states is spitted at the Fermi energy leading to an completely occupied lower band and an unoccupied upper band, which are separated by the energy U necessary to create a charge excitation by putting two electrons on one site. For a 1/4-filled, an additional band located at $3V$ above to occupied one is formed representing the charge excitation of shifting one electron to a neighboring site, such that it obtains three nearest-neighbors.

neglecting the third term. This case is illustrated on the right side of Fig. 2.1 for which in principle the same energy considerations apply. In case the bandwidth W is much larger then U ($U \ll t$), the cost for putting two electrons on the same site is negligible small compared to the energy gain for delocalizing an electron, such that the system remains metallic with an unchanged density of states. For U significantly exceeding W ($U \gg t$), double-occupied sites are impeded by U, such that the 1/2-filling gives one electron per site. The corresponding density of states is split at the Fermi energy into a completely occupied lower Hubbard band (LHB) and an unoccupied upper Hubbard band (UHB), which are separated by the energy U necessary to create a charge excitation by putting two electrons on one site.

2.2 Anti-ferromagnetic and quantum spin liquid state in Mott insulators

In this thesis, we mainly consider electronic correlations in 1/2-filled systems, such that we will focus on them in the following where we consider the spin-degree of freedom of the electrons. In the framework of quantum mechanics, the ground state with strictly localized electrons may be mixed with the excited state of an electron hopping forth and back to an neighboring site, which is referred to as virtual hopping. This virtual hopping lowers the net-energy and, in combination with the Pauli principle, leads to an anti-ferromagnetic (AFM) spin alignment as illustrated in Fig. 2.1. This is associated with an effective exchange interaction [47], usually called super exchange, with

$$|J| \propto \frac{t^2}{U} \quad . \tag{2.2}$$

In the last two decades, it turned out that the AFM ordering in the Mott-insulating state can be suppressed when the electrons are arranged on a lattice featuring geometrical frustration [44], such as on a triangular [27, 29, 30, 48, 49], Kagome [50–53] or hyperkagome lattices [54]. In a simple picture this is explained by the fact, that it is impossible to simultaneously realize the anti-ferromagnetic alignment of all spins, giving rise to an highly degenerate state as illustrated in Fig. 2.2 for a triangular lattice. Besides this geometrical frustration [55–57], quantum fluctuations [58] and disorder [34, 59–62] might play a crucial role to quench magnetic ordering. As a result, the onset of anti-ferromagnetic order, the Neel temperature T_{N}, is significantly lower then expected from the exchange interaction and in some case even suppressed to lowest temperatures. Instead of the ordered state, a degenerate non-ordered state with highly entangled spins and large entropy is achieved

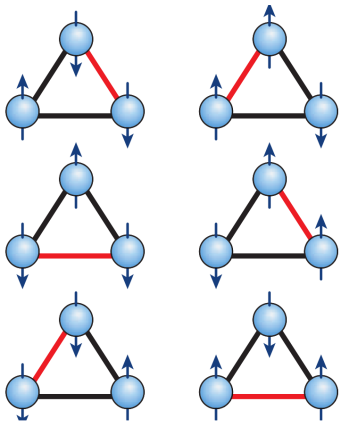

Figure 2.2: Spin alignment for $J < 0$ on a triangular lattice close to geometrical frustration. Since an anti-ferromagnetic arrangement can not be satisfied for all three spins simultaneously, two of them are aligned in parallel. This is achieved in six different configurations which all require the same energy, eventually giving rise to a six-fold degenerate spin state. Reproduced from Ref. [15].

which is interpreted as the realization of the quantum spin liquid state (QSL) [14, 15, 44, 45].

A theoretical description of the QSL on a fundamental level is far from being settled with numerous concepts being presented over the last years [44, 45]. Among them, the resonating valence bond (RVB) theory [14, 15] is mostly used as a framework to approach the QSL state. It considers valence bonds, i.e. a pair of spins with antiferromagnetic exchange interaction forming a spin-0 singlet state. The unique feature of the spin liquid is that the valence bonds are collectively entangled, not only with their neighbors but even over long distances clearly exceeding the lattice spacing and in principle with every other counterpart in the system. RVB theory predicts spinons, exotic quasi particles with charge $q = 0$ and spin $s = 1/2$ as excitation of the spin degree of freedom. Spinons are considered to from a magnetic fluid with fermionic statistics in the Mott insulator [21]. Whether the spinons are gapped or form a continuum is subject of much controversy, both from theoretical and experimental side [63–66]. Moreover, theories predict spin charge coupling via an emergent gauge field in the QSL state [67], invoking a contribution of spinons to low-energy optical conductivity for which only recently first evidence is provided [19].

However, up to now a smoking gun experiment to unequivocally identify the QSL state is missing and a variety of different experimental techniques is required [68]. First, one might look at the magnetic susceptibility, which usually follows the Curie-Weiss law $\chi = C/(T - T_{\mathrm{CW}})$ at high temperatures. Comparing the Curie temperature $|T_{\mathrm{CW}}|$ with the

onset of residual ordering or spin freezing at T_f gives a measure for the degree of frustration $f = |T_\mathrm{CW}|/T_\mathrm{f}$. For sufficiently large f, a spin liquid region might exist between $|T_\mathrm{CW}|$ and T_f. In contrast to a spin glass, the QSL neither shows a glassy freezing of spins nor any magnetic field dependence in the magnetic susceptibility upon cooling. The absence of magnetic ordering can be confirmed by neutron scattering, which also probes spin excitations and correlations. Nuclear magnetic resonance (NMR) measurements are also a tool to rule out the presence of a static ordered state with inequivalent magnetic sites or a static disordered state and the nuclear spin-lattice relaxation rate T_1^{-1} probes low-lying spin excitations. Thermal transport measurements can be used to distinguish between localized and itinerant electrons and specific heat measurements to probe the low-energy density of states.

2.3 The Mott transition

It is straight forward that upon increasing the interactions strength U/W, the system undergoes a phase transition from the metallic to the Mott-insulating state - the Mott transition. Despite great efforts for several decades, the Mott transition remains poorly understood on a fundamental level [8, 9, 47], mainly because the relevant degrees of freedom at the transition cannot be straightforwardly identified. This complicates the determination of an appropriate order parameter in analogy to the symmetry breaking principle in conventional critical phenomena, although different competing orders are often present in the vicinity of the transition. Numerical studies based on the dynamical mean-field theory (DMFT, cf. Ch. 2.4) favor a first-order transition [12, 13] while only scattered experimental proof exists for the associated phase coexistence [69, 70].

It is suggested, that the nature of the transition is influenced by the structure of the insulating state in proximity to the Mott-transition. In this respect, the absence of long-range magnetic ordering in QSL provides the unique opportunity to investigate the genuine Mott transition [17–20], which is solely mediated by Coulomb interactions without breaking any symmetry.

In many cases, an enhancement of the bandwidth W is experimentally achieved by applying external pressure p [17, 27, 30, 39, 69], effectively decreasing U/W, such that the corresponding phases can be represented in a p-T phase-diagram [1]. This is shown in Fig. 2.3(a) for a Mott insulator with a lattice featuring considerable frustration ($t = t'$), such that the QSL state is realized, and in panel (b) for a Mott insulator without sufficient frustration ($t > t'$) maintaining AFM order up to finite T_N [20]. The insulator-metal transition (IMT), terminating at the critical end point, is indicated by the black solid line and clearly differs in shape for the two cases.

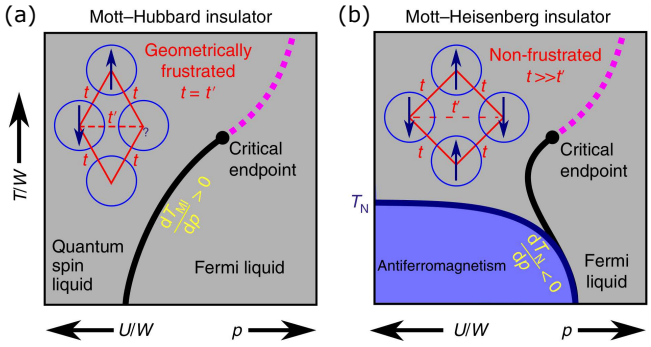

Figure 2.3: $p - T$ phase diagram for the Mott insulator hosting a QSL state (a) and a AFM state (b) at low temperatures. Note the different shapes of the phase boundaries (black solid lines) for the QSL and the AFM ordered case. Reproduced from Ref. [20].

The slope of the phase boundary is determined by the Clausius-Clapeyron equation $\frac{dT}{dp} = \frac{\Delta V}{\Delta S}$ [71], with V being the volume and S the entropy of the systems. In the AFM state, the entropy of the Mott insulator is smaller then in the metallic state, such that the entropy increases ($\Delta S > 0$) upon crossing the phase transition from the insulating to the metallic side while the volume deceases ($\Delta V < 0$) as this is achieved with applying pressure. Consequently $\frac{\Delta V}{\Delta S} < 0$ and the boundary line exhibits a negative slope. At temperatures above T_{N}, the entropy in the insulating state rises due to thermal fluctuations, eventually exceeding the entropy on the metallic side and resulting in a positive slope of the boundary line. Overall, a s-shaped phase boundary is achieved for the Mott insulator featuring AFM order. In the Mott insulator hosting the QSL state, the large entropy of the fluctuating spins in the insulating state exceeds the one in the metallic side already at $T = 0$, leading to qualitatively different phase boundary with monotonous positive slope [20].

2.3.1 Spinons at the Mott-transition

In contrast to magnons, the bosonic spin excitations in an AFM, spinons are fermions obeying the Fermi-Dirac statistics. This poses the questions, whether the spinon Fermi liquid realized in the insulting QSL state is compatible with the charge Fermi liquid in the adjacent metallic state [72, 73] and how the conceivable transformation of a spin Fermi surface to a conventional charge Fermi surface upon crossing the phase boundary might interfere with the Mott transition in a QSL.

One attempt to theoretically tackled this issue was provided by T. Senthil via a mean-field approach including fluctuations [23] which yielded the schematic phase diagram shown in Fig. 2.4. A cross over at T^* (dashed black line) from a quantum critical region to

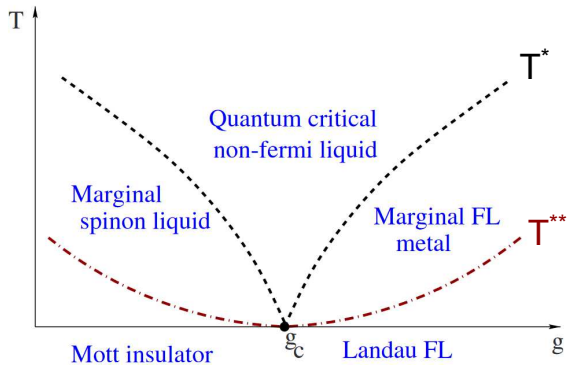

Figure 2.4: Possible theoretical scenario for the Mott transition from a spin liquid to a Fermi liquid. Plotted are the temperature scales T^* and T^{**} separating various regimes over the tuning parameter g, which in experiment can be pressure. Reproduced after Ref. [21].

a marginal Fermi liquid and to a marginal spinon liquid on the metallic and insulting side, respectively, is predicted, following the critical scaling $T^* \propto |g - g_c|^{\nu}$ with the tuning parameter g and the exponent $\nu \approx 0.67$. The Landau Fermi liquid and the Mott insulator hosting a spinon Fermi surface is achieved at $T^{**} \propto |g - g_c|^{2\nu}$ (dash-dotted red line). At zero temperature, a sharp Fermi-surface remains at the critical point although the Landau quasi particles die out and the Mott transition is considered to be continuous. Moreover, a divergence of the effective mass and an universal resistivity jump of the order of the von Klitzing constant $R_{\mathrm{K}} = \frac{h}{e^2}$ [74] right at the transition are predicted [21]. However, experimental evidence for this scenario is sparse [17].

On the other hand by combining RVB with dynamical mean field theory (DMFT), Lee, Florens and Dobrosavljević conclude, that the two Fermi surfaces do not merge at the Mott transition [22]. Spinons are well defined only deep in the insulating state and are destroyed by charge fluctuations upon approaching the Mott transition, which is predicted to be of first order even at zero temperature. In an intuitive picture, the spin follows the charge as soon as the electron start to delocalized, denying the existence of a coherent spinon Fermi-surface.

2.4 Dynamical mean field theory

The development of dynamical mean field theory (DMFT) yielded a very successful theoretical framework to approach electronic correlations and the Mott transition with a non-perturbative treatment [10, 12, 75]. It considers a single lattice site and estimates its environment with an self-consistently determined effective medium. In contrast to con-

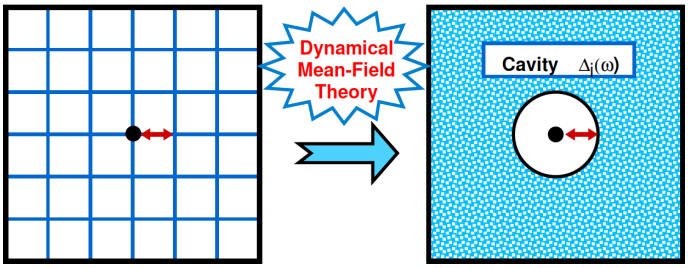

Figure 2.5: Dynamical mean field theory considers a single site and replaces its environment with a self-consistently determined effective medium. The local single-particle spectral function Δ_i describes the dynamics of electrons passing through the cavity around a given site i. Reproduced after Ref. [10].

ventional mean field theories, the description of the environment is not static but includes information about the dynamics of electrons passing through the given site. This is done via introducing a local single-particle spectral function Δ_i in a cavity surrounding the site i, as illustrated in Fig. 2.5, which can be interpreted as the available electronic states for an electron when leaving the cavity.

The from of Δ_i is adaptable to capture electronic correlations and/or disorder [12]; in absence of disorder Δ_i is the same for all sites. Fig. 2.6 shows Δ_i for a metal and a Mott insulator while the green dashed line indicates the Fermi energy. For broad bands when the on-site Coulomb repulsion is negligible, a metal is realized and Δ_i is finite at the Fermi energy. For a Mott insulator, the strong on-site Coulomb repulsion results in a gap of Δ_i at the Fermi energy, thus providing a natural oder parameter description for the Mott transition [10].

DMFT becomes exact in the limit of large coordination and maximal frustration, i.e. long-range and frustrating intersite hopping, and denies any magnetic or long-range ordering, making it the perfect choice to theoretically investigate the Mott transition in frustrated systems. Moreover, it is most reliable in the high-temperature region where incoherent behavior prevails and any spatial correlations effects become negligible. It therefore is not restricted to the transition region but correctly predicts many features at elevated temperatures which are experimentally observed in correlated electron systems at 1/2-filling with striking agreement. They are nicely summarized in Fig. 2.7 presenting the phase diagram for the maximally frustrated one-band Hubbard model as obtained by DMFT [25]. In the following, we will shortly overview the most relevant phenomena, such that we can conveniently refer to them later.

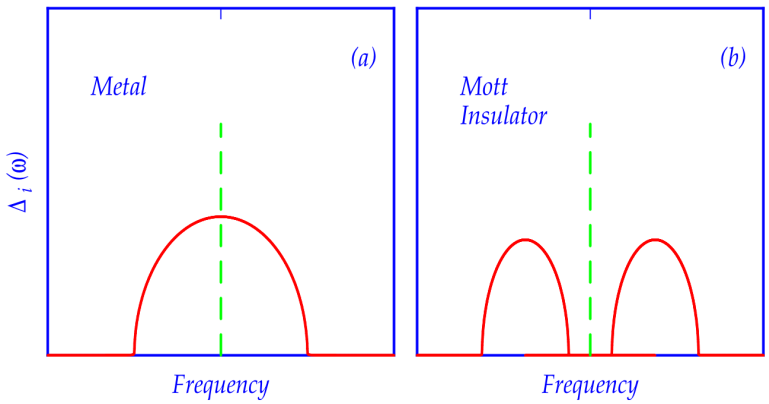

Figure 2.6: The local single-particle spectral function $\Delta_i(\omega)$ captures the dynamics of electrons passing through a given site and represents an order parameter for the Mott IMT. (a) For metallic behavior of the electron system, $\Delta_i(\omega)$ is finite at the Fermi energy (green dashed line) indicating available states to which electrons can delocalize to. (b) In the Mott insulating phase, $\Delta_i(\omega)$ is gapped at the Fermi energy and the electrons are localized on the site. Reproduced after Ref. [10].

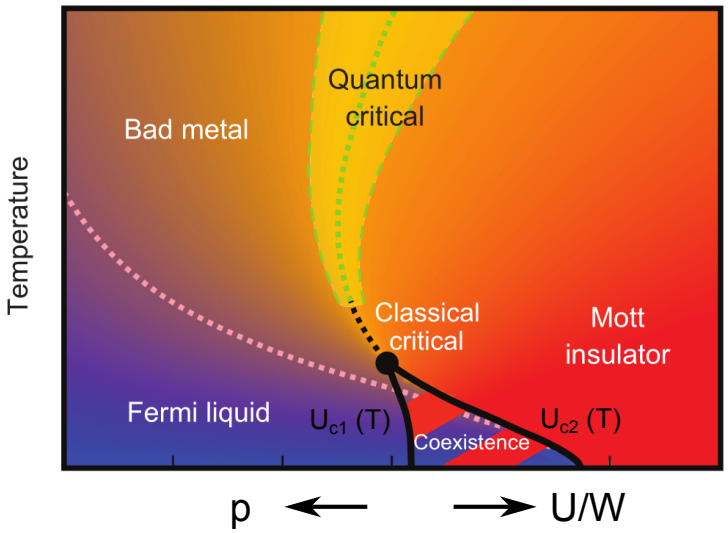

Figure 2.7: Phase diagram of the half-filled maximally frustrated Hubbard model as obtained by DMFT. The black solid lines U_{c1} and U_{c2} indicated the spinodals of the insulating and metallic phases, respectively. Most importantly, a phase coexistence region is predicted in between the two spinodals and below the critical point (black circle). The black dashed extension of U_{c1} is the quantum Widom line marking a gradual cross over from more insulating to more metallic transport properties which also features quantum critical scaling. The deep blue color represents areas of small resistivity and bright red of large resistivity while the yellowish region indicates quantum critical scaling. Reproduced after Ref. [25].

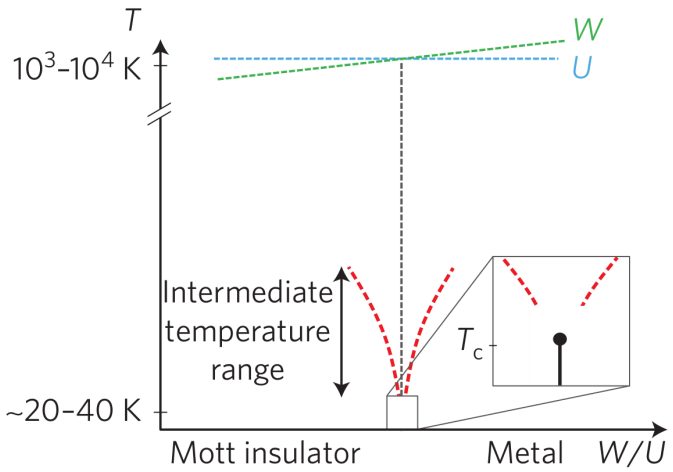

Figure 2.8: Schematic phase diagram of the Mott IMT. The competing energy scales are the bandwidth W and the Coulomb repulsion U which both are of the order $10^3 - 10^4$ K. For the critical end point of the transition usually $T_{\mathrm{crit}} < 100$ K is found, giving rise to an intermediate temperature $T_{\mathrm{crit}} < T \ll U, W$ where the system is on the verge of instability featuring quantum critical behavior. Reproduced after Ref. [39].

Phase Coexistence at the Mott transition

At low temperatures, the Mott insulating phase (red region) is separated from the metallic phase with Fermi liquid behavior (blue region) by a phase coexistence region associated to the first-order nature of the Mott transition. The coexistence region lies in between the metallic and insulating spinodals $U_{c1}(T)$ and $U_{c2}(T)$, respectively, and hosts spatially separated metallic and insulating puddles. Starting from a purely insulating phase, metallic puddles nucleate and grow upon decreasing the interaction strength U/W, for instance by applying external pressure. At the associated first-order transition line, a continuous path of metallic puddles is formed throughout the system in a percolation like manner such that the transport properties of the systems drastically change. The first oder transition line terminates at the critical end point at $T = T_{\mathrm{crit}}$ (black circle) featuring classical Ising scaling in its immediate proximity [76]. The phase coexistence was first indicated by a pronounced hysteresis in resistivity measurements [40, 69] and recently also by spatially resolved scanning near-field microscopy [77–79]. As a main outcome of this thesis, we will show that dielectric spectroscopy is an appropriate tool to unequivocally proof the presence of a coexistence phase and hence the first-order nature of a transition.

Quantum critical scaling and the Quantum widom line

The competing energy scales at the Mott transition are the bandwidth W, as a measure for the kinetic energy of the electrons, and the on-site Coulomb repulsion U. Usually U and W are of the order of eV, equivalent to $10^3 - 10^4$ K, while T_{crit} is in the range of several tens to a few hundreds K and about three orders of magnitude lower. This gives rise to a broad intermediate temperature range $T_{\mathrm{crit}} < T \ll U, W$, as illustrated in Fig. 2.8, where the system is on the verge of instability featuring quantum critical behavior. The latter is precisely described by DMFT [24, 25] predicting a more continuous cross over from the insulating to metallic side for $T > T_{\mathrm{crit}}$. In analogy to supercritical fluids, where the Widom line loosely separates regions with more liquid-like and more gaseous-like characteristics, the quantum Widom line (QWL) marks the crossover from more insulating to more metallic regions in a Mott insulator at elevated temperatures. A corresponding scaling of the resistivity curves was predicted by DMFT [24, 25] and recently verified in several organic dimer Mott insulator with remarkable agreement [17, 20, 39, 69].

Fermi liquid and Bad metal behavior

At low temperatures on the metallic side, a Fermi liquid region is found (blue region) where the effect of correlations is mapped onto well defined Landau quasi-particles (QP) by renormalization. Experimentally, the Fermi liquid is characterized by $\rho \propto T^2$ behavior in dc-transport consisting up to the coherence temperature T_{FL} and in optics with a scattering rate $\gamma \propto \omega^2$. At temperatures well exceeding T_{FL}, the T^2-behavior in $\rho(T)$ crosses over into a linear one and the optical conductivity $\sigma(\omega)$ reveals a transformation of the Drude peak at $\omega = 0$ to a far-infrared peak which significantly broadens and shifts to higher frequencies upon heating [80]. In the framework of DMFT [11, 26], this temperature range hosts well-defined QP excitations, so called resilient quasi-particles, which continuously dissolve upon further increasing T. In many correlated materials, such as Cuprates [81, 82], Vanadates [83] and organics [80], the T-linear increase in $\rho(T)$ upon heating up violates the Mott-Ioffe-Regel limit [84], where the mean free path between two scattering events of a charge carriers equals the lattice spacing $l \approx a$. This marks the cross over to bad metal behavior and resilient QP have completely disappeared.

3

Organic charge transfer salts as model compounds to study electronic correlations

In this chapter, we briefly introduce organic charge-transfer salts as model systems to study electronic correlations. Starting from some general considerations with special emphasis on their high tuneability, we will then go into detail for the κ-(BEDT-TTF)$_2$Cu$_2$(CN)$_3$, κ-[(BEDT-STF)$_x$-(BEDT-TTF)$_{1-x}$]$_2$Cu$_2$(CN)$_3$ and κ-(BEDT-TTF)$_2$Ag$_2$(CN)$_3$ salts which are investigated in this thesis. We briefly summarize their properties and give a collection of the open questions. Finally, we conclude this chapter with an overview of the anomalous dielectric response observed in the insulating state of numerous organic charge transfer salts.

3.1 Organic charge transfer salts

The organic charge transfer salts are a rather young class of materials which became valuable model systems in solid state research. Their modular composition with different sets of organic donor molecules D in combination with various atomic or molecular acceptors X turned out to be extremely versatile for tailoring systems with desired properties [2].

The electron donors D have a sufficiently low ionization energy I_0, which is the energy required to remove one electron from the highest occupied molecular orbital (HOMO), such that they can be easily reduced by the acceptors X with an accordingly high electron affinity A, which is the energy released by filling the lowest occupied molecular orbital (LUMO). Their combination leads to the formation of a charge transfer complex D$_m$X$_n$ according to the reaction scheme [85, 86]

$$[D_m] + [X_n] \rightarrow [D_m]^{+\delta} + [X_n]^{-\delta} \quad , \tag{3.1}$$

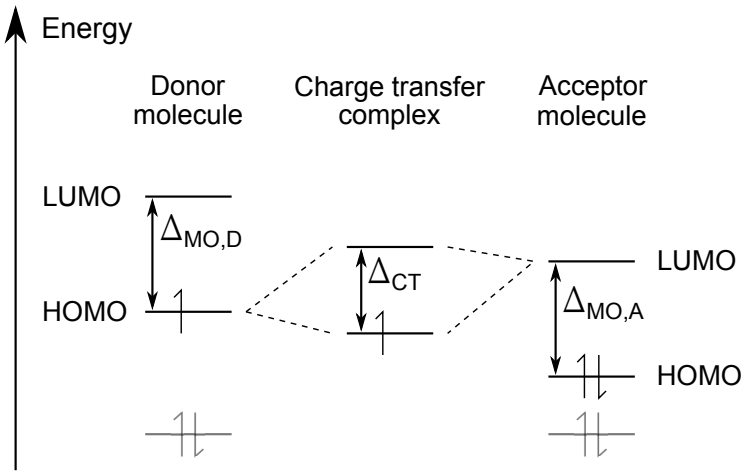

Figure 3.1: Sketch of the energy scales involved in the formation of a charge transfer complex. The distance between the HOMO and LUMO of the donor and acceptor molecule are denoted as $\Delta_{\mathrm{MO,D}}$ and $\Delta_{\mathrm{MO,A}}$, respectively. In the illustrated case, one electron is transferred from the HOMO of the donor to an energy level of the charge transfer complex which is lowered in energy due to the Coulomb interaction between the donor and acceptor molecule.

with m and n being integers and the charge transfer ration δ. The resulting electrostatic attraction between donor and acceptor stabilizes the crystals. The charge transfer requires the energy

$$\Delta_{\mathrm{CT}} = I_0 - A - C < 0 \quad , \tag{3.2}$$

where C takes into account the Coulomb-, polarization- and exchange-energy contributions [87].

Fig. 3.1 shows a scheme of the energy scales relevant for the charge transfer. Usually, the energy separation between the molecular orbitals of the constituents is much larger then the typical size of the intermolecular transfer integral t (not shown in Fig. 3.1), such that it is sufficient to describe the molecular orbitals with the HOMO and the LUMO. The distance between the HOMO and the LUMO of the donor and acceptor molecule are denoted as $\Delta_{\mathrm{MO,D}}$ and $\Delta_{\mathrm{MO,A}}$, respectively, and are usually of the order of several eVs, whereas $\Delta_{\mathrm{CT}} \approx 0.5$ eV. Hence, the energy scales can be ordered according to

$$t \ll \Delta_{\mathrm{CT}} < \Delta_{\mathrm{MO,A}} \lesssim \Delta_{\mathrm{MO,D}} \quad . \tag{3.3}$$

As a measure for the overlapping HOMOs and LUMOs between neighboring molecules, the transfer integral depends on the shape of the donor molecule and their orientation within the crystal structure which we both did not consider so far. However, in gen-

eral the overlap between neighboring donor molecules is sufficient for the formation of a HOMO and LUMO band while their overlap to the acceptors is usually negligible. The filling and the geometry of the HOMO band determine the electronic properties of the system, whereas the charge transfer band and the molecular orbital excitations are usually well above the Fermi energy. Or in other words, the charge transfer from the donors to the acceptors stabilizes the crystal whereas the electronic properties are governed by the transfer integrals between the donor molecules.

In principle, any combination of organic donors and any kind of acceptor is possible as long as Eq. 3.2 is satisfied and thus a large number of compounds could be synthesized since the beginning of the field in the 1960s. Most of the compounds are grown by electrochemical crystallization from their solution yielding high quality single crystals [88]. The most common acceptors are molecules with constituents from the chalcogens and halogens to achieve the required electron negativity, for instance X = Br, PF_6, AsF_6, SbF_6, TaF_6, SCN, FSO_3, NO_3, BF_4, ClO_4, ReO_4 and I_3.

Fig. 3.2 gives an overview of different organic donor molecules which are regularly used as building blocks in synthesizing organic charge transfer salts. Probably among the most studied are those with TMTTF (tetramethyltetrathiafulvalene) or BEDT-TTF (bis-(ethylenedithio)tetrathiafulvalene) donors, the latter sometimes is also abbreviated as ET. Most of them exhibit a planar structure and the orbitals of the constituting atoms are subject to sp^2-hybridization, resulting in molecular orbitals forming σ-bonds, which are mainly located in between the bonding constituents, as well as π-bonds extending perpendicular to the planar molecule.

Fig. 3.3 shows the HOMOs of a charge neutral BEDT-TTF molecule which are mainly centered on the sulfur atoms and the C=C double bonds. Due to the directional shape of the HOMO, the transfer integral to neighboring molecules strongly depends on the orientation of the molecules in respect to each other and favors their arrangement in stacks or layers. Moreover, the extent of the HOMO is small compared to the size of the donor molecule, usually resulting in the formation of a single, well defined band clearly separated from the other energy scales. This facilitates the design of compounds with narrow bands of reduced dimensionality, enhancing the electron density and therefore the influence of electronic correlations.

Up to now, we kept the discussion on the organic charge transfer slats very general which was tolerable for a basic introduction. Most of the arguments, however, become clearer when the actual crystal structure of a compound family is considered. Since the materials under study in this thesis belong to the (BEDT-TTF)$_2X$ salts, we will focus on them in the following.

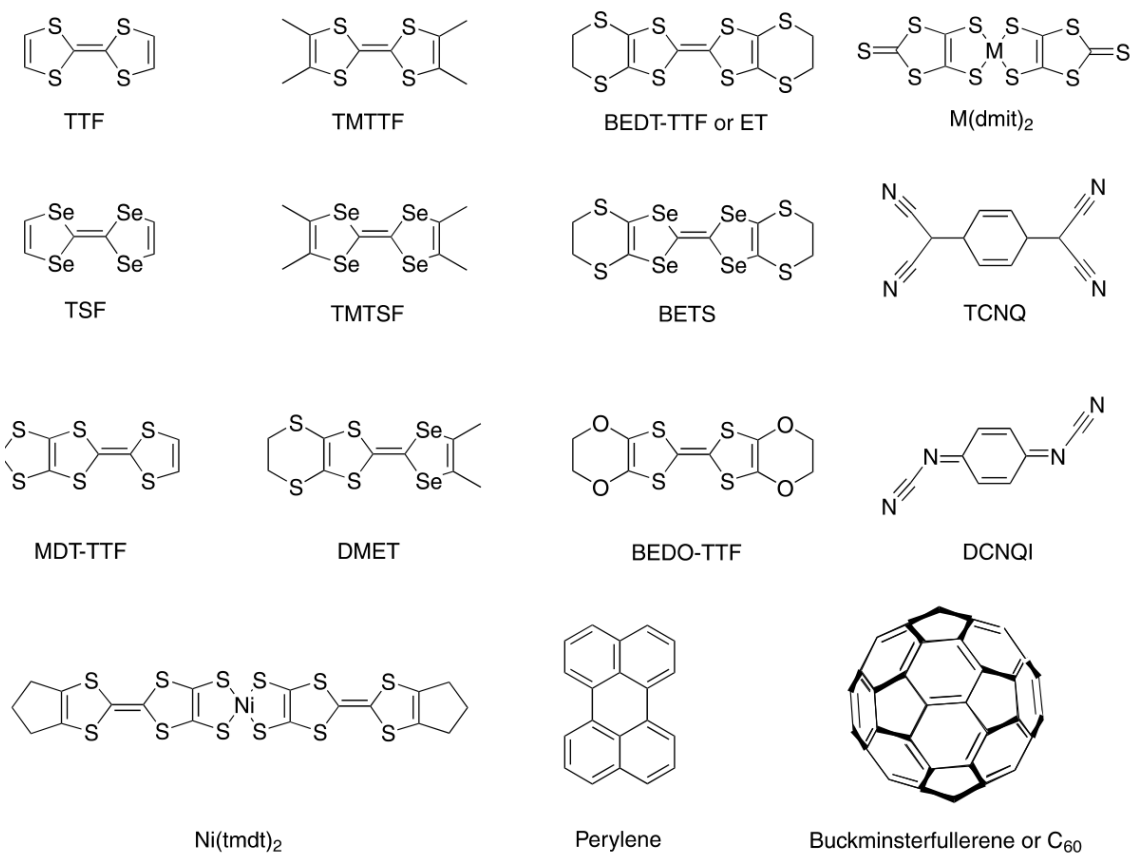

Figure 3.2: Overview of organic donor molecules which a regularly used in synthesizing organic charge transfer salts. Note the planar structure of most of the donors. Reproduced from Ref. [85].

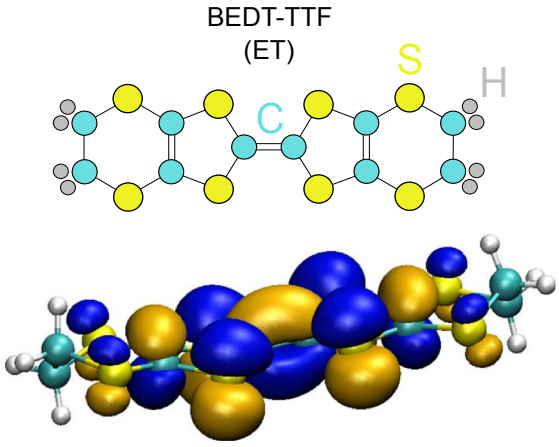

Figure 3.3: HOMO of a charge neutral BEDT-TTF molecule which are mainly centered on the sulfur atoms and the C=C double bonds. Reproduced from Ref. [89].

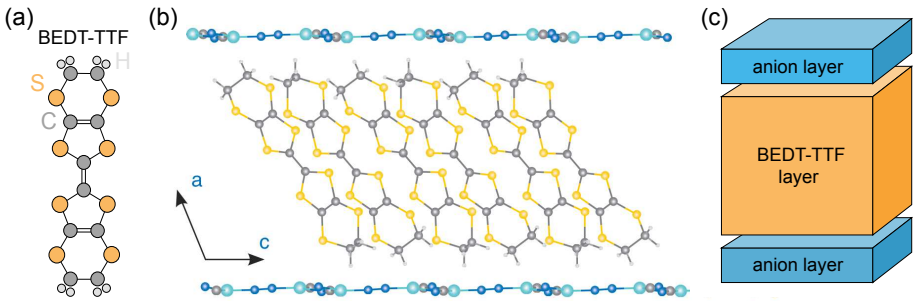

Figure 3.4: Crystal structure of the quasi-two dimensional organic charge transfer salts (BEDT-TTF)$_2X$. (a) Sketch of a planar BEDT-TTF molecule. (b,c) Typical layered structure wherein the BEDT-TTF layers (orange block) are separated by anion layers (blue blocks). Panel (b) is reproduced from Ref. [90].

3.2 Quasi-two dimensional (BEDT-TTF)$_2X$

Fig. 3.4 shows a scheme of a single BEDT-TTF molecule together with the typical structure of the (BEDT-TTF)$_2X$ salts. Most importantly, the BEDT-TTF molecules are arranged in layers alternating with layers of the acceptors X, the latter are also called anion layers. The layered structure has important implications on the physical properties of the compounds. First, the orbital overlap of the BEDT-TTF molecules to the anions is negligible small and their interaction is indirectly mediated via the hydrogen atoms in the ethylene end groups (EEG) of the BEDT-TTF molecule. On the other hand, the overlap of BEDT-TTF molecules within one layer gives rise to a quasi-two dimensional conducting layer forming a single narrow band which governs the electronic properties. This leads to a large in-plane/out-of-plane anisotropy while an in-plane anisotropy might also occur depending on the exact packing motif the of the BEDT-TTF molecules within one layer. Secondly, the reduced dimension of the quasi-two dimensional electron system with a narrow band enhances the electron density and amplifies the influence of electronic correlations.

3.2.1 Packing motifs

A large number of (BEDT-TTF)$_2X$ salts were synthesized so far while often more structures of the same composition exist, which are distinguished by the specific pattern of the arrangement of the BEDT-TTF molecules within one layer. This is usually referred to as the packing motif which is denoted with a greek letter as a prefix to the salt name. Fig. 3.5 shows the most common packing motifs in a top view of the BEDT-TTF layer. The packing motif determines the unit cell, indicted by the gray rectangle, and leads to different transfer integrals between the molecules giving rise to an in-plane anisotropy of the electronic properties.

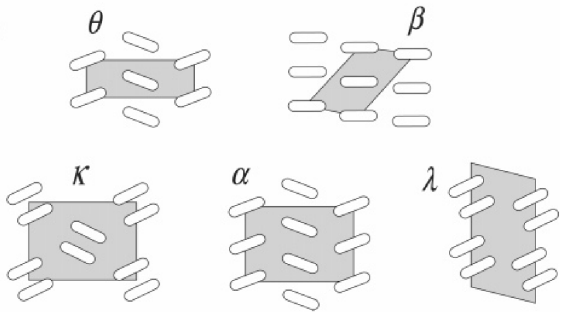

Figure 3.5: Arrangement of the BEDT-TTF molecules within one layer, also called packing motif. It determines the unit cell, indicted by the gray rectangle, and influences the transfer integrals between the molecules. Also, different crystals structures of the same chemical composition exist which are only distinguished by the packing motif. The κ and λ packings feature a dimerzation of the BEDT-TTF molecules, such that each dimer can be regarded as one lattice site resulting in an 1/2-filled system. Reproduced from Ref. [1, 85].

3/4-filling vs. 1/2-filling

Moreover, besides the charge transfer and the stoichiometry, the packing motif can influence the band filling. Usually, each anion receives one electron from the BEDT-TTF layer making it monovalent X^-. Then the D_2X stoichiometry implies positively charged cations $(BEDT\text{-}TTF)^{+1/2}$. As a result, most $(BEDT\text{-}TTF)_2X$ salts exhibit a 3/4-filled band which then is subject to electronic correlations. In this case, electronic correlations in form of the on-site U and the inter-site Coulomb repulsion V have to be considered. In case of a sufficiently narrow band this leads to a charge ordered insulting state which is usually non-magnetic.

On the other hand, in some packing motifs the BEDT-TTF molecules form dimers and the intra-dimer transfer integral is much larger then the inter-dimer, for instance in the κ or λ packing, such that each dimer can be regarded as one entity forming a lattice site. This doubles the unit cell and opens a dimerization gap leading to an effectively 1/2-filled system. For a narrow band the on-site Coulomb repulsion of a dimer can be sufficient to induce a Mott insulting state, also referred to as dimer Mott insulator. Depending on the geometrical arrangement of the dimers this is accompanied with AFM order or a QSL state, as discussed in detail in chapter 2. Fig. 3.6 displays selected packing motifs with the corresponding band filling wherein the dimers in the κ and λ packing are indicated by red circles.

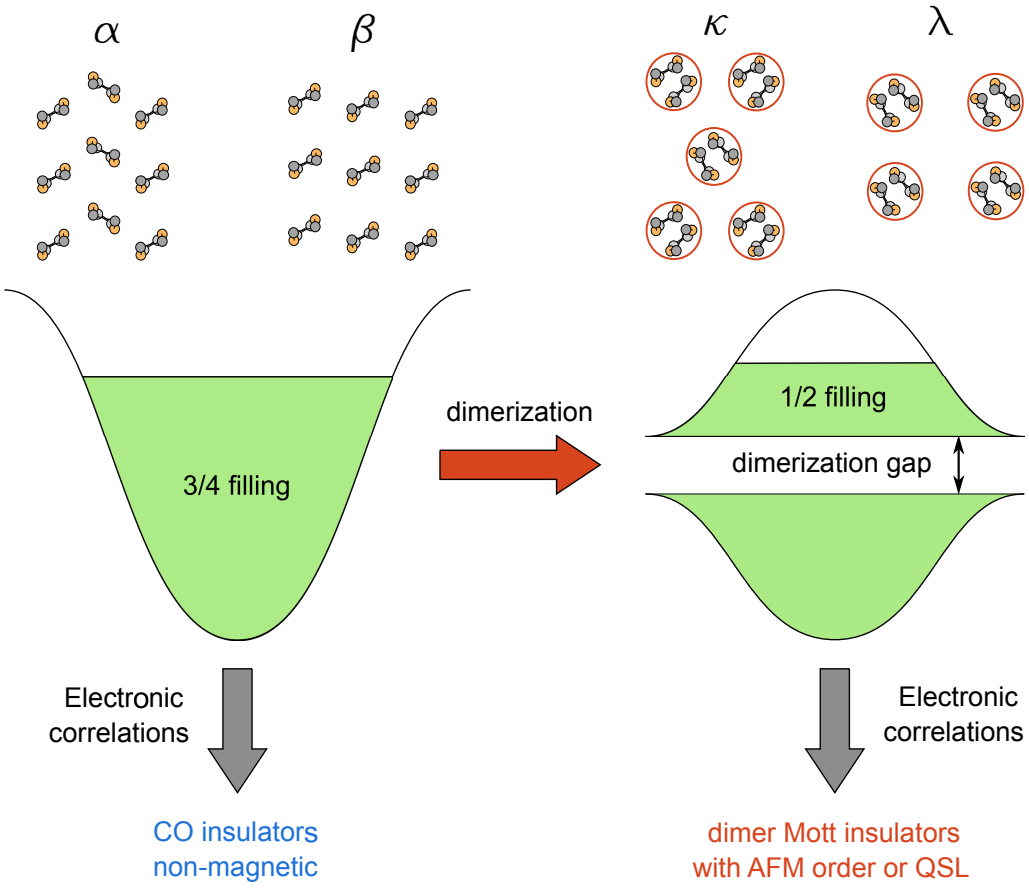

Figure 3.6: Influence of the packing motif of the BEDT-TTF molecules on the band filling. The A_2B stoichiometry and the charge transfer of one electron to each anion X^- implies $(BEDT\text{-}TTF)^{+1/2}$. This leads to a 3/4-filled band, as for instance in the α and β packing motifs, which subsequently can be subject to electronic correlations such that a charge ordered (CO) state is realized. In case of sufficient dimerization, realized for example in the κ and λ packings, each dimer can be regarded as one entity forming a lattice site, which are indicated by the red circles. As a result, the unit cell is doubled and a dimerization gap opens, leading to to an effectively 1/2-filled band. Electronic correlations then can lead to a Mott insulting state which can host an anti-ferromagnetic (AFM) ordered or a quantum spin liquid (QSL) state.

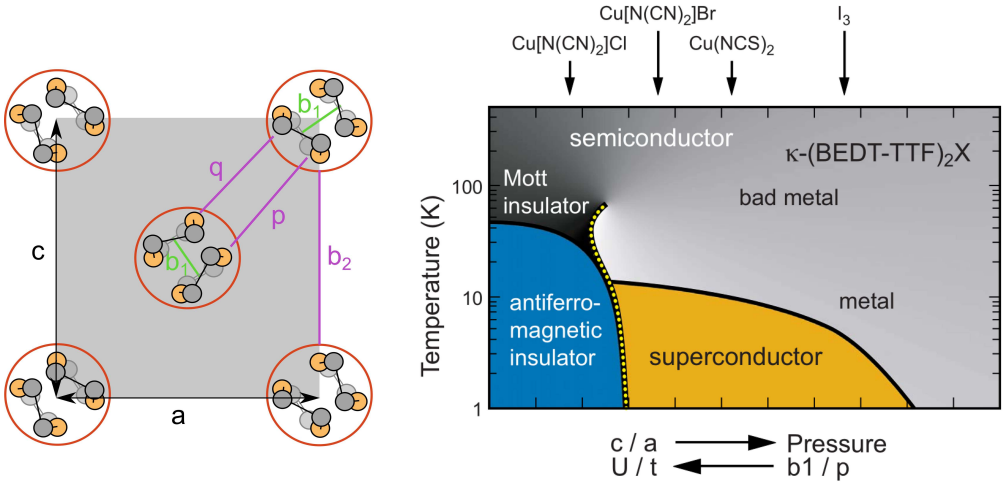

Figure 3.7: Generic phase diagram of the κ-(BEDT-TTF)$_2X$ salts and notation of the lattice parameters and transfer integrals as used in Refs. [91, 92]. Substituting the anions X influences the transfer integrals b_1 and p, resulting in a change of the effective strength of electronic correlations U/t. The same effect is also achieved by applying external pressure, reducing the band overlap by decreasing the lattice parameters a and c, such that the influence of electronic correlation diminishes upon increasing the pressure. The phase diagram is reproduced after [92].

Table 3.1: Lattice parameters and transfer integrals of selected κ-(BEDT-TTF)$_2X$ salts as reported in Ref. [91]. The assignment of the parameters is illustrated in Fig. 3.7. In particular, the inter-dimer transfer integral b_2 considerably changes upon substituting the anion X. Reproduced after Ref. [91].

X	T	b_1	b_2	p	q	a	b	c
Cu[N(CN)$_2$]Br	127 K	26.5	9.8	10.9	-3.8	12.878	29.681	8.484
Cu[N(CN)$_2$]Cl	127 K	27.3	10.4	10.5	-3.9	12.909	29.658	8.418
Cu(NCS)$_2$	104 K	27.2	11.1	11.9	-3.2	12.855	32.718	8.418

3.2.2 Tuning electronic correlations by chemical substitution

Up to now, the anion layers were solely considered as spacers in between the BEDT-TTF layers. Besides the packing motif, however, the arrangement of the BEDT-TTF molecules is also influenced by the choice of the anions X, eventually changing the lattice parameters and the transfer integrals. In this regard, one benefits from the possibilities that come with the inherent flexibility and control of chemistry for tuning the electronic properties and the influence of electronic correlations. As a well studied example, we review here the κ-(BEDT-TTF)$_2X$ salts with X=Cu[N(CN)$_2$]Cl, Cu[N(CN)$_2$]Br and Cu(NCS)$_2$ [39, 69, 90–99]. Tabel 3.1 lists the lattice parameters and the overlap integrals for X=Cu[N(CN)$_2$]Cl, Cu[N(CN)$_2$]Br and Cu(NCS)$_2$, as reported by *Mori* and collaborators in Ref.[91]. Thereby, we also follow their notation which is illustrated in Fig. 3.7. At this point it is important to emphasize, that the little change of the overlap integrals b_1 and p modifies the influence of electronic correlation. The on-site Coulomb repulsion on a dimer can be roughly estimated by $U \propto 2b_1$ [100] and the transfer integral with $t \propto p$. Upon substituting X=Cu[N(CN)$_2$]Cl with Cu[N(CN)$_2$]Br, the effective Coulomb repulsion U/t is reduced and the compound undergoes a Mott transition. By qualitatively comparing experimental observations, such as transport and magnetic properties, a generic phase diagram can be constructed, as shown in Fig. 3.7. Moreover, the salts with X=Cu[N(CN)$_2$]Cl and Cu[N(CN)$_2$]Br are isostructural and the properties can even be fine tuned by partially substituting Cl with Br [99].

Another procedure to chemically control the bandwidth is to partially substitute the donor BEDT-TTF molecules with one of its derivatives, such has the BEDT-STF or the BETS molecule [103–106]. Fig. 3.8 shows the generic phase diagram of λ-D_2GaCl_4 which is based on dc-transport [105] and ^{13}C-NMR measurements [101, 102] together with the molecular structure of the donor molecules D. Upon substituting the center S atoms ([Ne]3s^{2}3p^4) with larger Se atoms ([Ar]3d^{10}4s^{2}4p^4) and thereby replacing 3p with 4p electrons in the formation of the molecular orbitals, their overlap is drastically enhanced resulting in an effective increase of the bandwidth W. To that end, this provides another way to realize the bandwidth-controlled Mott transition in the (BEDT-TTF)$_2X$ salts.

3.2.3 Tuning electronic correlations with pressure

In contrast to chemical substitution, hydrostatic pressure allows in principle a continuous sweeping through the phase diagram and pressure-dependent dc-transport became a common tool to probe insulator-metal transitions. In that aspect, the organic charge transfer salts are advantageous because their composition of organic molecules makes them rather soft. A pressure of a few kilobars is often sufficient to induce a drastic change of their elec-

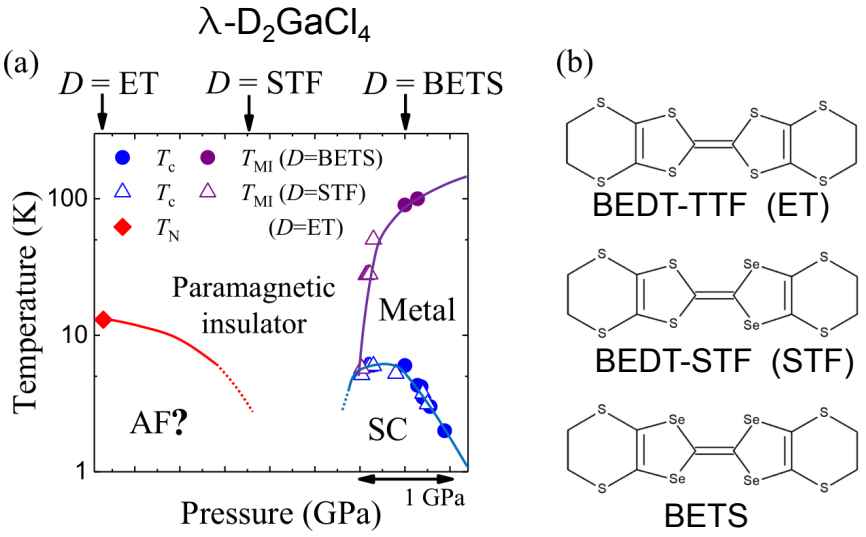

Figure 3.8: (a) Generic phase diagram of λ-D_2GaCl_4 upon substituting the donor molecules D, whose molecular structure is shown in panel (b). The center S atoms are replaced with the larger Se atoms, leading to a drastic enhancement of the molecular overlap and the bandwidth. As a result, substituting D provides an additional way to realize the bandwidth-controlled Mott transition in the (BEDT-TTF)$_2X$ salts. Reproduced from Refs. [101, 102].

tronic properties [2] which can be easily reached with piston type pressure cells or He-gas pressure cells [107, 108]. A well studied example is again κ-(BEDT-TTF)$_2$Cu[N(CN)$_2$]Cl, which undergoes a Mott insulator-metal transition (IMT) already at a pressure of 300 bar [39, 69, 96]. In Fig.3.9, the phase diagram in vicinity of the Mott transition and the underlying pressure-dependent dc-transport measurements are reproduced from Ref. [69]. The transport properties and the observed crossover lines are successfully predicted by DMFT. In particular renormalization group calculations within the framework of DMFT, indicated by the solid lines in Fig. 3.9(b), are in good agreement with temperature-dependence of the in-plane resistivity.

3.2.4 Disorder in the BEDT-TTF configuration

The BEDT-TTF molecules occur in two different configurations in respect to the orientation of their ethylene end groups (EEG), the staggered and the elclipesed configuration, which are both illustrated in Fig. 3.10. Low-frequency fluctuation spectroscopy measurements reveal a glassy freezing of the EEGs in various members of the κ-(BEDT--TTF)$_2X$ family [110, 111] with a slightly compound dependent glass temperature T_g around 100 K. In κ-(BEDT-TTF)$_2$Cu[N(CN)$_2$]Cl, κ-(BEDT-TTF)$_2$Cu[N(CN)$_2$]Br and κ-(BEDT-TTF)$_2$Cu(NCS)$_2$ it is found, that the glassy freezing of EEGs influences the

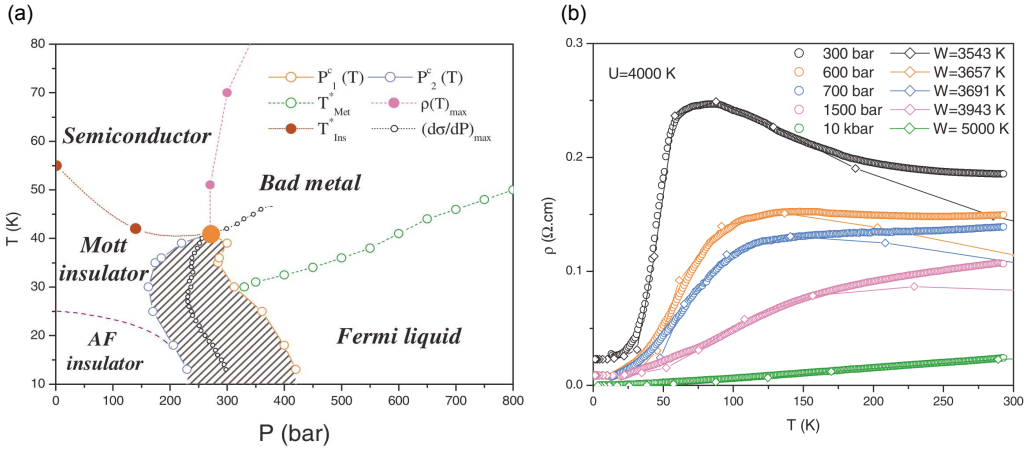

Figure 3.9: (a) Phase diagram of κ-(BEDT-TTF)$_2$Cu[N(CN)$_2$]Cl as obtained by dc-resistivity measurements in a He-gas pressure cell. Around a pressure of 300 bar, the Mott IMT is observed. The black shaded area indicates the region with pronounced hysteresis in the resistivity upon tuning the pressure at constant temperature. (b) The resistivity cures are well fitted with DMFT. Reproduced from Ref. [69].

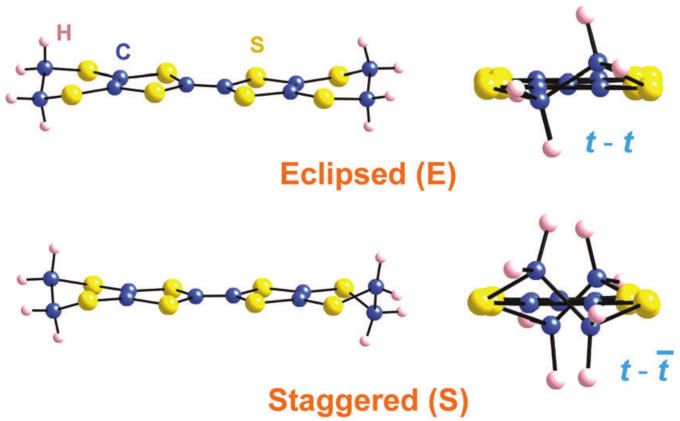

Figure 3.10: Eclipsed and staggered configuration of the ethylene end groups (EEG) of a BEDT-TTF molecule. Reproduced from Ref. [109].

Table 3.2: Lattice parameters of κ-CuCN at 300 K and κ-AgCN at 150 K as reported in literature.

	a (Å)	space group	b (Å)	c (Å)	α (°)	β (°)	γ (°)
κ-CuCN [62]	$P\bar{1}$	16.1221	8.591(6)	13.413	89.99(2)	113.43	90.01
κ-AgCN [30]	$P2_1/c$	15.055	8.7031	13.412	–	91.307	–

electronic properties as demonstrated by cooling rate-dependent transport measurements [110, 111].

3.3 Organic spin liquid compounds κ-(BEDT-TTF)$_2$Cu$_2$(CN)$_3$ and κ-(BEDT-TTF)$_2$Ag$_2$(CN)$_3$

Recently, the dimer Mott insulators κ-(BEDT-TTF)$_2X$ with X=Cu$_2$(CN)$_3$ and Ag$_2$(CN)$_3$, in the following abbreviated with κ-CuCN and κ-AgCN, respectively, draw a lot of attention since they are considered to host a quantum spin liquid state. Both compounds exhibit the typical layered structure of the (BEDT-TTF)$_2X$ salts (cf 3.2) which is exemplary shown in Fig. 3.11(a) for κ-CuCN. For both compounds, the X-ray structural data are solved in the $P2_1/c$ space group [33, 60]. Very recently, Pouget and collaborators [62] thoroughly investigated the crystal structure of κ-CuCNand discovered a triclinic $P\bar{1}$ symmetry with two inequivalent dimers in the unit cell, implying a weak charge imbalance between dimers in the whole temperature range. The lattice parameters are listed in Table 3.2.

Within one BEDT-TTF layer, the donor molecules form dimers, indicated by the red circles in Fig. 3.11(b), which are arranged on a triangular lattice. Each dimer transfers one electron to the anion layer, leaving behind one electron (or hole) per dimer. The intra-dimer transfer integral t_d is clearly larger then the inter-dimer integrals t and t', which are listed in Table 3.3, such that each dimer is considered as one lattice site resulting in a 1/2-filled band. Moreover, a spin 1/2 system on a triangular lattice is formed with values of t and t' close enough to each other to promote geometrical frustration.

The $[\mathrm{Cu_2(CN)_3}]^-$ and $[\mathrm{Ag_2(CN)_3}]^-$ anions polymerize constituting two-dimensional networks which are depicted in Fig. 3.11(c) and (b), respectively. They from keyholes or openings with a hexagonal shape for κ-CuCN and a rather rectangular one for κ-AgCN. Additionally, three dimers from the overlying BEDT-TTF layer are shown to illustrated their arrangement relative to the anion layers. For κ-CuCN, the dimers are located right above the hexagonal openings in the anion layer whereas for κ-AgCN, they lie on top of

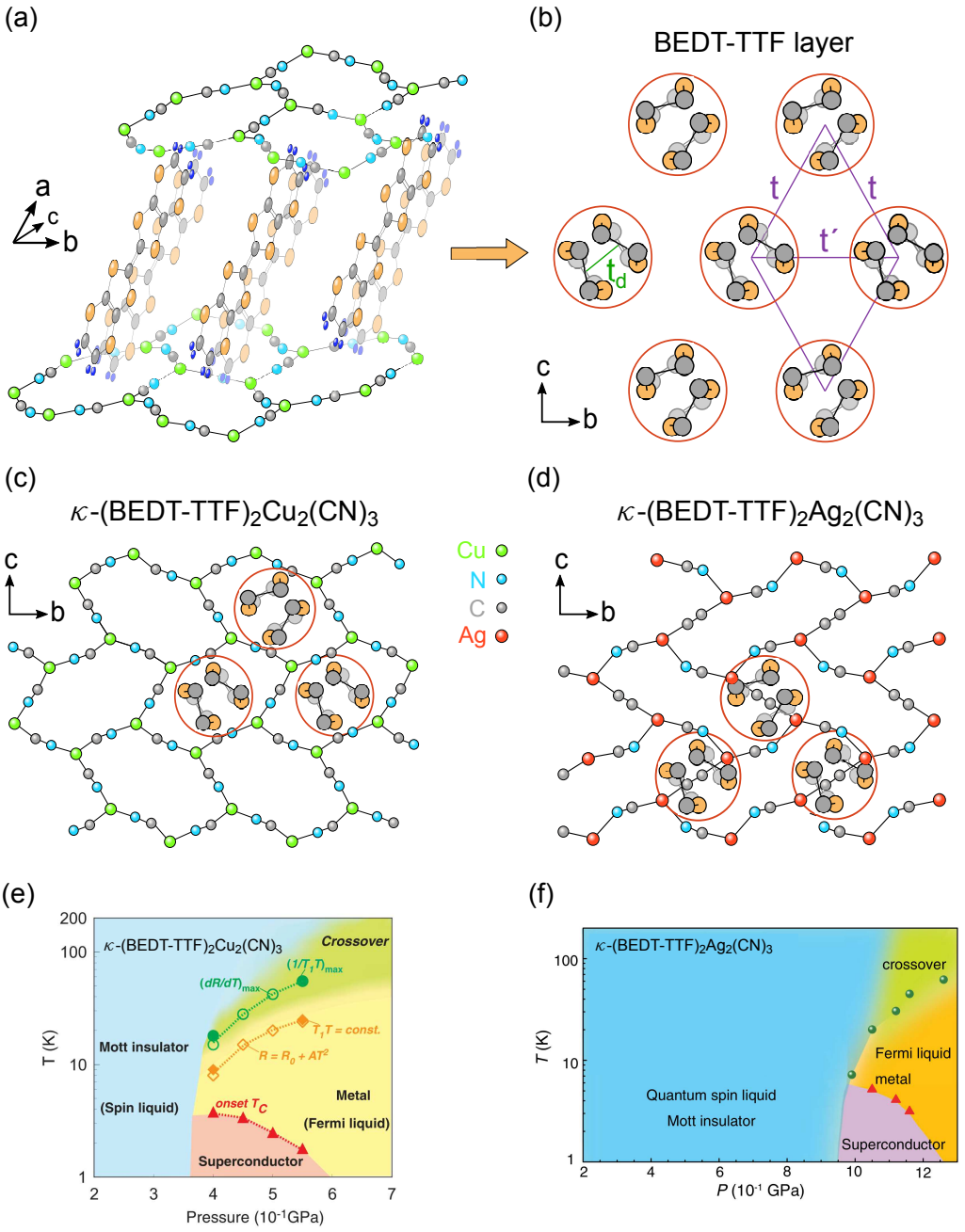

Figure 3.11: (a) Scheme of the layered crystal structure of κ-(BEDT-TTF)$_2X$ with X=Cu$_2$(CN)$_3$ or X=Ag$_2$(CN)$_3$. (b) Top view on one BEDT-TTF layer with the notation of the transfer integrals. The BEDT-TTF dimers are indicated by red circles. A single anion layer for X=Cu$_2$(CN)$_3$ (c) and Ag$_2$(CN)$_3$ (d) together with three dimers from the overlying BEDT-TTF layer to show their arrangement relative to the anion layer. Phase diagrams for X=Cu$_2$(CN)$_3$ (e) and X=Ag$_2$(CN)$_3$ (f). Both compounds feature a spin liquid state at low temperatures in their Mott insulting phase. Note that the Mott transition is located at higher pressures for X=Ag$_2$(CN)$_3$. Panels (e) and (f) are reproduced from Refs. [28, 30, 100].

Table 3.3: Transfer integrals in units of meV, which were calculated within a tight-binding approximation using the extended Hückel method as reported in Ref. [100]. t'/t is the degree of frustration. The calculated value for the strength of electronic correlations U/t is complemented with an experimentally determined value U/W_{exp} as reported in Ref. [20]. The magnetic properties at low temperatures depend on the degree of frustration.

X	t_{d}	t	t'	t'/t	U/t	U/W_{exp}	magnetic ordering
$Cu[N(CN)_2]Cl$	200	73	32	0.44	5.5	1.5	AFM with $T_{\mathrm{N}} = 25$ K
$Cu_2(CN)_3$	200	55	45	0.83	7.3	1.52	quantum spin liquid
$Ag_2(CN)_3$	264	53	48	0.90	10.5	1.96	quantum spin liquid

the rim next to a CN^- group linking the triangular coordination of Cu or Ag atoms. Each Cu or Ag atom is either neighbored by two N atoms and one C atom or by one N atom and two C atoms, giving rise to intrinsic disorder in the arrangement of the polar CN^- links.

The combination of geometrical frustration, inherent disorder in the anion network and quantum fluctuations impedes magnetic ordering down to mK temperatures despite a considerable high exchange coupling of $J_{\mathrm{CuCN}} \approx 240$ K [27, 48] and $J_{\mathrm{AgCN}} \approx 175$ [30] for κ-CuCN and κ-AgCN, respectively. Hence, it is well established that κ-CuCN and κ-AgCN host a QSL state at low temperatures in their Mott insulating phase [28, 29]. In contrast their sibling compound κ-$(BEDT\text{-}TTF)_2Cu[N(CN)_2]Cl$ (κ-CuCl) has a less frustrated trilingual lattice and an anion layer without disorder, such that AFM ordering is observed below $T_{\mathrm{N}} = 25$ K. At this point it is worthwhile to mention, that the AFM order in κ-CuCl can be suppressed upon introducing disorder with x-ray irradiation [59] while ^{1}H-NMR measurements do not reveal neither spin freezing, a spin gap nor critical slowing down. This indicates the formation of a QSL state in x-ray irradiated κ-CuCl and emphasizes the role of disorder for its realization.

Figs. 3.11(e) and (f) present the p-T phase diagrams of both compounds as obtained by pressure-dependent dc-transport measurements [28, 30]. First of all, we emphasize the similarity to the conceptual phase diagram of a QSL as shown in Fig. 2.3(a) with a positive slope of the Mott IMT due to the absence of long-range magnetic ordering. The pressure necessary to induce the IMT is significantly larger for κ-AgCN in comparison to κ-CuCN, indicating stronger electronic correlations for the former. This is in agreement with the effective correlation strength U/t estimated by means of *ab initio* density functional theory and extended Hückel calculations which is listed in Tabel 3.3 [20, 30, 98, 100, 112] and clearly increases from X=$Cu_2(CN)_3$ to $Ag_2(CN)_3$.

Upon crossing the IMT, a Fermi liquid with strongly renormalized Landau quasi-particles is found. A superconducting phase is observed at the critical pressure below 5 K and is

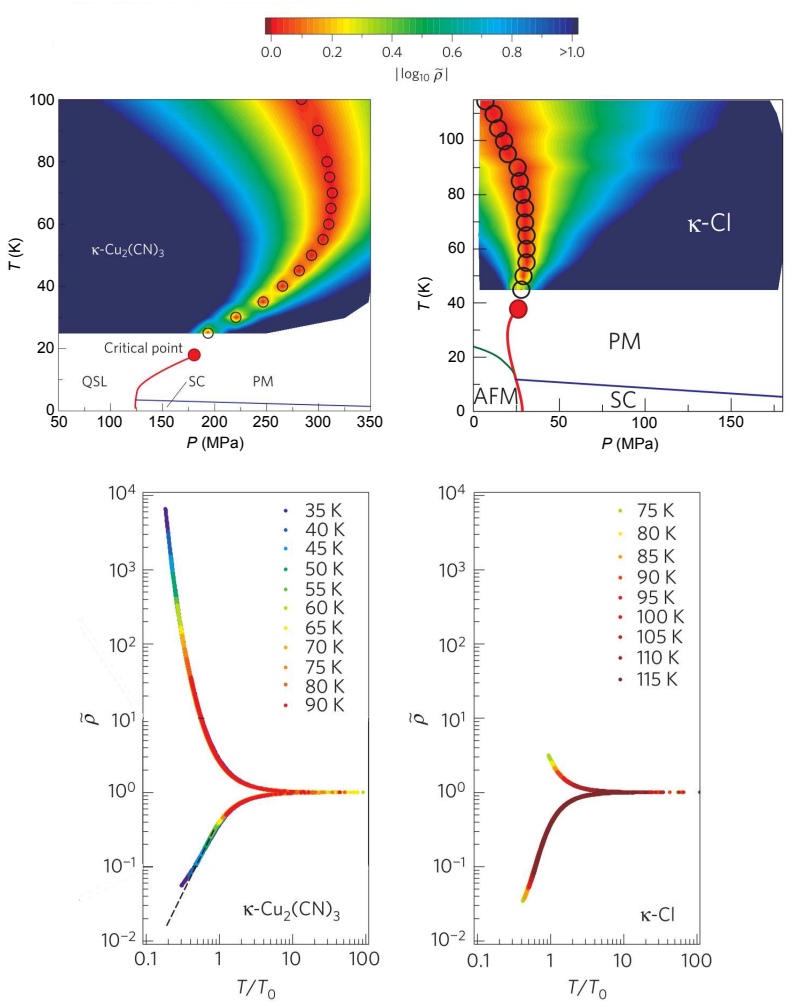

Figure 3.12: Phase diagrams of κ-(BEDT-TTF)$_2$Cu$_2$(CN)$_3$ (κ-Cu$_2$(CN)$_3$) and κ-(BEDT-TTF)$_2$Cu[N(CN)$_2$]Cl(κ-Cl) as obtained by dc-resistivity measurements in a He-gas pressure cell. The low temperature limit is set by the solidification point of the He-gas. The fan-shaped profile in $|log_{10}\tilde{\rho}|$ above the critical point, with $\tilde{\rho}$ being a normalized resistivity according to quantum critical scaling, indicates an extended cross over region which is also denoted as quantum Widom line. The lower panels demonstrate the bifurcation of $\tilde{\rho}$ into a metallic and an insulating branch when plotted over an correspondingly rescaled temperature. Reproduced after Ref. [39].

quenched to lower temperatures with increasing pressure. Upon heating, the systems exhibits signatures of bad metallic behavior with a linear temperature-dependence of the resistivity violating the Mott-Ioffe-Regel limit [11, 84]. In optics, the onset of bad metal behavior is accompanied by a transformation of the Drude peak at $\omega = 0$, originating from coherent Landau quasi-particles, to a far-infrared peak which significantly broadens and shifts to higher frequencies upon heating [80], indicating incoherent conduction processes [20, 113]. At higher temperature, the first-order transition is replaced by the QWL (cf. Ch. 2.4), a crossover region separating more insulating from more metallic behavior [20]. For κ-CuCN, quantum critical behavior in the vicinity of the QWL is observed in the resistivity measurements [39] and also magnetic torque measurements [114] are interpreted within this scenario. The former are shown in Fig. 3.12 and reveal a fan-shaped profile in $|log_{10}\tilde{\rho}|$, with $\tilde{\rho}$ being a normalized resistivity according to quantum critical scaling, as well as its bifurcation into a metallic and an insulating branch when plotted over an correspondingly rescaled temperature [17, 39].

3.3.1 κ-[(BEDT-STF)$_x$-(BEDT-TTF)$_{1-x}$]$_2$Cu$_2$(CN)$_3$

The approach to tune the bandwidth W of κ-CuCN via substituting the BEDT-TTF donors with BEDT-STF molecules (cf. Ch. 3.2.2) was recently applied by Y. Saito and collaborators [115]. Fig 3.13 shows a conceptual phase diagram of κ-[(BEDT-STF)$_x$-(BEDT-TTF)$_{1-x}$]$_2$Cu$_2$(CN)$_3$ (κ-STF$_x$-CuCN) which is based on optical spectroscopy and dc-transport measurements at ambient pressure on κ-[(BEDT-STF)$_x$-(BEDT-TTF)$_{1-x}$]$_2$-Cu$_2$(CN)$_3$ samples with various substitution levels x [116]. At the critical substitution $x_c \approx 0.12$, the system is close to the Mott insulator-metal transition and becomes metallic upon further raising x. The BEDT-STF substitution artificially distorts the triangular lattice, for low substitution level $x = 0.04$, however, the magnetic properties remain unchanged still showing the characteristics of a QSL.

3.4 6 K anomaly

Around $T^* \approx 6$ K an anomaly is observed in κ-CuCN in a variety of experiments including dielectric measurements [31], thermal expansion [117], specific heat [118], thermal conductivity [119], ultrasound propagation [120], ^{13}C NMR [48, 115], μSR [121], ESR [122], magnetic torque [114] and microwave dielectric properties [123]. In the just recently synthesized κ-AgCN, a corresponding anomaly was revealed around 20 K by ^{13}C NMR [30].

Various scenarios were proposed to explain the origin of the anomaly, among them are a spinon-pairing transition [73, 124–126] or formation of an exciton condensate [127] while

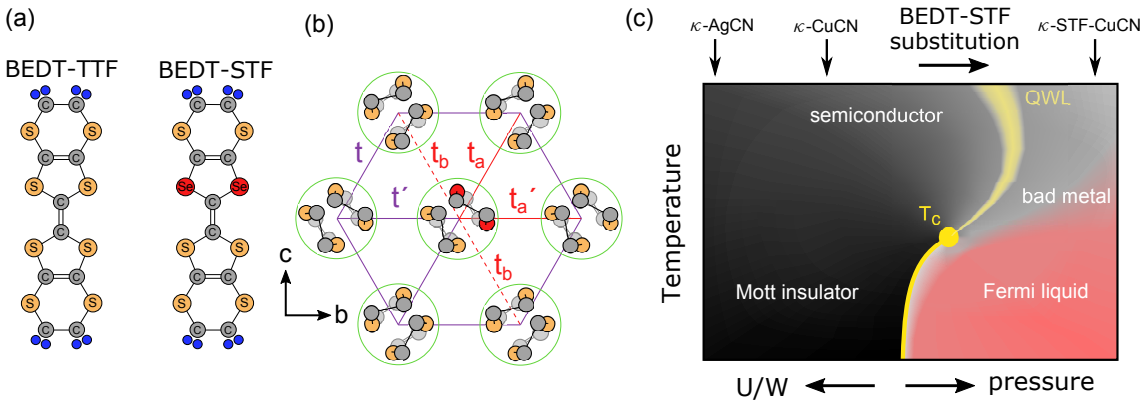

Figure 3.13: (a) Molecular structure of the BEDT-TTF and the BEDT-STF donors. (b) Sketch of a donor layer wherein the dimers a indicated by green circles. The inter-dimer transfer integrals t and t' are changed in the vicinity of the BEDT-STF molecule (red color). (c) Conceptual phase diagram of κ-[(BEDT-STF)$_x$-(BEDT-TTF)$_{1-x}$]$_2$Cu$_2$(CN)$_3$ (κ-STF$_x$-CuCN) upon increasing the substitution level x. The sibling compounds κ-AgCN is located far in the insulating state of the phase diagram.

a comprehensive explanation of all aspects of the observed anomaly remains a challenging task.

Another approach considers effects due to local spin defects which may arise from charged defects due to chemical impurities or a frozen random pattern of valence bonds [128]. Both scenarios are illustrated in Fig. 3.15, showing the triangular lattice wherein the valence bonds forming the spin-singlets are indicated by the blue thick lines. A charged defect (red dashed circle) may break a valence bond and give rise to a quasi-free local spin (blue arrow at (a)) which would explain the inhomogeneous NMR response [48, 129].

On the other hand, frozen valence bonds may arise from the disorder in the polar CN^- links which imposes a random electronic potential on the BEDT-TTF layers. This leads to a slight local modulation of the transfer integrals and thus to a weakly randomized magnetic interactions among neighboring spins. As a consequence, the fluctuation of the valence bonds is suppressed, such that they become quasi-static in a random pattern. Defects in this pattern might be present at the intersection of domains with differently oriented valence bonds and give rise to a localized quasi-free spin (blue arrow at (b)) [130, 131]. In a recent theoretical work [128], K. Riedl *et al.* propose that this randomly frozen pattern of valence bonds represents a valence bond glass (VBG) and that T^* corresponds to the onset of the corresponding freezing. For $T > T^*$, the valence bonds fluctuate constituting the QSL state, whereas for $T < T^*$ their freezing gives rise to localized quasi-

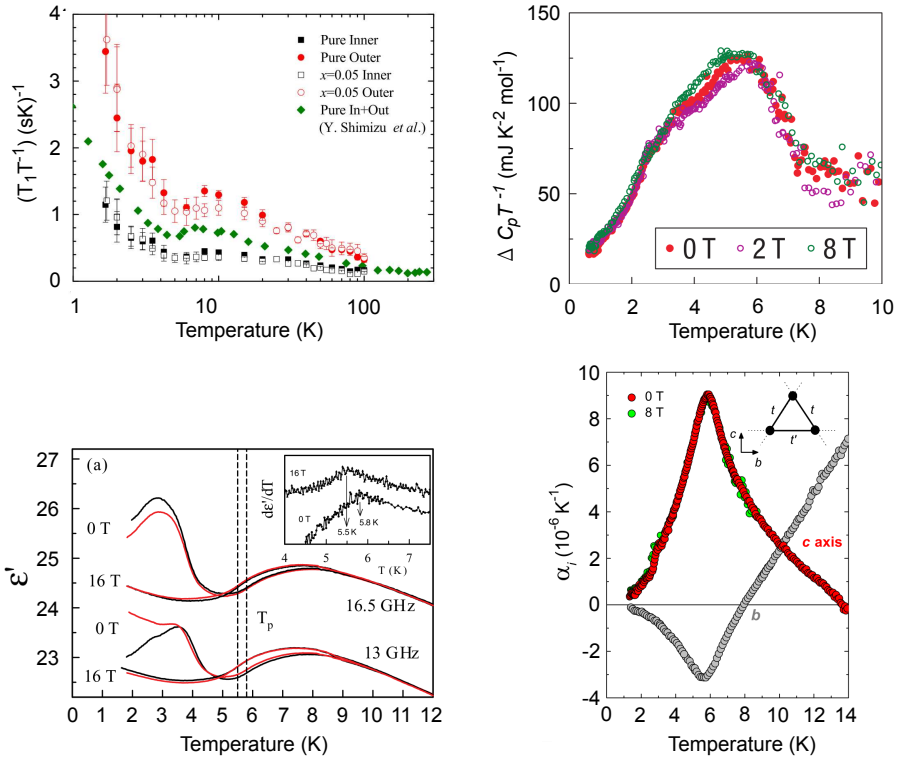

Figure 3.14: An anomaly around $T^* \approx 6$ K is observed in κ-CuCN in a variety of experiments. Here we exemplarily show its signatures in the spin-lattice relaxation time obtained by ^{13}C NMR measurements (reproduced after Ref. [115]), in thermal expansion (reproduced after Ref. [117]) and heat capacity (reproduced after Ref. [118]) as well as in the real part of the permittivity in the GHz range (reproduced after Ref. [123]).

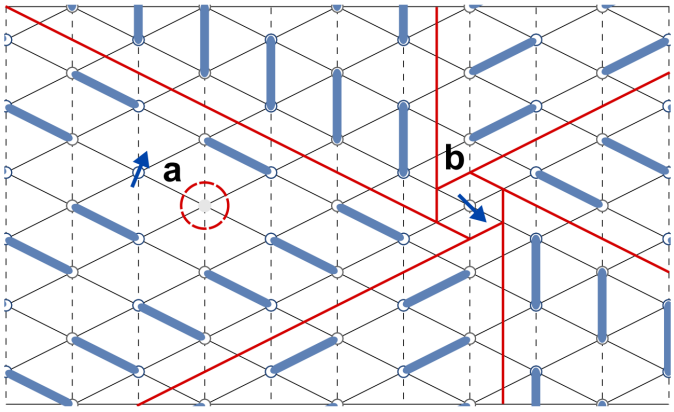

Figure 3.15: Illustration of local valence bond defects. The valence bonds forming the spin-singlets are indicated by the blue thick lines. A charged defect (red dashed circle) may break a valence bonds and give rise to a quasi-free local spin (blue arrow at (a)). In another scenario, fluctuations of the valence bonds are suppressed at low temperatures due to an interaction of the BEDT-TTF layer with the disorder in the polar CN^- links (not shown) in the anion layer. As a result, fluctuations of the valence bonds are suppressed at low temperatures leading to a quasi-static pattern of valence bonds. Local spin 1/2 defects may arise at the intersection of domains with differently oriented valence bonds (blue arrow at (b)). Reproduced after Ref. [128].

free spins which would explain the inhomogeneity in the NMR relaxation [48] and the peculiar behavior of low-temperature magnetic torque measurements [114].

3.5 Anomalous dielectric response in (BEDT-TTF)$_2X$

Besides the 6 K anomaly, dielectric spectroscopy in the audio and radio frequency also revealed a broad relaxor-type ferroelectric response (cf. Ch. 4.2.3) below 50 K and 80 K in κ-CuCN [31, 32, 137] and κ-AgCN[33, 34], respectively. Interestingly, a similar type of response is observed in various other quasi-two dimensional organic charge transfer salts which are subject to electronic correlations, mainly in the (BEDT-TTF)$_2X$ family [132, 133] and in compounds of the β'-type Pd(dmit)$_2$ salts [136]. Fig. 3.16 gives an overview of experimental findings available in literature, which by no means is complete. The characteristic signature in the permittivity is denoted as anomalous dielectric response (ADR) in the community while its explanation on a microscopic level is still lacking. In case of κ-CuCN, a corresponding feature is also observed as broad maximum in the magnetic susceptibility around 60 K [27] and in the ESR line width around 40 K [122]. The thermodynamic properties reveal an anomaly which might also be related to the ADE, in particular the specific heat exhibits a strong drop around 30 K [118] and the thermal expansion along the b-axis shows a maximum around 60 K and along c-axis a minimum around 30 K [117].

Previous attempts to link the ADR in κ-CuCN and κ-AgCN to charge disproportionation within the dimers due to intersite Coulomb repulsion, dubbed quantum electric dipole or paired-electron crystal [138–144], could not be verified in experiment because various spectroscopic methods have unanimously proven homogeneous charge distribution [33, 48, 61, 90, 145, 146]. At this point it is important to note, that α-(BEDT-TTF)$_2$I$_3$ undergoes a charge oder transition at $T_{\mathrm{CO}} = 135$ K and that the concomitant charge disproportionation is experimentally confirmed [147], whereas the ADR is observed well below 100 K (Fig. 3.16(d)) indicating that those two phenomena are not necessarily related to each other.

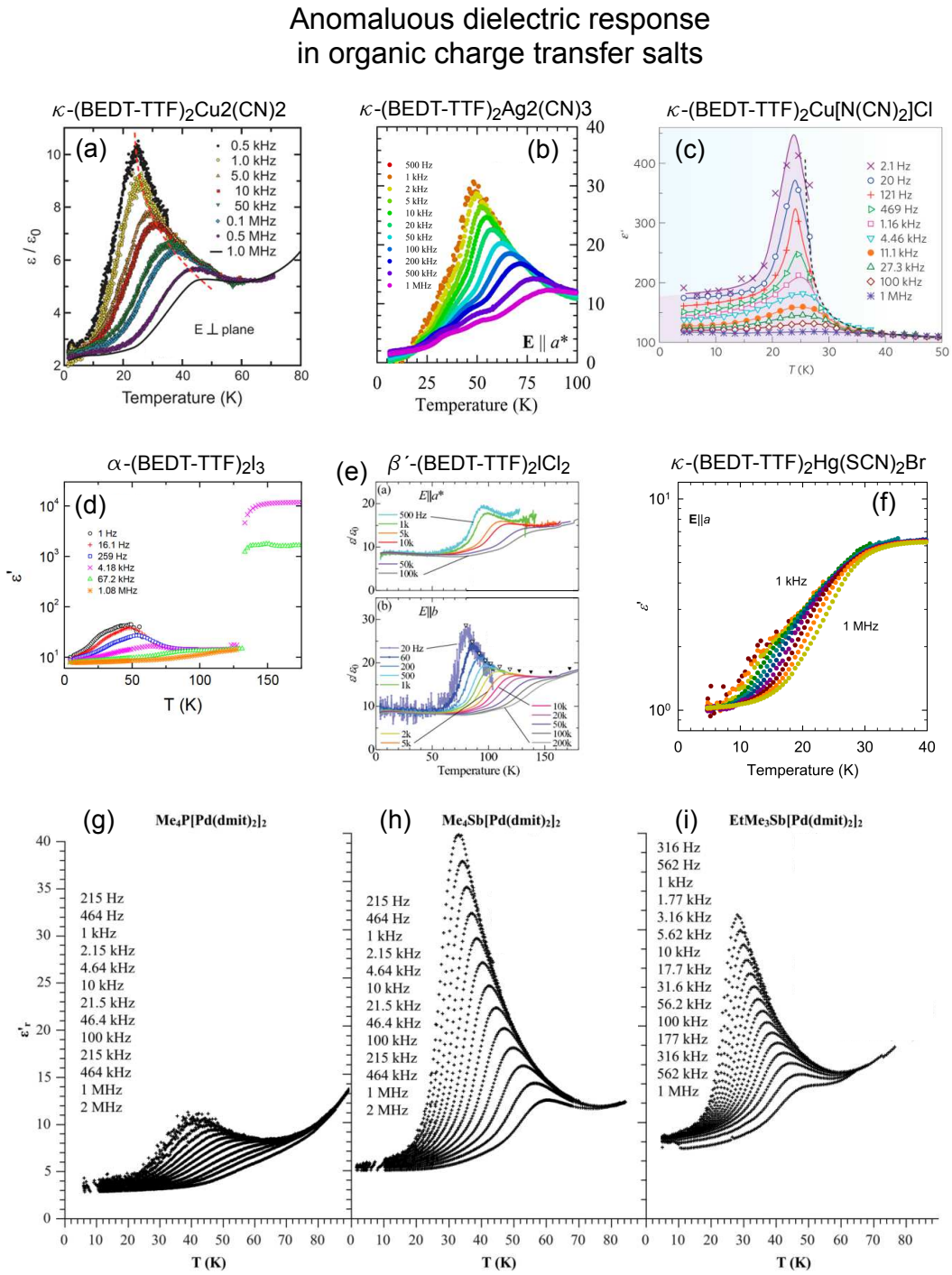

Figure 3.16: Overview of the anomalous dielectric response observed in the insulting state of various quasi-two dimensional organic charge transfer salts. Reproduced after Refs. [31](a) [33](b),[132](c),[133](d),[134](e),[135](f),[136](g-i).

4

Polarization effects

In this chapter, we review basic definitions of physical quantities and the measured observables, discuss the mechanism of dielectric relaxation and provide various models necessary to analyze the obtained data. In particular we will elaborate the Debye Model, relaxor ferroelectricity and Bruggeman's effective medium approximation.

4.1 Basic definitions

In a medium, an external electric field $\mathbf{E}$ induces a polarization field $\mathbf{P}$ which is per definition related to the dielectric displacement $\mathbf{D}$ by

$$\mathbf{D} = \varepsilon_0 \mathbf{E} + \mathbf{P}, \tag{4.1}$$

wherein ε_0 is the electric permittivity of vacuum. Thereby, Eq. 4.1 defines one of the auxiliary fields and is a necessary amendment to the Maxwell equations in matter. The relation between $\mathbf{E}$ and $\mathbf{P}$ is usually determined in experiment and gives a so called constitutive equation, which in case of a linear and isotropic dielectric medium is

$$\mathbf{P} = \varepsilon_0 \hat{\chi}_{\text{elec}} \mathbf{E}, \tag{4.2}$$

with the complex electric susceptibility $\hat{\chi}_{\text{elec}}$. This leads to [1]

$$\mathbf{D} = \varepsilon_0 \mathbf{E} + \mathbf{P} = \varepsilon_0 \underbrace{(1 + \hat{\chi}_{\text{elec}})}_{\hat{\varepsilon}_r} \mathbf{E} = \hat{\varepsilon} \mathbf{E}, \tag{4.3}$$

[1] In the SI unit system, $\hat{\varepsilon}$ has the dimension farad per meter $\frac{\text{F}}{\text{m}} = \frac{\text{A}^2 \cdot \text{s}^4}{\text{kg} \cdot \text{m}^3}$. The relative permittivity $\hat{\varepsilon}_r = \hat{\varepsilon}/\varepsilon_0$ is dimensionless and also used, while it happens that sometimes the index r is omitted such that it is mistaken as the permittivity $\hat{\varepsilon}$. In this thesis, we explicitly plot the permittivity in units of $\hat{\varepsilon}/\varepsilon_0$, which is dimensionless and corresponds to $\hat{\varepsilon}_r$

and thereby defines the permittivity $\hat{\varepsilon}$, which in the general case is a frequency-dependent, complex number [2]

$$\hat{\varepsilon}(\omega) = \varepsilon_1(\omega) - i\varepsilon_2(\omega). \tag{4.4}$$

Besides $\{\varepsilon_1,\varepsilon_2\}$, the electrodynamic properties of a solid are also commonly described via the complex conductivity[3]

$$\hat{\sigma} = \sigma_1 + i\sigma_2, \tag{4.5}$$

whose relation to the permittivity is a matter of definition. In dielectric spectroscopy [133, 148, 149],

$$\hat{\varepsilon} = \frac{-i\hat{\sigma}}{\omega} \tag{4.6}$$

is conventionally used. [4] Eq. 4.6 is convenient because in the audio- and radio frequency range, the medium of interest usually is placed between two plane-parallel electrodes forming a plate capacitor whose complex admittance

$$\hat{Y} = \frac{1}{\hat{Z}} = G + iB, \tag{4.7}$$

is measured with an impedance analyzer, wherein $\hat{Z}$ is the complex impedance, G the conductance and B the susceptance which gives the capacitance $C = B/\omega$. With the area of the plate electrodes A and the distance d between them, the conductivity is obtained by

$$\sigma_1 = \frac{d}{A}G \quad \text{and} \quad \sigma_2 = \frac{d}{A}B, \tag{4.8}$$

such that the permittivity is determined from the measured observables via

$$\varepsilon_1 = \frac{\sigma_2}{\omega} = \frac{dC}{A} \quad \text{and} \quad \varepsilon_2 = \frac{\sigma_1}{\omega} = \frac{d}{A}\frac{G}{\omega}. \tag{4.9}$$

[2] Whether a positive or a negative sign is used in Eq. 4.4 is a matter of choice but has to be consistent with the definition of the harmonic electric field $\mathbf{E} = \mathbf{E}_0 e^{\mp i\omega t}$ which goes into the Maxwell equations. Usually, in optics $\hat{\varepsilon} = \varepsilon_1 + i\varepsilon_2$ and $\mathbf{E} = \mathbf{E}_0 e^{-i\omega t}$ is used, whereas in dielectric spectroscopy, mainly using impedance analyzers to determine the permittivity, $\hat{\varepsilon} = \varepsilon_1 - i\varepsilon_2$ and $\mathbf{E} = \mathbf{E}_0 e^{+i\omega t}$ are used which corresponds to the convention in electrical engineering. However, in both cases $\varepsilon_2 > 0$ corresponds to a lossy dielectric whereas $\varepsilon_2 < 0$ represents an active medium (cf. Appendix A).

[3] The sign in $\hat{\sigma}$ usually is + and independent of the definition of the harmonic electric field.

[4] Here, the conventions in dielectric and in optical spectroscopy differ. In the latter, usually $\hat{\varepsilon} = 1 + i\frac{\hat{\sigma}}{\varepsilon_0\omega}$ [150] is used. Since the sign of ε_1 is consistent across the conventions, the sign of σ_2 is not and special care has to be taken in comparing σ_2 values obtained by different methods.

In particular, ε_1 is proportional to the measured capacitance C as one would expect.

Classical definition of polarization

In the section above, we gave the relation between $\mathbf{P}$ and $\mathbf{E}$ for a linear dielectric in Eq. 4.2, thereby defined the electric susceptibility χ_e and finally connected the measured quantities to $\hat{\varepsilon}$ while we skipped an explicit and microscopic definition of $\mathbf{P}$ itself. The classic definition is based on the concept of electric dipoles $\mathbf{d}$ as finite, well separated entities, for instance embodied by dipolar molecules. In the ionic limit, the electric dipole $\mathbf{d}$ is considered as a collection of point-shaped charges q_i at positions $\mathbf{r}_i$ and is defined as

$$\mathbf{d} = \sum_i q_i \mathbf{r}_i. \tag{4.10}$$

For a continuous charge density $en(\mathbf{r})$, with the electronic charge e and the $n(\mathbf{r})$ the number density, the electric dipole is

$$\mathbf{d} = \int en(\mathbf{r})\mathbf{r}d\mathbf{r}. \tag{4.11}$$

Besides the possibility that finite electric dipoles already exist at zero-field, they can also be induced as a response of the medium to an external $\mathbf{E}$-field. The ability of a medium to do so is the polarizability α, which is a complex scalar for an isotropic medium and defined by

$$\mathbf{d} = \alpha\mathbf{E}. \tag{4.12}$$

Usually, the polarization in macroscopic systems is introduced as the sum of electric dipole moments per unit volume V according to

$$\mathbf{P} = \frac{1}{V}\sum_V \mathbf{d}. \tag{4.13}$$

It can not be emphasized enough at this point, that the above definition of $\mathbf{P}$ is based on the presence of identifiable, polarizable entities. This, however, is not necessarily appropriate in bulk crystals where the electronic charge has a periodic and continuous distribution of which a fraction is also shared among ions in a delocalized manner. In particular, this becomes important when the bonding between the constituents has a

Figure 4.1: One-dimensional ionic crystal with a lattice spacing of a. The dashed gray boxes indicated the two possible choices of the unit cell. In the conventional definition of P (Eq. 4.13), its direction depends on the choice of the unit cell and therefore is not unambiguously defined.

mixed ionic/covalent character and the partitioning into localized polarization centers is not possible. Moreover, in an ionic periodic crystal, the direction of the polarization depends on the choice of the unit cell and therefor is not unambiguously defined, as illustrated in Fig. 4.1 for the most simple case of a one-dimensional chain of ions, which led to the discussion whether the polarization can be considered as an intrinsic bulk property or rather is determined by details of the surface termination.

This confusing and counterintuitive consequence of the definition of polarization was resolved by the development of the so-called *Modern theory of polarization* [151–154] by Resta and Vanderbilt in the early 90s. In the following, we shortly outline its main arguments and features to make the reader aware of this existence while a proper, comprehensive treatment of this theory is beyond the scope this experimental work.

Modern approach to polarization

Within the modern approach [151–154], the polarization is not a single-valued equilibrium property of the crystal in a given broken-symmetry state but rather focuses on the difference in polarization between an initial and a final state. The change of the system from the initial to the final state in response to a perturbation, for instance an electric field or crystal deformation, is considered as an rearrangement of charges which gives rise to an (adiabatic) charge flow $\mathbf{j}$. The polarization is then defined as

$$\Delta\mathbf{P} = \mathbf{P}^f - \mathbf{P}^0 = \int_0^{\Delta t} \frac{1}{V_{\text{cell}}} \int_{\text{cell}} \mathbf{j}(\mathbf{r}, t) d\mathbf{r} dt, \tag{4.14}$$

wherein $\mathbf{P}^0$ refers to the polarization of an initial, unperturbed state which is mostly of high-symmetry and $\mathbf{P}^f$ to the induced polarization of a final state at time Δt which can be of lower symmetry. This definition is not related to the periodic static charge distribution inside the bulk unit cell and naturally circumvents the unambiguity of the classical definition (Eq. 4.13) . Moreover, the modern approach has two main advantages. First, it is closer to the actual way the polarization is experimentally determined, which is ex-

actly by measuring a macroscopic, transient current flowing through the sample placed between two plane-parallel electrodes. The time-integrated value then gives the induced, macroscopic polarization. In that sense, experimental results are not affected by this new theoretical paradigm which is actually more harmonious with experimental pragmatism. And second, it naturally includes ionic and electronic contributions to the current. Within a quantum mechanical description, the latter is closely related to the phase of the electronic wave function which can be presented either as Bloch wavefunction or as Wannier wavefunction. Under the restriction, that the system remains insulting all along the path from the initial state 0 to the final state f, the polarization can be expressed as a Berry phase [151–153, 155, 156] according to

$$\Delta\mathbf{P} = \frac{1}{V_{\text{cell}}} \sum_i \left[q_i^f \mathbf{r}_i^f - q_i^0 \mathbf{r}_i^0 \right] \tag{4.15}$$

$$- \frac{2ie}{(2\pi)^3} \sum_n^{occ} \left[\int_{BZ} d^3\mathbf{k} e^{-i\mathbf{k}\cdot\mathbf{R}} \langle u_{n\mathbf{k}}^f | \frac{\partial u_{n\mathbf{k}}^f}{\partial \mathbf{k}} \rangle - \langle u_{n\mathbf{k}}^0 | \frac{\partial u_{n\mathbf{k}}^0}{\partial \mathbf{k}} \rangle \right], \tag{4.16}$$

wherein the first summation term accounts for ionic contribution of the nuclei in the unit cell and the second for the electronic contribution with the sum going over all occupied bands n, the integration over the Brillouin zone BZ and $u_{n\mathbf{k}}$ denoting the lattice periodical part of the Bloch wavefunction. Usually, the relaxed ionic position and a self-consistent charge density are calculated with standard electronic structure calculation codes and then put into Eq. 4.16, whereas, depending on the actual code, special care has to be taken in averaging the Berry phase over the Brillouin zone [157]. We will, however, not go further into detail with the modern approach of polarization, refer the reader to the reviews in literature [154, 158] and conclude for now, that it does not affected the usual experimental procedure in determining material parameters like $\hat{\varepsilon}$ but might be helpful in interpreting them on a microscopic level.

4.2 Polarization mechanisms

Different polarization mechanisms may contribute to $\mathbf{P}$, and thus to the measured $\hat{\varepsilon}$ of a dielectric medium, which in general can be divided into relaxation and resonance processes. They dominate $\hat{\varepsilon}(\omega)$ around a characteristic frequency which is reciprocal to the timescale the mechanism takes place. The schematic plot of $\varepsilon_1(\omega)$ and $\varepsilon_2(\omega)$ for a dielectric material over a wide frequency range in Fig. 4.2 illustrates the typical characteristic frequencies of dielectric relaxation as well as atomic and electronic resonance processes.

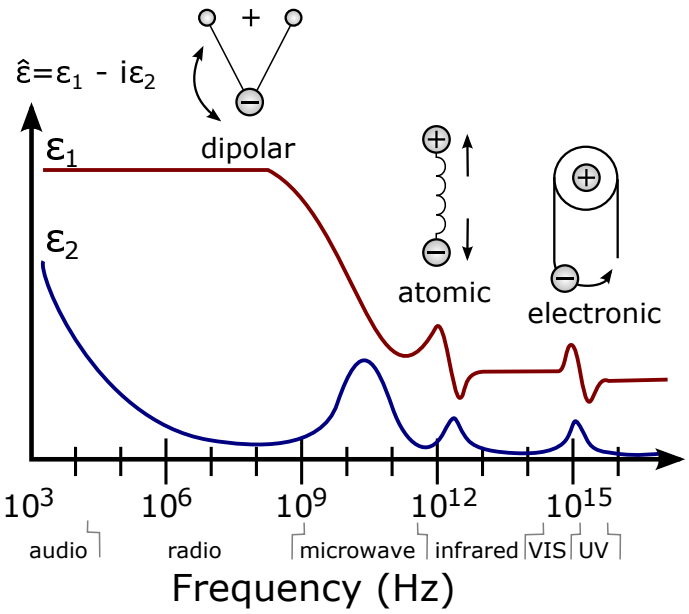

Figure 4.2: Sketch of the broad band permittivity spectrum $\hat{\varepsilon}(f)$ of a dielectric. From audio to the microwave frequencies, the response is governed by a so-called dielectric relaxation, referring to a finite displacement of charges, as for instance the case in the re-orientational motion of dipoles in an oscillating electric field. At higher frequencies, various resonances are usually observed. In the THz range, atomic or lattice (phonon) resonances dominate the spectrum while electronic processes are revealed in the visible and UV range.

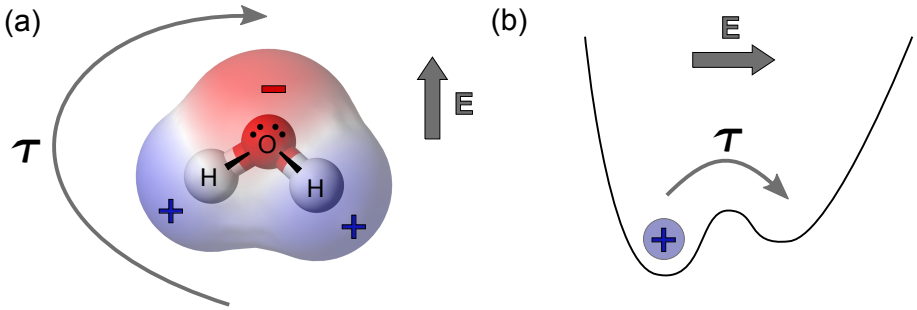

Figure 4.3: Sketch of the re-orientational motion of charge in an electric field, eventually leading to dielectric relaxation. (a) Illustration of a H_2O molecule and its dipole moment. An external electric field induces a re-orientational motion of the dipolar molecule. Due to its moment of inertia, the molecule can not follow the electric field instantaneously, giving rise to the relaxation time τ. (b) Electric charge in a double-well potential. The external applied electric field can promote a thermally activated motion of the charge from on minimum into the other. This process neither follows the electric field instantaneously but takes place on a time scale of τ after the electric field is applied.

4.2.1 Dielectric relaxation

In general, dielectric relaxation denotes reorientational processes in an external oscillating **E**-field, such as the rotation of dipolar molecules or local hopping processes of charged particles in double- or multi-well potentials [5], for example protons in hydrogen-bonded materials. In both cases, a permanent dipole moment is present whose rotation includes the movement of charge on a finite length-scale in response to an external **E**-field as illustrated in Fig. 4.3.

This dielectric relaxation process shows a characteristic signature in the temperature- and frequency-dependence of the permittivity $\hat{\varepsilon}(T, f)$ [133, 159], which are both illustrated in Fig. 4.4. In both plots, $\varepsilon_1(T, f)$ shows a step-like curve which is usually explained within the intuitive picture, that at low temperatures or high frequencies, the dipole cannot follow the applied ac **E**-field anymore. As a result, the polarization is lowered with decreasing T or increasing f and ε_1 diminishes from its quasi-static value $\varepsilon_{\text{stat}}$ to its high-frequency limit ε_{inf}, the latter usually is larger then 1 due to ionic and electronic processes at much higher frequencies (Fig. 4.2). The peak in ε_2 denotes the maximum absorption of electric energy when the reorientation frequency of the dipoles matches the frequency of the ac **E**-field.

[5] Which can formally also be treated as reorientation of a dipole moment.

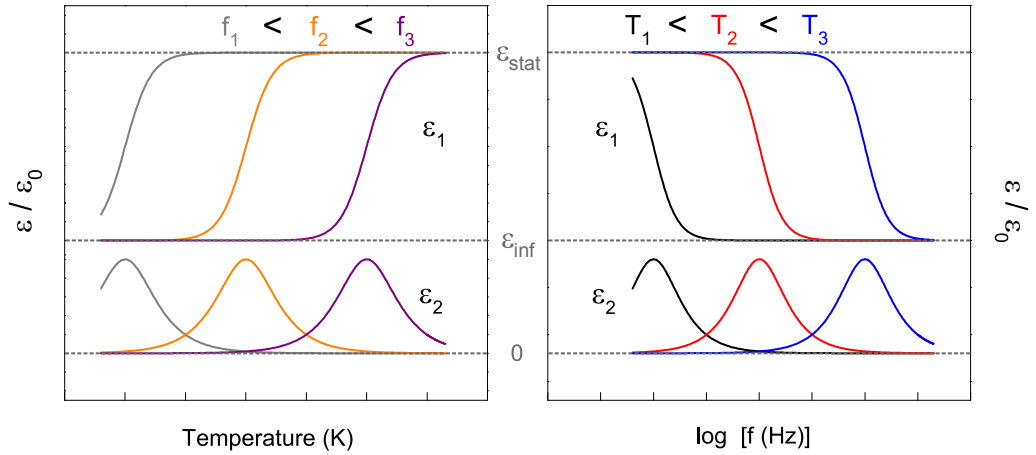

Figure 4.4: Schematic plot of the characteristic temperature and frequency-dependence of the permittivity for a dielectric relaxation process.

Debye and Havriliak-Negami Model

A simple quantitative description of the relaxation dynamics shown in Fig. 4.4 is given by the Debye model [149, 160]. It is based on the assumption of rigid, isolated dipoles fluctuating due to a stochastic force which competes with the alignment of the dipoles parallel to an external field. This gives rise to the relaxation time which characterizes the dynamics of the reorientational motion of a dipole after the field is switched off. For a simple relaxation mechanism with a single, frequency-independent relaxation time τ, we can extend this to an external ac field and assume that the change in polarization follows

$$\frac{d\mathbf{P}_{\mathrm{dip}}}{dt} = \frac{\mathbf{P}_{\mathrm{dip}}(0)e^{+i\omega t} - \mathbf{P}_{\mathrm{dip}}(\omega)}{\tau}, \tag{4.17}$$

wherein $\mathbf{P}_{\mathrm{dip}}(0)$ is the static polarization which we would obtain for $\omega \to 0$ and $\mathbf{P}_{\mathrm{dip}}(0)e^{+i\omega t}$ the polarization in the idealization that the dipoles could follow the ac electric field instantaneously. In simple words, the change in polarization scales with the difference of its actual value $\mathbf{P}_{\mathrm{dip}}(\omega)$ to the idealized one. For instance, if we would abruptly switch on an electric field at the time $t = 0$, the polarization would rise according to $\mathbf{P}(t) = \mathbf{P}_{\mathrm{dip}}(0)\left[1 - e^{-t/\tau}\right]$. Eq. 4.17 is easily solved with the ansatz:

$$\mathbf{P}_{\mathrm{dip}}(\omega) = \varepsilon_0\hat{\chi}_e(\omega)\mathbf{E}_0e^{+i\omega t} \quad \text{and} \quad \mathbf{P}_{\mathrm{dip}}(0) = \chi_{\mathrm{e},1}(0)\mathbf{E}_0, \tag{4.18}$$

wherein we used Eq. 4.2 for a linear dielectric medium and $\chi_{e,1}(0)$ denotes the electric susceptibility of the system to a static field . This straightforwardly gives

$$i\omega\hat{\chi}_e(\omega) = \frac{\chi_{e,1}(0) - \hat{\chi}_e(\omega)}{\tau} \tag{4.19}$$

which is solved for $\hat{\chi}_e(\omega)$ to

$$\hat{\chi}_e(\omega) = \frac{\chi_{e,1}(0)}{1 + i\omega\tau}. \tag{4.20}$$

Using Eq. 4.3 this becomes the well known Debye model with

$$\hat{\varepsilon}(\omega) = \varepsilon_{\text{inf}} + \frac{\Delta\varepsilon}{1 + i\omega\tau}, \tag{4.21}$$

wherein we account for high-frequency effects with ε_{inf} and replaced the static contribution into $\Delta\varepsilon = \varepsilon_{\text{stat}} - \varepsilon_{\text{inf}} = \chi_{\text{e},1}(0)/\varepsilon_0$. The same result is obtained in more rigorous derivations which are based on double-well potential or a memory function [149]. The real- and imaginary part are

$$\varepsilon_1 = \varepsilon_{\text{inf}} + \frac{\Delta\varepsilon}{1 + \omega^2\tau^2} \quad \text{and} \quad \varepsilon_2 = \frac{\omega\tau\Delta\varepsilon}{1 + \omega^2\tau^2}, \tag{4.22}$$

respectively, and are plotted in Fig. 4.5 as a function of frequency $f = \omega/2\pi$. Upon increasing f, a step-like decrease of $\varepsilon_1(f)$ is obtained whose frequency of inflection coincides with the peak position f_{max} in $\varepsilon_2(f)$, as indicated by the gray dotted line. Both give the characteristic relaxation time via $\tau = (2\pi f)^{-1}$.

In many systems, however, the experimentally observed peak- and step-widths are broader then expected from the Debye model and can become asymmetric. The latter indicates, that the short time dynamics at high frequencies are stronger pronounced then the long time dynamics at low frequencies. It is tempting to attribute this to a superposition of several Debye modes described by Eq. 4.21 while care must be taken in a straightforward assignment of those to independent relaxation processes [149, 161]. In contrast, an interpretation in the framework of cooperative relaxation processes is often more obvious and appropriate, for instance like a collective relaxation of dipoles due to their mutual interaction which is not considered in the simple Debye model. However, it is a challenging task to capture this cooperativity in a stringent theoretical description such

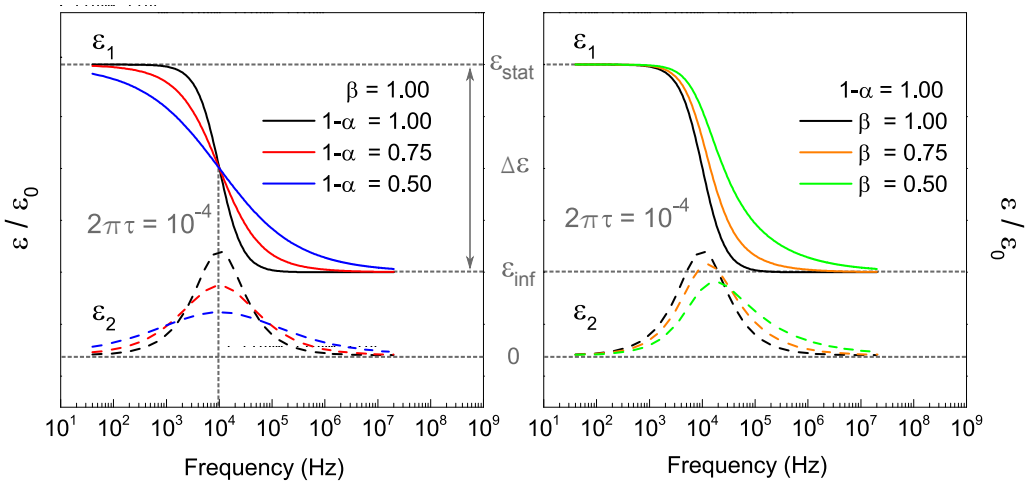

Figure 4.5: Frequency-dependence of the permittivity according to the Havriliak-Negami Model (Eq. 4.23) for different values of the symmetric broadening parameter $1-\alpha$ and the asymmetric broadening parameter β. Note that the maximum in ε_2 does not coincide with the predefined values of $(2\pi\tau)^{-1} = 10^4$ Hz for $\beta < 1$.

that an empirical extension of the Debye model to describe the spectra became widely accepted. This is the Havriliak-Negami model [162]:

$$\hat{\varepsilon}(\omega) = \varepsilon_\infty + \frac{\Delta\varepsilon}{(1 + (i\omega\tau)^{1-\alpha})^\beta}, \tag{4.23}$$

wherein the exponent $1-\alpha$ accounts for a symmetric and β for a asymmetric broadening of the step and peak width. Fig. 4.5 demonstrates the broadening in a plot of $\varepsilon_1(f)$ and $\varepsilon_2(f)$ for various values of $1-\alpha$ and β. The broadening ascribed to collective relaxation and cooperativity is often observed in liquid crystals [163], disordered or glassy matter [159], relaxor ferroelectrics [164], charged ordered systems [147, 165, 166] as well as in systems with charge- or spin density waves instabilities [167, 168]. The variation of Eq. 4.23 with different values of $1-\alpha$ and β is often found under specific names which we summarize in Table 4.1. It should be noted, that for $\beta < 1$, the point of inflection in $\varepsilon_1(f)$ and the peak position in $\varepsilon_2(f)$ at $f_{\max}$ is related to τ according to

$$f_{\max} = \frac{1}{2\pi\tau}\left[\sin\frac{(1-\alpha)\pi}{2\beta+2}\right]^{1/(1-\alpha)}\left[\sin\frac{(1-\alpha)\beta\pi}{2\beta+2}\right]^{-1/(1-\alpha)}, \tag{4.24}$$

Finally, it is instructive to mention, that the relaxation dynamics can also be determined in time-domain measurements by means of the response function $\Psi(t)$ which is defined via

Table 4.1: Nomenclature of the various models based on the Debye model to describe the relaxation dynamics of a dielectric relaxation process.

Debye	$1-\alpha = 1$	$\beta = 1$
Cole-Cole	$0 < 1-\alpha < 1$	$\beta = 1$
Cole-Davidson	$1-\alpha = 1$	$\beta < 1$
Havriliak-Negami	$0 < 1-\alpha < 1$	$\beta < 1$

$\mathbf{D}(t) = \varepsilon_0 \varepsilon_{\text{stat}} \mathbf{E}_0 (1 - \Psi(t - t'))$ [149]. For dielectric relaxation processes, a modification of this response function to

$$\Psi(t) = \exp\left\{\left(-\frac{t}{\tau}\right)^{\beta_{\text{KWW}}}\right\}, \tag{4.25}$$

is often experimentally observed, which is also denoted as stretched exponential or Kohlrausch-Williams-Watts (FFK) function. The relation between β_{KWW} of the KKW function in time-domain and $1-\alpha$ and β in frequency-domain was determined to $\beta_{\text{KWW}}^{1.23} = (1-\alpha)\beta$ in Ref. [169].

Arrhenius and Vogel-Fulcher-Tammann law

Let us now come to the temperature-dependent signature of dielectric relaxation processes which we mentioned above (Fig.4.4). The temperature-induced shift of the step and peak feature in $\varepsilon_1(f)$ and $\varepsilon_2(f)$, respectively, reflects the slowing down of the reorientational motion of the dipoles upon cooling. This is made plausible by considering thermally activated reorientation of dipoles across an energy barrier similar to the case shown in Fig. 4.3. In the simplest case this energy barrier is temperature-independent and τ follows a so called Arrhenius or activated behavior

$$\tau = \tau_{\text{A}} \exp\left\{\frac{\Delta_{\text{A}}}{T}\right\}, \tag{4.26}$$

wherein τ_{A} is the time scale for the response in the high-temperature limit and Δ_{A} the activation energy, which corresponds to the height of the energy barrier. In super-cooled liquids and glass formers, a deviation from Eq. 4.26 is observed in from of a diverging τ upon cooling [159, 170, 171] which instead is well described with the Vogel-Fulcher-Tammann (VFT) behavior

$$\tau = \tau_{\text{VFT}} \exp\left\{\frac{\Delta_{\text{VFT}}}{T - T_{\text{VFT}}}\right\}, \tag{4.27}$$

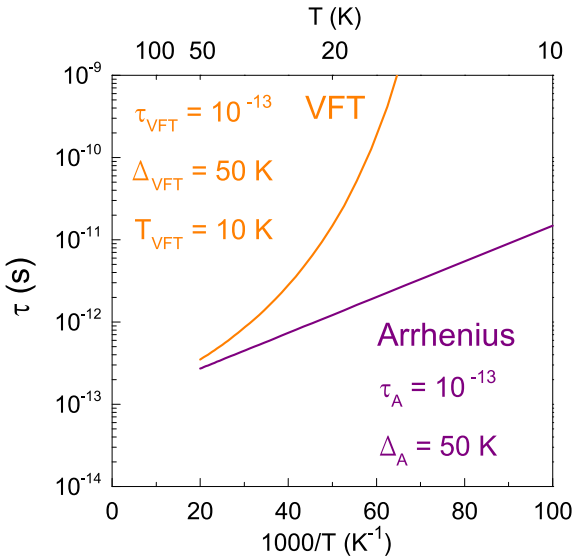

Figure 4.6: Comparison of the Arrhenius (Eq. 4.26) and the Vogel-Fulcher-Tammann (VFT) model (Eq. 4.27) for the temperature-dependence of the mean relaxation time τ of a dielectric relaxation process.

wherein τ_{VFT} corresponds to τ_{A}, the energy Δ_{VFT} to an activation energy for reorientational motion and T_{VFT} denotes the temperature where τ diverges. This super-Arrhenius behavior is often referred to as glassy dynamics and is ascribe to a growing number of correlated molecules with cooperative motion upon cooling [171]. Moreover, Eq. 4.27 also gives a good parametrization for the slowing down of molecular motion in disordered systems and the glass-like freezing of dipolar order in relaxor ferroelectrics [164].

In Fig. 4.6 we compare both models by plotting τ over $1000/T$, wherein we set $\tau_{\mathrm{A}} = \tau_{\mathrm{VFT}} \approx 10^{-13}$ s, as usually found for molecular dipolar motion [133, 159], $\Delta_{\mathrm{A}} = \Delta_{\mathrm{VFT}} = 50$ K and $T_{\mathrm{VFT}} = 10$ K. In this representation, the Arrhenius behavior follows a straight line whereas the VFT is characterized by the super-linear behavior with a diverging τ upon cooling.

4.2.2 Curie-Weiss law

In general, the temperature-dependence of the relaxation dynamics is determined by a slowing down of $\tau(T)$ as well as by an increase of $\Delta\varepsilon(T)$ upon cooling. The most simple model to capture the latter is the Curie law for the static electric susceptibility, which we will derive in the following.

The energy of a dipole moment in an external field is given by $W = -\mathbf{p}\cdot\mathbf{E} = -pE\cos\theta$, with θ being the angle spanned by $\mathbf{p}$ and $\mathbf{E}$. The alignment of $\mathbf{p}$ parallel to $\mathbf{E}$ is counteracted by the thermal energy $k_{\mathrm{B}}T$ which in time average favors an equal distribution

of alignments. In thermal equilibrium and with the assumptions, that the dipoles are allowed to rotated freely and that their interaction can be neglected, the average value of the dipole moment along the field direction is

$$\langle p \rangle = p \frac{\int_0^\pi \cos\theta e^{pE cos\theta/k_\mathrm{B}T} \sin\theta d\theta}{\int_0^\pi e^{pE cos\theta/k_\mathrm{B}T} \sin\theta d\theta} = p \left[\coth\left(\frac{pE}{k_\mathrm{B}T}\right) - \frac{k_\mathrm{B}T}{pE} \right]. \tag{4.28}$$

The term in the brackets is the Langevin function [6] and for small field strengths and high temperatures, such that $pE \ll k_\mathrm{B}T$, we get $\langle p \rangle = pE/3k_\mathrm{B}T$. The macroscopic polarization is given by $P = N\langle p \rangle$, with N being the number of dipole moments per unit volume, and we get

$$P = \frac{Np^2}{3k_\mathrm{B}T} E. \tag{4.29}$$

The factor 3 in the denominator stems from the assumption, that the dipoles are allowed to rotate freely which usually does not hold in solids. In case of a crystal wherein two (anti-parallel) directions of the dipoles are allowed, the factor 3 simple would vanish. However, comparing Eq.4.29 with the definition of the electric susceptibility for a static field, $\mathbf{P} = \varepsilon_0 \chi_{e,1}(0)\mathbf{E}$, the Curie law

$$\chi_{\mathrm{e},1}(0) = \frac{Np^2}{3\varepsilon_0 k_\mathrm{B}T} = \frac{C}{T}, \tag{4.30}$$

is obtained, wherein C is the Curie constant. The rise of $\chi_{\mathrm{e},1}(T)$ upon cooling is well documented in literature [164]. While C in Eq.(4.30) is defined in the quasi-static field, a decrease in $\chi_{\mathrm{e},1}(T = \text{const.})$ is observed with increasing frequency of an ac-field. This is explained by the considerations we made for the Debye model, wherein $\chi_{\mathrm{e},1}(0)$ is replaced by $\chi_{\mathrm{e},1}(f)$ of Eq.(4.20). It is therefore simpler to capture the observed frequency-dependence of the peak amplitude in $\chi_{\mathrm{e},1}(T)$ or $\varepsilon_1(T)$ within the framework of the Debye model, as we explicitly do in the following section, and keep C constant in frequency.

4.2.3 Relaxor ferroelectricity

In general, the overall temperature and frequency-dependence of a dielectric relaxation includes the one of $\tau(T)$, following an activated or VFT behavior, and the one of $\Delta\varepsilon(T)$,

[6] $L(x) = \coth(x) - \frac{1}{x} \overset{x \ll 1}{=} \frac{x}{3} - \frac{x^3}{45} + \mathcal{O}(x^5)$

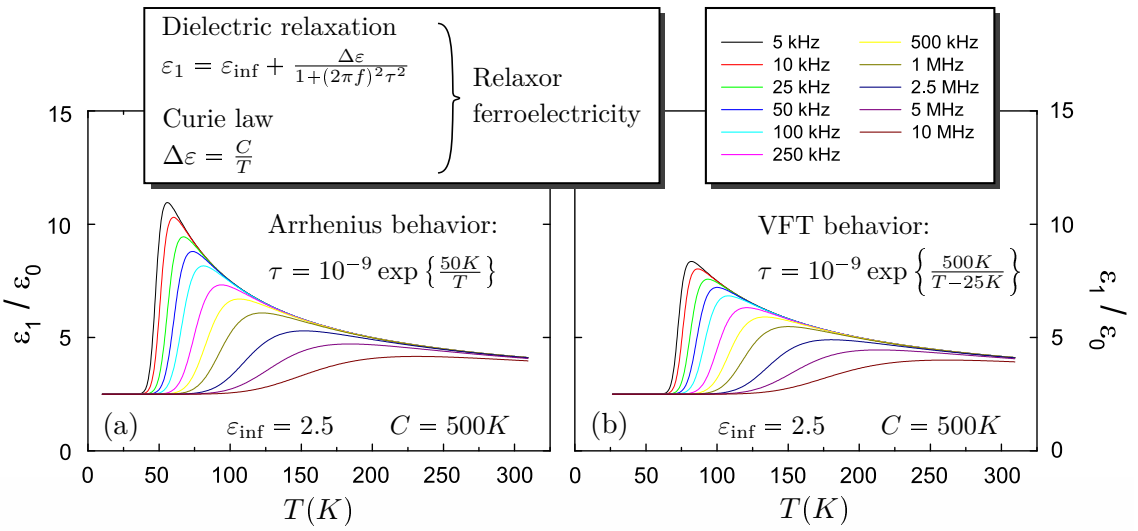

Figure 4.7: Schematic plot of the characteristic behavior for relaxor ferroelectricity in $\varepsilon_1(T, f)$. The Curie-like maximum in $\varepsilon_1(T)$ at low-frequencies diminishes in amplitude and shifts to higher temperatures upon increasing frequency. This behavior is well reproduced by combining the Debye model (Eg. 4.22) for $\varepsilon_1(f)$ with the Arrhenius ((a), Eg. 4.26) or VFT ((b), Eg. 4.27) behavior for $\tau(t)$ and the Curie-law for $\Delta\varepsilon_1(T)$ (Eg. 4.30).

following Curie behavior. Assuming an activated behavior for $\tau(T)$, for instance, and inserting Eqs.4.26 and 4.30 into Eq.4.22, we obtain

$$\varepsilon_1(T,\omega) = \varepsilon_{\rm inf} + \frac{\frac{C}{T}}{1+\omega^2\tau_{\rm A}^2\exp\left\{\frac{2\Delta_{\rm A}}{T}\right\}}, \tag{4.31}$$

which is plotted in Fig. 4.7(a) over temperature for different frequencies. The plot in panel (b) corresponds to the analog behavior wherein VFT behavior for $\tau(T)$ (Eq.4.27) is assumed. In both cases, a pronounced peak is observed for low frequencies reminiscent of the Curie behavior which shifts to higher temperatures, decreases in amplitude and broadens with increasing frequency. For the highest frequencies, the peak is completely suppressed and only the step feature originating for the dielectric relaxation (Fig. 4.4) remains. This dispersive behavior and the corresponding temperature-dependence are referred to as relaxor ferroelectricity which is observed in a wide range of lead based perovskites [164], polymers and insulating organic charge transfer salts [133].

Eq. 4.31 can be modified with the broadening parameters $1-\alpha$ and β of the Havriliak-Negami model (Eq.4.23) instead of assuming a simple Debye model (Eq.4.22) which, however, leads to rather bulky analytical expressions which we do not give here. Moreover, it

is instructive to note that the shape of the curves strongly depends on the size of C and Δ_{A}, or Δ_{VFT}, relative to each other and to the investigated temperature region as well as on the size of τ_{A} or τ_{VFT} relative to the probing frequency f. For instance, if $1/f \simeq \tau_{\mathrm{A}}$ and $T < C \simeq \Delta_{\mathrm{A}}$, the exponential in the denominator in Eq. 4.31 dominates and the a step-like increase of ε_1 upon raising the temperature is observed. In contrast, for $1/f \ll \tau_{\mathrm{A}}$ and $T \simeq \Delta_{\mathrm{A}} < C$, the Curie contribution in the numerator in the second term in Eq. 4.31 governs the behavior of ε_1 resulting in a peak like increase upon cooling. In that sense, a pure Curie peak or a simply step-like curve can be regard as the two limiting cases of Eq. 4.31. For analyzing measurement results with a behavior similar to what is shown in Fig. 4.7, it is common practice to fit the frequency dependence at constant temperature with Eq.4.23 and subsequently investigate the temperature-dependence of the obtained fitting parameters.

4.3 Lorentz field approximation and Clausius-Mossotti relation

The permittivity $\hat{\varepsilon}$ is defined within a macroscopic framework which is based on averaging $\mathbf{E}$ and $\mathbf{P}$ over a finite volume of the considered medium. A simple classical approach to do so is the Lorentz-field approximation which estimates the local electric field felt by a probe charge in a polarized bulk medium. It can be easily extended to the Clausius-Mossotti relation connecting the macroscopic $\hat{\varepsilon}$ of a medium to the microscopic polarizability α of the atoms or molecules constituting the medium. The Clausius-Mossotti relation strongly relies on the concept of electric dipoles $\mathbf{d}$ as finite, well separated entities, and therefore is in strong contrast to the modern approach of polarization. However, in the following we will shortly introduce the main considerations of the Lorentz-field approximation and the Clausius-Mossotti relation since they provide a convenient basis for the derivation of the effective medium approximations in chapter 4.4) which we will need in the results part of this thesis.

Lorentz field approximation

The main idea of the Lorentz field approximation is that the local field $\mathbf{E}_{\mathrm{loc}}$ experienced by a single probe ion or molecule in a polarized medium differs from the applied external field $\mathbf{E}_{\mathrm{ext}}$ due to the polarization of the medium surrounding the considered ion or molecule.

The formally correct way of determining $\mathbf{E}_{\mathrm{loc}}$ would be by solving Poison's equation, which, however, is extremely difficult because usually a large number of atoms has to be considered. This is circumvented in the Lorentz field approximation wherein the local field

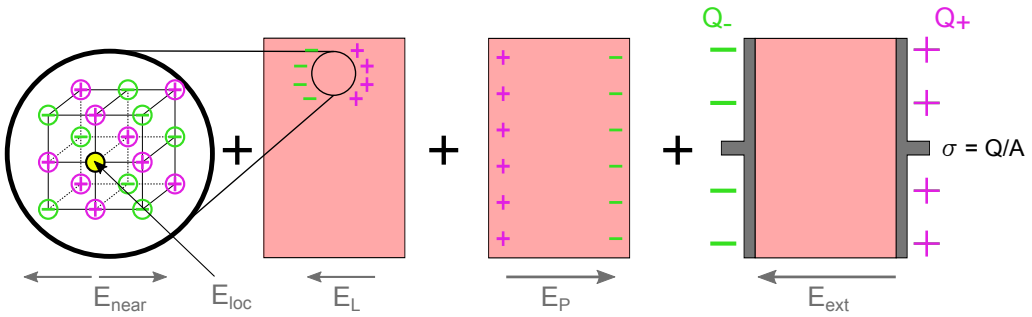

Figure 4.8: Schematics of the Lorentz field approximation and its decomposition of the electric field. An external electric field $\mathbf{E}_{\text{ext}}$ is applied to the specimen (pink medium) by means of two plane-parallel electrodes (gray areas). As a result, the specimen gets polarized giving rise to a depolarization field $\mathbf{E}_{\text{P}}$. In the Lorentz field approximation, the fields within a small cavity around the probe ion or molecule (yellow circle) are separately considered. This gives rise to the Lorentz field $\mathbf{E}_{\text{L}}$ due to the charge accumulating on the cavity surface and to the near field $\mathbf{E}_{\text{near}}$ due the to ions or molecules neighboring the probe charge within the cavity.

is divided into different components which can be estimated using a few simplifications. The single field components are illustrated in Fig. 4.8 showing a dielectric medium in an external field $\mathbf{E}_{\text{ext}}$ which is applied by means of two electrodes. Our probe charge is indicated by the yellow circle.

In response to $\mathbf{E}_{\text{ext}}$, the medium gets polarized giving rise to a depolarization field $\mathbf{E}_{\text{P}}$. The artifice of the Lorentz approximation is that we separately examine the fields within a small cavity around our probe ion or molecules which gives two additional fields to consider. First, the field at the center of the cavity due to the charge accumulating on its surface, which is denoted as the Lorentz field. Second, the field at the center due the to ions or molecules neighboring our probe charge within the cavity, denoted as the near field $\mathbf{E}_{\text{near}}$. The field components are given by

$$E_{\text{ext}} = \frac{\sigma}{\varepsilon_0}, \quad E_{\text{P}} = -\frac{\langle P \rangle}{\varepsilon_0}, \quad E_{\text{L}} = \frac{\langle P \rangle}{3\varepsilon_0} \quad \text{and} \quad E_{\text{near}} = 0, \tag{4.32}$$

wherein $\langle P \rangle$ is the polarization as an macroscopic average. Moreover, we consider a spherical cavity giving the factor $1/3$ in E_{L} and an isotropic medium, such that the near field is averaged to zero. We used the simplification, that the field due to the ions or

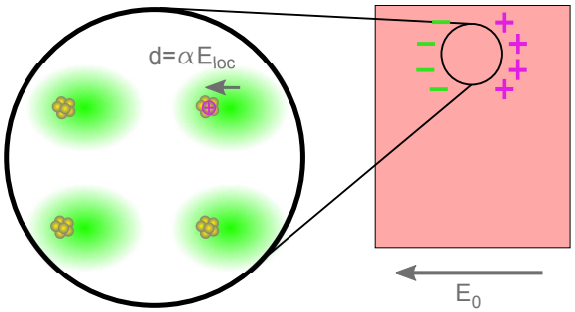

Figure 4.9: Simplified view of the Clausius-Mossotti relation, which assumes that the local field obtained by the Lorentz field approximation $\mathbf{E}_{\text{loc}}$ applies to all ions or molecules, illustrated as the green charge clouds around a yellow nucleus, in the medium. The ions or molecules get polarized, as illustrated by a shift of the green charge clouds relative to their a nuclei, giving rise to a dipole moment $\mathbf{d}$.

molecule surrounding our probe is approximated by a uniform polarization $\langle P \rangle$. This gives us for the local field

$$E_{\text{loc}} = E_{\text{ext}} + E_{\text{P}} + E_{\text{L}} + E_{\text{near}} = E_0 + \frac{\langle P \rangle}{3\varepsilon_0} \tag{4.33}$$

with the homogeneous field $E_0 = E_{\text{ext}} + E_{\text{P}}$ being averaged over the whole medium without the cavity. This gives the surprising result, that the local field is different from the macroscopically averaged one which is due to the artifice of locally examining a cavity wherein we did not account for the electric field of the probe charge itself.

Clausius-Mossotti relation

In a next step, we assume that the expression for the local field is valid for all ions or molecules in the medium. For a medium consisting of only one species of ions or molecules with the polariziablility α we can set

$$\langle P \rangle = nd = n\alpha E_{\text{loc}}, \tag{4.34}$$

which is illustrated in Fig. 4.9. Using Eqs. 4.33 and 4.34 we eliminate E_{loc} and get

$$\langle P \rangle = n\alpha \left(E_0 + \frac{\langle P \rangle}{3\varepsilon_0} \right). \tag{4.35}$$

We insert the constitutive equation

$$\langle P \rangle = \chi_e \varepsilon_0 E_0 = (\varepsilon_r - 1)\varepsilon_0 E_0 \tag{4.36}$$

with the relative permittivity $\hat{\varepsilon}_r = \hat{\varepsilon}/\varepsilon_0$ and finally obtain the Clausius-Mossotti relation

$$\frac{\hat{\varepsilon}_r - 1}{\hat{\varepsilon}_r + 2} = \frac{n\alpha}{3\varepsilon_0} \tag{4.37}$$

relating the macroscopic $\hat{\varepsilon}$ of the medium with the microscopic α of the ions or molecule constituting the medium. Several simplifications were necessary to finally end up with Eq. 4.37. We made a point dipole approximation for the ions or molecules, took the background due to the neighboring dipoles in the cavity as an averaged uniform and considered the shape and size of the cavity such that Maxwell equations can be averaged.

Shape factor

For non-spherical cavities the local field is modified resulting in an anisotropy of ε_r which then becomes a tensor. This change is taken into account by the depolarization or shape factor $\mathbf{L} = (L_x, L_y, L_z)$ with $|\mathbf{L}| = 1$. Consequently, the Clauius-Mossotti relation is modified to

$$\frac{\hat{\varepsilon}_{r,ii} - 1}{L_i(\hat{\varepsilon}_{r,ii} - 1) + 1} = \frac{n\alpha}{\varepsilon_0} \tag{4.38}$$

wherein the index ii denotes the component of the permittivity tensor. For instance if we apply an electric field along the x-axis, the shape factor for a sphere is $(1/3, 1/3, 1/3)$, for a plane disc in the y-z plane $(1, 0, 0)$ or for a needle with the main axis along the electric field $(0, 1/2, 1/2)$. It is important to emphasize, that the shape factor also accounts for the dimensionality of the cavity and hence of the considered system. For ellipsoidal cavities, the shape factor components can be determined according to

$$L_i = \frac{a_x a_y a_z}{2} \int_0^\infty \frac{ds}{(s + a_i^2)\sqrt{(s + a_x^2)(s + a_y^2)(s + a_z^2)}}, \tag{4.39}$$

with the principal semi-axes a_x, a_y and a_z of the ellipsoid.

4.4 Effective medium approximations

Effective medium approximations (EMA) seek to predict the properties of macroscopically inhomogeneous or composite materials in which the physical properties, such as conductiv-

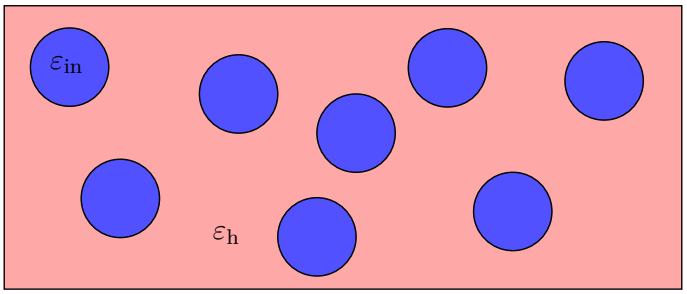

Figure 4.10: Schematic illustration of an inhomogeneous medium which is composed of a host medium with permittivity ε_{h} and spherical inclusions with permittivity $\varepsilon_{\mathrm{in}}$.

ity, permittivity or elastic modulus, vary in space. The most basic way to do so would be a simple mixing approach wherein the composite is modeled as the sum of its constituents weighted by their volume or mass ration. This approach, however, neglects polarization effects at the interfaces between the constituents and has problems in predicting the percolation threshold in insulator-conductor composites. Therefore, more sophisticated approaches base on the Lorentz-field approximation and the Clausius-Mossotti relation were developed already at the beginning of the 20th century. In the following, we will shortly introduce the Maxwell Garnet and the Bruggeman EMA for the effective permittivity of a composite material. The latter is still often used to predict the properties of a composite material.

4.4.1 Maxwell Garnett EMA

The Maxwell Garnett approximation is easily deduced from the Clauius-Mossotti relation in a few steps. First, we take the Clauius-Mossotti relation Eq.4.37 and replace ε_{r} of the previously pristine material with an effective permittivity $\varepsilon_{\mathrm{eff}}$ of the now inhomogeneous composite material. Since we now consider the inhomogeneities in a host material on a macroscopic scale, we also replace ε_0 of free space with ε_{h} of the host material and obtain

$$\frac{\hat{\varepsilon}_{\mathrm{eff}} - \hat{\varepsilon}_{\mathrm{h}}}{\hat{\varepsilon}_{\mathrm{eff}} + 2\hat{\varepsilon}_{\mathrm{h}}} = \frac{n\alpha}{3\hat{\varepsilon}_{\mathrm{h}}}. \tag{4.40}$$

In a second step, we assume that the spherical cavities are now filled with another material with the relative permittivity $\varepsilon_{\mathrm{in}}$ such that they form inclusions within the host

material with the relative permittivity ε_h, as illustrated in Fig. 4.10. The polarizability of a single spherical inclusion [7] in the host medium is given by

$$\alpha = a^3 \frac{\varepsilon_\mathrm{in} - \varepsilon_\mathrm{h}}{\varepsilon_\mathrm{in} + 2\varepsilon_\mathrm{h}}, \tag{4.41}$$

wherein a is the radius of the spherical inclusion. We insert Eq. 4.41 into the modified Clauius-Mossotti relation Eq.4.40 and obtain the Maxwell Garnett EMA [172]:

$$\frac{\hat{\varepsilon}_\mathrm{eff} - \hat{\varepsilon}_\mathrm{h}}{\hat{\varepsilon}_\mathrm{eff} + 2\hat{\varepsilon}_\mathrm{h}} = f_\mathrm{in} \frac{\hat{\varepsilon}_\mathrm{in} - \hat{\varepsilon}_\mathrm{h}}{\hat{\varepsilon}_\mathrm{in} + 2\hat{\varepsilon}_\mathrm{h}}, \tag{4.42}$$

wherein we identify $f_\mathrm{in} = \frac{na^3}{3}$ with the volume fraction of the spherical inclusions. Eq. 4.42 has several shortcomings. First, it is not symmetric in permuting the host with the inclusion material. This means, that it has to be known *a priori* what the receiving host and what the incorporated inclusion material is and that this does not follow from the knowledge of the volume fractions. Moreover, Eq. 4.42 predicts the percolation threshold at $f_\mathrm{in} = 1$. If we assume the inclusions to be conducting and the host to be insulating and increase $f_\mathrm{in} \to 1$ the composite will remain mainly insulating until $f_\mathrm{in} = 1$ is reached which disagrees with experimental observations. Another odd property of Eq. 4.42 is that ε_eff still depends on ε_h even in the case of $f_\mathrm{in} = 1$ wherein the host material is completely replaced by the inclusion material. An straightforward extension of the Maxwell Garnett EMA to account for several different inclusion materials is the Böttcher formula [173]

$$\frac{\hat{\varepsilon}_\mathrm{eff} - \hat{\varepsilon}_\mathrm{h}}{\hat{\varepsilon}_\mathrm{eff} + 2\hat{\varepsilon}_\mathrm{h}} = \sum_{in} f_\mathrm{in} \frac{\hat{\varepsilon}_\mathrm{in} - \hat{\varepsilon}_\mathrm{h}}{\hat{\varepsilon}_\mathrm{in} + 2\hat{\varepsilon}_\mathrm{h}}, \tag{4.43}$$

wherein the summation on the right hand side goes over the number of different inclusion materials. A main simplification of Eq. 4.43 is that it assumes the same Lorentz field acting on all inclusions irrespective of their permittivity. This leads to the same shortcoming as discussed above for the Maxwell Garnett EMA.

4.4.2 Bruggeman EMA

In the Bruggeman effective medium approximation (BEMA), the effective (homogenised) medium is consider as the background against which the polarization is determined. Or in other words, the polarization is considered as a quantity in respect to the effective medium including the host as well as the inclusions in contrast to the Maxwell Garnett

[7] In general, the polarizability of an ellipsoidal inclusion with ε_in in a host medium with ε_h is $\alpha_{ii} = \frac{a_x a_y a_z}{3} \left(\frac{\varepsilon_\mathrm{in} - \varepsilon_\mathrm{h}}{\varepsilon_\mathrm{h} + (\varepsilon_\mathrm{in} - \varepsilon_\mathrm{h}) L_i} \right)$

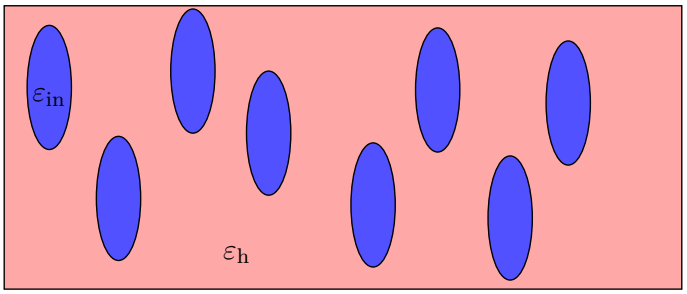

Figure 4.11: Schematic illustration of an inhomogeneous medium which is composed of a host medium with permittivity ε_{h} and ellipsoidal inclusions with permittivity $\varepsilon_{\mathrm{in}}$.

EMA where only the host acts as polarization background. For a two component composite with spherical inclusions the BEMA gives

$$(1-f_{\mathrm{in}})\frac{\hat{\varepsilon}_{\mathrm{h}}-\hat{\varepsilon}_{\mathrm{eff}}}{\hat{\varepsilon}_{\mathrm{h}}+2\hat{\varepsilon}_{\mathrm{eff}}}+f_{\mathrm{in}}\frac{\hat{\varepsilon}_{\mathrm{in}}-\hat{\varepsilon}_{\mathrm{eff}}}{\hat{\varepsilon}_{\mathrm{i}}+2\hat{\varepsilon}_{\mathrm{eff}}}=0, \tag{4.44}$$

wherein the volume fractions sum up to unity such that we used $f_{\mathrm{h}}=1-f_{\mathrm{in}}$. Formally, Eq. 8.3 is symmetric in permuting host and inclusions. For instance, we would obtain the same $\hat{\varepsilon}_{\mathrm{eff}}$ for metallic inclusions in an insulating matrix as for insulating inclusions in metallic matrix as long as the volume fractions would be the same.

For non-spherical inclusions which are all aligned in parallel, as illustrated in Fig. 4.11 for ellipsoids, $\hat{\varepsilon}_{\mathrm{eff}}$ becomes anisotropic although $\hat{\varepsilon}_{\mathrm{h}}$ and $\hat{\varepsilon}_{\mathrm{in}}$ are still isotropic. In this case, the BEMA for $\hat{\varepsilon}_{\mathrm{eff}}$ measured along the applied electric field is rewritten to

$$(1-f_{\mathrm{in}})\frac{\hat{\varepsilon}_{\mathrm{h}}-\hat{\varepsilon}_{\mathrm{eff}}}{\hat{\varepsilon}_{\mathrm{eff}}+L(\hat{\varepsilon}_{\mathrm{h}}-\hat{\varepsilon}_{\mathrm{eff}})}+f_{\mathrm{in}}\frac{\hat{\varepsilon}_{\mathrm{in}}-\hat{\varepsilon}_{\mathrm{eff}}}{\hat{\varepsilon}_{\mathrm{eff}}+L(\hat{\varepsilon}_{\mathrm{in}}-\hat{\varepsilon}_{\mathrm{eff}})}=0, \tag{4.45}$$

wherein L is the shape factor component of the inclusions along the applied electric field.

The main shortcoming of the BEMA model is, that the shape factor coincides with the percolation threshold $L=f_{\mathrm{c}}$. This is in contradiction to conventional percolation theory (cf Ch. 4.5) wherein f_{c} depends on more factors [174]. In case of spherical inclusions, for instance, the BEMA model predicts $L=f_{\mathrm{c}}=0.33$ which turned out to be incorrect in many real systems. Moreover, upon increasing the filling fraction of the inclusions, fluctuations of the local electric field are enhanced. Hence, the approximation that all inclusions are subject to the same local field is not valid anymore.

This has important implications on the predicted dielectric properties, especially in the case of metallic inclusions in an insulating host material. For a small filling fraction $f_{\mathrm{in}}<f_{\mathrm{c}}$, the system behaves as an insulator. Upon increasing the filling fraction until

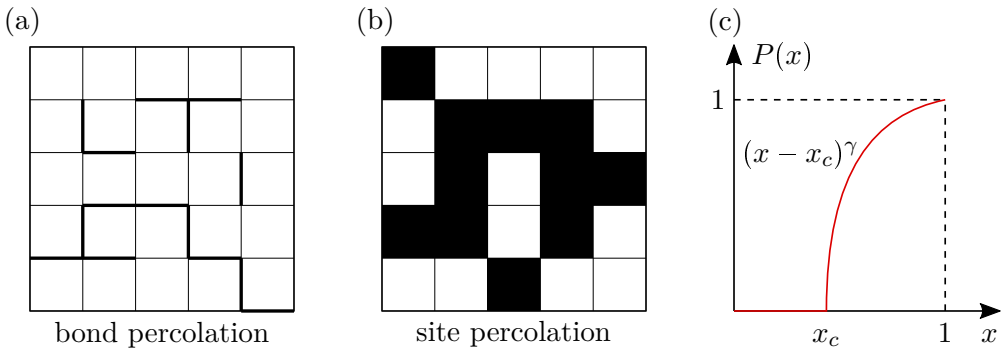

Figure 4.12: Square lattice with (a) bond percolation and (b) site percolation. (c) Plot of percolation probability $P(x)$ in dependence of the probability x that a single element of the lattice is occupied. Note that x can also be identified with the ration of filled elements. x_c denotes the percolation threshold at which $P(x)$ is non-zero and sharply increases.

$f_{\text{in}} = f_{\text{c}}$, the inclusions percolate forming a continuous path from one side of the composite sample to the opposite site, abruptly changing its transport properties.

4.5 Percolation

In general, percolation theory studies the characteristics of connected clusters in a random graph, or in other words, it describes the connectivity of arbitrary objects which are placed at random in a lattice. It can be used to describe a large number of problems in various fields ranging from growth models and the spread of epidemics to the motion of particles through a random medium. Most models can be divided into to two groups depending whether in the lattice either edges (bond percolation) or nodes (site percolation) are considered to be randomly occupied. Both cases are illustrated in Fig. 4.12(a) and (b) using the example of a square lattice whereas in general the lattice geometry can be arbitrary.

Whether a site or bond is occupied is determined with a probability $x = N_{\text{occ}}/N_{\text{all}}$, with the number of occupied sites N_{occ} and the total number of lattice sites or bonds N_{all}. Hence for $x = 0$, no bonds or sites are occupied while with increasing x, the likelihood of occupying nearest-neighbor elements rises, resulting in connected clusters which grow in size. In doing so, the specific event occurs when one cluster extends from one side of the lattice to the opposite, called the infinite cluster, such that a continuous path of occupied elements is spanned. This event, taking place at $x = x_c$, is called percolation threshold. Finally for $x = 1$, all elements of the lattice are occupied. Fig. 4.12(c) shows a plot of the

Table 4.2: Overview of the percolation threshold x_c for various lattices with different dimensionality. Reproduced after Ref. [175].

dimension	lattice	x_c site percolation	x_c bond percolation
1d	infinite line	1	1
2d	square	0.592746	0.5
2d	triangular	0.5	0.34729
2d	honeycomb	0.6962	0.65271
3d	diamond	0.43	0.388
3d	body-centered cubic	0.246	0.1803
3d	face-centered cubic	0.192	0.119

percolation probability $P(x)$, i.e. the probability that a cluster spans from one side to the opposite side of the lattice as a function of x. For $x < x_c$, the percolation probability is zero while for $x > x_c$, $P(x) \propto (x - x_c)^\gamma$ is found wherein the exponent γ depends on the dimensionality of the considered lattice. Moreover, the value of the percolation threshold x_c depends on the dimensionality, the size of the lattice and on the percolation model, i.e. site or bond percolation.

In Table 4.2, we summarize the percolation threshold for common lattices which are obtained by numerical methods. In general, the lattice specific details are of great importance for the numerical calculation of x_c. While the calculated values for site and bond percolation only moderately differ for a specific lattice, a large difference is observed in comparing different lattices. It is intuitive that for a one-dimensional lattice, the percolation threshold occurs solely at $x_c = 1$ since a single unoccupied element already interrupts the formation of an infinite cluster.

Percolation at a phase transition

It is instructive to note here, that a cluster of occupied elements is easily identified as an inclusion in a host medium as discussed above in terms of the EMAs. Therefore, percolation theory is often applied to describe the transport properties of a composite or inhomogeneous material and is a necessary complement to an EMA discussed above (Ch. 4.4), since the latter fails to do so at the percolation threshold.

Especially in the case of stark contrast for the transport properties of an occupied and unoccupied cluster, for instance for metallic inclusions in an dielectric host medium, the percolation threshold at x_c marks a drastic change in the physical properties of the entire

systems. In fact, the percolation threshold embodies very unique conditions at which special transport and optical phenomena show up. Note that one of the fingerprints of a first-order transition is the phase coexistence in proximity to the phase boundary which exactly corresponds to a percolating system. The prime example is the insulator to metal (IMT) phase transition, where at x_c the metallic clusters coalesce to an infinite one and the conductivity of the systems abruptly changes from insulating to conducting.

Divergent dielectric constant

Besides dc transport, the dielectric properties of percolating metal-insulator systems undergo drastic changes upon crossing the percolation threshold as well and have been subject of numerous investigations for half a century [176, 177]. As pointed out by Efros and Shklovskii [178], the static dielectric constant of a percolating system depends on the filling fraction m of the metallic phase and diverges at the percolation threshold

$$\varepsilon_1(\omega = 0, x) \propto (x_c - x)^{-q} \quad . \tag{4.46}$$

The critical exponent q depends on the dimension of the system; in 3D we expect q ranging from 0.8 to 1 [174, 178–180], while $q = 1.3$ is expected for 2D [178]. The BEMA model predicts $q = 1$ independent of the dimensionality of the percolating system [174].

The behavior according to Eq. 8.2 is illustrated in Fig. 4.13 together with simplified sketches of a percolating sample which is placed between two plane-parallel electrodes. The pink areas correspond to the dielectric host material, with $\varepsilon_\mathrm{d} > 0$, and the blue islands to the metallic inclusions, with $\varepsilon_\mathrm{m} < 0$. Note that the size of the metallic inclusions is extremely exaggerated while their number is underestimated. For $x = 0$ (inset **A**), the sample corresponds to a homogeneous dielectric and only its inherent polarization processes, i.e. the finite displacement of charges, contribute to ε_1. For $x > 0$ (inset **B**), metallic islands emerge which are separated by dielectric regions giving rise to many small capacitor-like arrangements. Since the charge carriers are mobile in the metallic puddles, they are allowed to redistribute and accumulate at the puddle boundaries, giving rise to the internal field $\mathbf{E}_\mathrm{int}$ in order to compensate the externally applied field. As a result, the field strength, and hence the polarization, in between two metallic puddles is strongly enhanced which is illustrated in Fig. 4.13 with the yellow colored regions. Upon increasing x, the metallic islands grow in number and size such that the surface of the capacitors rises and the distance between the metallic puddles decreases. As a result, the dielectric constant is drastically enhanced according to Eq. 8.2 and finally diverges at $x = x_c$ (inset **C**). It is important to note, that although an infinite cluster is already present, such that the dc conductivity follows metallic behavior, the polarization effects

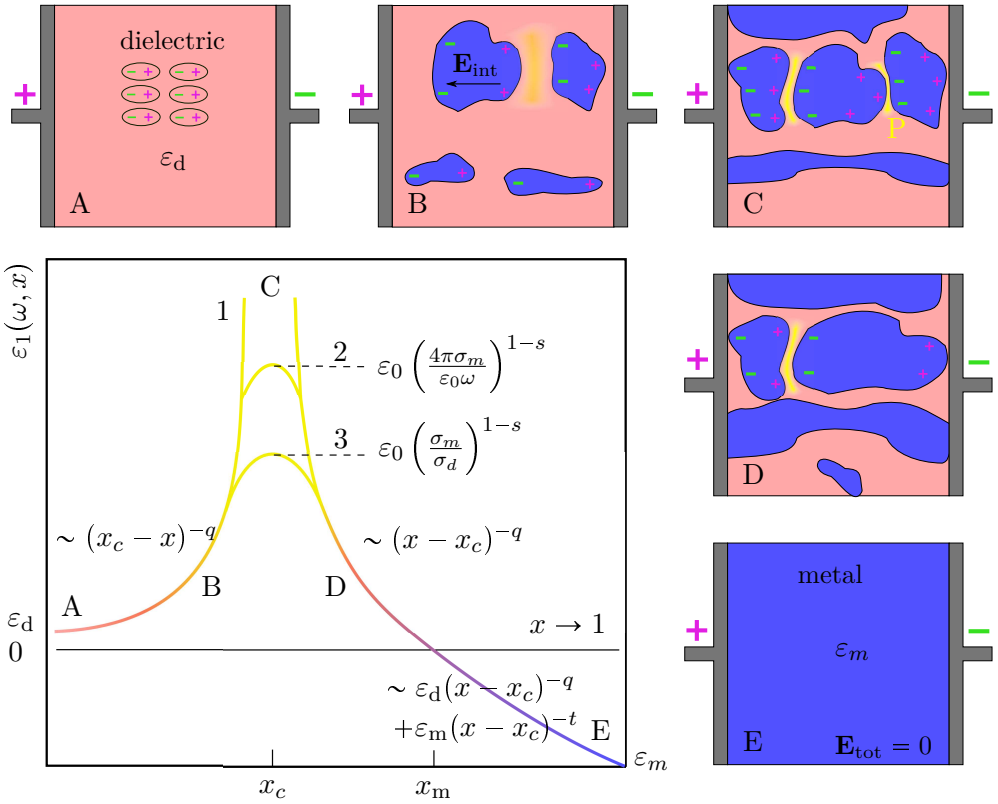

Figure 4.13: Divergence of ε_1 as a function of the metallic filling fraction x in a dielectric host medium. ε_d and ε_m denote the real part of the permittivity of the dielectric and the metallic fraction, respectively. The small insets show illustrations of the nucleation and growth of the metallic inclusions upon increasing x. Note that the size of the metallic inclusions is drastically exaggerated while their number is underestimated. With increasing x, many capacitor like arrangements occur where a dielectric region is sandwiched by two metallic regions. The charge carriers in the metallic puddles redistribute and accumulate at the puddle boundaries in order to compensate the externally applied field, giving rise to the internal field $\mathbf{E}_{\text{int}}$. As a result, the field strength, and hence the polarization, in between two metallic puddles is strongly enhanced which is illustrated with the yellow colored regions. Both effects lead to a drastic enhancement and finally to the divergence of $\varepsilon_1(x_c)$. Although an infinite cluster is already present, such that the dc-conductivity follows metallic behavior, the polarization effects captured by ε_1 are still governed by the finite clusters. For $x > x_c$, more and more clusters coalesce such that the number of capacitor-like arrangement decreases while concomitantly the effective screening in the metallic puddles of the applied field becomes more pronounced. The divergence at the percolation threshold x_c (curve 1) corresponds to the static limit at zero frequency. In the realistic case of non-zero frequency, the divergence becomes a finite maximum. For a highly insulating dielectric material with $\sigma_d(0) < \omega\varepsilon_0\varepsilon_1$ the amplitude follows curve 2. In case the non-zero conductivity, $\sigma_m > \sigma_d(0) > \omega\varepsilon_0\varepsilon_1$, of the host material is taken into account the amplitude of the maximum decreases to curve 3.

captured by ε_1 are still governed by the finite clusters. Upon further increasing x (inset **D**), more and more clusters coalesce such that the number of capacitor-like arrangement decreases while concomitantly the effective screening in the metallic puddles of the applied field becomes more pronounced. As a result, the dielectric constant declines with rising x according $\varepsilon_1 \propto (x - x_c)^{-q}$ until it eventually becomes negative at $x = x_m$, marking the onset of metallic behavior. Consequently, for $x \to 1$ (inset **E**) we get $\varepsilon_1 \to \varepsilon_\mathrm{m}$ which is sometimes quantified according to

$$\varepsilon_1(\omega = 0, x \to 1) \propto \varepsilon_{1,\mathrm{d}}(x - x_c)^{-q} + \varepsilon_\mathrm{m}(x - x_c)^{-t} \quad . \tag{4.47}$$

Frequency-dependence of the dielectric constant

In the real case of non-zero frequency, the divergence of ε_1 (curve 1) is replaced by a finite maximum at x_c, as indicated by the two additional curves in Fig. 4.13. Here, Efros and Shklovskii [178] distinguish two major cases. The first one corresponds to a highly insulating dielectric material with $\sigma_d(0) < \omega\varepsilon_0\varepsilon_1$ (curve 2) and a frequency-dependent amplitude of the percolation following the power-law

$$\varepsilon_1(\omega, x_c) = \varepsilon_\mathrm{d} \left(\frac{\sigma_\mathrm{m}}{\omega\varepsilon_0\varepsilon_\mathrm{d}} \right)^{1-S} \quad , \tag{4.48}$$

with the critical exponent $S = 0.62$ for 3D and $S = 0.5$ for 2D. In case the non-zero conductivity, $\sigma_\mathrm{m} > \sigma_d(0) > \omega\varepsilon_0\varepsilon_1$ (curve 3), of the host material is taken into account the amplitude of the maximum follows

$$\varepsilon_1(\omega, x_c) = \varepsilon_\mathrm{d} \left(\frac{\sigma_\mathrm{m}}{\sigma_\mathrm{d}} \right)^{1-S} \quad . \tag{4.49}$$

In standard percolation theory [178], the critical exponents q, t and S are predicted to obey

$$S = \frac{t}{q + t}. \tag{4.50}$$

The exponent t determines the behavior of the dc-conductivity

$$\sigma_\mathrm{dc} = \sigma_\mathrm{m}(x - x_c)^{-t} \quad \text{for} \quad x > x_c, \tag{4.51}$$

wherein σ_m is the dc conductivity in the metallic phase. In literature, various values for the critical exponents are predicted which are summarized in Table 4.3.

Table 4.3: Overview of critical exponents for the dielectric and transport behavior in percolating systems as reported in literature.

	Efros et al. [177, 178]		BEMA [181]		Clerc et al. [174]		Bergman et al. [182]	
dimension	2	3	2	3	2	3		
S	0.5	0.62	0.5	0.5	0.500	0.72	0.5	0.72
t	1.3	1.6	1.0	1.0	1.299	1.90	1.3	2.00
q	1.3	1.0	1.0	1.0	1.299	0.73	1.3	0.76

5

Experimental setup and data analysis

This chapter introduces the basic concept of dielectric spectroscopy and presents a setup for corresponding measurements in dependence of pressure, temperature and frequency which was established at the *1. Physikalisches Institut* during this PhD project. In particular, emphasis is put on the electrical feedthrough providing the necessary high-frequency characteristics, such as low attenuation and high cut-off frequency, while withstanding high-pressures. Subsequently, a description of the data analysis and of the investigated samples are given.

5.1 Dielectric spectroscopy

In general, dielectric spectroscopy refers to a variety of experimental methods determining the electrodynamic response of a medium in a broad frequency range. Fig. 5.1 gives an overview of these methods together with the corresponding frequency range and sample geometry. They can be divided into three groups. First, from the visible range to THz frequencies, optical methods such as Fourier-transform infrared (FT-IR) or Mach-Zehnder interferometers are used. Second, in the microwave regime, the sample terminates or connects a transmission line, mostly coaxial cables, and the microwave reflections or transmission is measured. Third, form several tens of MHz down to mHz frequencies, the sample is contacted by two plane-parallel electrodes in a plate capacitor like arrangement and the complex impedance of the sample is determined. In this thesis, the electrodynamic response of organic charge transfer salts in the audio- and radio frequency range is measured by means of the auto-balancing bridge (ac bridge) method which therefore will be shortly introduced in the following.

Auto-balancing bridge

The measurements presented in this thesis were performed with an *Agilent A4294* [184] precision impedance analyzer, which is based on the auto-balancing bridge method [183]. A simplified view of the corresponding measuring circuit is illustrated in Fig. 5.2. The

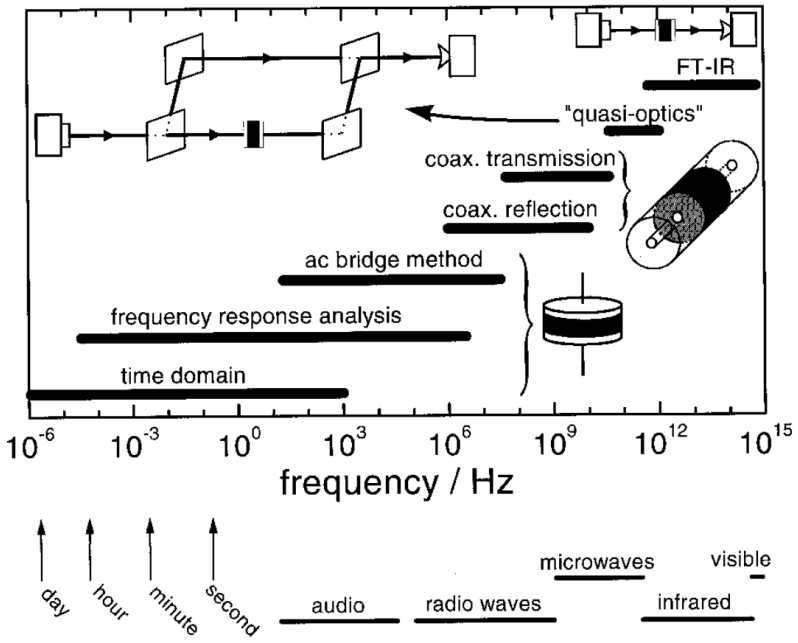

Figure 5.1: Overview of the various experimental methods subsumed by dielectric spectroscopy together with the corresponding frequency range and sample geometries. Reproduced from Ref. [159].

impedance analyzer is equipped with four terminals for BNC coaxial cables, denoted as H_c, H_p, L_p and L_c, which are used to connect the instrument with the sample holder. The outer conductors of the coaxial cables (blue lines) are put on ground to provide a proper shielding of the measurement signals, the latter are transported by the inner conductors (red and green lines). An ac voltage or current signal is applied to the sample via terminal H_c while the corresponding voltage U_x is independently measured at the H_p terminal. In order to minimize the spurious contribution from the cables, the terminals H_c and H_p are connected to each other right before the sample (red lines). The applied signal drives a current I_x from the H_c terminal through the sample to the L_c terminal, wherein the sample is represented by its complex impedance $\hat{Z}_x$. In order to precisely determine I_x with temporal resolution, the virtual ground method is applied. This is realized by adjusting the potential at the L_p terminal to ground via a so-called null loop (dash-dotted line in Fig. 5.2). In the most simple case, this is represented by an operational amplifier (op-amp), whose output is connected to the L_c terminal via the range resistance R_r to realize the necessary feedback to keep the virtual ground at $U = 0$ V (green line). As a result of the regulating feedback, the op-amp draws a current I_r through R_r to terminal L_c while the virtual ground condition $U = 0$ V implies that the currents I_r and I_x are the same. Or in other words, the currents balance, giving the name to this family of

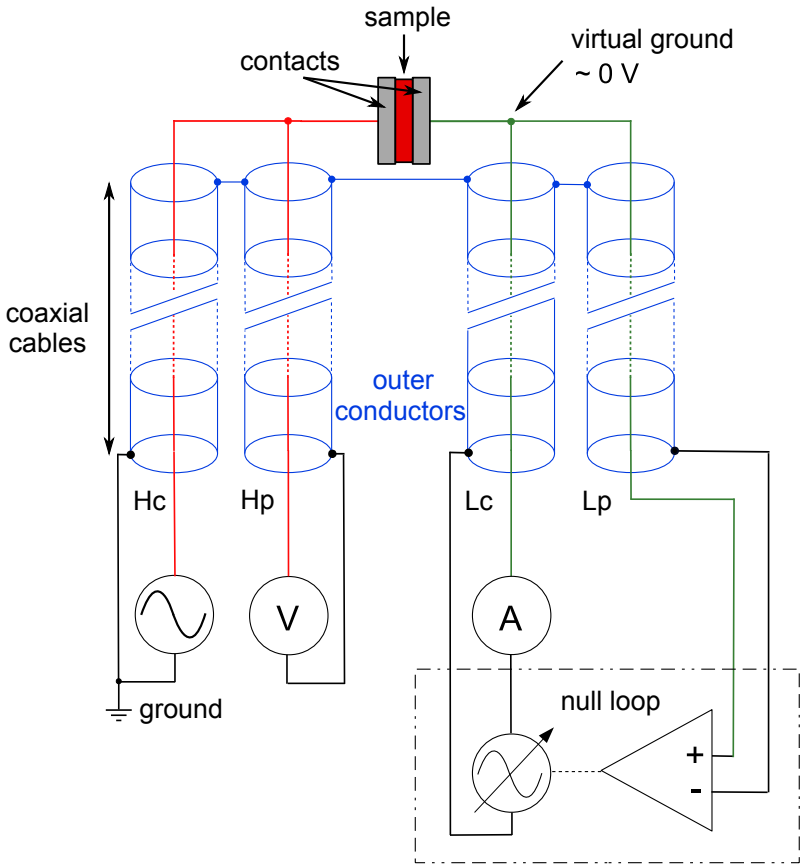

Figure 5.2: Simplified measurement circuit of an auto-balancing bridge which is usually employed for dielectric spectroscopy measurements in the audio- and radio frequency range. The bridge provides four terminals for BNC coaxial cables, denoted as H_c, H_p, L_p and L_c, which are connected to the sample holder. The outer conductors of the cables (blue lines) are put on ground and provide a proper shielding of the measurement signals while the latter are transported by the inner conductors (red and green lines). The sample impedance Z_x is determined by means of the virtual ground method using a null loop (dash-dotted line), wherein U_x and U_r are precisely measured with high temporal resolution while R_r is preset by the instrument. Based on Ref. [183].

measurement devices. The potential U_r is determined in the null loop between the op-amp and R_r such that I_r, and hence I_x, is precisely determined. Finally, the measurements of U_x and U_r with high temporal resolution and the adjusted value of R_r give a precise value of the sample impedance $\hat{Z}_x$ (see Fig. 5.2). It is trivial to remind, that in general there is a phase shift between U_x and U_r such that $\hat{Z}_x$ is a complex quantity.

The main advantages of the auto-balancing bridge method are the coverage of a wide frequency range, in our case from 40 Hz to in principle 110 MHz [184], while the latter value usually decreases to 10 MHz in case a custom made sample holder is used [183], as well as a high accuracy over a wide impedance range, usually from 10^{-3} to 10^{8} Ohm [184]. However, in order to enable the virtual ground method, the terminals have to be pair-wise connected, the L_c to the L_p and the H_c to the H_p, such that a two-point measurement configuration is realized. Therefore, spurious effects due to the contacts might contribute to the measured values and special care has to be taken in analyzing the obtained results in order to rule out these effects.

5.2 Setup

External pressure is a powerful tuning parameter in solid state research because the induced changes of the interatomic distances modify the electronic properties, such as bandwidth, electron and phonon density of states and electron hybridization [185, 186]. Changing the applied pressure in combination with the conventional temperature variation allows for exploring the phase diagram of compounds by measuring a single specimen; it became crucial in the investigation of structural phase transitions [187], metal-insulator transitions [10], superconductivity [188] as well as quantum criticality [189, 190].

Among the available methods enabling pressure-dependent measurements, dc-transport, X-ray diffraction and optical spectroscopy are well established [107, 108, 191]. Dielectric spectroscopy in a broad frequency range, however, has not been realized so far since it requires electrical connections with good high-frequency characteristics such as low attenuation and high cut-off frequency that is suitable for high-pressure usage. Therefore, a main part of this thesis was devoted to the design and manufacture of a novel electrical feedthrough for four coaxial cables and four copper wires into a piston type pressure cell ranging up to 10 kbar. In combination with a continuous flow cryostat, the cable length of the setup is minimized enabling dielectric spectroscopy measurements up to 5 MHz in frequency and down to 8 K.

In order to perform temperature-dependent measurements, the pressure cell is inserted into a commercial continuous flow He cryostat (KONTI by CryoVac GmbH & Co KG, Troisdorf, Germany) by using a custom made sample holder, as illustrated in Fig. 5.3.

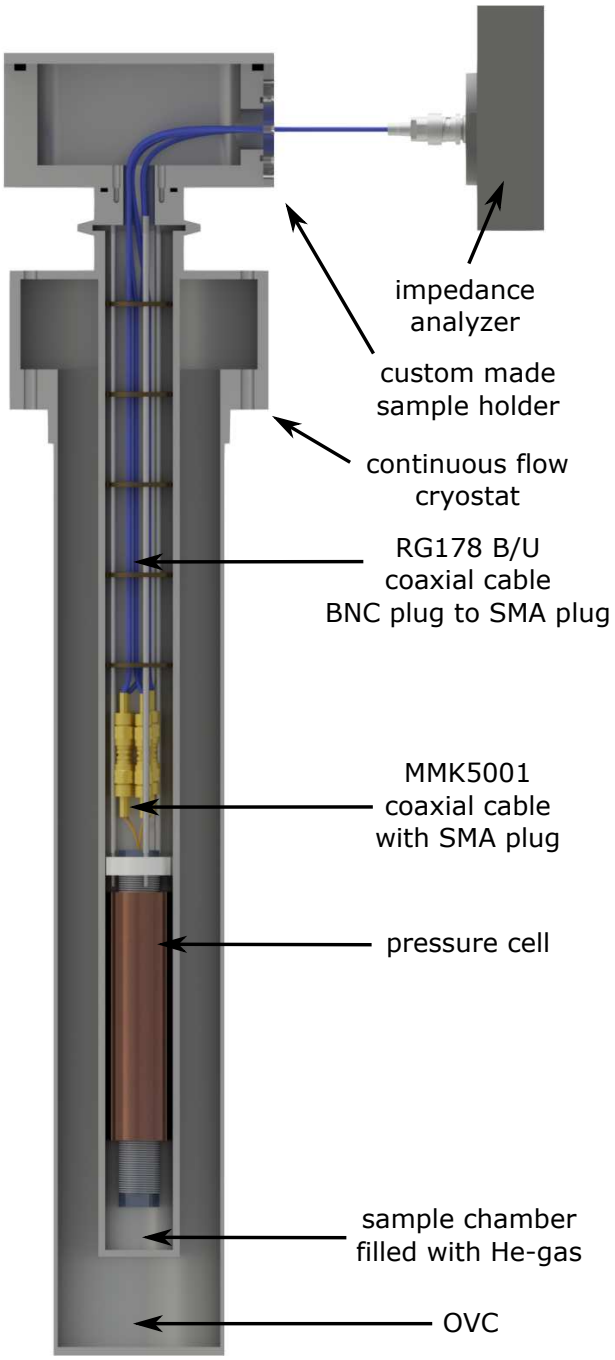

Figure 5.3: Illustration of the setup used for temperature and pressure-dependent dielectric spectroscopy. The pressure cell with the electrical feedthrough is mounted to a custom made sample holder for a commercial continuous flow cryostat. The sample holder provides four coaxial cables with SMA plug connectors to connect the feedthrough by means of four SMA jack to SMA jack adaptors. The coaxial cables of the sample holder pass a custom made vacuum sealed feedthrough and terminate in BNC plug connectors which are directly connected to the impedance analyzer located right next to the sample holder. This way, the total cable length is minimized to 50 cm and temperatures as low as 8 K are reached.

The cryostat provides a cylindrical sample chamber with 30 mm in diameter, enough to receive the pressure cell with a diameter of 26 mm. The sample chamber is filled with helium as exchange gas. To precisely adjust the temperature, a heating wire and a temperature sensor are attached to the cell on the outside (not shown in Fig. 5.3).

The sample holder provides a screw thread to receive the cell and four RG178 B/U coaxial cables terminated with SMA connectors [192]. The coaxial cables of the sample holder are connected to the ones of the feedthrough via four SMA jack to SMA jack adaptors. The coaxial cables of the sample holder pass through a custom made vacuum sealed feedthrough and terminate in BNC plug connectors which are directly connected to the *Agilent A4294* [184] impedance analyzer. The analyzer is located right next to the sample holder to minimize the required cable length that was in total 50 cm.

5.2.1 Pressure cell and feedthrough

In our setup, we employ a piston type pressure cell LC10 designed and manufactured by the Institute of High Pressure Physics of the Polish Academy of Sciences in Warsaw, Poland [193]. Except for the metal sealing rings, the entire cell is made from non-magnetic CuBe and sketched in Fig. 5.4. We use Daphne oil 7373 as a liquid pressure transmitting medium which has a good hydrostaticity and is inert to organic charge transfer salts. The sealing of the plug is ensured by a metal sealing ring, which is squeezed and deformed between the cell body and the plug while assembling the pressure cell. In addition to a metal sealing ring, the piston receives a rubber sealing ring to prevent a loss of the pressure medium while pressurizing the cell initially. The pressure is determined in-situ by an InSb semiconductor pressure gauge to recored the inherent pressure loss upon cooling.

In order to obtain a low attenuation and a high cut-off frequency of the feedthrough, it is important to provide proper shielding of the measurement signal along the cable path through the feedthrough. An incorporation of coaxial cables into a pressure resistant electrical feedthrough was, to the best of our knowledge, not realized yet, because their tubular structure is difficult to seal and is easily deformed upon applying pressure.

We solve this task with our newly developed electrical feedthrough for coaxial cables that achieves both, a pressure resistant sealing, while keeping good high frequency characteristics at the same time. A cross sectional sketch of the feedthrough is shown in the upper panel of Fig. 5.5. Instead of the commercially available dc-feedthrough, we use an empty CuBe plug with a drilling of 2 mm in diameter which is merging into a conical opening at the top.

We introduce four MMK 5001 coaxial cables [194] with an outer diameter of 0.53 mm, a SMA plug connector on one end and an open cable on the other end going into the

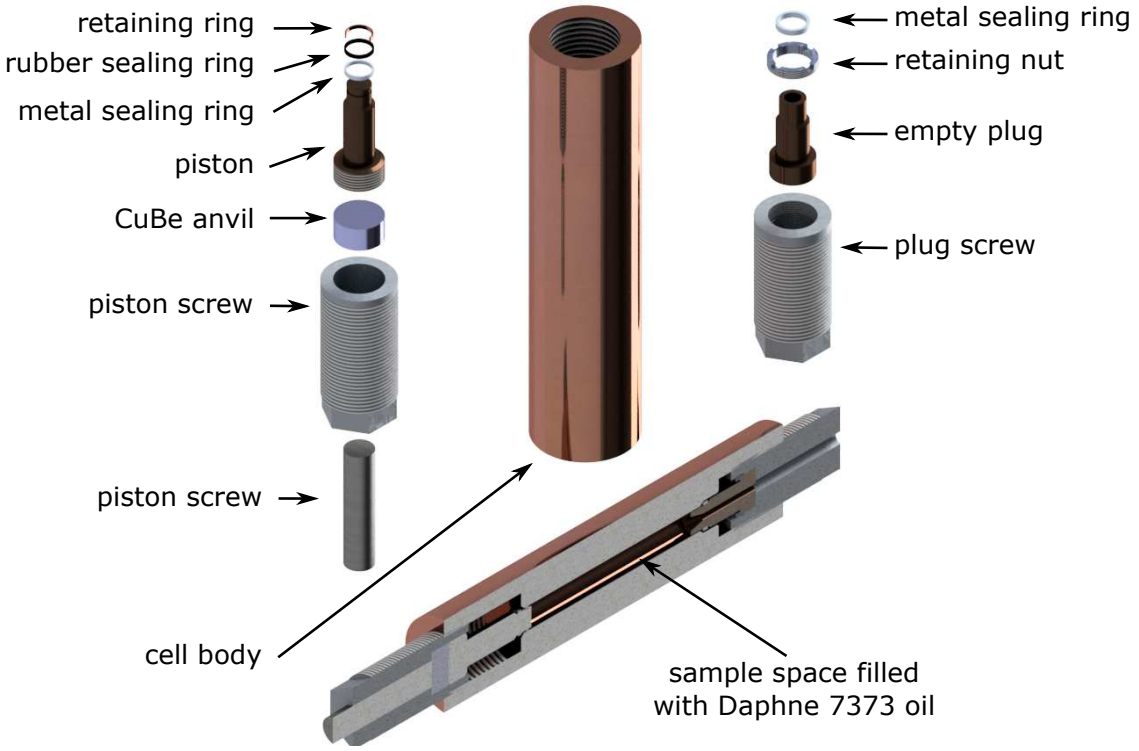

Figure 5.4: Sketch of the pressure cell used for dielectric spectroscopy measurements under pressure up to 10 kbar. The upper part shows an exploded-view-drawing of the cell, the lower part a cross section drawing of the assembled cell. The piston cell is of type LC10 and is designed and manufactured by the Institute of High Pressure Physics of the Polish Academy of Sciences in Warsaw, Poland [193]. Except for the metal sealing rings, it is made from non-magnetic CuBe; we assigned different colors to the parts to increase the contrast between the different parts in the picture.

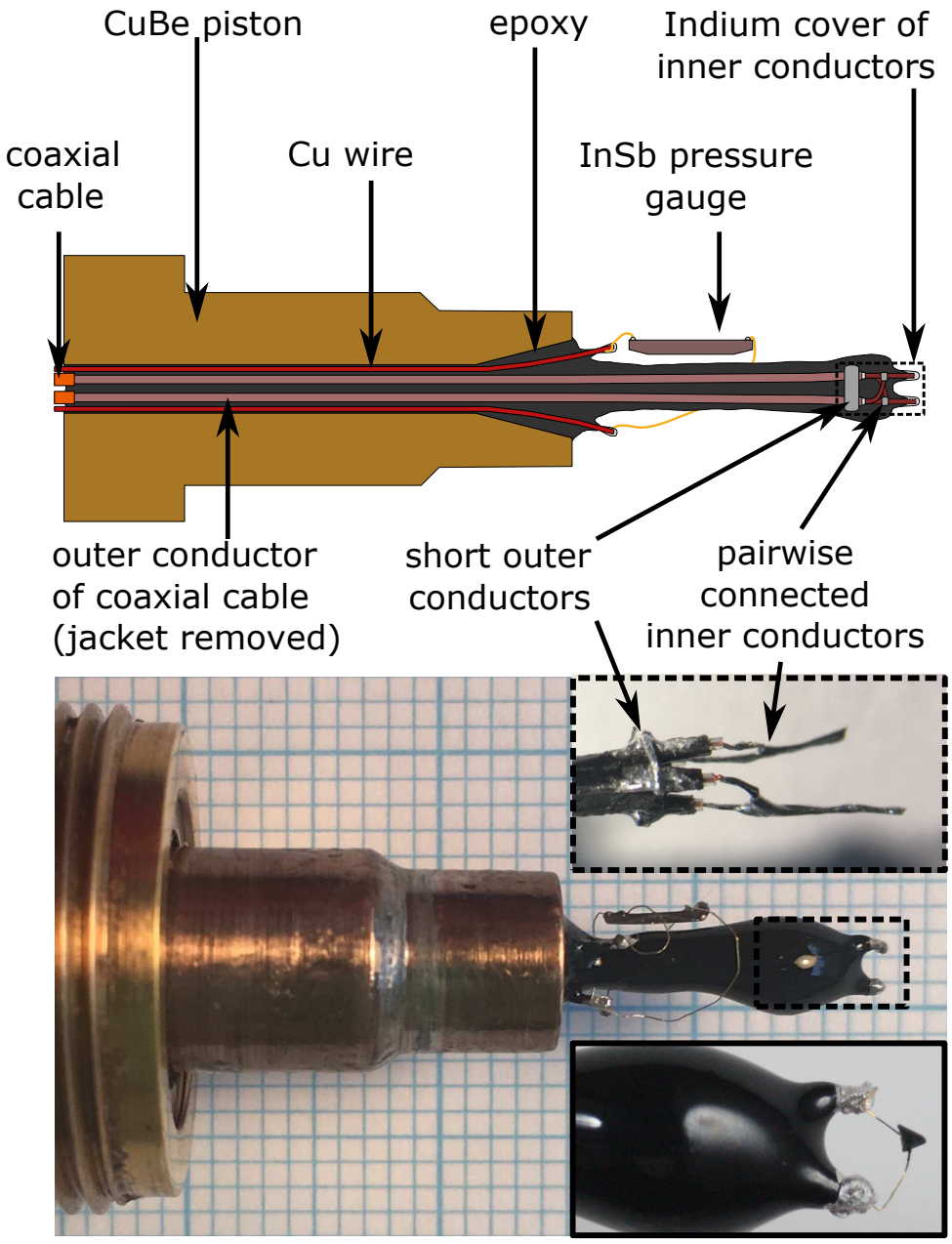

Figure 5.5: Illustration of the electrical feedthrough for coaxial cables mounted in a CuBe plug. The upper panel depicts a cross sectional sketch of the feedthrough, showing only two of the four coaxial cables and four copper wires. A picture of the feedthrough and the InSb semiconductor pressure gauge is shown in the lower panel. The inset within the dashed lines shows the outer conductors of the coaxial cables which are connected to each other by soldering a thin CuAg wire in a loop around them, and the inner conductors of the coaxial cables which are pairwise connected to each other and terminate in two pins. The inset in the solid lines shows the pins of the feedthrough, which are covered with indium to additionally seal the gap between the pins and the surrounding epoxy. A single crystalline sample is mounted with carbon paste and gold wires to the pins.

pressure cell. For the stretch the coaxial cables are running through the feedthrough, which is appoximately 50 mm, the outer jacket is carefully extracted, reducing the diameter to 0.43 mm. Moreover, we lay open the inner conductors at the cable end by carefully removing the outer conductor and the dielectric of the coaxial cables on a length of approximately 8 mm. As discussed above in Ch. 5.1, the inner conductors of the coaxial cables should be pairwise connected to be compatible with the auto-balancing bridge method used in a wide range of commercially availably impedance analyzers. This way, two terminals are formed to which the sample will be connected.

In addition to the coaxial cables, four copper wires with polyurethane insulation and a total diameter of 0.2 mm (AWG 32) are introduced into the feedthrough, forming pins to which the InSb pressure gauge will be connected by means of thin gold wires in a real four point configuration, as shown in the lower panel of Fig. 5.5.

In a first step, a pressure-resistant epoxy is filled into the feedthrough up to the conical opening to permanently glue the coaxial cables and the copper wires in such a way that the open cable end is still flexible and can be processed. The outer conductors of the coaxial cables are connected to each other by soldering a thin CuAg wire in a loop around them. The inner conductors are pairwise soldered to each other such that two pins are formed by the remaining cable ends, as shown by the dashed lines in the inset of Fig. 5.5.

In a second step, the coaxial cables are fully covered with pressure-resistant epoxy except the two pins formed by the inner conductors of the coaxial cables. It is very crucial, that the part where the outer conductor and the dielectric end is well covered with epoxy and only the two pins formed by the inner conductors protrude. This way, we provide a pressure-resistant sealing of the coaxial cable and minimize the part of the cable without the outer conductor. The latter ensures proper shielding of the measurement signal as close to the sample as possible and hence enhances the high frequency characteristics of the pressure feedthrough. Finally, when the epoxy is fully cured and hardened, an indium cover is deposited onto the pins and the surrounding epoxy by means of a soldering iron to create an additional sealing.

The sample is electrically contacted by attaching two gold wires with carbon paste to opposite crystal surfaces, on the other end, the gold wires are connected to the two pins of the feedthrough with silver paste. The InSb pressure gauge is connected to the ends of the copper wires with thin gold wires and indium as solder.

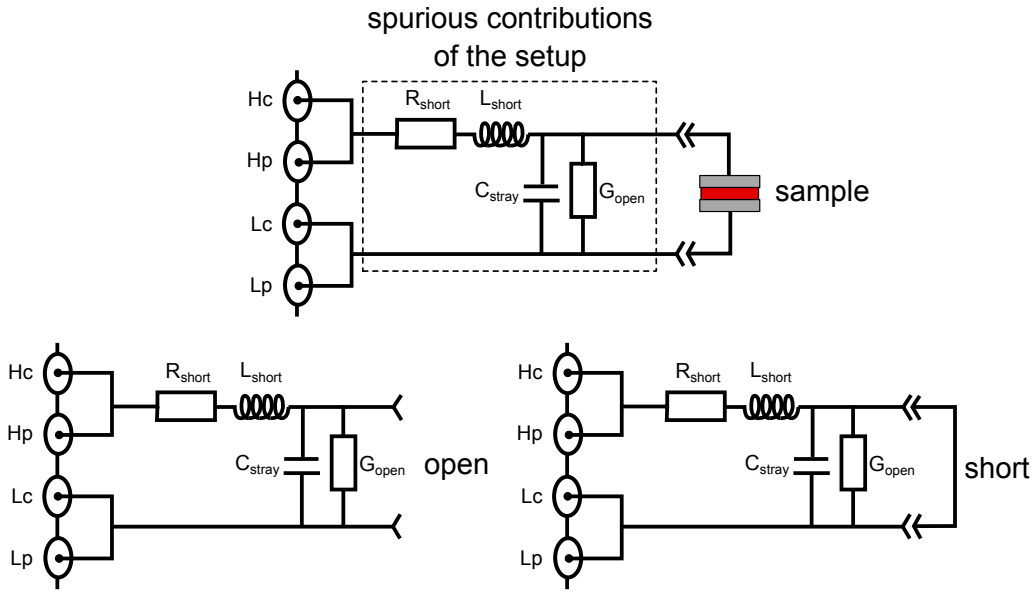

Figure 5.6: Equivalent circuit for the spurious effects due to the setup and the commonly used open and short compensation measurements to determined them. Based on Ref. [183].

5.2.2 Compensation measurements characterizing the setup

The influence of the setup on the measured dielectric response is determined by means of the open and short compensation measurements, the corresponding equivalent circuits are illustrated in Fig. 5.6.

The open compensation refers to a measurement without any sample wherein the two pins of the feedthrough are just left open. It determines the stray admittance $\hat{Y}_{\text{stray}} = G_{\text{open}} + i\omega C_{\text{stray}}$, which can be considered as a measurement of the background due to the setup, and gives an upper limit of its impedance range, which however, also depends on the used impedance analyzer.

The short compensation determines $\hat{Z}_{\text{short}} = R_{\text{short}} + i\omega L_{\text{short}}$, which is also referred to as residual impedance, wherein the two contacts are shorted by means of a thin gold wire. Z_{short} provides information on possible spurious resonance in the wiring of the setup and also on its low impedance limit.

In microwave spectroscopy, an additional load compensation is usually used which refers to a measurement of a calibrated reference of $\hat{Z}_{\text{load}} = 50\ \Omega$. It is used to detect any artificial reflections of the microwave signal in the transmission lines. In the radio and audio frequency range, however, these spurious effects are usually neglected and a load compensation is only recommended in case the impedance of the investigated sample stays in the range of the load reference [183]. Since the impedance of our sample changes over

several orders of magnitude upon cooling and applying pressure, a load compensation would in contrary induce additional errors and is not recommended. Finally, it should be mentioned here, that the compensation measurements have to be performed with the same device at the same settings as used for the actual sample measurements.

5.2.3 Open compensation measurement

In Fig. 5.7, we plot the frequency and the temperature dependence of C_{stray} and G_{open} for several temperatures and pressures. The measurements were performed with an Agilent A4294 impedance analyzer with an applied test signal of $U_{\text{osc}} = 0.5$ V. The equivalent circuit of the most simple model for the open compensation is also pictured in the inset of Fig. 5.7(a). C_{stray} and G_{open} should be as small as possible and give an estimate for the impedance and frequency range of the setup when a highly resistive sample is measured.

In Fig. 5.7(a) and (b), we plot C_{stray} and G_{open} as a function of frequency for several temperatures at 10 kbar. For $f < 10^4$ Hz, the measured impedance is at the limit of the analyzer, resulting in a decreased accuracy and giving rise to the observed fluctuations in C_{stray} and G_{open}. In the frequency range 10^4 Hz $< f < 10^6$ Hz, we obtain a value of $C_{\text{stray}} = 40$ fF at $T = 295$ K, which is slightly decreasing upon cooling. In the same frequency range, G_{open} rises by two orders of magnitude due to cross-talk between the pins, which increases with frequency but decreases upon cooling by a factor of 5 from room temperature to 10 K. For $f > 5 \times 10^6$ Hz, C_{stray} slightly decreases and G_{open} shows a strong downturn, which we ascribed to a reduced phase resolution of the used impedance analyzer at high frequencies [184].

In Fig. 5.7(c) and (d), the temperature dependence of C_{stray} and G_{open} is plotted for several pressure values at $f = 100$ kHz , respectively. The decrease of C_{stray} and G_{open} upon cooling is qualitatively the same, whereas only C_{stray} is pressured-dependent. We attributed the temperature dependence of both quantities to the thermal contraction of the coaxial cables and the concomitant change in the cable geometry. The measurement at ambient pressure is performed with an open pressure cell in helium gas. Upon filling the oil and densifying it with increasing pressure, the dielectric constant of the matter between the open contacts is enhanced, resulting in a growth of C_{stray} whereas G_{open} is pressure-independent.

To conclude, the open compensation measurement reveals small values for C_{stray} and G_{open} of the sample holder and the electrical feedthrough, making them suitable for low-temperature high-pressure dielectric spectroscopy measurements up to 5 MHz.

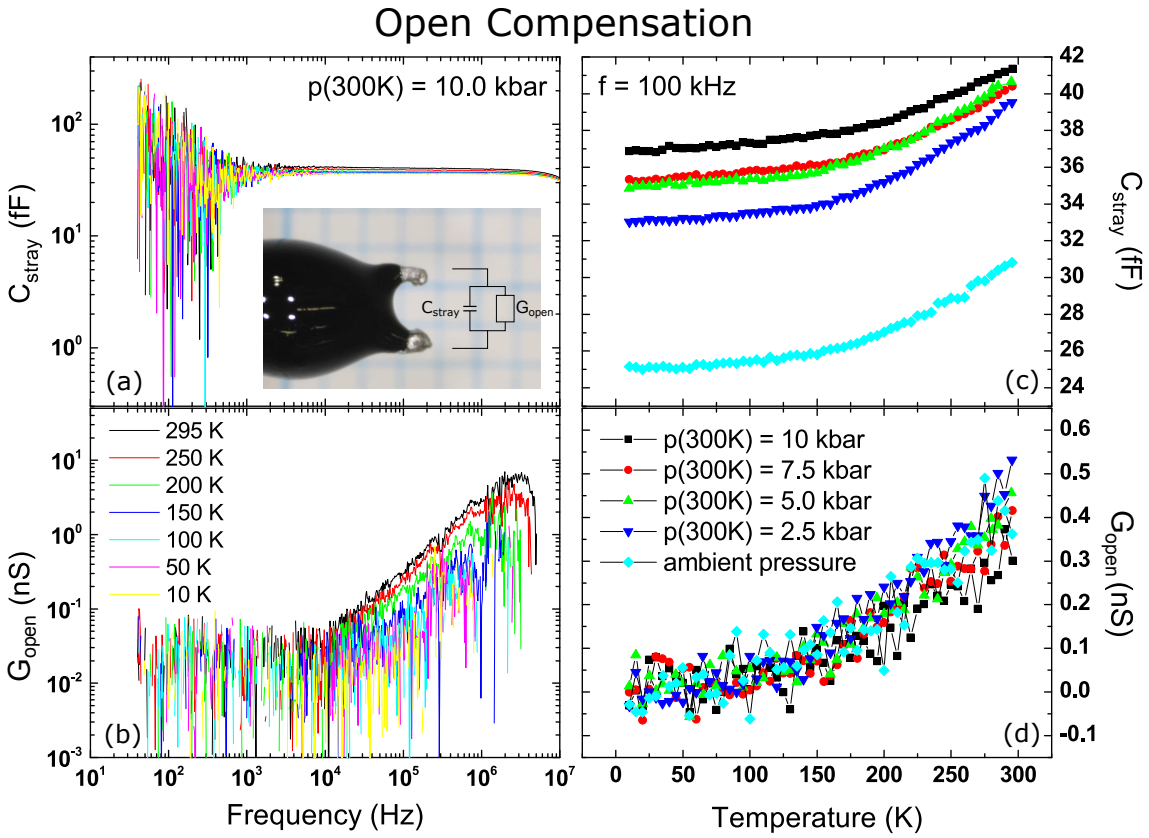

Figure 5.7: Open Compensation measurement of the setup with pressure cell and electrical feedthrough for the low temperature high-pressure dielectric spectroscopy measurements. The inset in panel (a) shows a picture of the empty sample holder with a scheme of the equivalent circuit. The measurements were performed with an Agilent A4294 impedance analyzer with an applied test signal of $U_{\mathrm{osc}} = 0.5$ V. Panels (a) and (b) show plots of the frequency dependence of the stray capacitance C_{stray} and the conductance G at 10 kbar for different temperatures, respectively. In panel (c) and (d), C_{stray} and G are plotted as a function of temperature for the different applied pressure values.

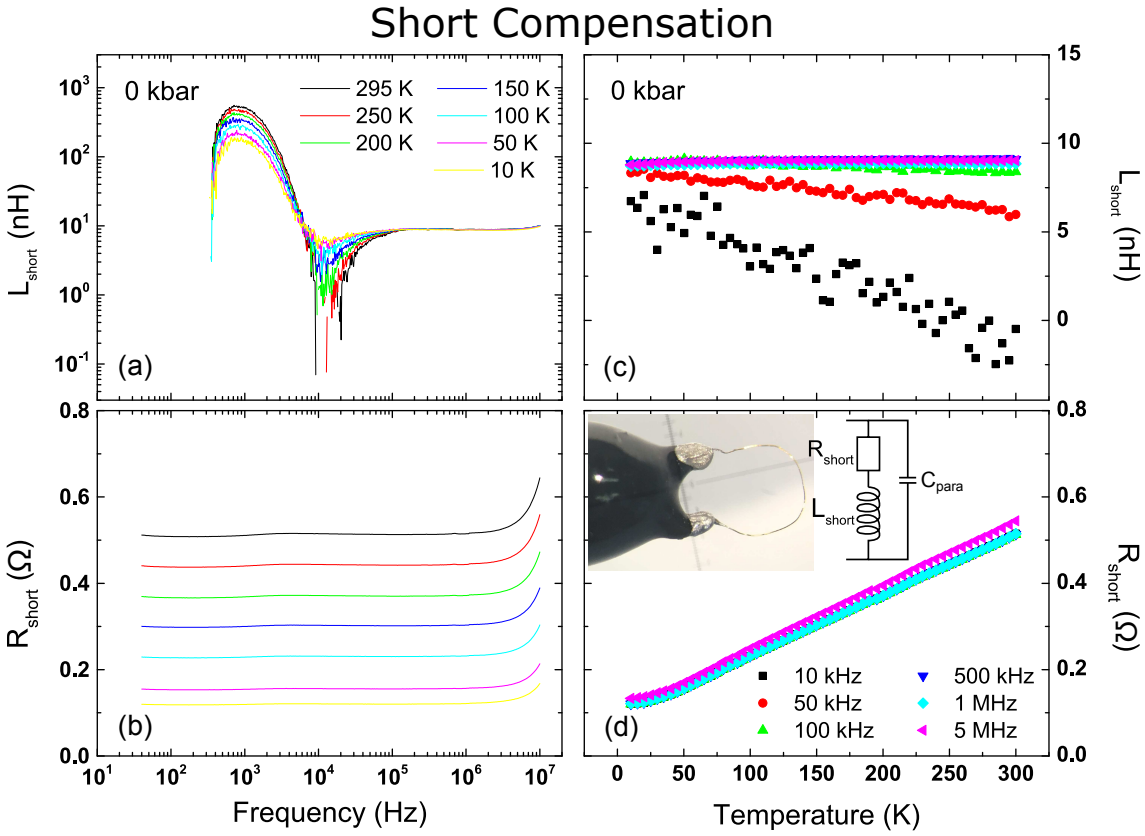

Figure 5.8: Short Compensation measurement of the setup wherein the pins of the pressure cell are shorted with a gold wire. This is shown in detail in the inset in panel (d) together with a scheme of the equivalent circuit. The measurements were performed with an Agilent A4294 impedance analyzer with an applied test signal of $U_{\mathrm{osc}} = 0.5$ V. Panels (a) and (b) show plots of the frequency dependence of L_{short} and R_{short} at ambient pressure for different temperatures, respectively. In panel (c) and (d), L_{short} and R_{short} are plotted as a function of temperature for various probing frequencies.

5.2.4 Short compensation measurement

In Fig. 5.8, the frequency and temperature-dependence of a short compensation measurement at ambient pressure is presented. For this measurement, it is important to mimic the measurement configuration which is usually used for a sample. To that end, a gold wire with a length of 10 mm and a diameter of 25 μm is attached to the pins by silver paste as normally used to connect a sample to the feedthrough pins. The measurement was performed with an Agilent A4294 impedance analyzer with an applied test signal of $U_{\mathrm{osc}} = 0.5$ V.

$R_{\mathrm{short}}(T)$ is plotted in Fig. 5.7(d), showing a linear decrease upon cooling, from around 0.5 to 0.1 Ω, as expected for a metallic wire. Interestingly, the corresponding plot of $L_{\mathrm{short}}(T)$ in panel (c) shows a strong frequency dependence. While for low frequencies, $L_{\mathrm{short}}(T)$ is enhanced upon cooling, it is nearly temperature-independent for high frequencies. To understand this behavior, we should have a look at the frequency dependence $L_{\mathrm{short}}(f)$ plotted in Fig. 5.7(a) for several temperatures as indicated. $L_{\mathrm{short}}(f)$ exhibits a resonant-like feature in form of a pronounced maximum around 1 kHz which is followed by a weak dip at 10 kHz. This corresponds to the self-resonant frequency (SRF) of the gold wire loop, i.e. the frequency at which the parasitic capacitance C_{para} of the wire loop resonates with its ideal conductance. We have good reason to assume C_{para} to be in parallel to the short compensation model, as shown in the inset of panel (d), because otherwise, C_{para} would block the current at low frequencies resulting in a high R_{short} which obviously is not the case. For this configuration, the SRF is defined as

$$\omega_{\mathrm{SRF}} = \sqrt{\frac{1}{L_{\mathrm{short}} C_{\mathrm{para}}} - \left(\frac{R_{\mathrm{short}}}{L_{\mathrm{short}}}\right)^2}, \tag{5.1}$$

wherein clearly R_{short} gives the dominating contribution. Hence, the change of the resonant feature in $L_{\mathrm{short}}(f)$ upon heating originates from the temperature-dependence of $R_{\mathrm{short}}(T)$. With estimates of $L_{\mathrm{short}} \approx 10$ nH as obtained for $f > 500$ kHz, and for instance $R_{\mathrm{short}} \approx 0.5\ \Omega$ and $f_{\mathrm{SRF}} \approx 8$ kHz at 295 K, we approximate $C_{\mathrm{para}} \approx 40$ nF, which is a surprisingly high value. We attribute this to an imperfect connection of the gold wire to the indium pins by means of silver paste, whose modeling probably would require a more sophisticated equivalent circuit. However, the decreasing amplitude of the resonance can be explained by its dependence on $R_{\mathrm{short}}(T)$, which is captured by the damping factor $\xi = \frac{R_{\mathrm{short}}}{2}\sqrt{\frac{C_{\mathrm{para}}}{L_{\mathrm{short}}}}$. We will, however, not go into detail with this considerations of basic circuit theory (inset in panel (d)) and conclude, that care has to be taken in analyzing low frequency data ($f < 50$ kHz) of highly conducting samples with inductive properties, such as metallic ones.

5.2.5 Measured observables

Besides the complex impedance $\hat{Z}$, the response of the sample can also be presented using the complex admittance $\hat{Y}$. Whether to use $\hat{Z}$ or $\hat{Y}$ is a matter of choice, since they are straightforwardly related to each other. For the sake of completeness,this relation is

$$\hat{Z} = R + iX = \frac{1}{\hat{Y}} = \frac{G}{G^2 + B^2} + i\frac{-B}{G^2 + B^2}, \tag{5.2}$$

or vice versa

$$\hat{Y} = G + iB = \frac{1}{\hat{Z}} = \frac{R}{R^2 + X^2} + i\frac{-X}{R^2 + X^2}, \tag{5.3}$$

with R as the resistance of the sample, X the reactance, G the conductance and B the susceptance. $\hat{Z}$ and $\hat{Y}$ are extensive quantities and therefore not suitable to properly describe the electrodynamic response of the investigated physical system. This is usually done by determining one of the intensive quantities listed below. While in principle they all contain the same information, their preferably used to describe different kinds of charge transport processes inherent to the investigated system. For example, whether dielectric relaxation or dc-conduction processes prevail in the overall transport properties.

Conductivity and resistivity

In case dc-conduction processes due to quasi-free charge carriers dominate the transport properties, the resistivity $\hat{\rho}$ and the conductivity $\hat{\sigma}$ are usually used, wherein the former is used for rather insulating and the latter for rather conducting media. $\hat{\rho}$ or $\hat{\sigma}$ is straightforwardly determined from the measured impedance or admittance, respectively, via

$$\hat{\rho} = \rho_1 + i\rho_2 = \frac{A}{d}R + i\frac{A}{d}X \tag{5.4}$$

and

$$\hat{\sigma} = \sigma_1 + i\sigma_2 = \frac{d}{A}G + i\frac{d}{A}B, \tag{5.5}$$

with the area of the plane-parallel electrodes A and the distance d between them. Analog to the relation between $\hat{Z}$ and $\hat{Y}$ in Eqs. 5.2 and 5.3, $\hat{\rho}$ and $\hat{\sigma}$ are related to each other according to $\hat{\rho} = 1/\hat{\sigma}$.

Permittivity and dielectric modulus

We already introduced the permittivity $\hat{\varepsilon}$ in Ch. 4.1 as a main quantity entering Maxwell's equation which is preferably used to describe transport processes due to the charge dis-

placements over a limited distance, i.e. dielectric relaxation. It is obtained from the measured admittance via

$$\hat{\varepsilon} = \varepsilon_1 - i\varepsilon_2 = \frac{d}{A}\frac{B}{\varepsilon_0\omega} - i\frac{d}{A}\frac{G - G_0}{\varepsilon_0\omega}, \tag{5.6}$$

wherein $\omega = 2\pi f$ is the angular frequency of the applied ac signal. In case the sample is not completely insulating, its dc-conductance G_0 gives a considerable contribution to ε_2 such that the low-frequency spectrum is dominated by the corresponding $\varepsilon_2 \propto \omega^{-1}$ term. Therefore, in order to reveal the possible presence of a relaxation mode it is common procedure to subtract this part [32, 133, 195].

In some materials classes one is interested in the dielectric properties at higher temperatures, at which ε_1 can increase to rather high values due to increasing dc-conduction or possible electrode polarization (EP). In this case, analyzing the dielectric modulus

$$\hat{M} = \frac{1}{\hat{\varepsilon}} = \frac{1}{\varepsilon_1 - i\varepsilon_2} = \frac{\varepsilon_1}{\varepsilon_1^2 + \varepsilon_2^2} + i\frac{\varepsilon_2}{\varepsilon_1^2 + \varepsilon_2^2} = M_1 + iM_2 \tag{5.7}$$

provides some advantages, which was first introduced in 1967 as an analogy to the mechanical modulus in the viscoelastic relaxation of polymers [196]. First, both ε_1 and ε_2 can become rather large for high dc-conduction and EP effects such that the presence of a relaxation mode is easily obscured or overseen. Contrary, since both go into the denominator of the dielectric modulus (Eq. 5.7), M_1 and M_2 become small and the possible presence of a relaxation mode is still easily detectable. Second, the signature of a Debye relaxation is shifted to higher frequencies in $\hat{M}$ [197], such that it might get easier to distinguish it from EP effects which are usually observed at low frequencies f <1 kHZ and are not shifted.

Analyzing the dielectric response via $\hat{M}$ is usually done for the investigation of electrical relaxation phenomena in vitreous ionic conductors [198] and polymer electrolytes [199] and recently also for epoxy resins [197].

Subtracting the open and short compensation measurements

The measurement of a sample yields data in from of $\hat{Y}_{\text{sample}} = G_{\text{sample}} + iB_{\text{sample}}$ or $\hat{Z}_{\text{sample}} = R_{\text{sample}} + iX_{\text{sample}}$, which of course also include spurious contribution originating from the setup. In case for highly insulating samples with $G_{\text{sample}} \ll B_{\text{sample}}$, it is sufficient to only consider the open compensation measurement yielding $\hat{Y}_{\text{stray}} = G_{\text{open}} + i\omega C_{\text{stray}}$.

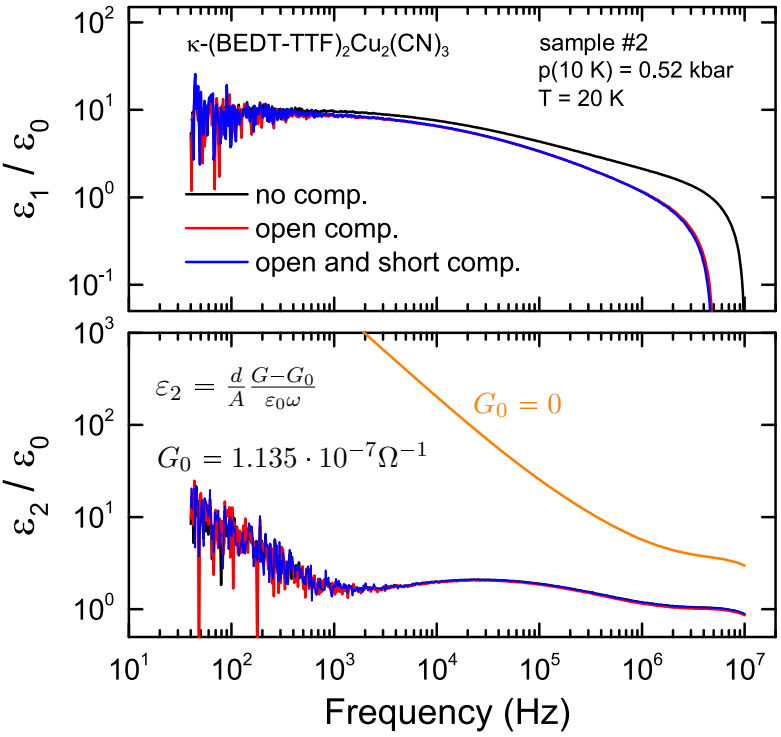

Figure 5.9

Hence, the admittance used to calculate the electrodynamic response (cf. Ch. 5.1) of the sample is corrected according to

$$\hat{Y} = \hat{Y}_{\text{sample}} - \hat{Y}_{\text{stray}}. \tag{5.8}$$

For samples with considerably high conductivity, $G_{\text{sample}} \gtrsim B_{\text{sample}}$, also the short compensation yielding $Z_{\text{short}} = R_{\text{short}} + i\omega L_{\text{short}}$ has to be taken into account, such that the admittance is obtained by

$$\hat{Y} = \frac{1 - \hat{Y}_{\text{stray}} \left(\hat{Z}_{\text{sample}} - \hat{Z}_{\text{short}} \right)}{\hat{Z}_{\text{sample}} - \hat{Z}_{\text{short}}}. \tag{5.9}$$

In the ideal case, the measurement parameters and conditions, such as pressure, temperature, probing frequencies and U_{osc}, of the sample and the compensation measurements should be the same.

The effect of the compensation corrections is exemplarily demonstrated in Fig. 5.9 for the frequency-dependence of the permittivity, which is calculated from $\hat{Y}$ using Eq. 5.6. The black solid lines correspond to $\varepsilon_1(f)$ and $\varepsilon_2(f)$ as directly obtained from the sample

measurement, i.e. without any compensation correction. The red lines only take into account the open compensation (Eq. 5.8) whereas for the blue lines both open and short are considered (Eq. 5.9). For these variations, a finite dc-conductance of $G_0 = 1.135 \cdot 10^{-7}\ \Omega^{-1}$ is already taken into account in determining $\varepsilon_2(f)$. If we neglect the dc-contribution by setting $G_0 = 0$ (orange line), $\varepsilon_2(f)$ is dominated by the corresponding f^{-1} obscuring the presence of a relaxation mode centered around 30 kHz.

In Fig. 5.9, a considerable difference in $\varepsilon_1(f)$ is observed when comparing the non-compensated (black line) with the open compensated measurement (red line), whereas these measurements perfectly match in $\varepsilon_2(f)$. This clearly shows, that C_{stray} has a considerable influence on the obtained data and has to be taken into account, while the influence of G_{open} is negligible compared to the samples conductivity, even in the case the rather lager dc-conductivity G_0 is already subtracted. These findings are confirmed when comparing the open compensated (red line) with open and short compensated (blue line), where nearly no difference in observed in $\varepsilon_1(f)$ as well as in $\varepsilon_2(f)$. The short compensation becomes important in case the sample's impedance is very, $R_{\text{short}}/R_{\text{sample}} \lesssim 0.1$, low and spurious effects associated with a rather large current flowing through the setup wiring, L_{short}, have to be considered. However, since $R_{\text{short}} \lesssim 0.6\ \Omega$, the sample's impedance remains high enough to neglect these contributions even in its metallic regime at high pressures.

5.2.6 Comparison ambient pressure and pressure dependent setup

In order to test the performance of our setup, we conducted measurements of a test sample at ambient pressure in He-gas mounted on the pressure feedthrough and in a standard ambient-pressure setup serving as a reference. For this purpose, sample #2 of κ-(BEDT-TTF)$_2$Cu$_2$(CN)$_3$ (cf. Ch. 5.4) is used whereby the contacts and the gold wires contacting the sample were not modified. The sample was first measured in the standard setup and subsequently in the pressure cell at ambient pressure without using oil. Both measurements were performed up to 10 MHz with an applied test signal of $U_{\text{osc}} = 0.5$ V. The pressure-dependent results, their comprehensive analysis and discussion will be presented in full detail in chapters 7 and 8.

Fig. 5.10(a) displays the temperature dependence of the real part $\varepsilon_1(T)$ for $f = 100$ kHz. Most importantly, there is good agreement between the two experiments in the different setups. The observation of the broad peak around $T = 27$ K is consistent with literature [31, 32, 137] proofing the proper operation of our pressure setup. In Fig. 5.10(b), we plot $\varepsilon_1(f)$ and $\varepsilon_2(f)$ as a function of frequency at $T = 27$ K, right at the peak temperature in $\varepsilon_1(T)$. With increasing frequency, $\varepsilon_2(f)$ shows a roll-off with an inflection point at

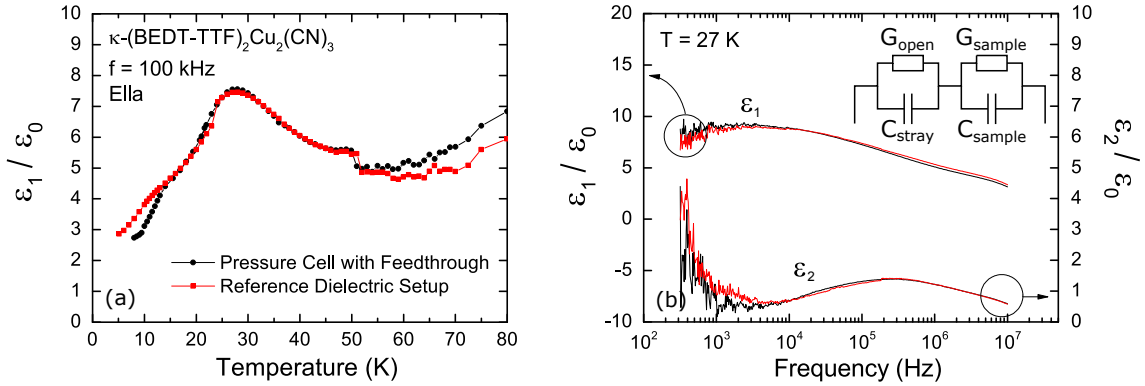

Figure 5.10: Dielectric spectra of κ-(BEDT-TTF)$_2$Cu$_2$(CN)$_3$ of sample #2 recorded along the a-axis. The measurements in the pressure cell with our novel feedthrough (shown in black) are compared to data taken in a conventional dielectric spectrometer setup serving as reference (red). Panel (a) shows the temperature dependence of the real part of the permittivity $\varepsilon_1(T)$ with a broad peak at $T = 27$ K; the findings are consistent with reports in the literature [31, 32, 137]. The frequency dependence of the permittivity at $T = 27$ K is plotted in panel (b) wherein the open compensation for each setup is considered. We observe an inflection with increasing frequency in $\varepsilon_1(f)$ and a maximum in $\varepsilon_2(f)$ which agrees well with previous reports in literature [31, 32, 137]. The good agreement between both measurements in the temperature and frequency dependence verifies the proper operation of our pressure feedthrough.

$f = 3 \times 10^5$ Hz, right where $\varepsilon_2(f)$ exhibits a broad maximum. Both features are signatures of a dielectric relaxation (cf. Ch. 4.2.1) which is well described in the Havriliak-Negami model. We emphasize the good agreement between the measurements performed with the pressure feedthrough and the conventional setup serving as a reference.

5.2.7 Conclusion

We have developed an electrical feedthrough for four coaxial cables and four copper wires into a piston type pressure cell ranging up to 10 kbar. In combination with a continuous flow cryostat, the cable length is minimized enabling high-pressure dielectric spectroscopy measurements up to $f = 5$ MHz in frequency and temperatures down to 8 K. We performed open compensation measurements, i.e. background measurements of the response originating from the pressure setup without sample, to obtain its high frequency characteristics. The stray capacitance of the pressure setup is determined to $C_{\text{stray}} = 40$ fF, enabling the measurement of small single crystals with a weak dielectric response. The proper operation is verified by comparing measurements of a test sample, a single crystal of κ-(BEDT-TTF)$_2$Cu$_2$(CN)$_3$, in the pressure setup at ambient pressure as well as in a conventional dielectric spectroscopy setup. Finally it should be emphasized here, that the custom made sample holder, receiving the pressure cell with the feedthrough, is designed to be compatible with the *Agilent A4294* [184] as well as with the *Novocontrol Alpha-A* analyzer [200], whereby the latter has to be equipped with a *ZG4* interface.

5.3 Extrinsic effects

Dielectric spectroscopy in general is a two-point method and special care has to be taken in order to exclude artefacts originating from contacts and/or resonance effects in the measurement circuit. In the following, we will shortly overview the mechanisms giving rise these spurious effects and how to evaluate their influence on the obtained data.

5.3.1 Contact contribution

Due to the two-point measurement configuration usually applied in dielectric spectroscopy, the obtained data may include contributions from polarization effects at the contacts which have to be conscientiously ruled out or determined. In literature, these contributions are usually referred to as Maxwell Wagner type relaxation, Schottky contacts or electrode polarization. The latter usually denotes peculiar polarization effects at electrodes in liquid conductors, such as ionic solutions, and should not be used when referring to measurements on single crystals. The Maxwell Wagner relaxation generally describes charge accu-

mulation at interfaces of any kind, such as in heterogeneous media (cf. Ch.4.4), at grain boundaries, phase boundaries as well as at contact-sample interfaces. This term captures a rather broad range of effects whereas here we want to discuss the effects at the interface of a single crystalline sample with its contacts. In our case, the sample exhibits semiconducting behavior and the contacts are formed by amorphous carbon (carbon paste) with metallic properties, such that Schottky contacts are formed at the sample-contact interfaces.

Schottky Contact

For a semiconductor-metal junction in thermal equilibrium, the chemical potential μ of the charge carriers has to be constant across the interface, resulting in a bending of the valence band $E_{\mathrm{v}}^{\mathrm{n}}$ and conduction band $E_{\mathrm{c}}^{\mathrm{n}}$. This band deformation is schematically illustrated for a n-type semiconductor in Fig.5.11, wherein E_{D} is the energy level of the donor states, $e\Phi_{\mathrm{M}}$ is the work function of the metal, $e\chi$ the electron affinity, eV_{n} the energy difference between conduction band and chemical potential with $e\Phi_{\mathrm{H}} = e\chi + eV_{\mathrm{n}}$ as the energy difference between μ and E_{vac}.

The band deformation gives rise to a depletion zone right at the interface wherein the mobile majority charge carries are forced away by the electric field associated with the band bending, which is illustrated for a n-type semiconductor with $\Phi_{\mathrm{H}} > \Phi_{\mathrm{M}}$ in Fig. 5.11(b). In this case, electrons diffusion from the n-type semiconductor into the metal, such that the depletion zone is positive in the semiconductor and negative in the metal. This gives rise to a potential barrier of height $e\Phi_{\mathrm{B}}$ which impedes the electron transport across the interface and results in non-ohmic behavior of the junction. For $\Phi_{\mathrm{H}} < \Phi_{\mathrm{M}}$ (not shown in Fig. 5.11), electrons diffuse from the metal into the n-type semiconductor which bends the conduction band to lower energies into the Fermi level of the metal and allows coherent electron transport across the junction.

The same considerations apply for hole transport in p-type semiconductors with the difference, that $\Phi_{\mathrm{H}} < \Phi_{\mathrm{M}}$ gives rise to an effective barrier for holes, impeding coherent charge transport, and $\Phi_{\mathrm{H}} > \Phi_{\mathrm{M}}$ leads to ohmic behavior.

In Fig. 5.11(c,d), we additionally considered a voltage U applied to the junction. A positive voltage (panel (c)) lowers the potential energy of the electrons in the metal, effectively decreasing the potential barrier and facilitating electron transport across the junction. Contrary, a negative voltage (panel (d)) lifts the potential energy of the electrons, enhancing the effective barrier at the interface such that electron transport across the junction is further suppressed.

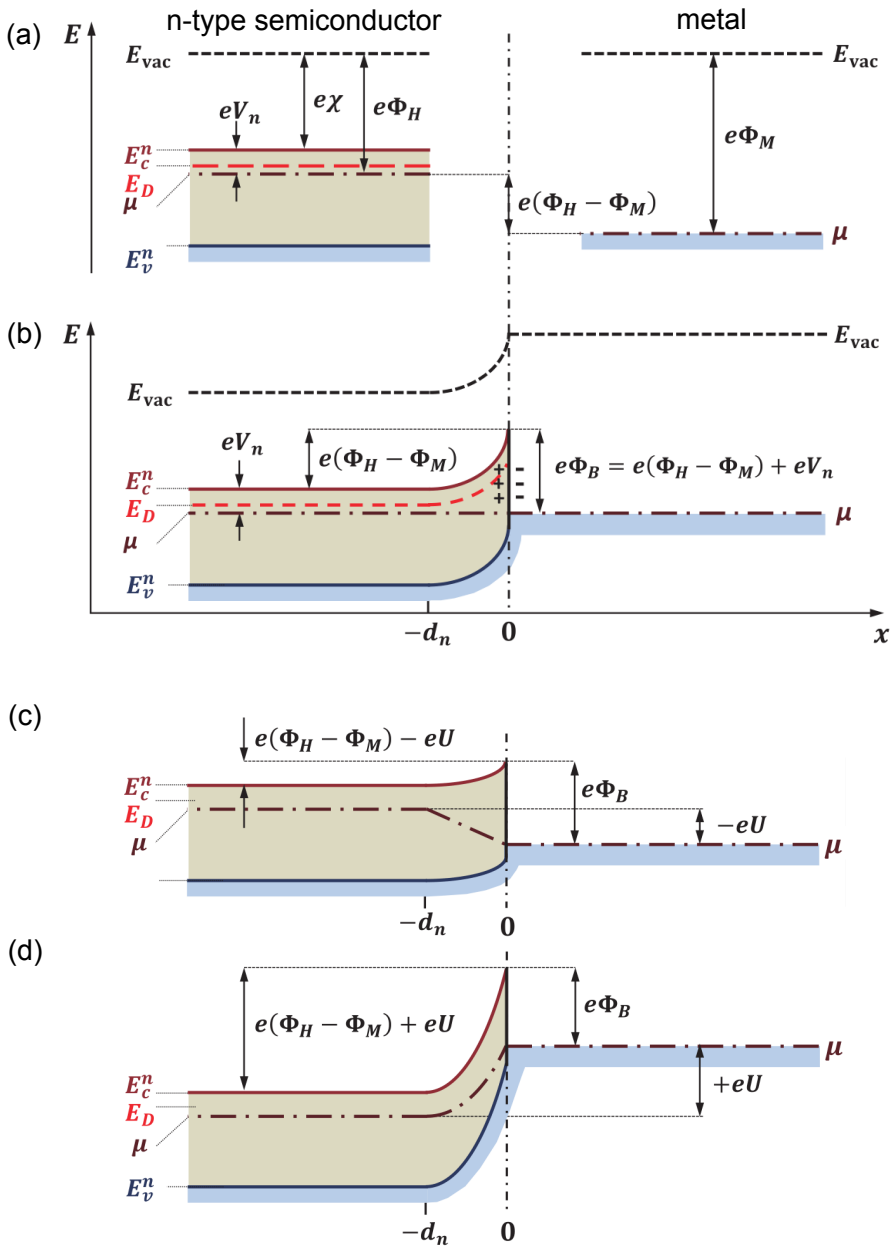

Figure 5.11: Schematically illustration of a Schottky contact in thermal equilibrium. (a) Band scheme of a n-type semiconductor (left) and a metal (right) which are still separated from each other. (b) Scheme of the band deformation at the semiconductor-metal junction. (c) Schottky contact under applied voltage with positive sign, lowering the energy of the electrons by $-eU$. (d) Schottky contact under applied voltage with negative sign, increasing the energy of the electrons by $+eU$. Reproduced after Ref. [201](pp. 528, 531).

The depletion zone within the metal is negligible small, usually around 1 nm, due to its high density of free electrons. In contrast, the thickness of the depletion zone in a n-type (p-type) semiconductor depends on the charge carrier density n, the difference $\Phi_{\mathrm{M}} - \Phi_{\mathrm{H}}$ ($\Phi_{\mathrm{H}} - \Phi_{\mathrm{M}}$) as well as on the applied voltage and is given [201] as

$$d_{\mathrm{n}} \;=\; \left(\frac{2\varepsilon_1 \varepsilon_0}{en} (\Phi_{\mathrm{M}} - \Phi_{\mathrm{H}} \pm eU) \right)^{1/2}, \tag{5.10}$$

with ε_1 as the real part of the permittivity of the semiconductor. It is intuitive that the modified charge density in the depletion zone influences the impedance of the junction and gives rise to the capacitance

$$C_{\mathrm{depl}} \propto \frac{1}{d_{\mathrm{n}}} \propto \left(\frac{2\varepsilon_1 \varepsilon_0}{en} (\Phi_{\mathrm{M}} - \Phi_{\mathrm{H}} \pm eU) \right)^{-1/2}, \tag{5.11}$$

which eventually is responsible for the spurious effects attributed to the contact contribution. With the help of Eqs. 5.11 and 5.11 we can easily apply several procedures to estimate the influence of the contacts to our experimental results.

- Modifying Φ_{M} by using a different contact material, such as gold paste. For negligible contact contribution, the measured dielectric properties should not change.

- Comparison of samples with varying contact area A while the ration A/d is kept constant, wherein d is the sample thickness determining the distance between the contacts. In case of spurious effects originating from the contacts, the measured dielectric response should change upon varying A/d.

- The charge carrier density corresponds to the number of electrons that are thermally excited across the charge gap Δ. For an intrinsic semiconductor without doping it is given as

  $$n(T) \propto \exp\left\{ -\frac{\Delta}{k_{\mathrm{b}} T} \right\}. \tag{5.12}$$

  Upon cooling, free charge carries in the semiconductor freeze out which has an strong impact on d_{n} and hence on C_{depl}. According to Eq. 5.11, the contact contribution should be dominant at elevated temperatures with large $n(T)$.

- For linear dielectrics, tuning the voltage U of the applied ac-signal should have an impact on the measured dielectric response according to $\varepsilon_1(U) \propto U^{-1/2}$ in case of relevant contact contributions.

5.4 Investigated samples

In the following, the necessary information on the investigated samples are provided. All samples were grown by the standard electrochemical synthesis method [35, 202] yielding high-quality single crystals. The κ-(BEDT-TTF)$_2$Cu$_2$(CN)$_3$ (κ-CuCN) sample 1 and sample A3 were grown at our institute by Ralph Hübner with the assistance of Anja Löhle while sample 2 was provided by John Schlueter from the Material Science Division at the Argonne National Laboratory, USA. Table 5.1 summarizes the properties of these two crystals. The entire series of κ-[(BEDT-STF)$_x$-(BEDT-TTF)$_{1-x}$]$_2$Cu$_2$(CN)$_3$ (κ-STF$_x$-CuCN) samples, listed with details in Table 5.2, were synthesized by Yohei Saito at the deparment of physics of the Hokkaido University, Japan. Unfortunately, the synthesize of the κ-(BEDT-TTF)$_2$Ag$_2$(CN)$_3$ (κ-AgCN) compound is very challenging and crystals are rare, such that only one crystal, grown at our institute by Ralph Hübner with the assistance of Anja Löhle, was available for pressure-dependent dielectric spectroscopy measurements.

In general, the crystals exhibit a plate-like shape with a typical dimensions of $60 \times 250 \times 250$ μm^3 along a-,b- and c-directions, respectively, wherein a large sample to sample variation is observed in their form and thickness d, i.e. the extension along a-direction. The κ-phase and the crystal directions were determined by means of Fourier-transform infrared (FTIR) spectroscopy [203].

All samples presented in this thesis were contacted out-of-plane with $E \parallel a$ by attaching gold wires with carbon paste covering opposite crystal surfaces, which was done for sample 1 by the author and otherwise by our technician Gabriele Untereiner. Fig. 5.12 shows photographs of three samples to exemplarily illustrate the contacts and the varying sample shapes. We roughly estimated the area A on the crystal surface covered by carbon paint and took this as the current cross section in order to determine the intensive quantities such as $\hat{\varepsilon}$ or $\hat{\rho}$ (cf. Ch. 5.1).

All measurements were performed with two contacts in a pseudo four-point configuration (cf. Ch. 5.1) using an Agilent 4294 Impedance Analyzer. The applied ac voltage was set to 0.5 V, making sure that we operate in the Ohmic regime. The ambient pressure measurement of sample 1 was performed by Annette Böhme during her Bachelor project [1]. The majority of the κ-[(BEDT-STF)$_x$-(BEDT-TTF)$_{1-x}$]$_2$Cu$_2$(CN)$_3$ samples were measured by Maxim Wenzel during his Bachelor project. Both projects were conceived and supervised by the author at PI1. All other measurements, especially the pressure-dependent, were carried out by the author.

[1] In her Bachelor thesis, sample 1 is denoted as "Probe 7".

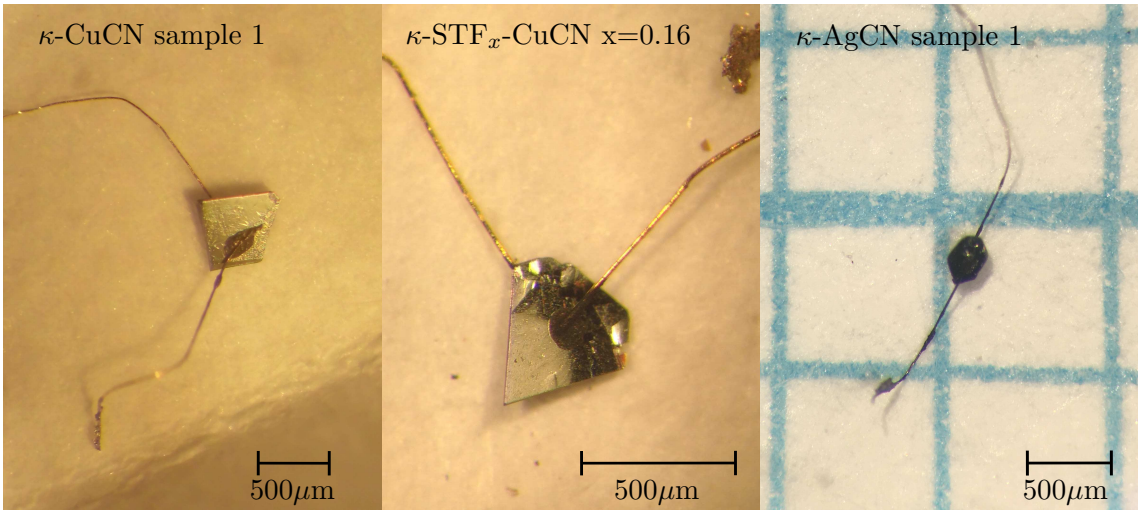

Figure 5.12

κ-CuCN (lab name)	contact direction	contact surface A $(\mu m)^2$	thickness d (μm)	sample grower
sample 1 (A1)	**E** || **a**	184000	80	R. Hübner
sample 2 (A7)	**E** || **a**	196350	60	J. Schlueter

Table 5.1: κ-(BEDT-TTF)$_2$Cu$_2$(CN)$_3$ (κ-CuCN) samples which were investigated in the pressure-dependent dielectric spectroscopy measurements. d refers to the sample extension along the a-direction and A to the estimated area covered by carbon paste forming the contacts.

κ-STF$_x$-CuCN (lab name)	contact direction	contact surface A $(\mu m)^2$	thickness d (μm)	sample grower
x=0.00 (A3)	**E** || **a**	170000	100	R. Hübner
x=0.04 (4%A)	**E** || **a**	196351	80	Y. Saito
x=0.10 (10%B)	**E** || **a**	94248	80	Y. Saito
x=0.10 (10%C)	**E** || **a**	142600	40	Y. Saito
x=0.12 (12%A)	**E** || **a**	60000	50	Y. Saito
x=0.16 (16%A)	**E** || **a**	62800	20	Y. Saito
x=0.19 (19%A)	**E** || **a**	188500	30	Y. Saito
x=0.25 (25%A)	**E** || **a**	152000	40	Y. Saito

Table 5.2: κ-[(BEDT-STF)$_x$-(BEDT-TTF)$_{1-x}$]$_2$Cu$_2$(CN)$_3$ (κ-STF$_x$-CuCN) samples, which were investigated in the ambient pressure setup for dielectric spectroscopy measurements.

κ-AgCN (lab name)	contact direction	contact surface A $(\mu\text{m})^2$	thickness d (μm)	sample grower
sample (A5)	**E** $\|\|$ **a**	58800	80	R. Hübner

Table 5.3: κ-(BEDT-TTF)$_2$Ag$_2$(CN)$_3$ (κ-AgCN) samples which were investigated in the pressure-dependent dielectric spectroscopy measurements.

6

Overview of the results

The intent of this chapter is to give a first overview of the dielectric response over the entire phase diagram of κ-(BEDT-TTF)$_2$Cu$_2$(CN)$_3$ (κ-CuCN), κ-[(BEDT-STF)$_x$-(BEDT-TTF)$_{1-x}$]$_2$Cu$_2$(CN)$_3$ (κ-STF$_x$-CuCN) and κ-(BEDT-TTF)$_2$Ag$_2$(CN)$_3$ (κ-AgCN). As we will see, it is then beneficial for the further proceeding to divide the obtained results into two parts which are then presented and discussed in detail in the subsequent chapters. The first part (Ch. 7) deals with the dielectric response observed in the Mott insulating phase of the investigated compounds wherein special focus is put onto the frequency-dependent analysis revealing peculiar relaxation dynamics. The second part (Ch. 8) is dedicated to the polarization phenomena observed in proximity to the phase boundary which unequivocally reveal a phase coexistence region and verify the first order scenario for the Mott transition.

6.1 κ-(BEDT-TTF)$_2$Cu$_2$(CN)$_3$

Let's first have a look at the resistivity of κ-CuCN as a function of temperature and applied pressure. Fig. 6.1(a) displays the $\rho_1(T)$ curves probed at $f = 7.5$ kHz for sample #2. The indicated pressure values were recorded at $T = 10$ K.

Most importantly, our results are in good agreement with four-point dc-measurements reported in literature [17, 28], although we measured at finite frequency in a two-point configuration. Up to $p = 1.22$ kbar, the sample exhibits purely resistive behavior with $d\rho_1/dT > 0$. At $p = 1.45$ kbar and above, a maximum in $\rho_1(T)$ is observed that shifts to higher T with increasing pressure; concomitantly the resistivity is reduced. The maximum at $T_{\max}$ marks the onset of the metallic transport regime with $d\rho_1/dT < 0$ which is also referred to as Brinkman-Rice line [204]. Its determination is exemplarily shown in Fig. 6.1(b) for a pressure of 1.69 kbar wherein $T_{\max}$ is indicated by the cyan arrow.

Within the metallic regime, we can further distinguish between the Fermi liquid (FL) at low temperatures, characterized by $\rho_{1,\mathrm{FL}} = \rho_0 + AT^2$, and bad metal behavior at temperatures above (cf. Ch.2.4). We remind here, that the experimental setup did not allow for cooling below 8 K such that the super-conducting state below $T_{\mathrm{SC}} = 4$ K could

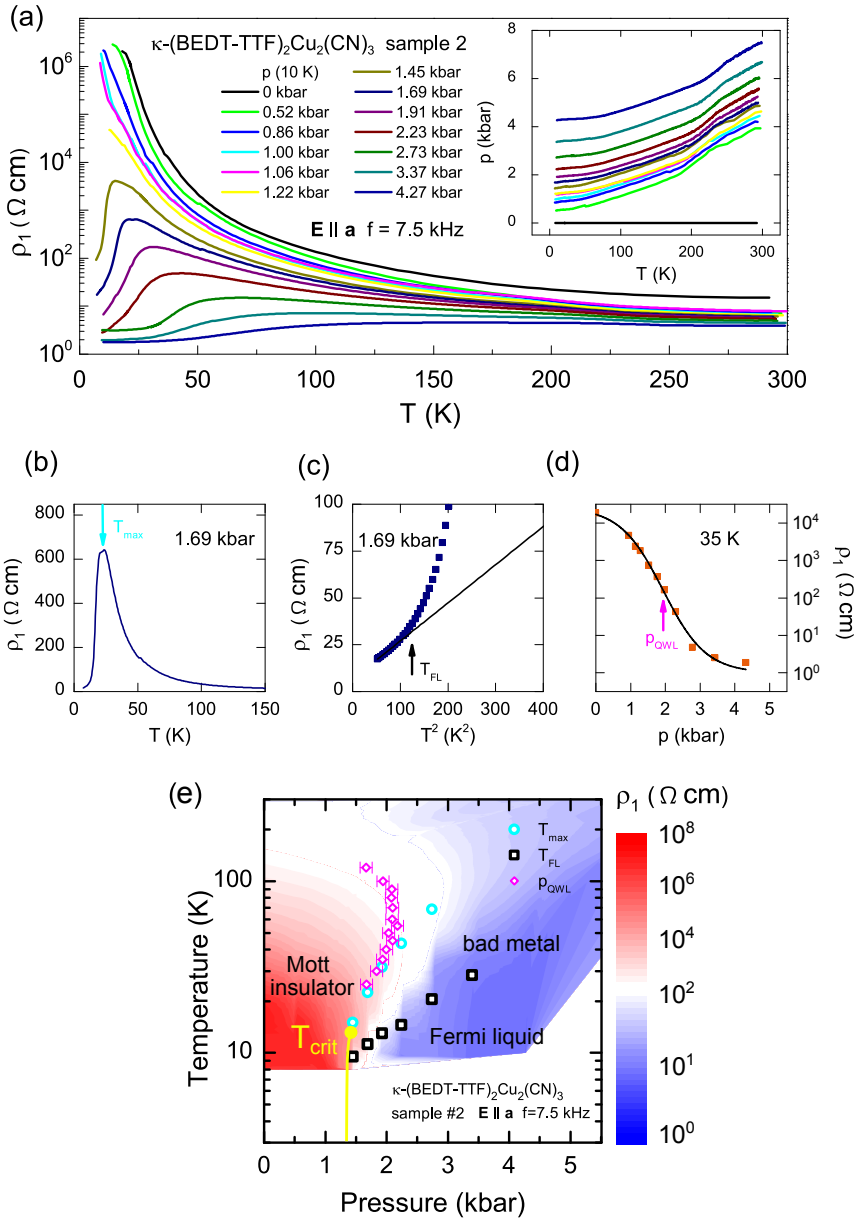

Figure 6.1: (a) $\rho_1(T)$ of κ-(BEDT-TTF)$_2$Cu$_2$(CN)$_3$ for sample #2 under hydrostatic pressure, measured along a-direction and at 7.5 kHz. With increasing pressure, $\rho_1(T)$ is reduced, revealing the insulator-metal transition for $p >$ 1.45 kbar. The inset in panel (a) displays the in-situ measured pressure loss upon cooling. (b) The maximum in $\rho_1(T)$ (cyan arrow) directly indicates the onset of metallic conduction. (c) We define T_{FL} as the temperature at which ρ_1 deviates from $\rho_{1,\mathrm{FL}} = \rho_0 + AT^2$ by more then 10%. (d) The quantum Widom line (QWL) is determined by fitting $\rho_1(p)$ (orange squares) at constant temperature with $log(\rho_1) = c[(1 - \tanh(b(p - p_{\mathrm{QWL}}))]$ (black line). (e) Phase diagram which is based on a contour plot of $\rho_1(p, T)$, including T_{max}, T_{FL} and p_{QWL}. The yellow line represents an estimate of the Mott transition line with an critical end point at T_{crit}=(1.45 kbar,16 K).

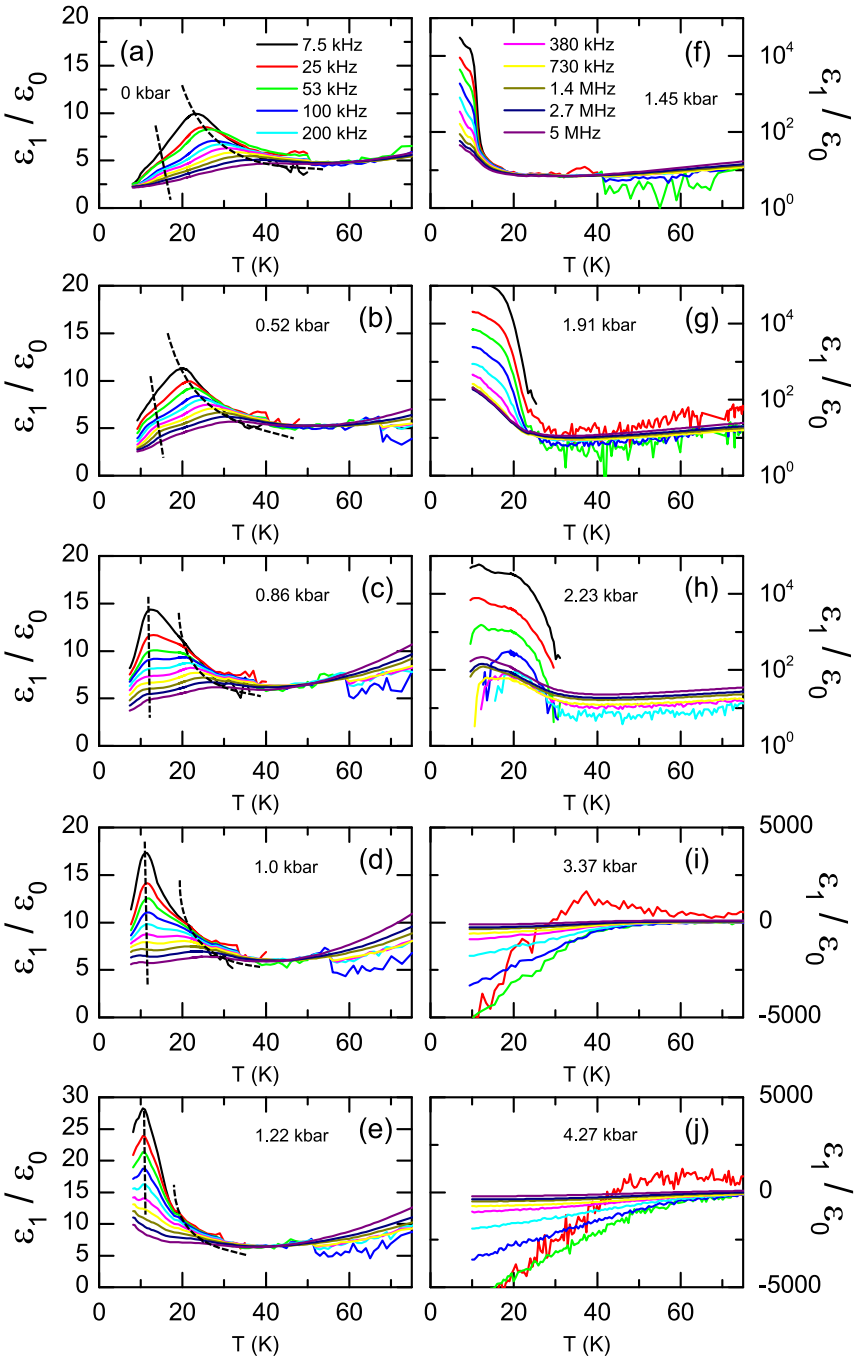

Figure 6.2: Plot of $\varepsilon_1(T)$ for sample #2 for several frequencies upon increasing pressure. (a) At 0 kbar and below 40 K, the HT peak dominates $\varepsilon_1(T)$ while the LT peak is hardly seen as a shoulder like feature around $T = 15$ K. (b-e) Upon pressurizing, the HT peak shifts to lower temperatures while the LT peak grows in amplitude and develops into a well pronounced second peak, eventually becoming the dominant feature in $\varepsilon_1(T)$ above $p \gtrsim 0.86$ kbar. (f-h) In the coexistence phase between $p = 1.45$ and 2.23 kbar, an enormous increase of ε_1 is observed which is strongly frequency dependent and attributed to spatially separated metallic and insulting regions. (i,j) Above $p = 3.37$ kbar, $\varepsilon_1 < 0$ for nearly all frequencies indicating metallic behavior.

not be reached. Following the common procedure, T_{FL} is defined as the temperature at which the deviation in $\rho_1(T)$ from the characteristic T^2 behavior of a Fermi liquid exceeds 10%. This is most accurately done in a plot of ρ_1 (royal squares) and $\rho_{1,\mathrm{FL}}$ (black line) over T^2 which is shown in Fig. 6.1(c) for 1.69 kbar wherein the T_{FL} is indicated by the black arrow.

The inset in Fig. 6.1(a) shows the decrease of the in-situ recorded pressure upon cooling. The step like features around 220 K correspond to the solidification temperature of the pressure transmitting oil. Below 50 K, the pressure saturates and becomes nearly temperature-independent. For the 0 kbar measurement, the sample was cooled in the pressure cell which was left opened and filled with He contact gas, such that pressure loss upon cooling is negligible.

The precise in-situ measurement of $p(T)$ enables us to analyze $\rho_1(p)$ at constant temperature. In particular, we determine the quantum Widom line (QWL) (cf. Ch. 2.4) by fitting $\rho_1(p)$ (orange squares) at constant temperature with $log(\rho_{1,\mathrm{QWL}}) = c[(1-\tanh(b(p-p_{\mathrm{QWL}}))]$ (black line), as examplarily shown in Fig. 6.1(d). This procedure [20] yields the QWL as the point of inflection at p_{QWL} which is indicated by the magenta arrow.

Finally, Fig. 6.1(d) shows a contour plot of $\rho_1(p,T)$ based upon which we construct the phase diagram by including the determined values of T_{FL}, T_{max} and p_{QWL}. At lowest temperatures and $p < 1.45$ kbar, the sample remains in the Mott insulating phase as schematically indicated by the red color. The sharp drop in $\rho_1(T)$ for $p_{\mathrm{IMT},\#2} = 1.45$ kbar (panel (a)) marks the Mott transition which we indicate with the yellow line. For temperatures and pressures above its critical end point, approximately at T_{crit}=(1.45 kbar,16 K), the transition becomes a gradual cross over centered around the QWL. This regime is characterized with intermediate values of ρ_1 as indicated by the white color coding. The area between T_{max} and T_{FL} refers to a bad metal while the Fermi liquid is found below T_{FL}. Overall, our preliminary phase diagram of sample #2 agrees well with previously published versions [17, 28].

With this detailed phase diagram at hand, we now can turn to the dielectric response in the different regimes of κ-CuCN. For a first overview, we plot $\varepsilon_1(T)$ of sample #2 in Fig. 6.2 for selected frequencies and pressures as indicated. Starting from ambient conditions, a pronounced peak dominates the temperature dependence of $\varepsilon_1(T)$ below 50 K that shifts to higher temperatures with increasing frequency. This behavior resembles the well-known phenomenology of relaxor ferroelectrics (cf. Ch. 4.2.3) and, referring to the (BEDT-TTF)$_2X$ family in general, is dubbed anomalous dielectric response (ADE, cf. Ch.3.5). A corresponding feature in κ-CuCN was first reported in ambient pressure studies by Abdel-Jawad *et al.* [31] and later confirmed by Pinterić and collaborators [32, 34, 137]; in this thesis we label it as high temperature (HT) peak.

Upon increasing pressure, the HT peak shifts to lower temperatures and eventually moves out of the window of accessible temperatures for $p \geqslant 1.22$ kbar. A comparison with the phase diagram in Fig. 6.1(e) clearly shows, that the HT peak in $\varepsilon_1(T)$ is only observed in the insulating phase.

Moreover, a closer look at the ambient pressure measurement reveals a shoulder-like feature around $T = 15$ K, which we denote as low-temperature (LT) peak; it evolves into a small second peak for frequencies between $f = 53$ and 200 kHz. As pressure rises, this LT feature becomes a well-defined peak, it grows in amplitude and eventually dominates the spectrum at $p = 0.86$ kbar, as seen in Fig. 6.2(c).

Both peaks shift to lower temperatures with pressure, but this trend is more pronounced for the HT peak (cf. Fig. 7.9). Although the HT feature seems to maintain its amplitude and width, it becomes secondary. We will, however, shift the detailed analysis of the pressure and frequency-dependence of the HT and LT peak to chapter 7.

Most important are the drastic changes of the dielectric response around the insulator-metal transition (IMT) at $p_{\mathrm{IMT},\#2} = 1.45$ kbar [17, 35]. For $p = 1.45$ up to 2.2 kbar, ε_1 is strongly enhanced for $T < 20$ K with a frequency-dependent amplitude even exceeding 10^5 at $f = 7.5$ kHz (Fig. 6.2(f-h)). As pressure increases further, the onset of the dielectric anomaly shifts to higher temperatures, reaching about 30 K at $p = 2.23$ kbar, for instance (Fig. 6.2(h)). We ascribe this observation to a coexistence region centered around the Mott IMT, wherein spatially separated insulating and metallic regions give rise to a percolation-like behavior, which we will elaborate on in Chapter. 8. At $p = 3.37$ kbar and higher [Fig. 6.2(i-j)], ε_1 becomes negative and large for nearly all frequencies indicating purely metallic behavior; only for the lowest frequencies a slight peak remains.

In the following, we apply the same presentation scheme to the results obtained on sample #1 in order to verify the reproducibility of our findings. Fig. 6.3 shows the $\rho_1(T)$ curves probed at $f = 10$ kHz for sample #1 whereby the indicated pressure values were recorded at $T = 10$ K. The inset shows the in-situ measured pressure $p(T)$ and the panels (b-d) the determination of T_{FL}, T_{max} and p_{QWL}. The contour plot of $\rho_1(p, T)$ and the phase diagram of sample #1 are presented in Fig. 6.3(d). Qualitatively, there is good agreement between both samples of completely different origin and growth conditions whereas the IMT in sample #1 is observed at a slightly lower pressure of $p_{\mathrm{IMT},\#1} = 1.05$ kbar. Consequently, also the QWL line for sample #1 is slightly shifted towards lower pressures as compared to sample #2. This deviation could be attributed to a hysteresis effect, since the measurement sequence for sample #1 started with the highest pressure whereas for sample #2 with the lowest. However, it is not clear if this really holds here since each measurement starts at room temperature well above the IMT. Therefore, it might also indicate an enhanced degree of structural disorder in sample #1. Such

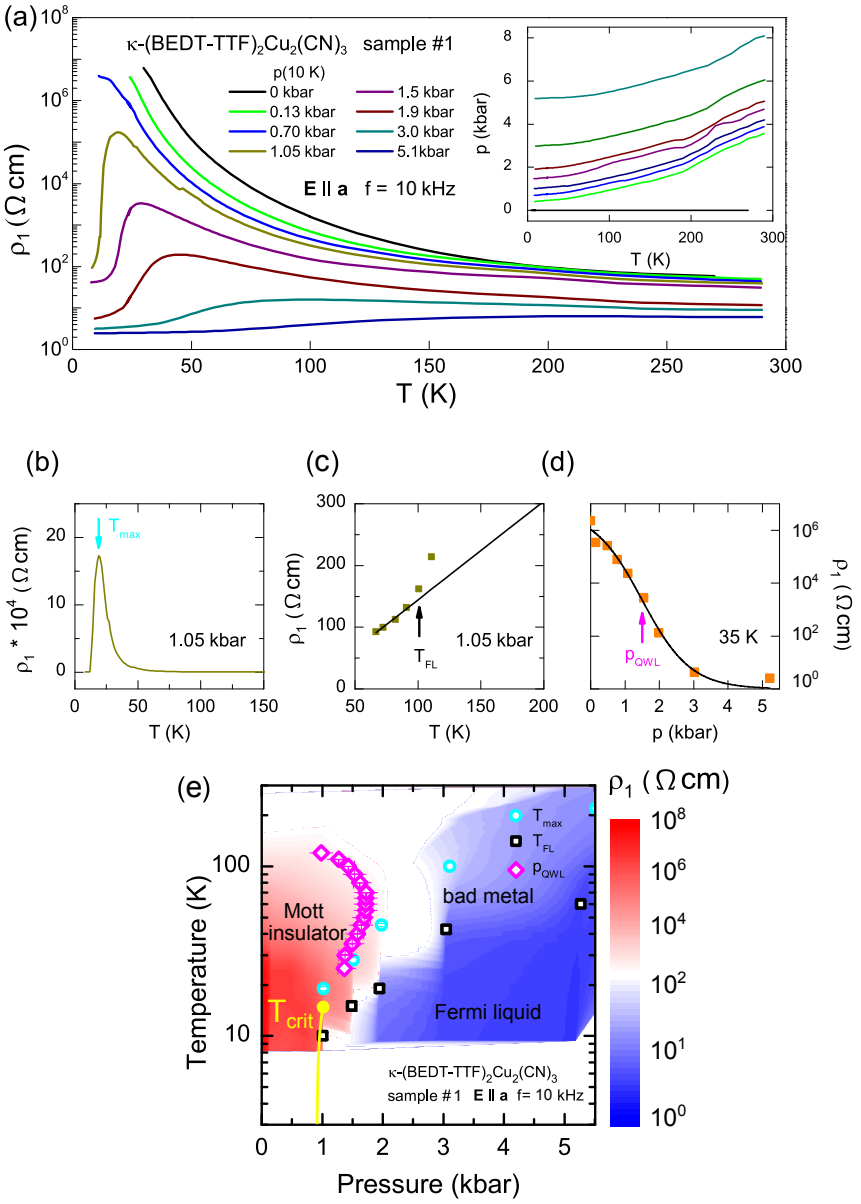

Figure 6.3: (a) $\rho_1(T)$ of κ-(BEDT-TTF)$_2$Cu$_2$(CN)$_3$ for sample #1 under hydrostatic pressure, measured along a-direction and at 10 kHz. The insulator-metal transition and the QWL are shifted to lower pressures compared to sample #2, indicating higher structural disorder in sample #1. The inset in panel (a) displays the in-situ measured pressure loss upon cooling. (b) The maximum in $\rho_1(T)$ (cyan arrow) directly indicates the onset of metallic conduction. (c) We define T_{FL} as the temperature at which ρ_1 deviates from $\rho_{1,\mathrm{FL}} = \rho_0 + AT^2$ by more then 10%. (d) The quantum Widom line (QWL) is determined by fitting $\rho_1(p)$ (orange squares) at constant temperature with $log(\rho_1) = c[(1 - \tanh(b(p - p_{\mathrm{QWL}}))]$ (black line). (e) Phase diagram which is based on a contour plot of $\rho_1(p, T)$, including T_{max}, T_{FL} and p_{QWL}. The yellow line represents an estimate of the Mott transition line with its critical end point T_{crit}=(1.05 kbar,16 K).

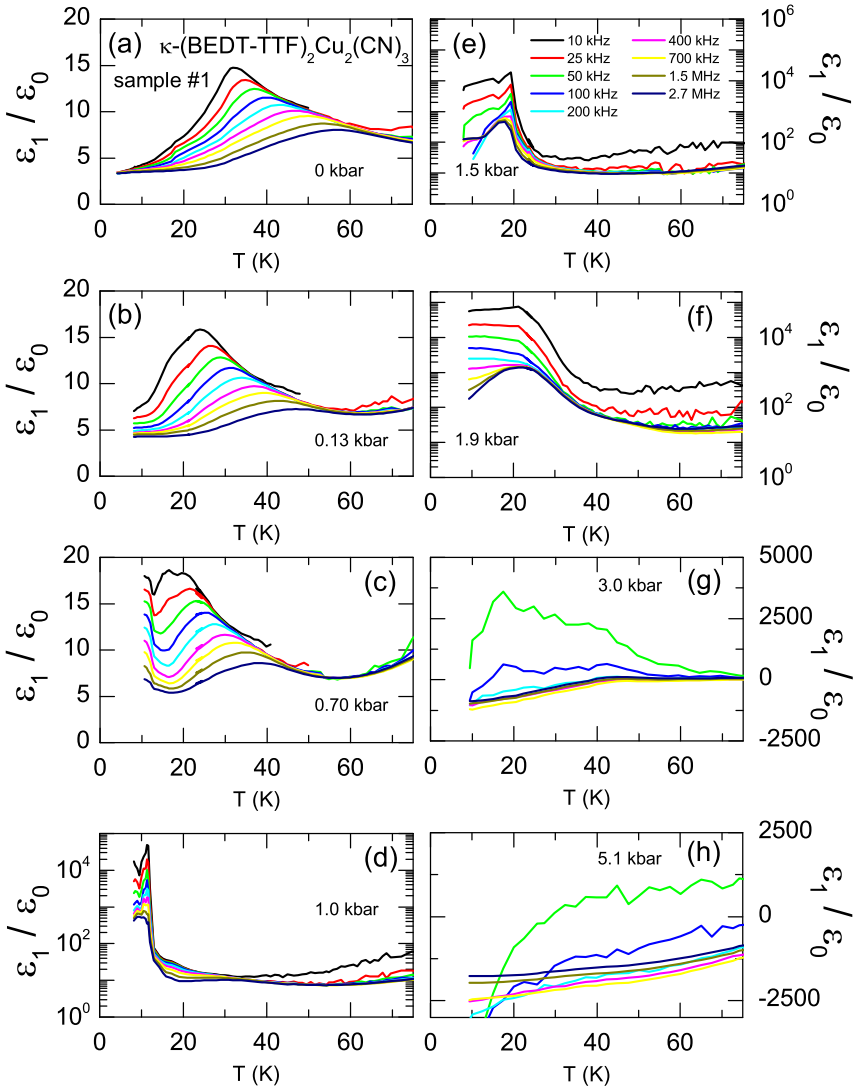

Figure 6.4: Plot of $\varepsilon_1(T)$ for sample #1 for several frequencies upon increasing pressure. (a-c) Shift of the HT peak towards lower temperatures upon pressure. At ambient pressure, the LT peak is completely concealed by the HT peak and becomes visible at $p = 0.13$ kbar. (d-f) The strong enhancement of ε_1 is already observed for $p = 1.05$ and extends to 1.9 kbar. (g,h) The metallic behavior sets in above $p = 3.0$ kbar where $\varepsilon_1 < 0$ for nearly all frequencies.

a sample dependence is confirmed by disorder studies on the sister compound κ-(BEDT-TTF)$_2$Cu[N(CN)$_2$]Cl, which reveal a shift of p_{IMT} to lower pressures upon x-ray irradiation [205].

The pressure evolution of $\varepsilon_1(T)$ for sample #1 is presented in Fig. 6.4 for selected frequencies. As usual, the indicated pressure values were recorded at 10 K. Unfortunately, only a few measurements in the Mott insulating phase could be performed before the sample broke. Nevertheless, despite the low pressure resolution, it is obvious that the HT peak in $\varepsilon_1(T)$ shifts towards lower temperatures upon increasing pressure resembling the findings for sample #2. In contrast, the LT peak is barely visible up to 0.45 kbar and becomes evident at 0.7 kbar. The detailed investigation of the HT and LT peak for sample #1 is also shifted to chapter 7.

The strong enhancement of ε_1 by several orders of magnitude upon entering the coexistence regime is already observed at $p = 1.05$ kbar and extends up to 1.9 kbar (Fig. 6.4(f)). We emphasize that this is in accordance with the shift of the IMT in sample #1. Interestingly, the plateau-like shape of $\varepsilon_1(T)$ is observed only for $f \leqslant 400$ kHz whereas for higher frequencies a slight downturn occurs. Upon increasing pressure further, metallic behavior with $\varepsilon_1 < 0$ sets in whereas only for the lowest frequencies positive values remain. Except for the slight shift of the IMT towards lower pressures in sample #1, the findings obtained from both samples agree well and confirm reproducibility.

6.2 κ-[(BEDT-STF)$_x$-(BEDT-TTF)$_{1-x}$]$_2$Cu$_2$(CN)$_3$

Complementary to tuning the bandwidth W of κ-(BEDT-TTF)$_2$Cu$_2$(CN)$_3$ with hydrostatic pressure, we stepwise enhance W by partially substituting the BEDT-TTF (ET) donors with BEDT-STF (STF) molecules (cf. Ch. 3.3.1) and thus obtain κ-[(BEDT--STF)$_x$-(BEDT-TTF)$_{1-x}$]$_2$Cu$_2$(CN)$_3$ (κ-STF$_x$-CuCN). We remind here, that this substitution does not change the valency of the donor molecule and is distinct from charge carrier doping. Nonetheless, we can drive the system from the Mott insulating to the metallic state upon increasing the substitution level x (cf. Ch. 3.2.2). This is nicely demonstrated in Fig. 6.5, wherein we plot $\rho_1(T)$ for all measured substitution levels x as indicated.

Most importantly, the behavior upon rising x resembles what is observed for the pristine samples upon increasing pressure. For $x < 0.12$, purely resistive behavior is observed with $d\rho_1/dT > 0$. At $x = 0.12$, a maximum in $\rho_1(T)$ appears that shifts to higher T upon rising x accompanied with an overall trend of diminishing resistivity for $T < 150$ K. At this point it is important to mention, that the contact geometry (cf. Table 5.2) shows a strong sample to sample dependence and gives only a rough estimate for the conduction cross section, eventually leading to the non-monotonic behavior of ρ_1 in dependence of x for

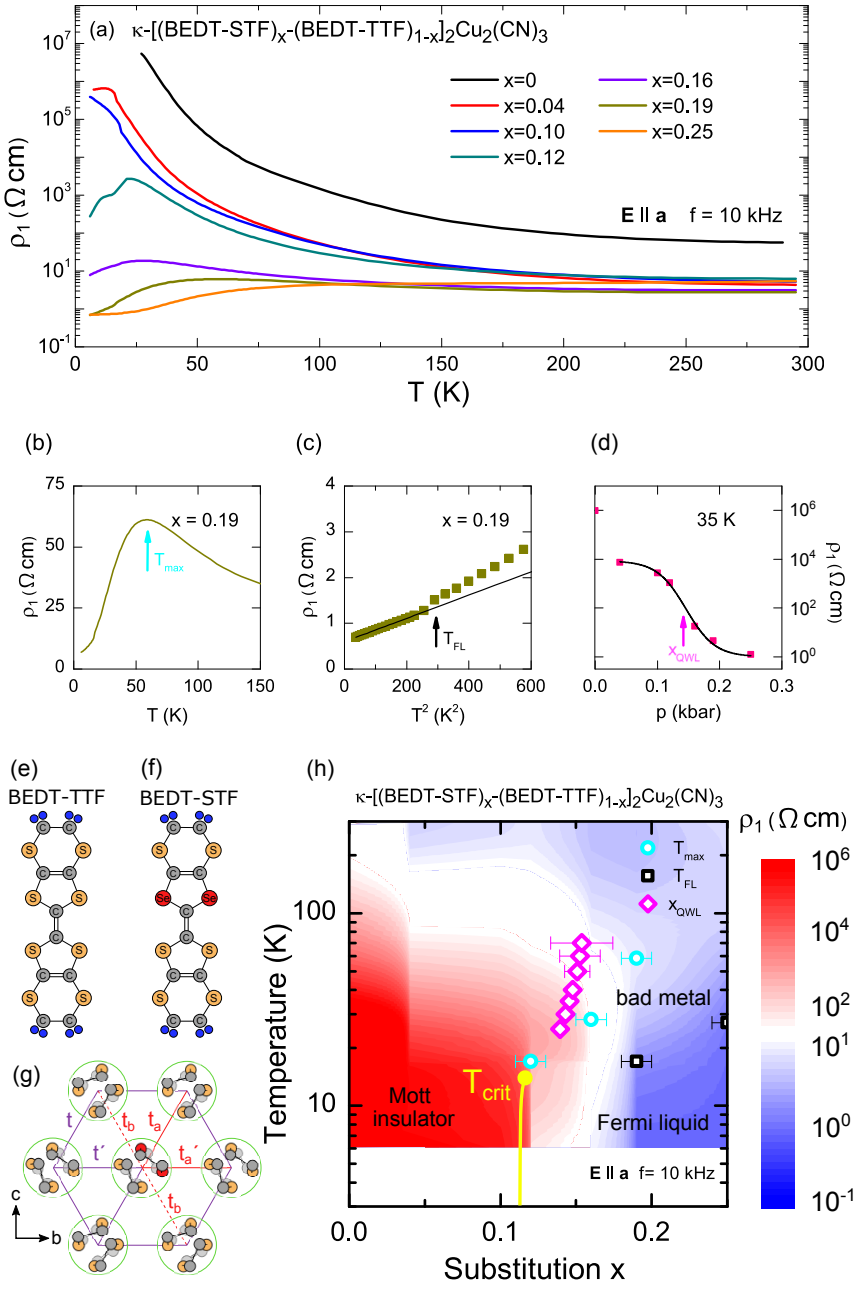

Figure 6.5: (a) $\rho_1(T)$ of κ-[(BEDT-STF)$_x$-(BEDT-TTF)$_{1-x}$]$_2$Cu$_2$(CN)$_3$ upon increasing substitution x, measured along a-direction and at 10 kHz. The insulator-metal transition is observed around $x = 0.12$. (b) The maximum in $\rho_1(T)$ (cyan arrow) directly indicates the onset of metallic conduction. (c) We define T_{FL} as the temperature at which ρ_1 deviates from $\rho_{1,\mathrm{FL}} = \rho_0 + AT^2$ by more then 10%. (d) The quantum Widom line (QWL) is determined by fitting $\rho_1(x)$ (pink squares) at constant temperature with $log(\rho_1) = c[(1 - \tanh(b(x - x_{\mathrm{QWL}}))]$ (black line). (e) Phase diagram of κ-[(BEDT-STF)$_x$-(BEDT-TTF)$_{1-x}$]$_2$Cu$_2$(CN)$_3$ which is based on a contour plot of $\rho_1(x, T)$, including T_{max}, T_{FL} and x_{QWL}. The yellow line represents an estimate of the Mott transition line with its critical end point T_{crit}=(0.12,16 K).

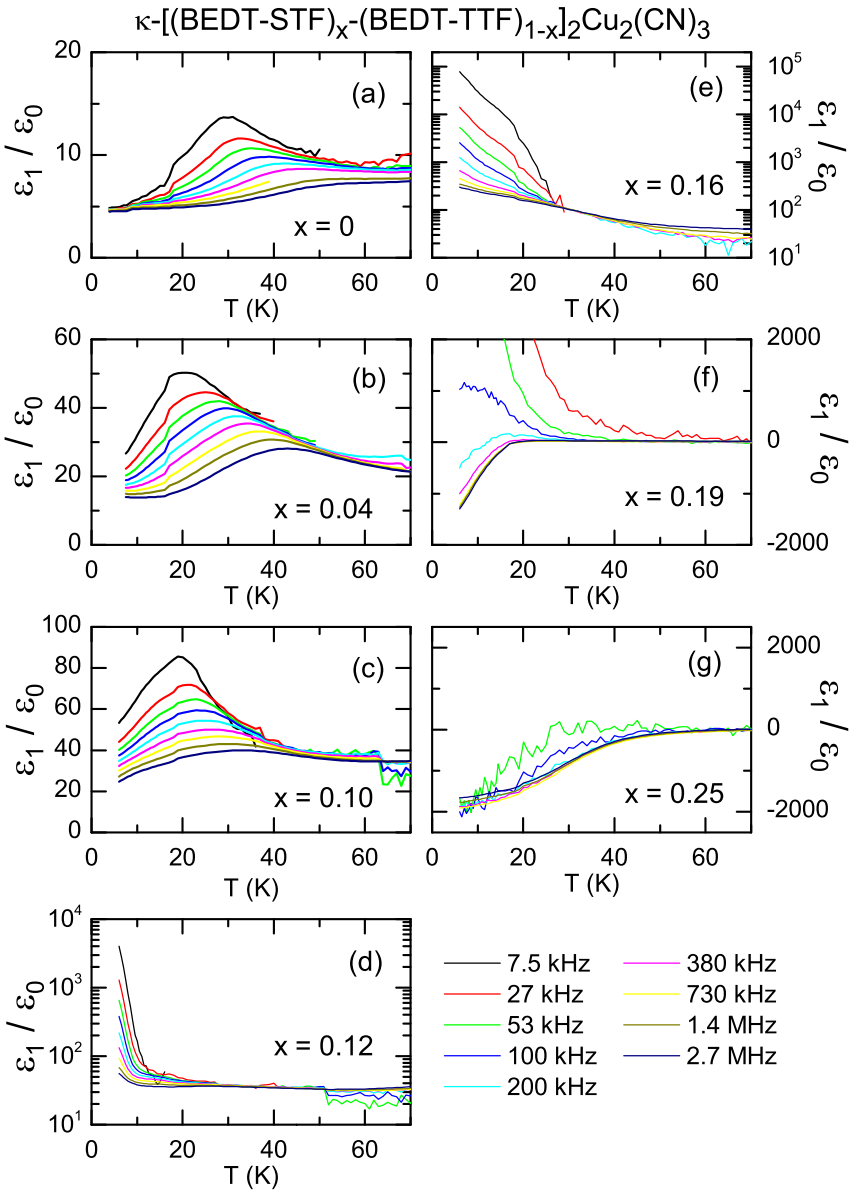

Figure 6.6: Plot of $\varepsilon_1(T)$ for various samples of κ-[(BEDT-STF)$_x$-(BEDT-TTF)$_{1-x}$]$_2$-Cu$_2$(CN)$_3$ with different substitution levels as indicated. (a) At $x = 0$ and below 40 K, the HT peak dominates $\varepsilon_1(T)$ and completely conceals the LT peak. (b-c) With rising the substitution level, the HT peak shifts to lower temperatures. The LT peak is concealed by the former and becomes apparent as a weak shoulder around $T = 15$ K only for $x = 0.10$. (f-h) At $x = 0.12$, the phase coexistence region is reached yielding an enormous increase of ε_1 which is strongly frequency dependent. (i,j) For $x \geqslant 0.19$, the samples exhibit metallic behavior at low temperatures with $\varepsilon_1 < 0$ for nearly all frequencies.

$T > 150$ K. Moreover, $\rho_1(T)$ of the pristine sample is significantly higher when compared to the substituted samples, which we also attribute to sample to sample variation since it stems from another sample grower. Overall, however, the signature of the Mott transition is clearly revealed while the experimental setup did not allow for cooling below 5 K such that the super-conducting state below $T_{\mathrm{SC}} = 2$ K could not be reached.

The determination of T_{max} and T_{FL} are exemplarily shown in Fig. 6.5(b) and (c), respectively, and follow the same procedure as applied for the pressure-dependent measurements. Likewise, panel (d) shows the determination of the QWL by fitting $\rho_1(x)$ (pink squares) at constant temperature with $log(\rho_1) = c[(1 - \tanh(b(x - x_{\mathrm{QWL}}))]$ (black line), whereby the point of inflection at x_{QWL} (magenta arrow) corresponds to the QWL.

In Fig. 6.5(h), we can construct a preliminary phase diagram by including T_{max}, T_{FL} and x_{QWL} into a contour plot of $\rho_1(x, T)$. Despite the fact that only seven different substitution levels were available, the result is detailed enough to reveal all regimes which have been reported previously in κ-CuCN. Moreover, the phase diagram resembles the one obtained by means of the pressure-dependent measurements (Fig. 6.1(e)), thus demonstrating that the STF substitution is a proper way to achieve the bandwidth-tuned Mott transition. The yellow line indicates the estimated transition line with a critical end point at T_{crit}=(0.12,16 K). Panels (e,f) illustrate a BEDT-TTF and a BEDT-STF molecule, respectively, while panel (g) shows a sketch of the in-plane dimer packing motif and indicates the alternation of the transfer integrals upon BEDT-STF substitution.

With this phase diagram in mind, we now can turn to the dielectric response observed in the various regimes of κ-STF$_x$-CuCN. Fig. 6.6 shows $\varepsilon_1(T)$ at different substitutions x as indicated. Upon increasing the substitution level from $x = 0$ to 0.10, the HT peak below 50 K shifts towards lower temperatures (Fig. 6.6(a-c)) similar to the behavior under rising pressure (Figs. 6.4 and 6.2). When probing with a frequency of $f = 100$ kHz, for instance, the maximum is observed at $T = 38$ K for $x = 0$ and moves to 22 K for $x = 0.10$. On the other hand, a considerable gain in amplitude of the HT peak is observed with rising x, reaching values of $\varepsilon_1(T)$=80 at $f = 7.5$ kHz for instance, which is absent in the pressure dependence. Furthermore, the LT peak is not revealed for $x = 0.04$ and becomes apparent as a weak shoulder around 15 K for $x = 0.10$, rather resembling the pressure-dependent observations for sample #1. The pressure and frequency evolution of both peaks is shifted to chapter 7 as well.

Upon increasing the substitution to $x = 0.12$, the IMT is reached and ε_1 exhibits a strong upturn at 10 K with a frequency-dependent amplitude reaching 10^4 at $f = 7.5$ kHz (Fig. 6.6(d)) which eventually shifts to 30 K for $x = 0.19$ (Fig. 6.2(h)). For $x = 0.19$ and higher substitution, κ-STF$_x$-CuCN becomes mostly metallic with ε_1 being negative for nearly all frequencies and only for the lowest frequencies a slight peak remains.

Overall, the dielectric response upon rising the substitution is in striking agreement with the one observed for pristine κ-(BEDT-TTF)$_2$Cu$_2$(CN)$_3$ under increasing pressure. For this reason, we again split the results for κ-STF$_x$-CuCN into two parts. The dielectric response of the κ-STF$_x$-CuCN crystals with $x = 0$, $x = 0.04$ and $x = 0.1$, remaining insulating down to lowest temperatures, is analyzed in detail in Ch. 7 while the behavior around the IMT, i.e. samples with $x \geqslant 0.12$, is elaborated in Ch. 8.

6.3 κ-(BEDT-TTF)$_2$Ag$_2$(CN)$_3$

In addition to applying hydrostatic pressure and the substitution of donor molecules, we modify the bandwidth W by replacing the Cu$_2$(CN)$_3$ anion with Ag$_2$(CN)$_3$ (cf. Ch. 3.2.2), yielding κ-(BEDT-TTF)$_2$Ag$_2$(CN)$_3$ (κ-AgCN). This drastically reduces the bandwidth and enhances the effective Coulomb repulsion U/t (cf. Tabel 3.3), such that κ-AgCN at ambient pressure is located deep in the Mott insulating state (cf. Fig. 3.11). Consequently, κ-AgCN undergoes a Mott transition at a comparably high pressure of 9 kbar, such that our experimental range only covers its insulting phase. Still, this enables us to scrutinize the dielectric response in the Mott insulating phase with a higher pressure resolution.

Fig. 6.7 shows $\rho_1(T)$ curves for κ-AgCN at various pressures as indicated and probed at $f = 10$ kHz. The inset shows the in-situ measured pressure. Upon increasing pressure, $\rho_1(T)$ continuously decreases while the overall insulating behavior with $d\rho_1/dT > 0$ is maintained for all measurements. Unfortunately, due to the pressure loss upon cooling and the fact that our setup is restricted to pressures below 10 kbar, we were not able to reach the insulator-to-metal transition.

Nevertheless, the signature of the $\rho_1(T)$ serve as a good reference point for classifying the observed dielectric response upon increasing pressure. Figs. 6.8 and 6.9 present the pressure evolution of the dielectric response of κ-AgCN by plotting $\varepsilon_1(T)$ for selected frequencies and pressures as indicated. At ambient pressure and below 100 K, we observe a broad peak in $\varepsilon_1(T)$ which shifts to higher temperatures and decreases in amplitude for increasing frequencies (Fig. 6.8(a)). These findings are in full agreement with a previous ambient pressure report by Pinterić and collaborators [33, 34]. The peak features the same signature as the relaxor-ferroelectric response observed in the sibling compound κ-CuCN, with the difference that it is shifted to higher temperatures and exhibits a larger amplitude for κ-AgCN. It is straightforward to label this relaxor ferroelectric peak as HT peak in analogy to the nomenclature we introduced for κ-CuCN. A closer look reveals an additional shoulder like feature below 50 K which is more pronounced for higher frequencies. As we will see in the following, this shoulder does not correspond to the LT peak but constitutes an additional, distinct feature, such that we will refer to it as anomaly from now on.

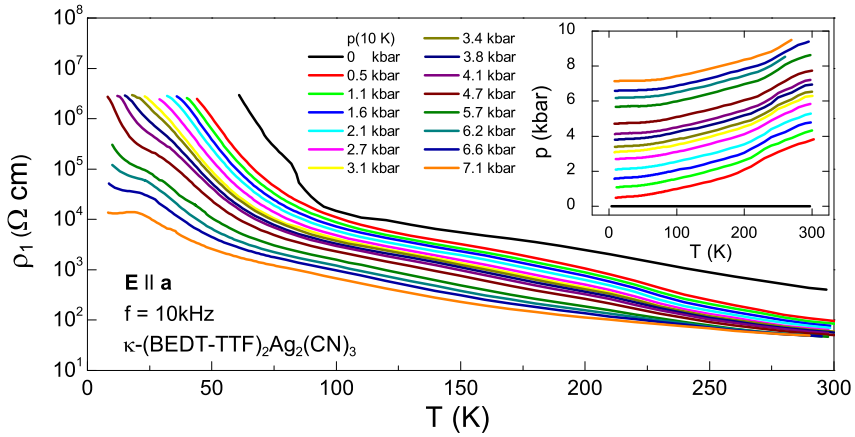

Figure 6.7: $\rho_1(T)$ of κ-(BEDT-TTF)$_2$Ag$_2$(CN)$_3$ for various pressures as indicated, measured along a-direction and at 10 kHz. The inset shows the in-situ measured pressure. Upon increasing pressure, $\rho_1(T)$ continuously decreases while the overall insulating behavior with $d\rho_1/dT > 0$ is maintained. Due to the pressure loss upon cooling and the fact that our setup is restricted to pressures below 10 kbar, we were not able to reach the insulator-to-metal transition around 9 kbar.

From ambient pressure up to $p = 2.1$ kbar (Fig. 6.8(a-e)), the HT peak shifts to lower temperatures and slightly loses in amplitude while the anomaly feature keeps its shoulder like shape and does not change noticeable as a function of pressure. As pressure rises further (Figs. 6.8(f,g) and 6.9(a-c)), the HT peak diminishes further while the anomaly feature gains in amplitude and eventually becomes a well-defined peak which, for instance, is located around 13 K at 4.1 kbar. Starting from 3.4 kbar, a third feature appears in between the HT peak and the anomaly, located around 30 K and eventually dominating $\varepsilon_1(T)$ at 4.7 kbar (Fig. 6.9(a-d)). Upon increasing the pressure further up to 7.1 kbar (Fig. 6.9(e-h)), the HT peak continues to move to lower temperatures as pressure rises while keeping its magnitude. Simultaneously, the third features strongly grows in amplitude and shifts towards lower temperatures, masking the anomaly previously observed around 13 K. There is a striking agreement between the pressure evolution of the third feature and the one observed for the LT peak in κ-CuCN, clearly identifying it as the LT peak in κ-AgCN.

We conclude for now, that analogues of the HT and LT peak are revealed in $\varepsilon_1(T)$, whereas in contrast the anomaly as an additional features is only observed in κ-AgCN. The detailed analysis of these features, in particular their pressure and frequency-dependence, is also shifted to Ch. 7.

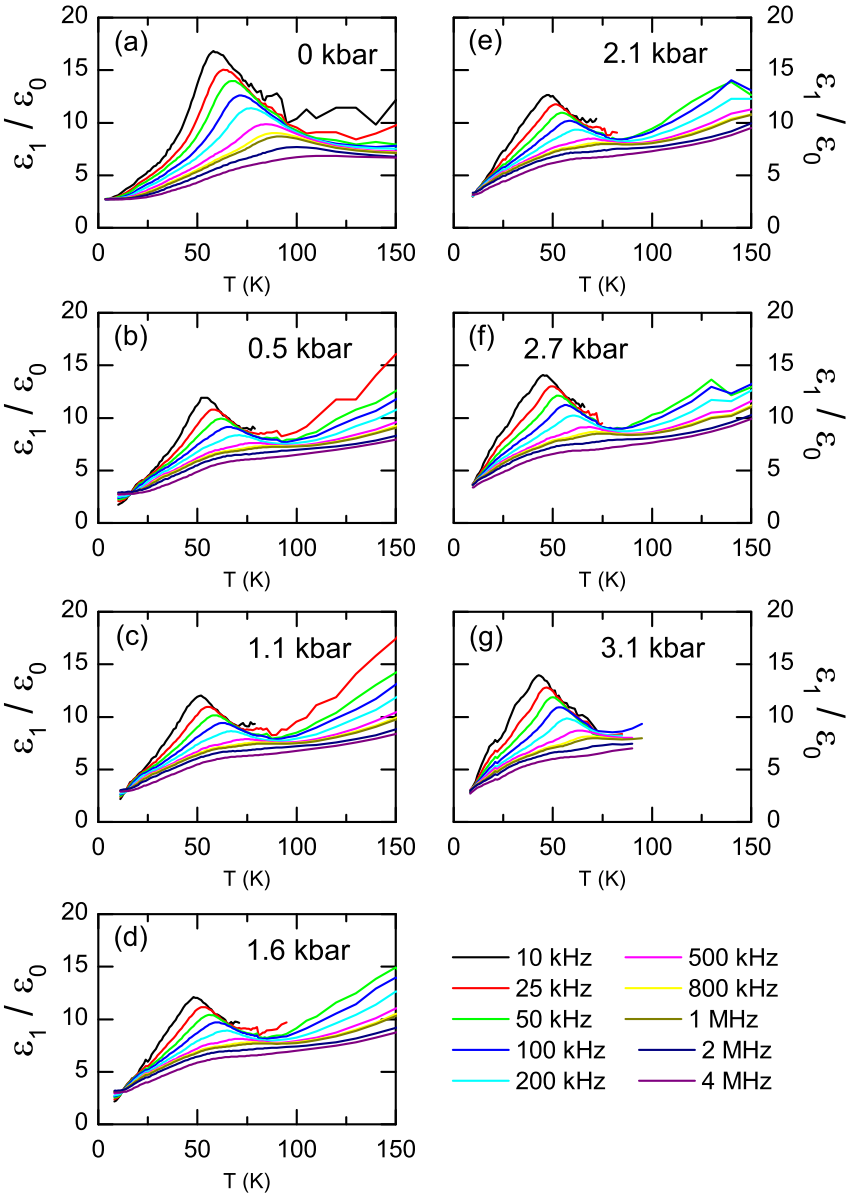

Figure 6.8: $\varepsilon_1(T)$ of κ-(BEDT-TTF)$_2$Ag$_2$(CN)$_3$ for selected frequencies and at pressures ranging from 0 kbar to 3.1 kbar. (a) At 0 kbar and below 100 K, a broad dispersive peak dominates $\varepsilon_1(T)$ reminiscent of relaxor-ferroelectricity which is labeled as HT peak. Additionally, a shoulder like feature is revealed below 50 K labeled as anomaly. (b-g) Upon increasing pressure, the HT peak shifts towards lower temperatures and slightly diminishes in amplitude while the anomaly features remains unchanged. $\varepsilon_1(T)$ for pressures exceeding 3.1 kbar is presented in Fig. 6.9

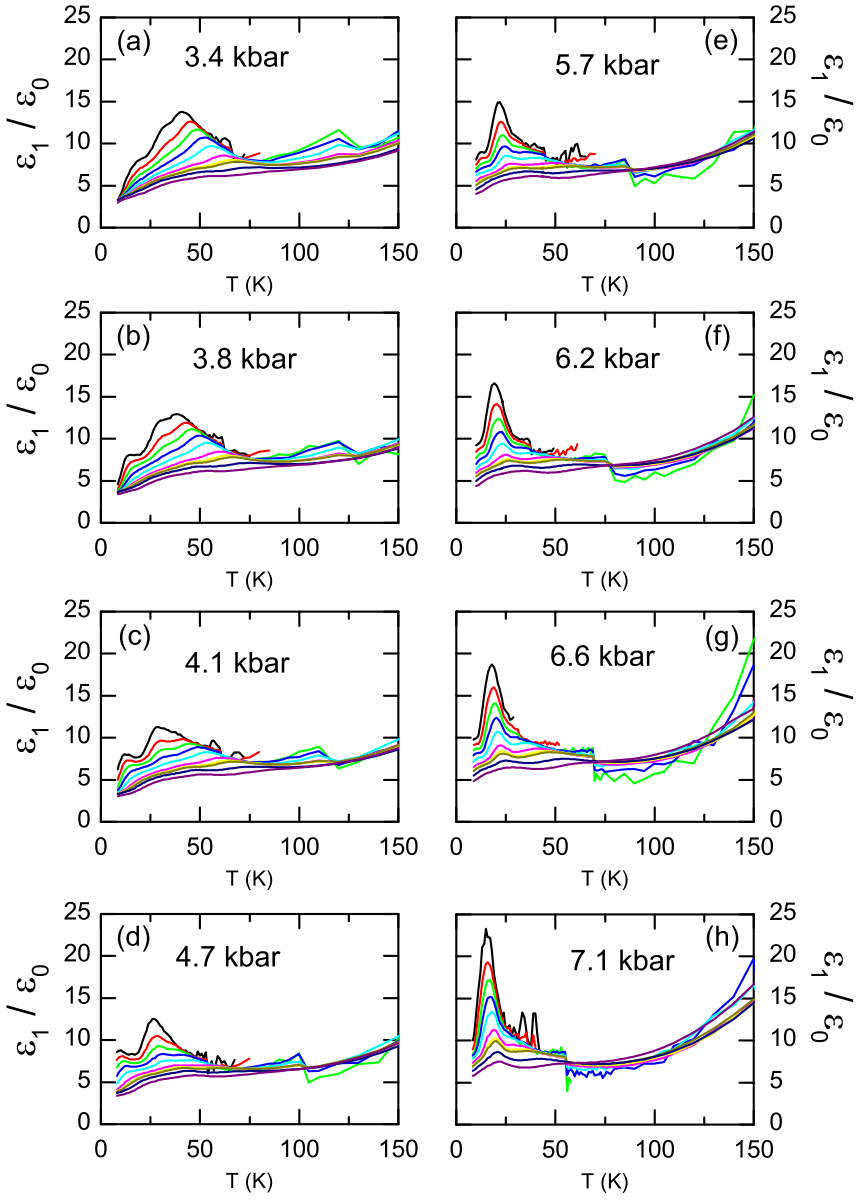

Figure 6.9: $\varepsilon_1(T)$ of κ-$(BEDT\text{-}TTF)_2Ag_2(CN)_3$ for selected frequencies and pressures ranging from 3.4 kbar to 7.1 kbar. (a-d) Upon increasing the pressure from 3.4 kbar to 4.7 kbar, the HT peak continues to shift towards lower temperatures and the anomaly develops into a well-defined peak which, for instance, is located around 13 K at 4.1 kbar. Simultaneously, a third feature becomes apparent in between the HT peak and the anomaly eventually dominating $\varepsilon_1(T)$ at 4.7 kbar, which we refer to as LT peak. (e-h) For further pressurizing the sample up to 7.1 kbar, the LT peak grows in amplitude and shifts towards lower temperatures , masking the anomaly features previously observed around 13 K, while the HT peak remains at it magnitude.

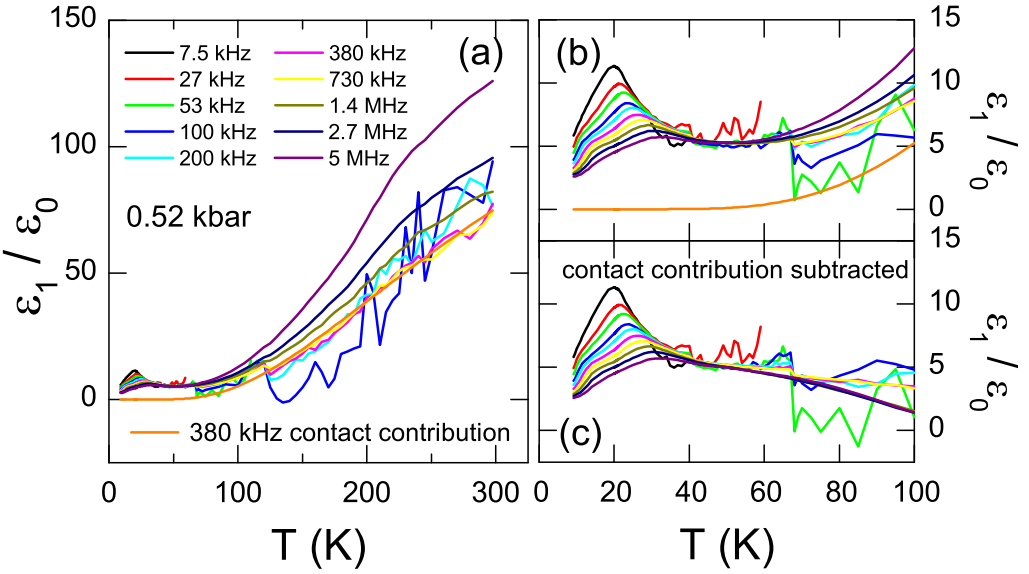

Figure 6.10: (a) Plot of $\varepsilon_1(T)$ for the entire temperature range and at 0.52 kbar. Additionally, we determine the contact contribution by fitting the high temperature part with Eq. (6.1), as exemplarily shown for f = 380 kHz (orange line). (b) Detailed view of the relaxor ferroelectric relaxation at low temperatures including the contact contribution. (c) Relaxor ferroelectric response after the contact contribution has been subtracted, clearly showing that the contact contribution is negligible below T = 60 K.

6.4 Contact contribution

Here we estimate the contract contribution to $\varepsilon_1(T)$. At elevated temperatures, the samples exhibit semi-conducting transport properties. The contacts are formed by amorphous carbon (carbon paste) with metallic properties (cf. Ch. 5.4), such that Schottky contacts may form at the sample-contact interfaces (cf. Ch. 5.3). As a result, a depletion zone builds up at the interface giving an additional contact contribution (Eq. 5.11) to the measured permittivity with the characteristic temperature-dependence

$$\varepsilon_{1,\mathrm{depl}}(T) \;=\; \frac{d\,C_0}{A\,\varepsilon_0}\exp\left\{\frac{-\Delta}{2k_\mathrm{B}T}\right\}, \tag{6.1}$$

wherein Δ denotes the charge gap across which charge carries have to be thermally excited and C_0 is the capacitance of the depletion zone in the high temperature limit. In Fig. 6.10(a) we exemplarily plot $\varepsilon_1(T)$ of κ-CuCN sample #2 up to room temperature, for p = 0.52 kbar and probed at various frequencies as indicated. In the temperature range 300 K > T >75 K, we observe a decrease of $\varepsilon_1(T)$ upon cooling which is very well described by Eq.(6.1) (orange line) and hence is attributed to the contact contribution.

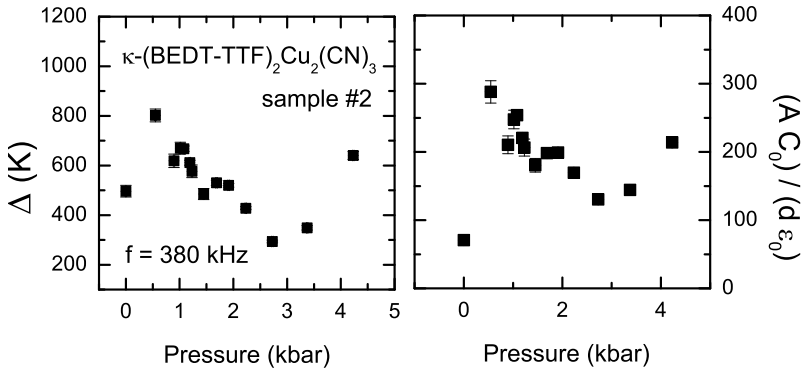

Figure 6.11: Parameters as obtained by fitting $\varepsilon_1(T)$ in the temperature range 300 K $> T >$75 K with Eq. (6.1).

Most importantly, the contact contribution is negligible below 60 K (Fig. 6.10(b)) and does not influence the analysis of the relaxor-like dielectric response performed in the next chapter. In this thesis, we therefore do not subtract the contact contribution unless stated otherwise. We also note, that this effect would be too weak to explain the huge enhancement of $\varepsilon_1(T)$ close to the phase boundary. If we have a look at $\rho_1(T)$ and $\varepsilon_1(T)$ for κ-CuCN sample #2 at 1.91 kbar, for instance, we see that $\rho_1(p = 1.91 \text{ kbar}, T = 10 \text{ K}) \sim \rho_1(p = 1.91 \text{ kbar}, T = 300 \text{ K})$ (cf. Fig. 6.1), such that the spurious contact contribution to ε_1 should be the same at 10 K and 300 K. On the other hand, we see that $\varepsilon_1(p = 1.91 \text{ kbar}, T = 10 \text{ K}) \gg \varepsilon_1(p = 1.91 \text{ kbar}, T = 300 \text{ K})$ (cf. Fig. 6.2), which can not be explained by solely considering the contacts, corroborating our phase coexistence scenario.

The obtained fitting parameters are plotted in Fig. 6.11 as a function of pressure for various frequencies as indicated. There is a jump in both quantities when going from ambient pressure to $p > 0$ kbar. We attribute this to the effect of pressure loss upon cooling giving an additional contribution to the temperature-dependence of $\varepsilon_1(T)$, which however, is also well captured by Eq.(6.1). Upon intensifying pressure, the effective interaction strength U/W decreases resulting in an enhanced delocalization of charge carriers which eventually leads to a reduction of Δ as observed in experiment. Since this effect is equivalent to increasing the number of free charger carriers n, also C_0 decreases. A minimum is reached for both parameters at $p = 2.7$ kbar followed by a subsequent increase, which might reflect an enhancement of Φ_{H}, the distance between the vacuum level and the chemical potential of the sample, which turns from a low gapped semiconductor into a metal in this pressure range.

7

Dielectric response in the Mott insulating state

After the short overview of the experimental findings in the previous chapter, we scrutinizes in this one the dielectric properties of the dimer Mott insulators κ-CuCN ,κ-STF$_x$-CuCN and κ-AgCN on the insulting side of the phase diagram.

Fist we will investigate the dielectric response of κ-CuCN at ambient pressure and familiarize ourself with the analyzing procedure. By comparing three samples of different origin, we also get insight into the sample to sample variation of the dielectric response. Subsequently, we will elaborate the pressure evolution of the dielectric response in κ--CuCN. We complement our pressure-dependent studies on κ-CuCN with investigating κ-STF$_x$-CuCN in dependence of the substitution x. Moreover, we analyze the pressure-dependent measurements of κ-AgCN in detail, extending our investigations further into the insulating state of the κ-(BEDT-TTF)$_2X$ salts.

7.1 Dielectric response of κ-(BEDT-TTF)$_2$Cu$_2$(CN)$_3$ at ambient pressure

Let us now have a detailed look at the temperature and frequency-dependence of the dielectric response of κ-CuCN at ambient pressure to familiarize ourself with the observed features and the analysis procedure. The ac-resistivity $\rho_1(T)$ and $\varepsilon_1(T)$ are presented in Fig. 7.1 exemplarily for sample #2. Below 50 K, $\varepsilon_1(T)$ is dominated by the dispersive HT peak (Fig.7.1(a)), shifting to higher temperatures and diminishing in amplitude for increasing frequencies. In the same temperature range, $\rho_1(T)$ deviates from an exponential upturn and drops to lower values upon cooling (Fig.7.1(b)) wherein the onset of this behavior shifts to higher temperatures upon increasing frequencies. Overall, the dispersive behavior in $\varepsilon_1(T)$ and $\rho_1(T)$ resemble the characteristics of relaxor-ferroelectricity (cf. Ch. 4.2.3).

As already mentioned in Ch. 6, a closer look at Fig. 7.1(a,b) reveals the LT peak as a second shoulder like feature in $\varepsilon_1(T)$ located around 15 K as well as in $\rho_1(T)$ at sightly

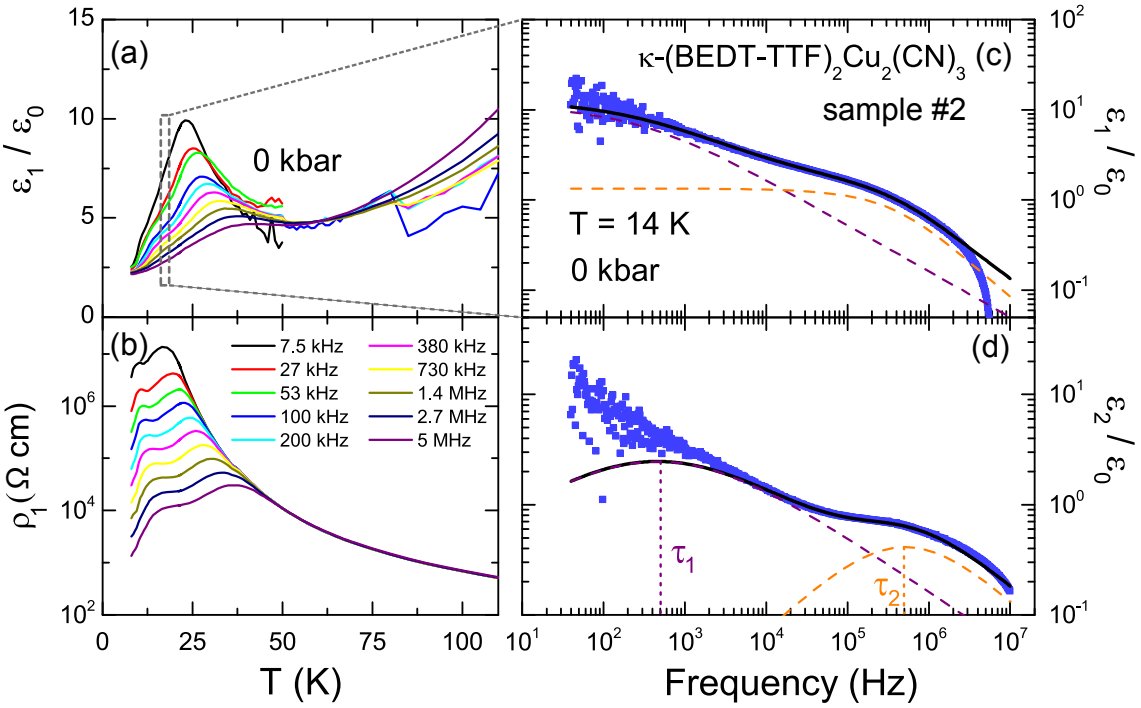

Figure 7.1: Overview of the ac-transport and dielectric properties of κ-(BEDT-TTF)$_2$-Cu$_2$(CN)$_3$ at ambient pressure. (a) The temperature-dependence of the real part of the permittivity $\varepsilon_1(T)$ probed at different frequencies as indicated. Below 50 K, $\varepsilon_1(T)$ is dominated by a dispersive peak which shifts to higher temperatures and decreases in amplitude for increasing frequencies. This peak exhibits the characteristic signature of relaxor-ferroelectricity and will be label throughout this thesis as high-temperature peak (HT). (b) Temperature-dependence of the ac-resistivity $\rho_1(T)$ for various frequencies as indicated. Sightly below the temperature of the HT peak, $\rho_1(T)$ deviates from the expected increase upon cooling and drops to lower values instead. The onset of the drop shifts to higher temperatures upon increasing frequencies which corresponds to the signature of relaxor-ferroelectricity. Around 15 K, the presence of a second feature is revealed as a weak shoulder in $\varepsilon_1(T)$ and as a pronounced bump in $\rho(T)$ which we label as low-temperature peak (LT). Frequency dependence of $\varepsilon_1(f)$ (c) and $\varepsilon_2(f)$ (d) at $T = 14$ K revealing two relaxation modes which are best fitted with two Cole-Cole modes (cf. Ch. 4.2.1). The purple and orange dashed line represent the fit of mode 1 and mode 2, respectively, and the full black line is their sum according to Eq. (7.1).

lower temperatures. As shown in Figs. 6.2 and 6.4, the LT peak grows in amplitude upon pressurizing and exhibits a distinct pressure evolution compared to the HT peak thus emphasizing its presence as an independent second feature.

7.1.1 Frequency-dependent analysis

The frequency dependence of the permittivity at constant T is plotted exemplarily in Fig. 7.1(c,d) for $T = 14$ K. We can distinguish two relaxation modes as two roll-offs in the real part $\varepsilon_1(f)$ and two broad maxima in the imaginary part $\varepsilon_2(f)$. It is instructive to note, that even at low temperatures κ-CuCN is not completely insulating and hence the dc-conductivity σ_{dc} gives a considerable contribution to the imaginary part. Here we follow the common procedure for organic charge transfer salts and subtract this part: $\varepsilon_2(f) = [\sigma_1(f) - \sigma_{dc}]/2\pi f\varepsilon_0$ [32, 195].

The two relaxation modes are best described by the sum of two Cole-Cole modes:

$$\hat{\varepsilon}(\omega) - \varepsilon_{\text{inf}} = \frac{\Delta\varepsilon_1}{1 + (\mathrm{i}\omega\tau_1)^{1-\alpha_1}} + \frac{\Delta\varepsilon_2}{1 + (\mathrm{i}\omega\tau_2)^{1-\alpha_2}} \quad , \tag{7.1}$$

wherein $\tau_{1,2}$ are the relaxation times, $\omega = 2\pi f$ the angular frequency of the applied electric ac-field, $1-\alpha_{1,2}$ are the parameters describing the symmetric broadening of the relaxation time distribution functions, $\Delta\varepsilon_1$ and $\Delta\varepsilon_2$ are the dielectric strengths of the corresponding modes, with $\Delta\varepsilon_1 + \Delta\varepsilon_2 = \varepsilon_{\text{static}} - \varepsilon_{\text{inf}}$, wherein $\varepsilon_{\text{static}}$ and ε_{inf} are the values for low and high frequencies, respectively. In Fig. 7.1(c,d), the purple and orange dashed line represent the fit of mode 1 and mode 2, respectively, while the full black line is their sum according to Eq. (7.1). Considering a Cole-Cole mode, the mean relaxation time corresponds to the point of inflexion in $\varepsilon_1(f)$ and to the maximum in $\varepsilon_2(f)$ (Fig. 7.1(d)).

In Fig. 7.2, we compare the dielectric response for three different samples originating from different batches which are described in detail in Ch. 5.4. For sample #2, the HT peak is shifted to lower temperatures compared to the other samples. For instance for $f = 100$ kHz, the maximum is observed at $T = 28$ K for sample #2, in contrast to 40 K for the other two samples which are found to agree with a previous report [31]. No clear indication for the presence of the LT peak is seen in samples #1 and #3 at ambient pressure but become evident for the former upon pressurizing as well (cf. Fig. 6.4(b,c)). The sample dependence is also seen in the parameters obtained from fitting the frequency dependence with Eq. (7.1) which are plotted as a function of inverse temperature in Fig 7.2(d-f).

Let us first discuss mode 1 in more detail. The dielectric strength $\Delta\varepsilon_1(T)$ resembles $\varepsilon_1(T)$ for low frequencies and exhibits a maximum located around $T = 28$ K for sample #1, $T = 20$ K for sample #2 and $T = 26$ K for sample #3 (Fig 7.2(d)). With decreasing temperature, $1-\alpha_1(T)$ diminishes for all samples indicating a symmetric broadening of mode

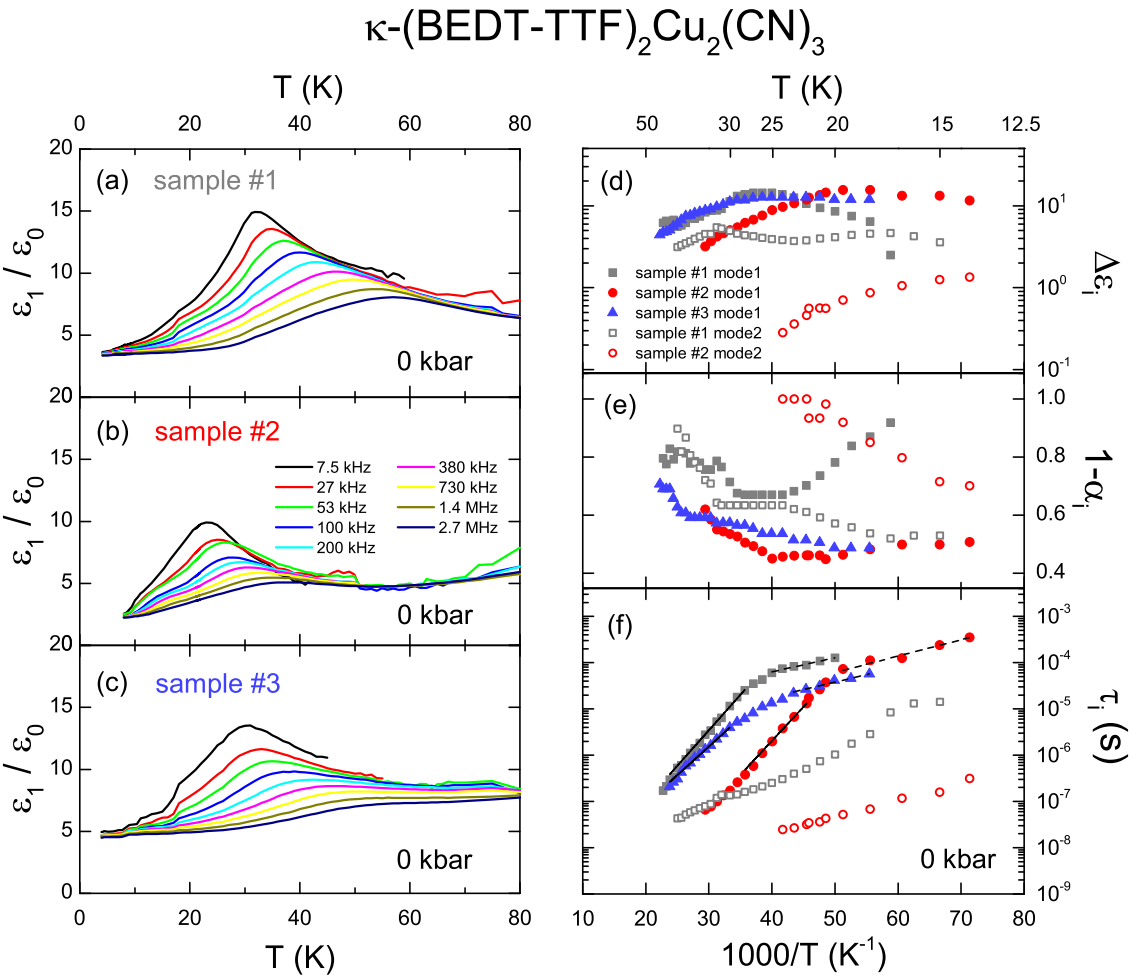

Figure 7.2: Dielectric response of κ-(BEDT-TTF)$_2$Cu$_2$(CN)$_3$ for three samples of different origin. (a-c) Plot of $\varepsilon_1(T)$ for selected frequencies as indicated. For sample #2, the HT peak is shifted to lower temperatures and the LT is more pronounced in comparison to the other samples. (d-f) Arrhenius plot of the fit parameters for both modes as obtained from the fits of the frequency-dependent data according to Eq. (7.1).

1; only for sample #1 a clear restrengthening below a broad minimum around $T = 25$ K is observed. Simultaneously, the relaxation time $\tau_1(T)$ increases upon cooling, providing evidence for the slowing down of the dielectric relaxation. In relaxor ferroelectrics, the observed signature in $\tau_1(T)$ and $1 - \alpha_1(T)$ is usually ascribed to cooperative motion and glassy freezing [164]. Interestingly, we observe a change in the slope of τ_1 which is rather broad and located around $T = 28$ K for samples #1 and #3; for sample #2 it is shifted to $T = 20$ K and rather sharp. A similar feature in $\tau_1(T)$ was previously observed at ambient pressure around $T = 17$ K and attributed to a bifurcation temperature T_B [32]; here free charge carries start to freeze out and hopping-like conduction sets in. A closer look at the pressure-dependent analysis in chapter 7.2 will show, that the kink in $\tau_1(T)$ at T_B corresponds to the change over from the HT to the LT peak in T_B.

Mode 2 is observed in samples #1 and #2 only. It's contribution $\Delta\varepsilon_2$ to the dielectric response is inferior compared to mode 1 and shows a strong sample dependence. For sample #1, $\Delta\varepsilon_2(T)$ is by a factor of 5 smaller compared to mode 1 and exhibits a weak bump around $T = 32$ K whereas it is a factor of 10 smaller and increases monotonously upon cooling for sample #2 (Fig 7.2(d)). τ_2 becomes larger as the temperature is reduced while $1 - \alpha_2$ decreases; again indicating that the corresponding relaxation freezes out.

The sample dependence of the dielectric response of κ-CuCN is in agreement with a previous report and ascribed to a varying degree of disorder [32]. The disorder induced variations of the peak position and the relaxation dynamics are confirmed by disorder studies, revealing a shift of the $\varepsilon_1(T)$ maximum to lower temperatures upon x-ray irradiation [206]. Thus we ascribe the shift of the HT peak in sample #2 to an increase degree of disorder. Up to now, only a single relaxation mode was identified in the frequency-dependent analysis. As we will discuss later in detail (cf. Ch. 7.5.4), the mode 2 becomes apparent in samples with an increased amount of structural disorder.

7.2 κ-(BEDT-TTF)$_2$Cu$_2$(CN)$_3$ pressure-dependent analysis

Here we continue with the pressure evolution of the LT and HT peaks as observed in sample #2. In Fig. 7.3(a), we plot $\varepsilon_1(T)$ at $f = 100$ kHz and fit the HT and LT peaks with two Gaussian functions according to

$$\varepsilon_1/\varepsilon_0 = y_0 + \frac{A_{\mathrm{HT}}}{\sqrt{\pi/2}W_{\mathrm{HT}}} \exp\left(\frac{-2(T - T_{\mathrm{HT}})}{W_{\mathrm{HT}}}\right)^2 + \frac{A_{\mathrm{LT}}}{\sqrt{\pi/2}W_{\mathrm{LT}}} \exp\left(\frac{-2(T - T_{\mathrm{LT}})}{W_{\mathrm{LT}}}\right)^2 , \tag{7.2}$$

where y_0 is an offset, $T_{\mathrm{HT,LT}}$ the center, $A_{\mathrm{HT,LT}}$ the area and $W_{\mathrm{HT,LT}}$ the width of the Gaussian representing the HT and LT peak. The obtained fitting parameters are plotted

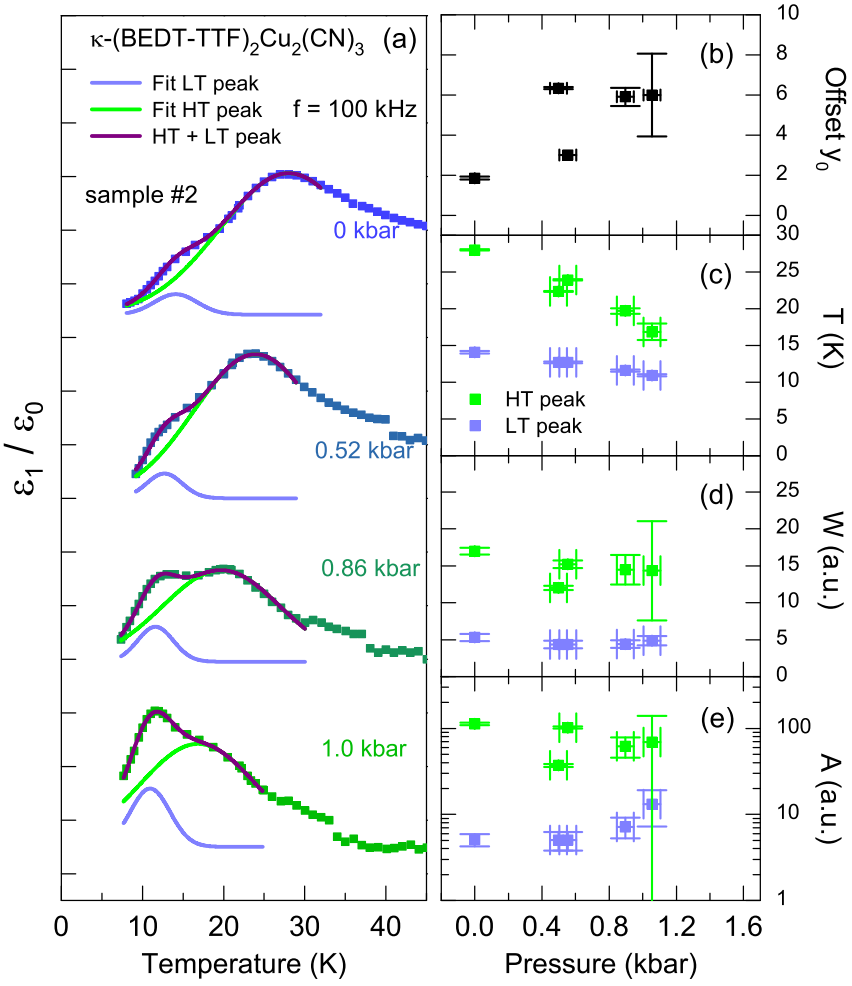

Figure 7.3: Fits of the HT and LT peak of sample #2 with two Gaussians according to Eq. 7.2. (a) Plot of $\varepsilon_1(T)$ and the respective fitting contributions for various pressures as indicated. (b-d) Pressure dependence of the offset y_0 (b), the Gaussian peak width W (c) and the peak area A (d).

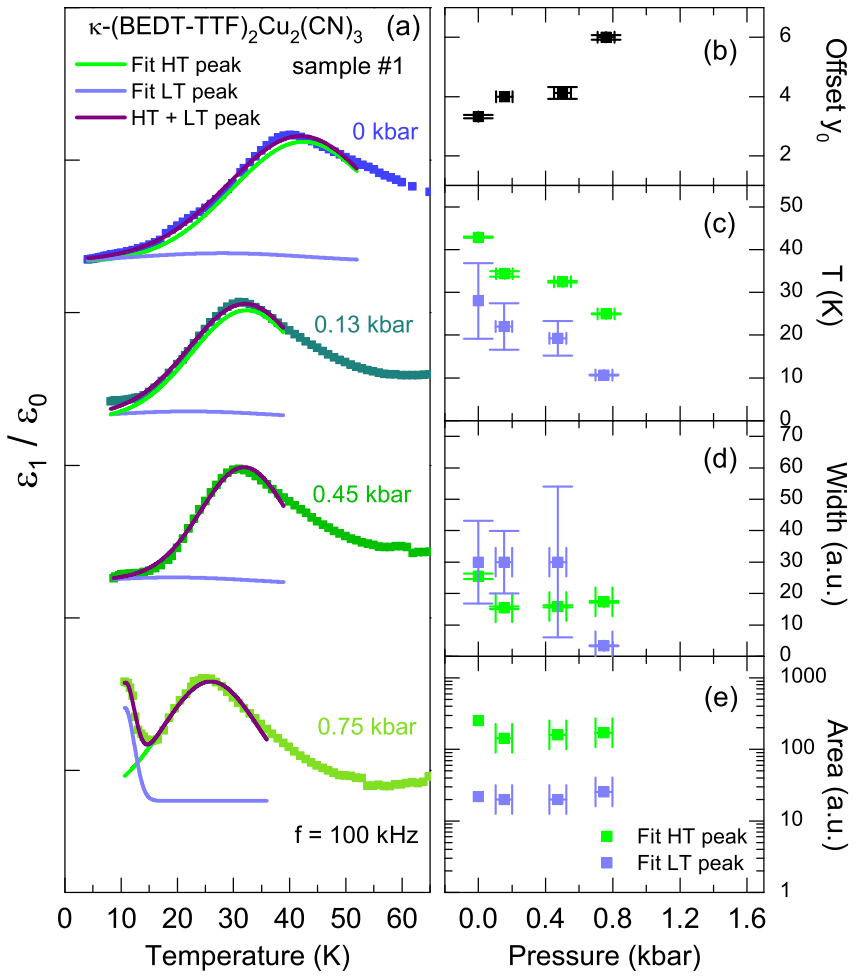

Figure 7.4: Fitting $\varepsilon_1(T)$ of sample #1 with Eq. 7.2. (a) Plot of $\varepsilon_1(T)$ and the respective fitting contributions for various pressures as indicated. (b-d) Pressure dependence of the offset y_0 (b), the Gaussian peak width W (c) and the peak area A (d).

as a function of pressure in Fig. 7.4(b-e). The increase of the offset y_0 upon pressure (Fig. 7.3(b)) is in agreement with the growth of a background contribution to $\varepsilon_1(T)$ seen in Fig. 6.2(a-e) for $T > 40$ K. Both peaks exhibit a shift upon pressure which is more pronounced for the HT peak (Fig. 7.3(c)). The width is pressure-independent for both peaks (Fig. 7.3(d)) while A_{HT} diminishes and A_{LT} rises upon pressure (Fig. 7.3(e)), representing the grows of the LT contribution to $\varepsilon_1(T)$.

In Fig. 7.4(a), we also fit $\varepsilon_1(T)$ at f =100 kHz for sample #1 with Eq. 7.2 and plot the pressure dependence of the fitting parameters in panels (b-e). The offset increases from $y_0 = 2.5$ to $y_0 = 6$ (Fig. 7.4(b)) while both peak positions shift towards lower temperatures upon pressure (Fig. 7.4(c)), similar to what is observed for sample #2. From 0 to 0.45 kbar, the HT peak gives a good description of $\varepsilon_1(T)$ while the LT peak is barely present and gives an imperceptible contribution with increased width and diminished area in respect to the HT peak. Eventually at 0.75 kbar, the LT peaks becomes evident at 10 K as a sharp feature with a slight increase in A_{LT}.

7.2.1 Pressure evolution of mode 1

Similar to the procedure at ambient pressure (Fig. 7.1(c,d)), the frequency dependence of the permittivity is fitted with two Cole-Cole modes according to Eq. 7.1 for all sets of p and T values where the crystals are still insulating. The obtained fitting parameters for mode 1 are plotted as a function of inverse temperature in Fig. 7.5. For both samples, the peak in $\Delta\varepsilon_1(T)$ shifts to lower temperatures and increases in amplitude as pressure is applied (Fig 7.5(a,d)) similar to the pressure evolution of $\varepsilon_1(T)$ where the appearance of the LT feature broadens the relaxation. This is less pronounced for sample #1 for which the LT peak becomes apparent only at 1.0 kbar. The resulting lower values of $1-\alpha_1$ do not indicate more cooperativity or glassy behavior compared to ambient pressure. For sample #1, a restrengthening of $1 - \alpha_1$ persists up to 1.0 kbar (Fig. 7.5(e)). Most importantly, the kink in $\tau_1(T)$ at T_{B} shifts to lower temperatures while the corresponding relaxation time gets shorter.

For $T > T_{\mathrm{B}}$, we can describe the temperature dependence of the relaxation time τ_1 by an activated behavior

$$\tau_1 = \tau_{\mathrm{HT}} \exp\left\{\frac{\Delta_{\mathrm{HT}}}{T}\right\} \quad , \tag{7.3}$$

which is represented by the black solid lines in Fig. 7.5(c,f). Likewise for $T < T_{\mathrm{B}}$, $\tau_1(T)$ also can be fitted with an activated behavior in analogy to Eq. (7.3), which is illustrated by the red solid lines in Fig. 7.5(c,f).

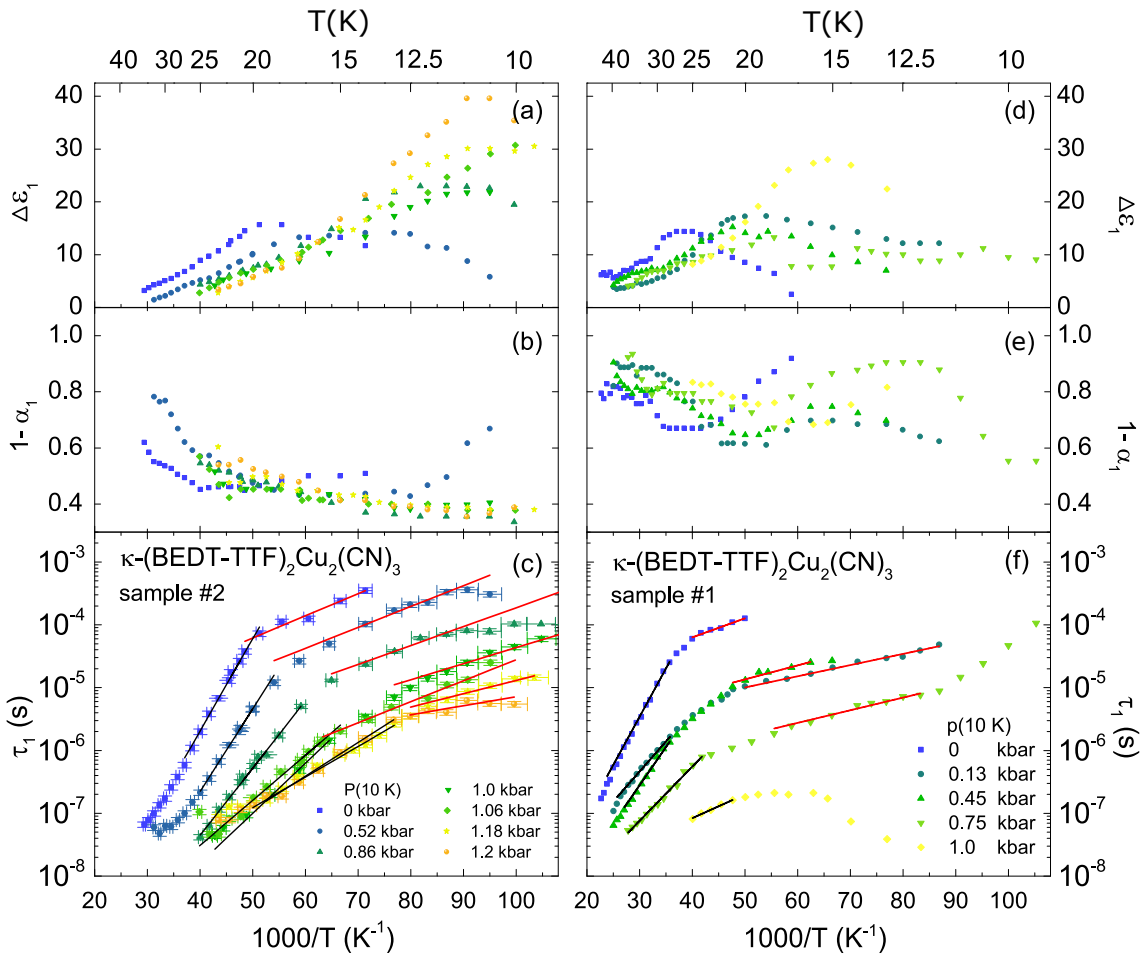

Figure 7.5: Arrhenius plot of the Cole-Cole parameters of mode 1 for both samples at different pressures as indicated. (a,d) Dielectric strength $\Delta\varepsilon_1(T)$, (b,e) distribution of relaxation times $1-\alpha_1(T)$ and (c,f) mean relaxation time $\tau_1(T)$. The black and red lines represent fits with Eq. (7.3) above and below the kink in $\tau_1(T)$ at T_B, respectively.

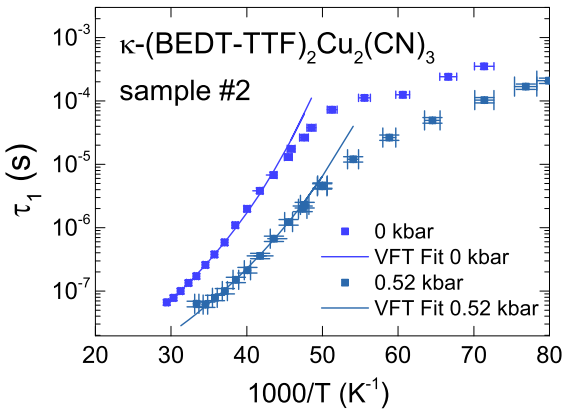

Figure 7.6: τ_1 of sample #2 at 0 kbar and 0.52 kbar. For these two pressures, $\tau_1(T)$ also can be fitted with the Vogel-Fulcher-Tammann behavior according to Eq. (7.4) (solid lines). The obtained values are summarized in Table 7.1.

Table 7.1: When fitting $\tau_1(T)$ obtained for sample #2 at low-pressure in the temperature range above T_B with the Vogel-Fulcher-Tammann behavior Eq. (7.4), the following parameters for the energy barrier Δ_{VFT}, characteristic temperature T_{VFT}, and relaxation time τ_{VFT} are obtained.

	0 kbar	0.52 kbar
Δ_{VFT} (K)	104 ± 24	94 ± 29
T_{VFT} (K)	12 ± 2	10 ± 2
τ_{VFT} (s)	(5.3 ± 3.9) $\cdot 10^{-10}$	(3.6 ± 4.1) $\cdot 10^{-10}$

At this point we should note, that the temperature dependence of the relaxation time for sample #2 at $p = 0$ and 0.52 kbar can also be modeled by the Vogel-Fulcher-Tammann equation (cf. Ch. 4.2.1)

$$\tau_1 = \tau_{VFT} \exp\left\{\frac{\Delta_{VFT}}{T - T_{VFT}}\right\} \quad , \tag{7.4}$$

which is illustrated in Fig. 7.6. In general Eq. (7.4) describes the slowing down of molecular motion in disordered systems and the glass-like freezing of dipolar order in relaxor ferroelectrics. The energy Δ_{VFT} can be interpreted as a temperature-dependent activation energy for re-orientational motion, T_{VFT} denotes the temperature where τ_1 diverges and τ_{VFT} is the time scale for the ac response in the high-temperature limit. The obtained values are summarized in Table 7.1.

The parameters obtained by fitting $\tau_1(T)$ with the activated behavior (Eq.(7.3)) for the HT mode ($T > T_B$) and the LT mode ($T < T_B$) are plotted in Fig. 7.7 as a function of pressure. The values of Δ_{HT} at 0 kbar are in good agreement with previous ambient-

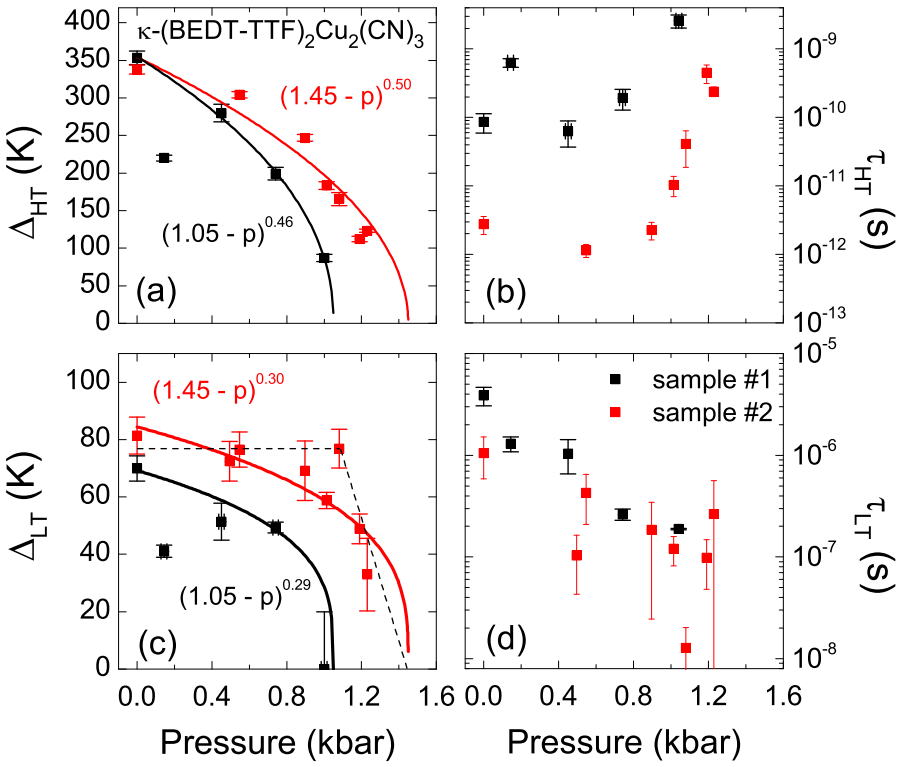

Figure 7.7: Pressure dependence of the parameters obtained from fitting $\tau_1(T)$ with Eq. (7.3) as done in Fig. 7.5(c,f). (a) The activation energy Δ_{HT} nicely follows a mean field behavior (solid lines) according to Eq. (7.6), whose results are summarized in Tabel 7.2. (b) The time scale τ_{HT} for the ac response in the high-temperature limit qualitatively showing the same behavior. (c) The pressure evolution of Δ_{LT} noticeably deviates from mean field behavior (solid lines), for sample #2 it rather seems to be constant and abruptly decreases around 1.1 kbar, reminiscent of a first-order phase transition (dotted black line). (d) The high-temperatures relaxation τ_{LT} decreases upon pressure for both samples.

Table 7.2: Pressure evolution of the mean field parameters of Δ_{HT} and Δ_{LT} in analogy to Eq. (7.6) using fixed $p_{\mathrm{IMT},\#2}$=1.45 kbar and $p_{\mathrm{IMT},\#1}$=1.05 kbar for sample #2 and sample#1, respectively.

sample #2	A	z	sample #1	A	z
Δ_{HT}	294 ± 16	0.50 ± 0.09	Δ_{HT}	347 ± 5	0.46 ± 0.03
Δ_{LT}	75 ± 2	0.30 ± 0.04	Δ_{LT}	68 ± 4	0.29 ± 0.05

pressures studies [32]. Upon increasing pressure, Δ_{HT} decreases for both samples. The solid lines represent mean field fits according to

$$\Delta_{\mathrm{i}} = A \cdot (p_{\mathrm{IMT}} - p)^{z} \quad , \tag{7.5}$$

with i = {TH,LT}, A being a coefficient and z the critical exponent. The insulator-metal transition was fixed to $p_{\mathrm{IMT},\#2}$ = 1.45 kbar [17, 35] and $p_{\mathrm{IMT},\#1}$ = 1.05 kbar for sample #2 and sample #1, respectively, as obtained from their phase diagrams (cf. Figs. 6.3(e) and 6.1(e)). For sample #2, Δ_{LT} noticeably deviates from mean field behavior and rather seems to be constant until it abruptly decreases around 1.1 kbar, reminiscent of a first-order phase transition (dotted black line). Nevertheless, we also include tests for mean-field behavior, represented by the solid lines. For sample #1, due to the low number of data points it is difficult to pin down, whether Δ_{LT} follows mean-field behavior or not. However, the obtained mean-field parameters are listed in Table 7.3 and show good agreement between the samples for the critical exponents. Likewise, the time scale τ_{HT} seems to be constant up to 0.6 kbar and then increases by several orders of magnitude when pressure rises further, whereas the absolute values are sample dependent and differ by two orders of magnitude. For both samples, τ_{LT} decrease upon pressurizing with good quantitative agreement.

7.2.2 Pressure evolution of T_{B}

Let us now have a closer look at the relation of mode 1 to the HT and LT peak. In Fig. 7.8, we plot $\varepsilon_1(T)$ probed at f = 100 kHz and at various pressures as indicated together with the fits of the HT and LT peaks from Fig. 7.3. The lower panels present τ_1 and τ_2 as a function of temperature including the fits of the former according to Eq. (7.3) for the temperature range above (black line) and below (red line) the kink at T_{B}. First of all, the temperature at which the fits of τ_1 intersect precisely determines T_{B}. Moreover, this representation emphasizes that for both samples the kink in $\tau_1(T)$ at T_{B} corresponds to the temperature where the HT peak in $\varepsilon_1(T)$ diminishes. We will discuss the pressure evolution of τ_2 in detail in chapter 7.2.3 and note for the moment, that it does not exhibit

Table 7.3: Parameters from fits of the pressure evolution of the high-temperature peak T_{HT}, the bifurcation temperatures T_{B} and the low-temperature peak T_{LT} according to Eq. (7.6) using fixed $p_{\mathrm{IMT},\#2}$=1.45 kbar and $p_{\mathrm{IMT},\#1}$=1.0 kbar for sample #2 and sample#1, respectively.

sample #2	A	z	sample #1	A	z
T_{LT}	13.0± 0.1	0.18 ± 0.01	T_{LT}	26.7± 2.0	0.67 ± 0.06
T_{B}	18.1 ± 0.2	0.26 ± 0.02	T_{B}	26.1 ± 0.7	0.18 ± 0.03
T_{HT}	23.8 ± 0.5	0.41 ± 0.08	T_{HT}	42.5 ± 1.0	0.37 ± 0.02

a distinct feature at $T = T_{\mathrm{B}}$. In particular this confirms our assignment of the relaxation dynamics observed in $\tau_1(T)$ for $T > T_{\mathrm{B}}$ to the HT peak and for $T < T_{\mathrm{B}}$ to the LT peak in chapter 7.2.1.

In Fig. 7.9, we plot the pressure dependence of T_{B}, determined from the intersection of the Arrhenius fits of τ_1 (cf. Fig. 7.8), together with the positions of the HT and LT peaks, as obtained from the analysis of $\varepsilon_1(T)$ (cf. Figs. 7.3 and 7.4). Comparing the two samples, the overall behavior for sample #1 is clearly shifted towards lower temperatures, which is in agreement with its shift of the Mott transition (cf. Fig. 6.3). Moreover, the LT peak is weakly pronounced at low pressures resulting in rather large error bars for T_{LT}. Besides that, there is good agreement in the qualitative behavior of both samples. The dashed lines in Fig. 7.9 represent extrapolations according to

$$T_{\mathrm{i}} = A \cdot (p_{\mathrm{IMT}} - p)^z \quad , \tag{7.6}$$

with i = {TH,B,LT} the three characteristic temperatures, A being a coefficient and z the critical exponent. Consistent with the procedure for the activation energies in section 7.2.1, the insulator-metal transition was set to $p_{\mathrm{IMT},\#2}$ = 1.45 kbar [17, 35] and $p_{\mathrm{IMT},\#1}$ = 1.05 kbar for sample #2 and sample #1, respectively. The obtained parameters are listed in Table 7.3 and show good agreement between the samples for the critical exponent of T_{HT}, whereas for T_{B} and T_{LT} the determined exponents exhibit a large discrepancy which is most likely due to the weak appearance of the LT peak for sample #1. It is important to emphasize, that for the HT mode there is only little mismatch between the critical exponents of determined here and the ones obtained by fitting the activation energies Δ_{HT} (cf. Fig. 7.7).

7.2.3 Pressure evolution of mode 2

In the Arrhenius plot of Fig. 7.10 the parameters of the second mode $\Delta\varepsilon_2(T)$, $1 - \alpha_2(T)$ and $\tau_2(T)$ are shown as obtained from the Cole-Cole fits. The dielectric strength $\Delta\varepsilon_2$

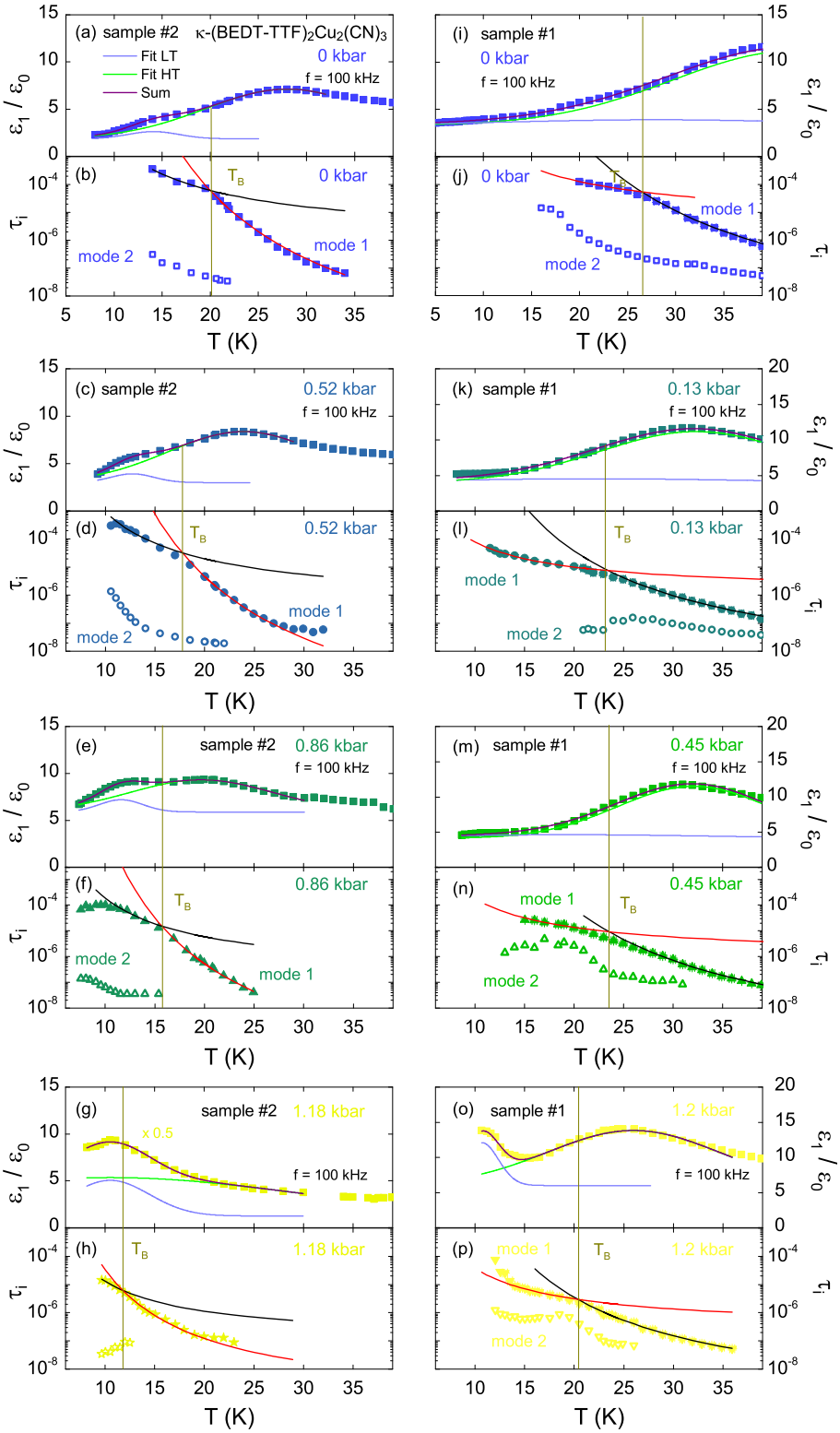

Figure 7.8: Temperature dependence of the dielectric constant $\varepsilon_1(T)$ probed at $f = 100$ kHz including the fits of the HT and LT peak with Eq. (7.2). The lower panels show the relaxation time $\tau_1(T)$ and $\tau_2(T)$, the former with the fits from Fig. 7.5(c,f) according to Eq. (7.3) for the temperature range above (black line) and below (red line) the kink at T_B. This presentation emphasizes, that the crossover from the HT to the LT peak coincides with the kink in $\tau_1(T)$ at T_B.

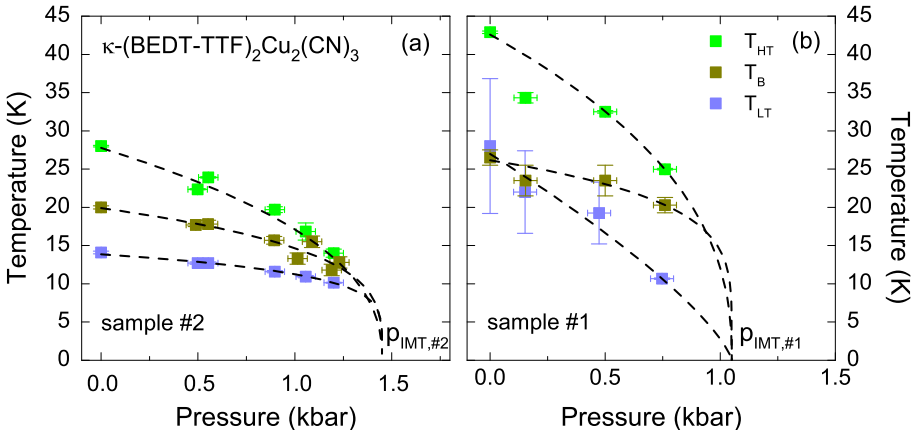

Figure 7.9: Pressure dependence of the bifurcation temperature T_{B} and the positions of the high and low-temperature peak, T_{HT} and T_{LT}. The the dashed lines represent extrapolations according to Eq. (7.6), whereby the insulator-metal transition is fixed to $p_{\mathrm{IMT},\#2}$=1.45 kbar and $p_{\mathrm{IMT},\#1}$=1.05 kbar.

monotonously grows upon cooling for sample #2 while for sample #1 it exhibits a maximum around 30 K at 0 kbar which shifts towards lower temperatures and diminishes upon increasing pressure. Throughout the whole pressure range $\Delta\varepsilon_2$ is smaller than the one of mode 1 by approximately a factor of 10 and 2 for sample #2 and sample #1, respectively. For both samples, the mode shifts towards lower temperatures with rising pressure. A drop in $1-\alpha_2(T)$ indicates a considerable broadening of the mode upon cooling which gets less pronounced for increasing pressure. The temperature dependence of τ_2 is sample-dependent and strongly influenced by pressure. Sample #2 shows a monotonic increase in $\tau_2(T)$ at p =0 and 0.52 kbar which is suppressed for 0.86 kbar and eventually becomes decreasing upon further increasing the pressure. For sample #1, the monotonic rise is much steeper and observed down to 15 K at ambient pressure which saturates into a plateau upon increasing pressure and shows the onset of a shallow minimum around 12 K. In other words, $\tau_2(T)$ depends on pressure in a non-monotonic way.

7.3 κ-[(BEDT-STF)$_x$-(BEDT-TTF)$_{1-x}$]$_2$-Cu$_2$(CN)$_3$ substitution-dependent analysis

Although one Gaussian would give sufficient fits of $\varepsilon_1(T)$, we keep the procedure consistent to the analysis of the pressure-dependent data by fitting $\varepsilon_1(T)$ of κ-STF$_x$-CuCN with two Gaussians according to Eq. (7.2), which is shown in Fig. 7.11(a) for selected x. This way,

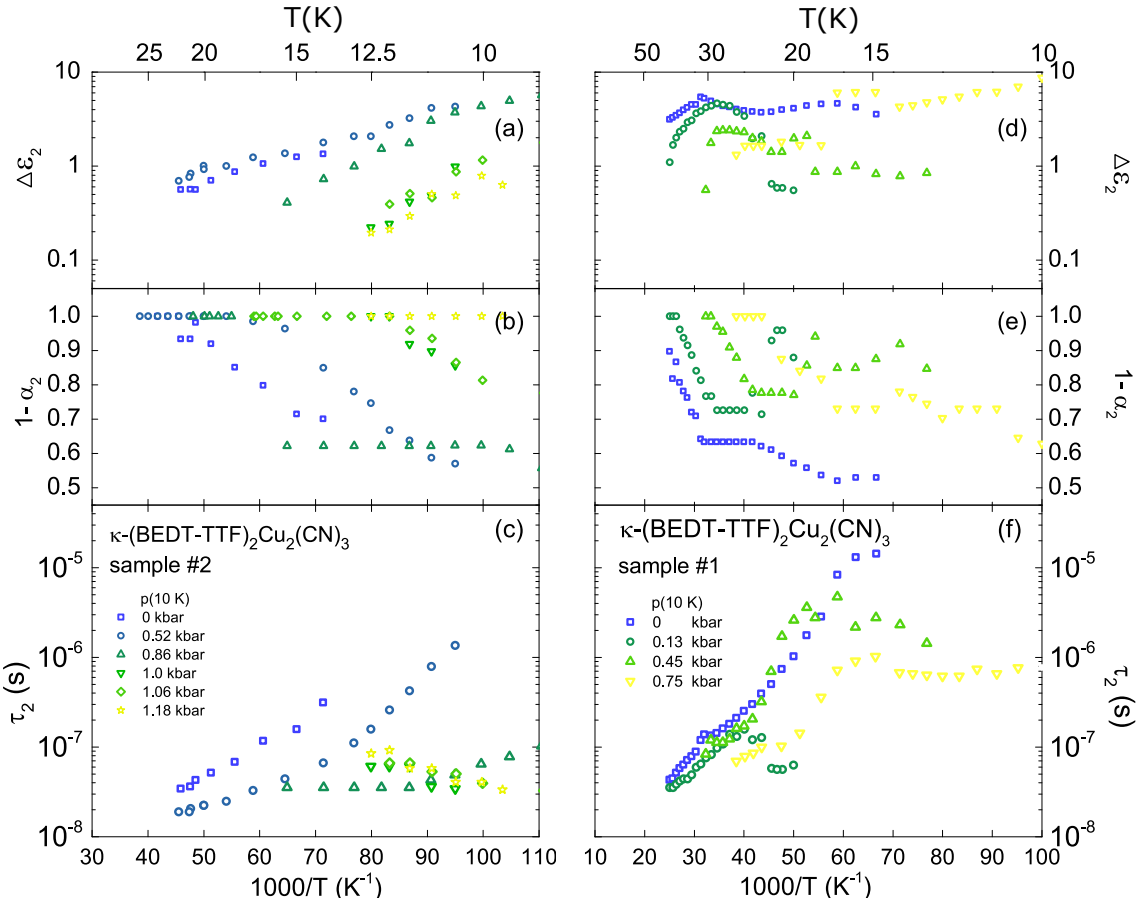

Figure 7.10: Temperature dependence of the parameters describing mode 2 in κ-(BEDT-TTF)$_2$Cu$_2$(CN)$_3$ at various pressures as indicated. (a) Dielectric strength $\Delta\varepsilon_2$, (b) distribution of relaxation times $1-\alpha_2$ and (c) mean relaxation time τ_2 in an Arrhenius plot versus inverse temperature.

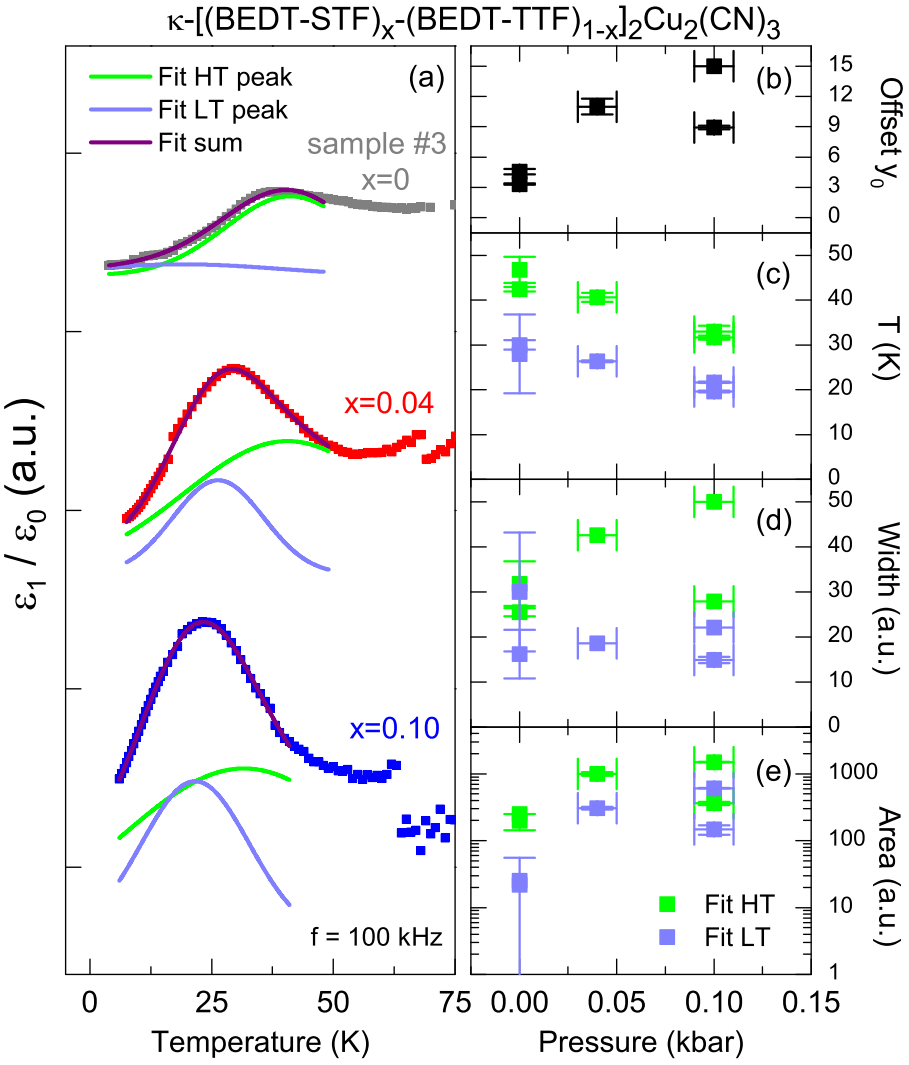

Figure 7.11: (a) Fitting ε_1 of κ-[(BEDT-STF)$_x$-(BEDT-TTF)$_{1-x}$]$_2$Cu$_2$(CN)$_3$ with two Gaussians according to Eq. (7.2) to account for the HT and LT peak. (b-d) Plot of the obtained offset y_0 (b), the Gaussian peak width W (c) and the peak area A (d) as a function of substitution x.

we probe the substitution-dependent shift of the HT and estimate the contribution of the LT peak which we assume to be concealed by the former. The obtained fitting parameters are plotted in panels (b-e) as a function of x. With increasing substitution, the offset grows from $y_0 \approx 4$ to $y_0 \approx 15$ which is twice as much of the enlargement obtained in the pressure-dependent analysis. The positions of the HT and LT peak shift to lower temperatures with rising x resembling the corresponding shift upon pressure in pristine κ-CuCN observed for sample #1. The determined width seems rather sample-dependent though it shows a trend of increasing width for the HT peak. The area of both peaks strongly increases upon rising the substitution level consistent with the overall enhancement in $\varepsilon_1(T)$ while the contribution of the LT peak remains below the one for the HT peak.

7.3.1 Substitution-dependence of mode 1 and mode 2

The frequency dependence of the permittivity for $x = 0$, $x = 0.04$ and $x = 0.10$ is fitted with two Cole-Cole modes according to Eq. (7.1) and is consistent with the analysis for the pressure-dependent data on κ-CuCN (cf. Figs. 7.1, 7.5 and 7.10). The obtained fitting parameters for both modes are presented in Fig. 7.12 as a function of inverse temperature.

A peak in $\Delta\varepsilon_1(T)$ is observed for all substitutions (full symbols in Fig 7.12(a)) which shifts to lower temperatures and increases in amplitude as x rises. As expected, this behavior resembles the one of $\varepsilon_1(T)$ in the low frequency limit. For all substitution levels, the dielectric strength $\Delta\varepsilon_2(T)$ (open symbols in Fig 7.12(a)) seems to follow the one for mode 1 while remaining one order of magnitude smaller then the latter.

Both modes clearly broaden upon cooling; while with $1 - \alpha_1 < 0.7$ mode 1 is already rather broad when it enters the experimental frequency window, mode 2 with $1 - \alpha_2 \approx 1$ around 30 K is narrow. As already mentioned above, the considerable lower values of $1-\alpha_1$ upon increasing x do not indicate more cooperativity or glassy behavior compared to the pristine sample but are rather attributed with the growth of the LT peak contribution broadening the dielectric relaxation.

There is a considerable shift of $\tau_1(T)$ towards lower temperatures upon rising the substitution level from $x = 0$ to $x = 0.04$ (full symbols in Fig 7.12(c)), which, however, halts upon further increasing x to 0.10. This is rather surprising since one would expect a further shift towards lower temperatures with rising x in analogy to the observations upon increasing pressure (Fig. 7.5(c)). At this point one should remember the strong sample to sample variation of the dielectric relaxation which is exposed via different curves in $\tau_1(T)$ for different samples (Fig. 7.2). However, a kink in $\tau_1(T)$ is still observed for all substitution levels which indicates T_B and agrees well with the pressure-dependent results for κ-CuCN (Fig. 7.5(c)). In analogy to the pressure-dependent analysis, for each substi-

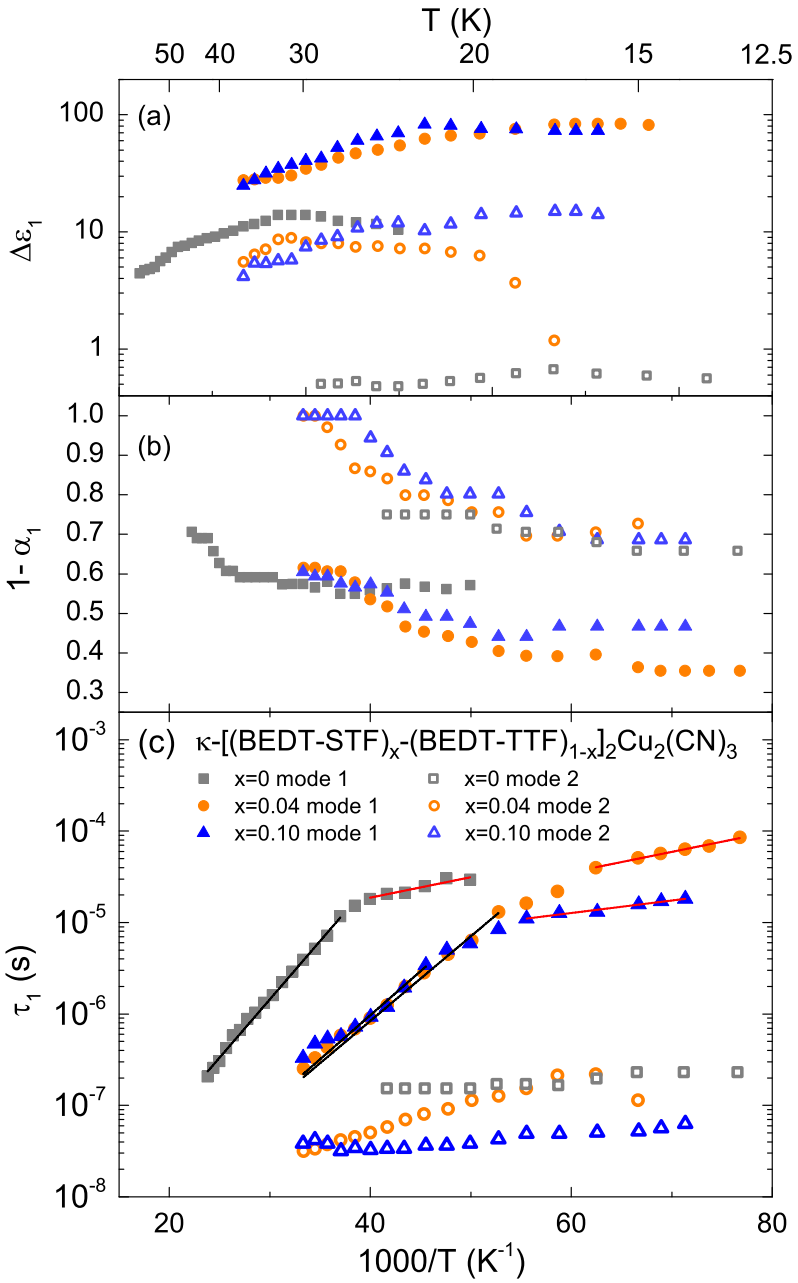

Figure 7.12: Arrhenius plot of the Cole-Cole parameters for both modes of κ-[(BEDT-STF)$_x$-(BEDT-TTF)$_{1-x}$]$_2$Cu$_2$(CN)$_3$ with different substitution levels x as indicated. (a) Dielectric strength $\Delta\varepsilon_i(T)$, (b) distribution of relaxation times $1-\alpha_i(T)$ and (c,f) mean relaxation time $\tau_i(T)$. The black solid and dotted lines represent fits with Eq. (7.3) above and below the kink in $\tau_1(T)$ at T_B, respectively.

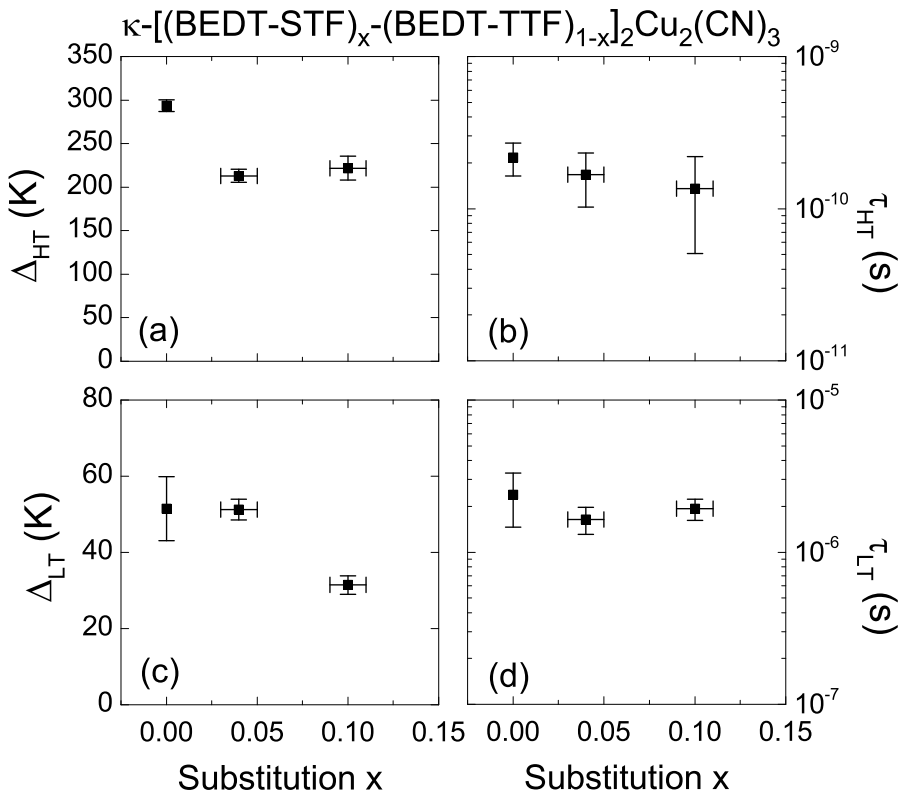

Figure 7.13: Substitution dependence of the parameters obtained from fitting $\tau_1(T)$ with Eq. (7.3) as done in Fig. 7.12(c,f). Unfortunately, crystals with only three different substitution levels remaining in the insulating phase were available. (a) The activation energy Δ_{HT} of the HT peak, (b) time scale τ_{HT} for the ac response in the high-temperature limit, (c) activation energy Δ_{LT} of the LT peak and (d) the extrapolated ac response in the high-temperature limit for the LT peak. Overall, the substitution-dependence of the parameters agrees well with the corresponding pressure-evolution presented in Fig. 7.7.

tution level we fit $\tau_1(T)$ above and below the kink with an activated behavior according to Eq. (7.3) which is represented by the black and red lines, respectively.

For $x = 0$, $\tau_2(T)$ remains constant upon cooling whereas a slight increase is observed for $x = 0.04$ and $x = 0.1$ which is more pronounced for the former. The overall behavior of $\tau_2(T)$ with rising the substitution level is similar to the one observed for the κ-Cu-CN sample #2 upon increasing pressure (Fig. 7.10(c)).

The parameters obtained by fitting $\tau_1(T)$ with Eq. (7.3) are plotted in Fig. 7.13 as a function of the substitution level x. The activation energy Δ_{HT} of the HT peak considerably drops upon rising the substitution from the pristine crystal to $x = 0.04$, whereas increasing further to $x = 0.10$ has no influence. Contrary, Δ_{LT} stays constant around 50 K up to

$x = 0.04$ and decreases to 30 K upon rising x to 0.10, reminiscent of the corresponding pressure-evolution. For both modes, the time scales of the high-temperature extrapolation τ_{HT} and τ_{LT} are in good quantitative agreement with their pressure-dependent counterparts. Overall, the substitution-dependence of the fitting parameters presented in Fig. 7.13 resembles the pressure-dependent behavior for $p < 0.8$ kbar, whereas for the former the drastic changes upon approaching the IMT are not revealed due to the lack of suitable substitution levels close enough to the phase boundary.

In Fig. 7.14, we plot $\varepsilon_1(T)$ probed at $f = 100$ kHz and at various substitution levels as indicated together with the fits of the HT and LT peaks from Fig. 7.11. The corresponding lower panels present τ_1 and τ_2 as a function of temperature including the fits of the former (Fig. 7.12) according to Eq. (7.3) for the temperature range above (black line) and below (red line) the kink. Consistent with the procedure for the pressure-dependent results, T_{B} is determined as the temperature where the fits for τ_1 intersect. It is worthwhile to note, that $\tau_2(T)$ does not exhibit a distinct feature at $T = T_{\mathrm{B}}$.

In Fig. 7.14(g), T_{B} is plotted over x together with the positions of the HT and LT peak. Since only samples with three different substitution levels are located on the insulting side of the Mott transition, a more comprehensive analysis of the substitution-dependence of T_{HT}, T_{B} and T_{LT} is denied. However, it obviously deviates from the corresponding pressure evolution observed in pristine κ-CuCN. T_{B} still is interpreted as the temperature where the HT peak diminishes, but since the HT and LT peaks strongly overlap for $x = 0.04$ and $x = 0.10$ T_{B}, the latter is difficult to pin down. As a result, T_{LT} is located above T_{B} which is clearly in contrast to the findings for the pressure its pressure evolution.

7.4 κ-(BEDT-TTF)$_2$Ag$_2$(CN)$_3$ pressure-dependent analysis

To deconvolve peaks in $\varepsilon_1(T)$ and to trace their pressure evolution in more detail, we fit $\varepsilon_1(T)$ at 100 kHz with two Gaussians according to Eq. (7.2) accounting for the HT and the anomaly (A) peak. For pressures exceeding 3.4 kbar, we use an additional Gaussian to consider the LT peak. This is shown in Fig. 7.15(a) for selected pressures as indicated and the obtained fitting parameters are plotted as a function of pressure in Fig. 7.15(b-e). To obtain converging fits, we reduced the number of free fitting parameters by keeping the offset constant at $y_0 = 0$ for all pressures investigated (Fig. 7.15(a)). The HT peak position T_{HT} continuously shifts to lower temperatures showing a slight bump around 3 kbar (Fig. 7.15(c)). The latter is also observed for T_{A} where it is even more pronounced. Most likely, the bump in T_{HT} and T_{A} is due to the emergence of the LT peak which is not considered yet by the third Gaussian. The width appears rather volatile, especially for the anomaly at low pressures where it is not that strongly pronounced yet. The area

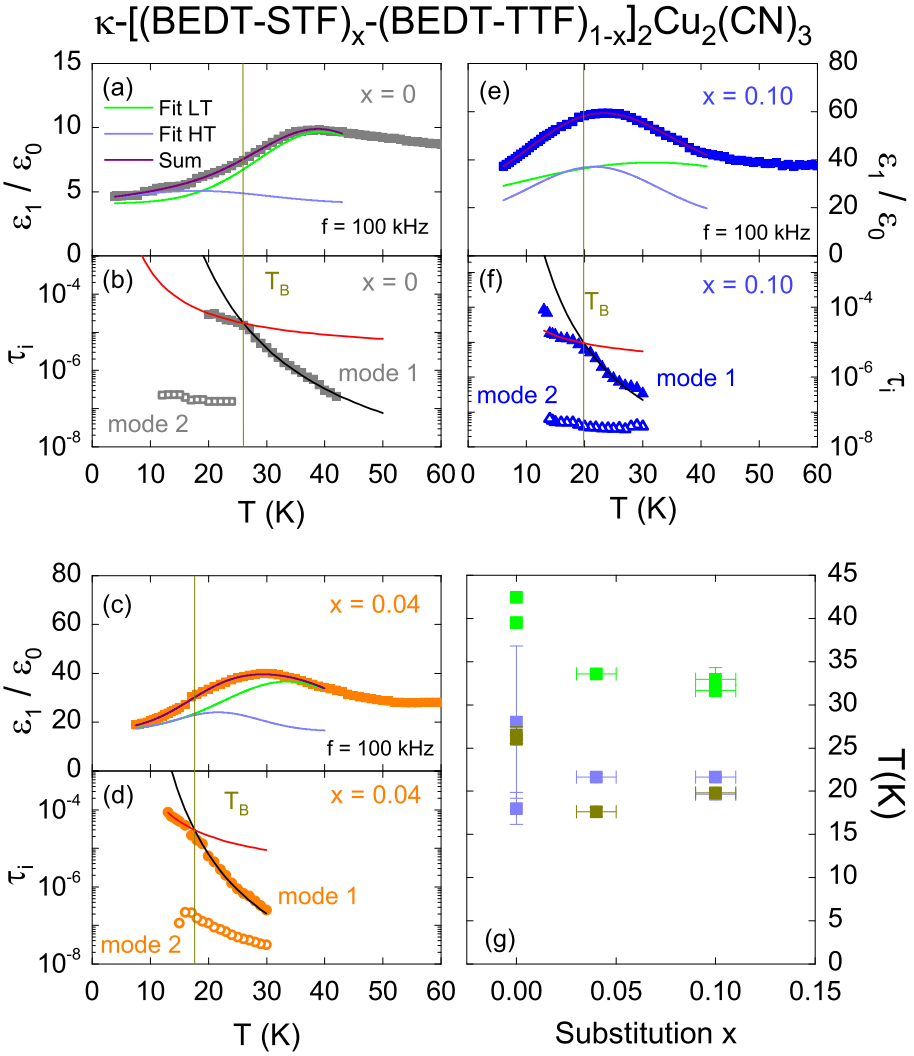

Figure 7.14: Temperature dependence $\varepsilon_1(T)$ of κ-[(BEDT-STF)$_x$-(BEDT-TTF)$_{1-x}$]$_2$-Cu$_2$(CN)$_3$ probed at $f = 100$ kHz and for different substitution levels and including the fits of the HT and LT peak with Eq. 7.2. The corresponding lower panels show the relaxation time $\tau_1(T)$ and $\tau_2(T)$, the former with the fits from Fig. 7.12(c) according to Eq. (7.3) for the temperature range above (black line) and below (red line) the kink at T_B. This presentation emphasizes, that the crossover from the HT to the LT peak coincides with the kink in $\tau_1(T)$ at T_B. (g) The bifurcation temperature T_B and the positions of the high and low-temperature peak, T_{HT} and T_{LT}, plotted over x.

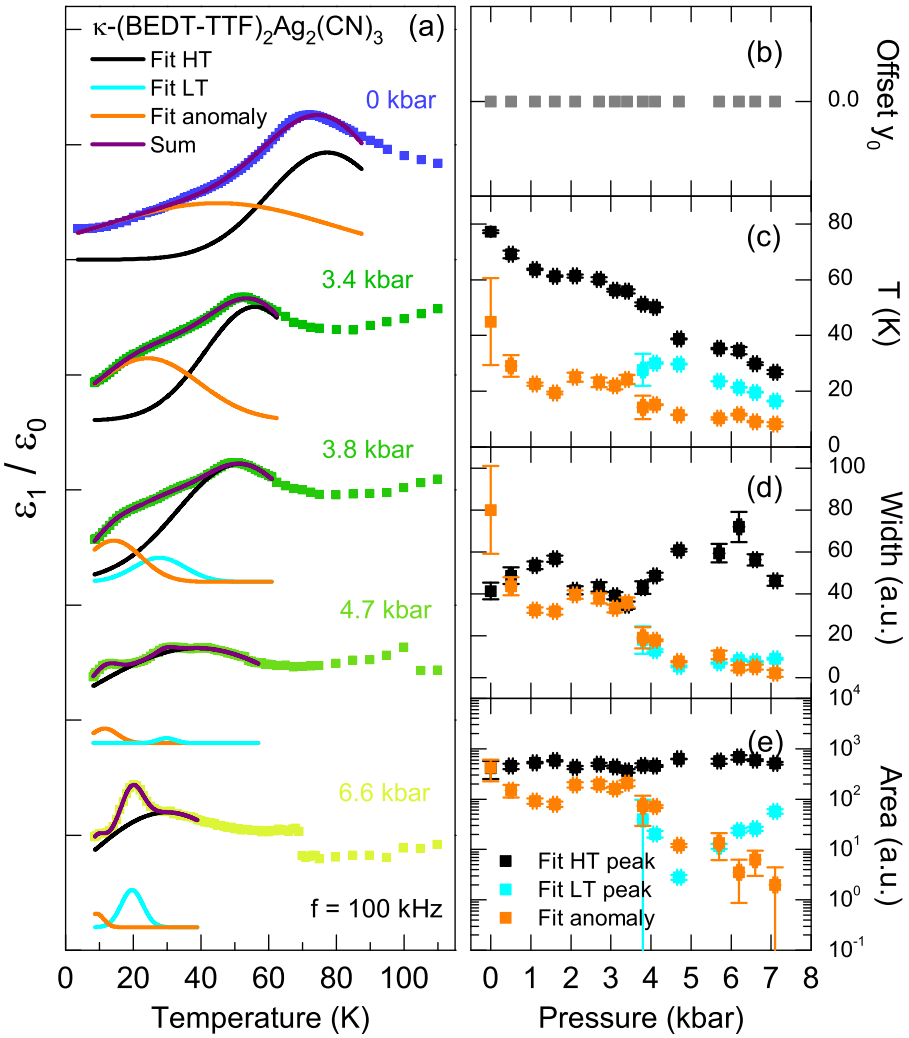

Figure 7.15: (a) Fits of the HT and anomaly peak in $\varepsilon_1(T)$ of κ-(BEDT-TTF)$_2$Ag$_2$(CN)$_3$ with two Gaussians according to Eq. 7.2. For pressures exceeding 3.4 kbar, a third Gaussians is used to accord for the LT peak. (b-d) The offset was kept constant for all pressures at $y_0 = 0$ (b), pressure dependence of the Gaussian peak width W (c) and the peak area A (d).

of the Gaussian is a direct measure for the contribution of corresponding peak to $\varepsilon_1(T)$ (Fig. 7.15(c)). It stays constant around a value of 500 for the HT peak from ambient pressure up to 7.1 kbar. It exhibits a maximum around 3 kbar for the anomaly which again is most likely due to the emerging LT peak which is not fitted yet by the third Gaussian, such that its contribution is included in the anomaly peak. The area of the LT peak grows upon increasing the pressure from 4.7 to 7.1 kbar, clearly rising above the one of the anomaly peak.

7.4.1 Pressure evolution of mode 1

The frequency dependence of the permittivity of κ-AgCN at constant temperature is fitted with two Cole-Cole modes according to Eq. (7.1). The obtained fitting parameters for mode 1 are plotted in Fig. 7.16 as a function of inverse temperature. We observe a pronounced peak in $\Delta\varepsilon_1(T)$ shifting to lower temperatures as pressure is applied, reminiscent to the pressure evolution of $\varepsilon_1(T)$ (Figs. 6.8 and 6.8). Interestingly, the amplitude of the peak first diminishes upon pressurizing and starts to rise again for $p \geqslant 4.7$ kbar (green spheres) right where the LT peak in $\varepsilon_1(T)$ gets enhanced. The broadening parameter $1 - \alpha_1$ shows a pronounced minimum which is rather shallow from 0 to 3.1 kbar and gets strongly pronounced and broader above 3.4 kbar (Fig. 7.16(b)). Upon applying pressure, the position of the minimum shifts towards lower temperatures coinciding with the peak position in $\Delta\varepsilon_1(T)$. The relaxation time $\tau_1(T)$ slows down upon cooling exhibiting a clear kink which shifts to lower temperatures as pressure is increased while the corresponding relaxation time gets shorter. In analogy to the nomenclature introduced for κ-CuCN in Ch. 7.2.1, we denote the kink position as the bifurcation temperature T_B.

It is important to mention, that upon increasing the pressure from 3.4 to 3.8 kbar a considerable drop in $\tau_1(T)$ for $T < T_\mathrm{B}$ is observed which coincides with the appearance of the LT peak in $\varepsilon_1(T)$. Therefore, it reasonable to attribute the relaxation dynamics observed in $\tau_1(T)$ for $p < 3.4$ kbar to the anomaly and for $p > 3.4$ kbar to the LT peak. This assignment will be confirmed later in section 7.4.3.

For all pressures investigated, $\tau_1(T)$ above and below T_B can be nicely described by an activated behavior according to Eq. (7.3). Following the arguments above, the black, orange and cyan lines in Fig. 7.16(c) indicate the fits attributed to the HT, A and LT peak, respectively. The intersection of fits precisely determines T_B, as we will show in detail later (Fig. 7.19).

Fig. 7.17(a,b) presents the parameters obtained from fitting $\tau_1(T)$ with Eq. 7.3. The activation energy Δ_HT of the HT peak decreases with rising pressure exhibiting a small bump around 3 kbar. Up to 2 kbar, the activation energy of the anomaly peak stays

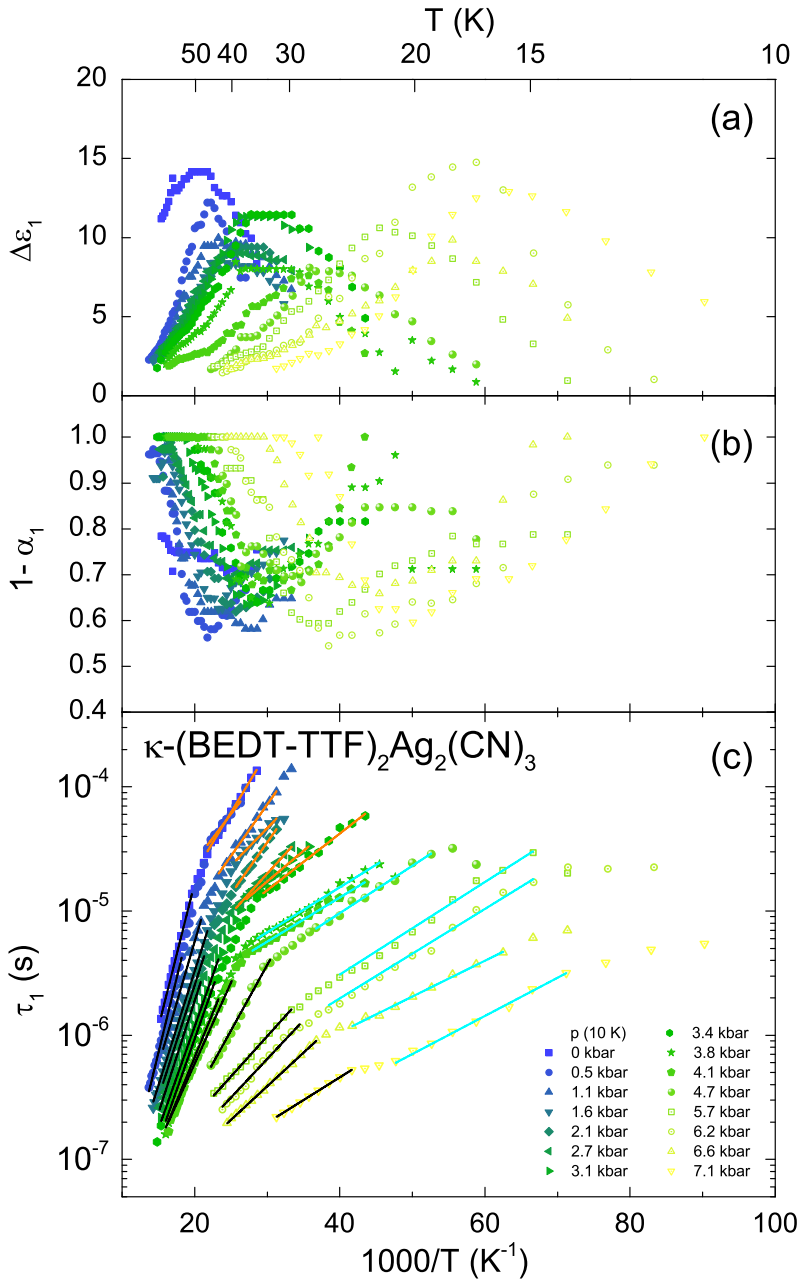

Figure 7.16: Arrhenius plot of the Cole-Cole parameters of mode 1 for κ-(BEDT-TTF)$_2$-Ag$_2$(CN)$_3$ at different pressures as indicated. (a,d) Dielectric strength $\Delta\varepsilon_1(T)$, (b,e) distribution of relaxation times $1-\alpha_1(T)$ and (c,f) mean relaxation time $\tau_1(T)$. The black lines represent fits with Eq. (7.3) above the kink in $\tau_1(T)$ at T_B. For $T < T_B$, fits of $\tau_1(T)$ with Eq. (7.3) are indicated by orange and cyan lines which are assigned to the anomaly and LT peak, respectively.

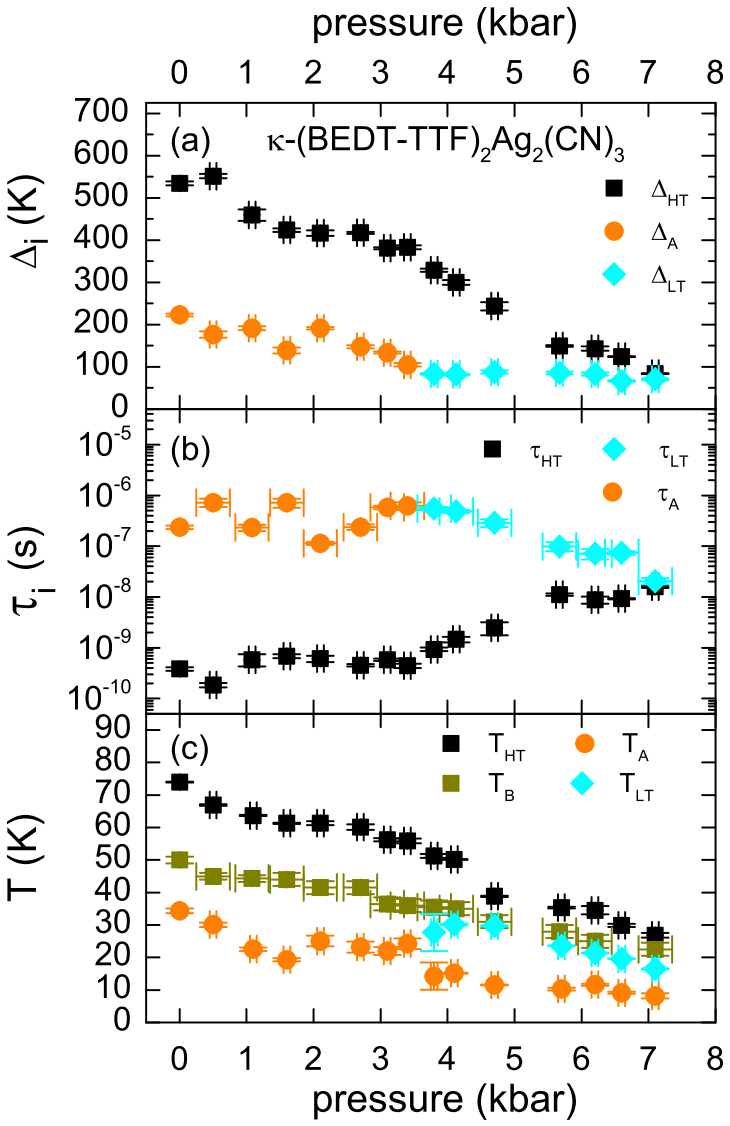

Figure 7.17: (a,b) Pressure dependence of the parameters obtained from fitting $\tau_1(T)$ with Eq. (7.3) (cf. Fig. 7.16(c)). For $p > 3.4$ kbar, the anomaly peak is masked by the emerging LT peak such that the obtained parameters are attributed to the latter. The activation energy (a) and the time scale for the ac response in the high-temperature limit (b) of the relaxation dynamics attributed to the HT, the anomaly and LT peak. (c) The pressure evolution of T_{HT}, T_{A} and T_{LT} together with T_{B}.

constant with $\Delta_A \approx 180$ K and then slightly drops to 100 K upon pressurizing to $p = 3.4$ kbar. For pressures exceeding 3.4 kbar, the anomaly peak is masked by the growing LT peak such that the relaxation dynamics observed for $T < T_B$ are governed by the latter; it's activation energy remains constant around $\Delta_{LT} \approx 80$ K up to 7.1 kbar. From ambient pressure up to 3.4 kbar, τ_A is fluctuating between 10^{-7} and 10^{-6} s. In the same pressure range, τ_{HT} is constant around $5 \cdot 10^{-10}$ s and then significantly slows down for pressure exceeding 3.4 kbar, similar to the behavior of it's analog in κ-CuCN (Fig. 7.7). Starting from 3.8 kbar up to 7.1 kbar, τ_{LT} decreases by two orders of magnitude reminiscent to the behavior of the corresponding parameter in κ-CuCN. In Panel (c), we additionally plot the peak positions T_{HT}, T_A and T_{LT} together with T_B to emphasize the assignment of the relaxation dynamics to the corresponding peak observed in $\varepsilon_1(T)$ (cf. Fig.7.15). The pressure evolution of Δ_{HT} and Δ_A resemble the one of T_{HT} and T_A, respectively. In contrast to that, Δ_{LT} stays constant while T_{LT} decreases to 16.5 K upon pressurizing up to 7.1 kbar.

7.4.2 Pressure evolution of mode 2

Let us now discuss the characteristics of mode 2 in κ-AgCN, which is presented in Fig. 7.18 by plotting the corresponding parameters in an Arrhenius fashion. In general, mode 2 shifts to lower temperatures as pressure rises. The dielectric strength $\Delta\varepsilon_2(T)$ stays well below its counter part of mode 1 for all temperatures up to 3.4 kbar, whereas upon further increasing pressure, mode 2 gains in amplitude and $\Delta\varepsilon_2(T)$ approaches the values of its counterpart $\Delta\varepsilon_1(T)$.

Mode 2 significantly broadens upon cooling as indicated by a decrease of $1 - \alpha_2$ which, however, is shifted to lower temperatures as pressures rises resembling the observed behavior of mode 2 in κ-CuCN.

Interestingly, the temperature dependence of $\tau_2(T)$ is strongly influenced by pressure. Up to 3.1 kbar, we observe a rather steep increase which languishes upon further increasing pressure. While at 3.8 kbar, $\tau_2(T)$ increases monotonically upon cooling, a local minimum is observed around around 20 K for pressures between 4.1 kbar 5.7 kbar. At 6.2 kbar and above, $\tau_2(T)$ regains its strictly monotonic behavior, which however, is not as steep as before.

We conclude, that the non-monotonic temperature-dependence of $\tau_2(T)$ upon applying pressure is in accordance with the findings for κ-CuCN, whereas in the latter, a recovering of the purely monotonic behavior is not observed.

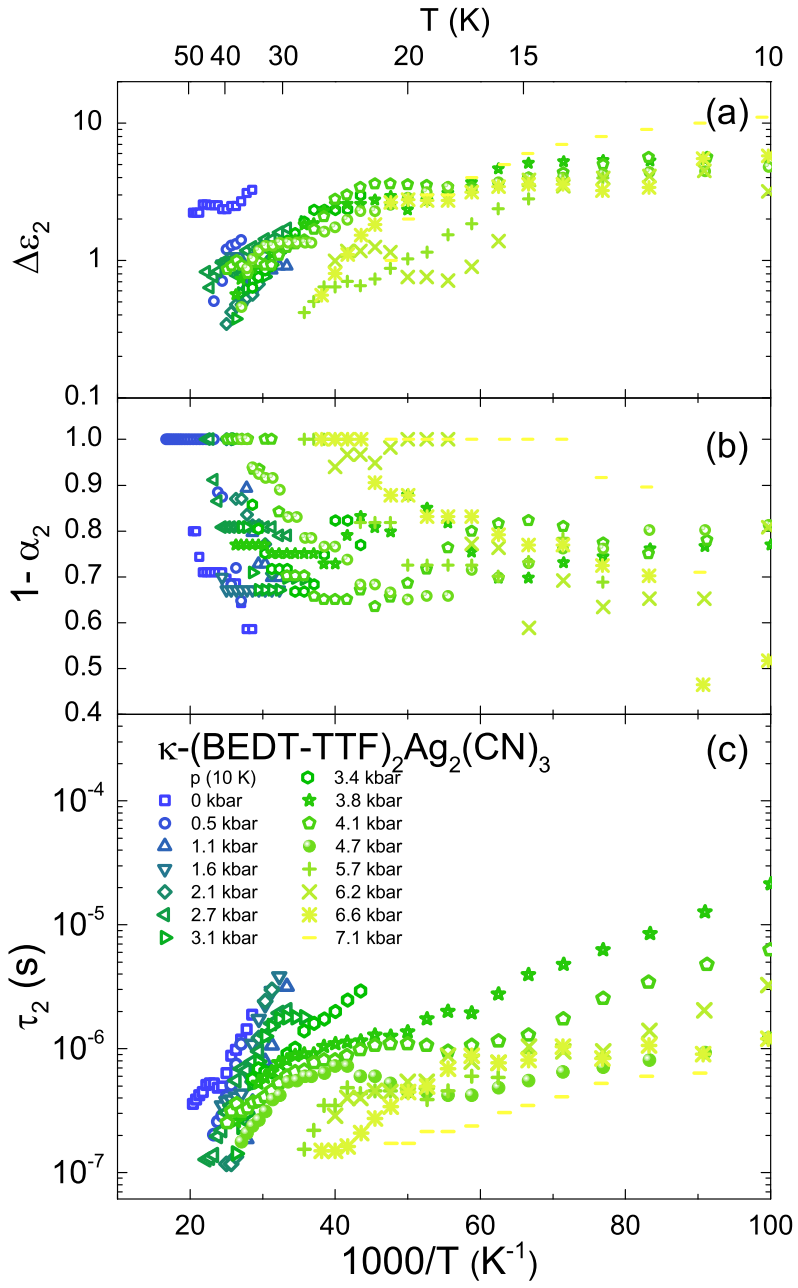

Figure 7.18: Temperature dependence of the parameters describing mode 2 in κ-(BEDT-TTF)$_2$Ag$_2$(CN)$_3$ at various pressures as indicated. (a) Dielectric strength $\Delta\varepsilon_2$, (b) distribution of relaxation times $1 - \alpha_2$ and (c) mean relaxation time τ_2 in an Arrhenius plot versus inverse temperature.

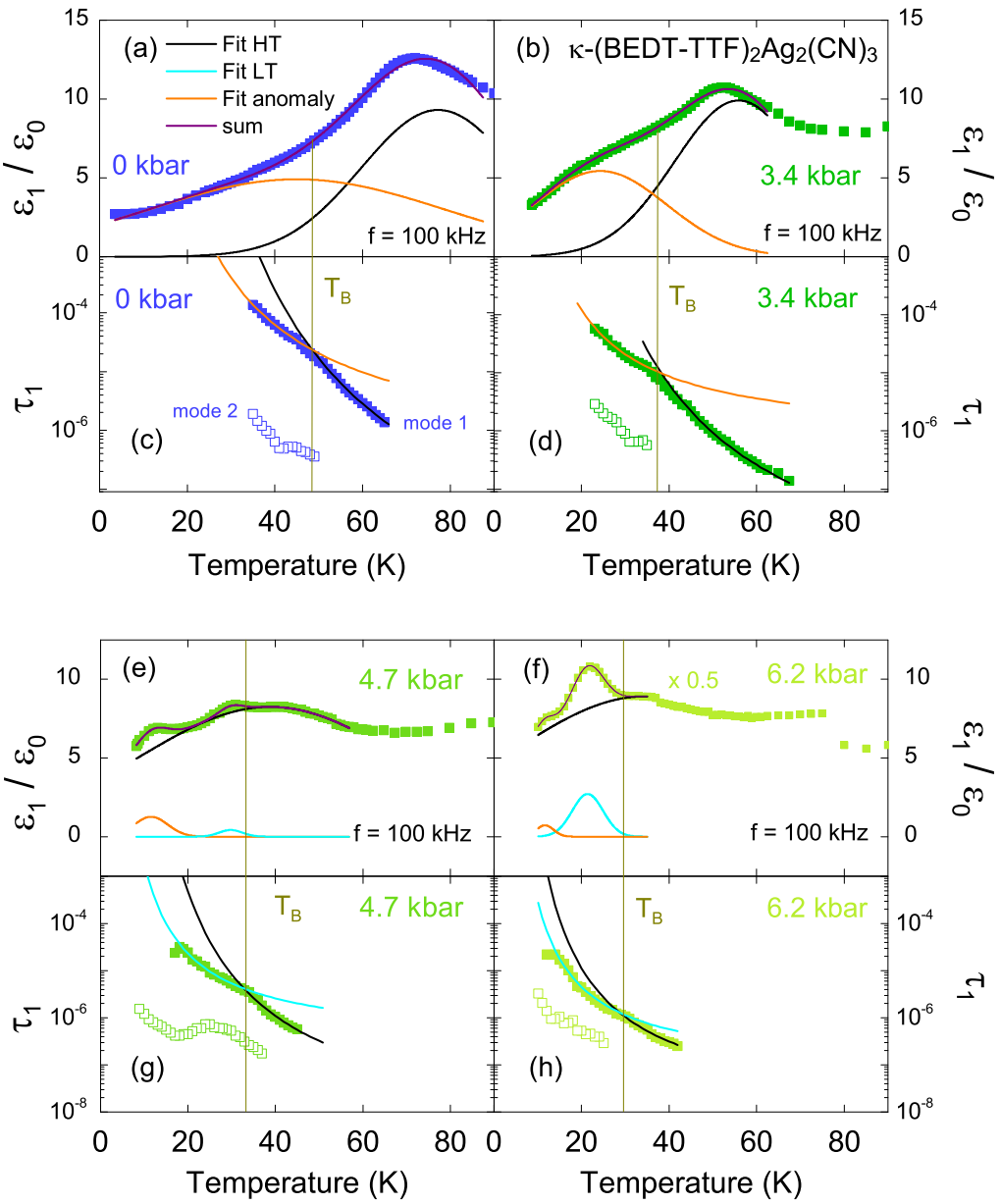

Figure 7.19: Temperature dependence of the dielectric constant $\varepsilon_1(T)$ probed at f = 100 kHz including the fits of the HT and the anomaly peak Eq. (7.2). For pressures exceeding 3.4 kbar, a third Gaussian is used to account for the emerging LT peak. The lower panels show the relaxation time $\tau_1(T)$ and $\tau_2(T)$, the former with the fits from Fig. 7.5(c,f) according to Eq. (7.3) for the temperature range above (black line) and below (red line) the kink at T_B. This presentation emphasizes, that the crossover from the HT to the LT peak coincides with the kink in $\tau_1(T)$ at T_B.

7.4.3 Pressure evolution of T_B

In analogy to the analysis above, we verify in the following the relation of mode 1 to the HT and LT peak for κ-(BEDT-TTF)$_2$Ag$_2$(CN)$_3$ as well. In Fig. 7.8, we plot $\varepsilon_1(T)$ probed at $f = 100$ kHz and at various pressures as indicated together with the fits of the HT, LT and anomaly peaks from Fig. 7.15. The lower panels present $\tau_1(T)$ and $\tau_2(T)$ as a function of temperature including the fits of the former according to Eq. (7.3) for the temperature range above (black line) and below (orange and cyan line) the kink at T_B. Consistent with the procedure for κ-CuCN, T_B is determined as the temperature at which the fits of $\tau_1(T)$ intersect. As expected, T_B corresponds to the kink in $\tau_1(T)$. At the same temperature, the HT peak in $\varepsilon_1(T)$ diminishes and the anomaly, for pressures below 3.4 kbar, or the LT peak, for pressure above 3.4 kbar, are dominant. In particular this confirms our assignment of the relaxation dynamics observed in $\tau_1(T)$ for $T > T_B$ to the HT peak and for $T < T_B$ to the anomaly and the LT peak in section 7.2.1. We note, that $\tau_2(T)$ does not exhibit a distinct feature at $T = T_B$.

7.5 Discussion

Our pressure-dependent investigations unveil that the dielectric response of κ-CuCN, κ-STF$_x$-CuCN and κ-AgCN contains two main dielectric contributions, the high-temperature (HT) and the low-temperature (LT) peak. Additionally, a high frequency mode (mode 2) is observed, whose characteristics shows strong sample to sample variations. In κ-AgCN, the pressure-dependent measurement reveal a third contribution, dubbed here anomaly (A), which is not seen in the other compounds.

7.5.1 High-temperature peak

The HT peak was first observed by Abdel-Jawad *et al.* [31] in κ-CuCN and is also referred to as anomalous dielectric response (ADR) (cf. Ch. 3.5). Our result show, that the HT peak shifts toward lower temperatures upon approaching the IMT while its amplitude is not enhanced, in contrast to the LT peak. We therefore assign the HT peak to the dielectric response of the Mott insulating fraction in contrast to the LT peak, which is attributed to a growing metallic filling fraction upon entering the coexistence phase. However, there is no consensus on the intrinsic origin of the HT peak.

In a first approach one considers single BEDT-TTF molecules as lattice points taking into account the inter- and intra-dimer charge degrees of freedom; in contrast to the dimer-approach which neglects the intra-dimer degrees. As a consequence, κ-CuCN, κ-STF$_x$-CuCN and κ-AgCN are regarded as a $\frac{3}{4}$-filled systems, making them instable to-

wards a charge-ordered state, which is competing with the dimer Mott insulating state. Starting from the $\frac{3}{4}$-filled extended Hubbard model theory predicts fluctuating charge disproportionation within a dimer giving rise to quantum electric dipoles [138, 140]. For κ-CuCN, the dielectric response in the audio and radio frequency range [31] was seen as a consequence. However, infrared vibrational spectroscopy clearly discards a sizable charge disproportionation on the dimers [90]. Also excitations in the THz region were erroneously assigned to collective optical excitations of these quantum electric dipoles [207], but later found to be lattice vibrations including molecular vibrations and coupling to the anions [60].

At this point we have to mention, that a recent theoretical study investigates the cross over from a quarter-filled system with CO ground state to the DMI state due to strong dimerization [208]. At high energy (eV, optical frequencies), the DMI is stable whereas at very low energy (10^{-10} ev$\approx$ 10 kHz) CO becomes dominant leading to domains of different charge polarities. The resulting domain walls are considered to give rise to the HT peak. Whether this sufficiently explains the absence of a charge disproportionation in optics is still under discussion. Moreover in Ref. [62], the crystal structure of κ-(BEDT-TTF)$_2$Cu$_2$(CN)$_3$ was determined to either be P1 or P$\bar{1}$ with two unequal dimers per unit cell, implying a weak charge disproportionation between dimers in the whole temperature range, instead of the first considered P2$_1$/c space group wherein the four dimers in the unit cell are equivalent by symmetry.

During the last years evidence has accumulated that the interaction between the cationic (BEDT-TTF)$_2^+$ and the anionic Cu$_2$(CN)$_3^-$ layer is crucial for the understanding of these charge-transfer salts [32, 60, 62]. The anion layer exhibits intrinsic disorder since the Cu atoms are triangularly coordinated by polar CN$^-$ links in two different configurations (cf. Ch.3.3); either Cu is neighbored by two N atoms and one C atom or by one N atom and two C atoms. The orientation of the CN links within the anion layer might be coupled giving rise to the presence of domains with differently oriented CN links which are mapped onto the BEDT-TTF layer via hydrogen bonds. In Refs. [32, 34, 137], Pinteric *et al.* consider the phase boundaries separating domains with differently oriented CN links as point and/or line defects carrying charge responding to the applied ac field. Upon cooling, the size of cooperatively relaxing region grows, increasing the energy cost for local rearrangements and eventually slowing down the response. The relaxor ferroelectric and glassy behavior are attributed to strong lattice effects observed at 6 K, constraining the effective dynamics of κ-(BEDT-TTF)$_2$Cu$_2$(CN)$_3$ as complex cation-anion system.

To our understanding, however, this picture implies the shift of domain boundaries by flipping CN links in the anion layer. Recent DFT calculations found, that flipping a CN link which is mainly oriented along the b-directions costs 174 meV, whereas flipping one

which is mainly oriented along the c-directions is 10-15 meV [60]. Even for the latter one, the flipping would freeze out at higher temperatures than the relaxor ferroelectric peak is observed. So far, the concept of domain walls is put forward in both approaches whereas their origin is still an open question.

However, the domain wall picture is corroborated by extension of the relaxation time τ_{HT} and decrease of Δ_{HT} upon intensifying pressure, indicating that the domains increase in size and are easier to move. In case of κ-STF$_x$-CuCN, a corresponding dependence of τ_{HT} and Δ_{HT} upon rising the substitution level x is not clearly revealed, even not for $x = 0.10$ which is already close to the IMT transition. Here, the substituted BEDT-STF molecules locally distorting the crystal structure might impede the shifting of domain walls. On the other hand, a decrease of τ_{HT} and barrier energy E_{VFT} upon x-ray irradiation, reported by Sasaki *et al.* [206] , infer more domains with smaller size. This can be explained by a larger number of charged defects in the anion layer upon irradiation which act as pinning centers. The qualitatively similar but quantitatively slightly different behavior found in our samples #1 and #2 corroborates these observations.

However, we emphasize here again, that the HT peak is also observed in several other organic dimer Mott insulators [33, 134, 136] with triangular lattice (cf. Ch. 3.5, Fig. 3.16), showing that its emergence is independent of details in the crystal structure, for instance disorder in the anion layers. Another approach relates it to configuration disorder in the ethylene end groups (EEG) of the BEDT-TTF molecules (cf. Ch. 3.2.4). However, the freezing temperature of the EEGs, whether in a disorder or ordered configuration, in general does not coincide with the temperature range of the HT peak [111]. In regard to this it is worthwhile to mention, that a corresponding relaxor ferroelectric peak is also observed in the β'-Pd(dmit)$_2$ salts [136]. While Pd(dmit)$_2$ molecules to not exhibit EEGs, hydrogen atoms are found in their anion layers Me_4Pd, Me_4Sb and $EtMe_3Sb$, wherein Et denotes C_2H_5 and Me CH_3. This poses the question, whether the characteristics of the relaxor ferroelectric response, such as peak temperature and dispersive behavior, are connected to structural degrees of freedom related to hydrogen atoms, which could be clarified with dielectric spectroscopy measurements on deuterated samples. Finally we note, that the pressure evolution of $\tau_1(T)$ related to the HT peak ($T < T_{\mathrm{B}}$) is very different to the pressure evolution of the α-relaxation observed in glass forming polyalcohols [209], indicating that these phenomena originate from different physics.

Our results reveal a shift of the HT peak to lower temperatures upon increasing pressure. It is interesting to recall that also x-ray irradiation leads to a shift of the HT peak to lower temperatures [206]. High-energy irradiation causes crystal defects mainly in the anion layer and is supposed to increase the number of charge carriers. Similar to the rising pressure, the conductivity of the sample is enhanced compared to the pristine case. This

clearly indicates that the relaxor-ferroelectric HT peak is influenced by screening due to free charge carriers.

In Fig. 7.20(a), we plot T_{HT}, as determined from the peak position in $\varepsilon_1(T)$ at ambient pressure and $f = 100$ kHz, over the mass of one stoichiometric unit D_2X for various (BEDT-TTF)$_2X$ salts. The values for newly synthesized λ-ET-GaCl$_4$ and λ-STF-GaCl$_4$ compounds were provided by Yohei Saito and Olga Iakutkina from our institute while we used literature reports for β'-ICl$_2$ [134] and α-(BEDT-TTF)$_2$I$_3$[133]. Using this representation, we follow an approach applied for the (TMTTF)$_2X$ and (TMTSF)$_2X$ organic charge transfer salts in order to check a phononic origin of the HT peak. Interestingly, T_{HT} rises with increasing mass for the pristine compounds κ-CuCl, κ-CuCN and κ-AgCN whereas the opposite trend is observed upon BEDT-STF (STF) substitution. An decreases of T_{HT} upon replacing BEDT-TTF (ET) with BEDT-STF is also observed for λ-ET-GaCl$_4$ and λ-STF-GaCl$_4$. This clearly shows, that mass enhancement in the anion layer has a different effect on the HT peak than in the donor layer, which speaks against a purely phononic origin common to all compounds. To verify these findings also for the λ-type salts, investigations on compounds with different anions, such as λ-ET-GaBr$_4$ or λ-ET-FeCl$_4$, are required.

On the other hand, replacing the anions or substituting donor molecules has an dramatic impact on the effective Coulomb repulsion U/W (cf. Ch. 3.2.2). Furthermore, the pressure evolution of T_{HT} in κ-CuCN and κ-AgCN also clearly reveals, that the HT peak is sensitive to modifying U/W. Therefore, U/W is determined by fitting the optical conductivity spectra $\sigma_1(\omega)$ at 10 K which were obtained from infra-red spectroscopy measurements performed by Andrej Pustogow, Mathias Bories, Miriam Sanz-Alonso and Weiwu Li at our institute [19, 20]. In Fig. 7.21, we follow the common fitting procedure [92, 203, 210] using the sum of one Fano mode (green line), accounting for the ν_3 vibration mode, and four Lorentzians, capturing contributions of an in-gap contribution (blue line) of unknown origin, the lower Hubbard band (cyan line), the dimer band (magenta line) and an high energy contributions (yellow line) from the charge transfer band and inter-band transitions. The fitting was performed by Ece Uykur and the author. Doing so, we obtain sufficiently good fits in the frequency range from 1000 cm^{-1} to 5000 cm^{-1}, as exemplarily shown in Fig. 7.21(a) for κ-CuCN. The Coulomb repulsion U and the bandwidth W are determined from the peak position of the Hubbard Lorentzian (cyan lines) as the maxium position and the half width at half maxium, respectively, as illustrated in detail in Fig. 7.21 for κ-AgCN. The thus obtained values are summarized in Table 7.4. Interestingly, U/W increases going from κ-STF$_{0.04}$-CuCN to κ-STF$_{0.10}$-CuCN although the latter is closer to the IMT (cf. Fig. 6.5). We ascribe this to the enhanced in-gap contribution for $x = 0.10$ complicating

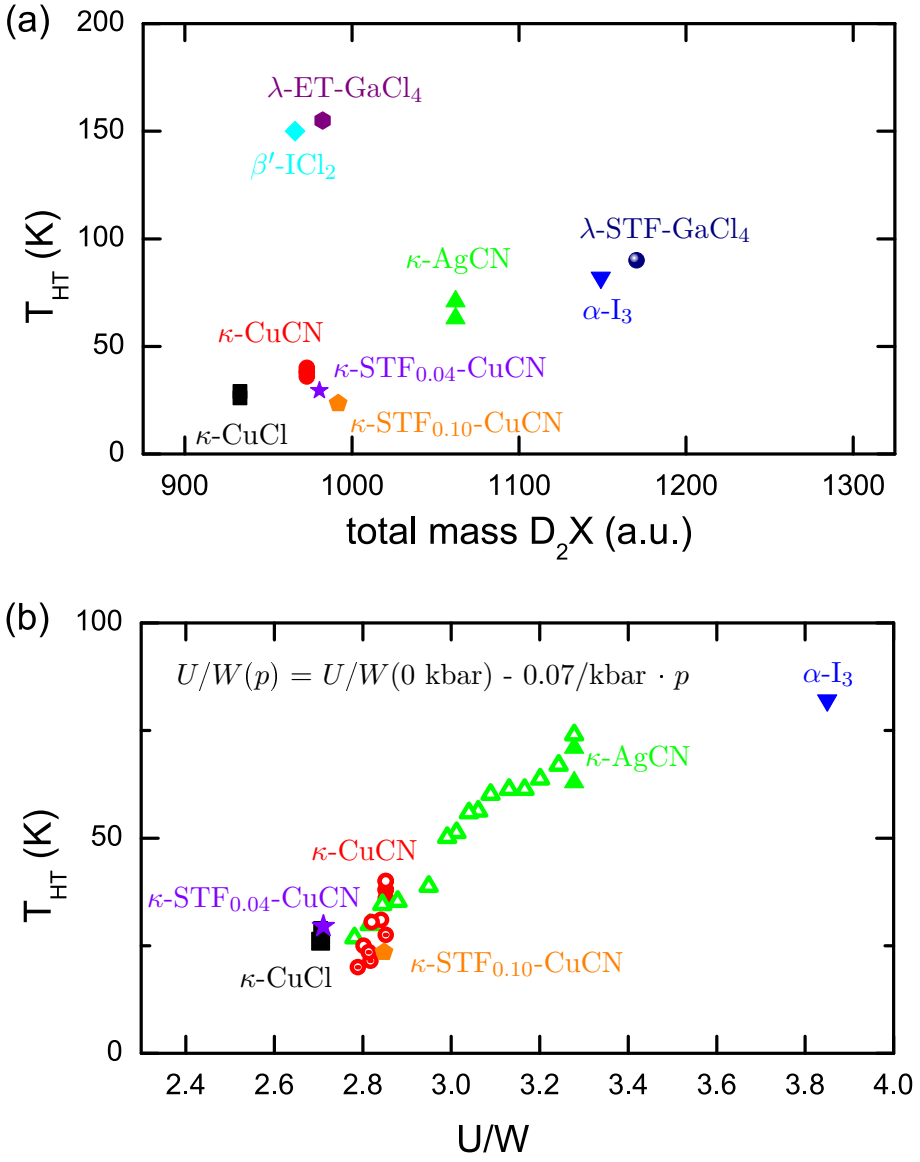

Figure 7.20: Position of the HT peak, T_{HT}, probed at $f = 100$ kHz plotted over (a) the total mass of one stoichiometric unit D_2X of two donor molecules D and one anion unit X, and (b) over the effective Coulomb repulsion U/W, as determined from optical conductivity (cf. Fig.7.21), for various organic charge transfer salts. (a) T_{HT} rises with increasing anion mass whereas enhancing the mass of the donors via BEDT-STF (STF) substitution results in a drop of T_{HT}, both for the λ-type and the κ-type salts. (b) Unfortunately, optical spectroscopy measurements necessary to determine U/W are only available for a limited number of salts. However, in this representation the ambient pressure values (full symbols) for the κ-(BEDT-TTF)$_2X$ salts fall onto one line. Our pressure-dependent results (open symbols) are included by assuming the pressure dependence of $U/W(p)$ as denoted in panel (b), which gives a nice interpolation of the ambient pressure results.

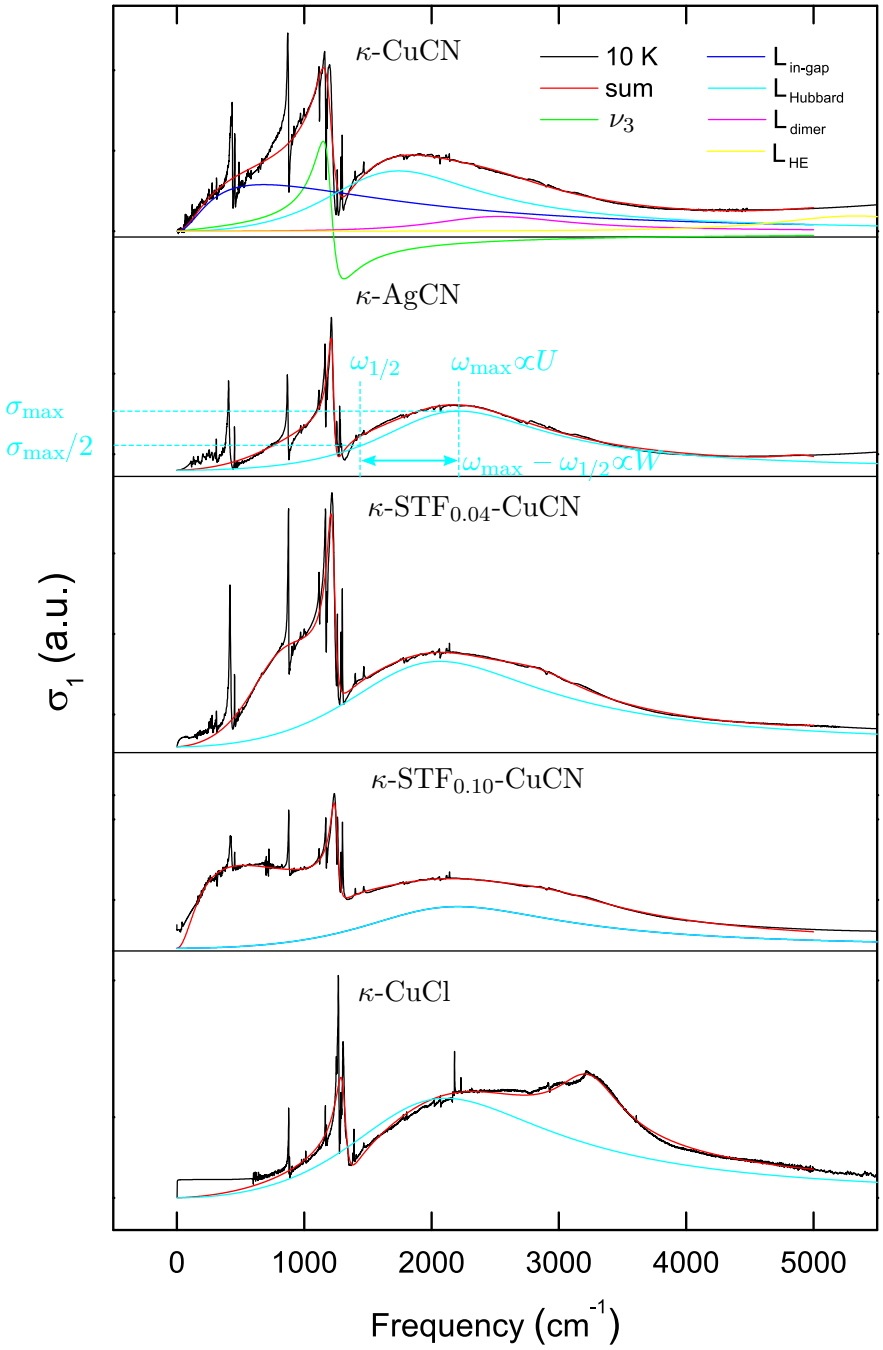

Figure 7.21: Optical conductivity of various κ-type organic charge transfer salts, measured at 10 K. The spectra are fitted with the sum (red lines) of a Fano mode (green line), accounting for the well known ν_3 vibration mode, and four Lorentzians capturing contributions of an in-gap contribution (blue line) of unknown origin, the lower Hubbard band (cyan line), the dimer band (magenta line) and an high energy contributions (yellow line) from the charge transfer band and inter-band transitions. The Coulomb repulsion U and the bandwidth W are determined from the peak position of the Hubbard Lorentzian (cyan lines) as the maxium position and the half width at half maxium, respectively, as exemplarily shown for κ-AgCN.

Table 7.4

	U [cm^{-1}]	W [cm^{-1}]	U/W
κ-CuCl	2109	780.5	2.70
κ-CuCN	1745	613	2.85
κ-STF$_{0.04}$-CuCN	2066	761.5	2.71
κ-STF$_{0.10}$-CuCN	2209	776.5	2.85
κ-AgCN	2217	676	3.28
α-I$_3$	1817	472.5	3.85

the fitting which was changed as little as possible for the different compounds to ensure consistency.

In Fig. 7.20(b), we plot T_{HT} over (U/W). Unfortunately, optical conductivity measurements under pressure are not available for all of our compounds, preventing a determination of the pressure-dependence of $U/W(p)$. Therefore, we make an educated guess of $U/W(p) = U/W(0\ \mathrm{kbar}) - 0.07/\mathrm{kbar} \cdot p$ for both, κ-CuCN and κ-AgCN, and include the thus obtained values $T_{\mathrm{HT}}(U/W)$. The open and open dotted red circles represent our pressure-dependent results for κ-CuCN sample #1 and #2, respectively, and the green open triangles for κ-AgCN. Under the restriction that our assumptions for $U/W(p)$ is correct, T_{HT} falls on one line for all compounds. However with this preliminary analysis, we can not distinguish whether the origin of the HT peak is directly connect to the presence of electronic correlations, or if this observation is due to the enhanced screening of some other yet unknown effect by charge carriers, which become more and more delocalized upon decreasing U/W. What speaks against screening is that one also expects a decrease of the HT peak amplitude upon intensifying pressure, which we do not observe, neither for κ-CuCN (cf. Figs. 6.2,6.4,7.3 and 7.4) nor for κ-AgCN (cf. Figs. 6.8,6.9 and 7.15). However, determining U/W for λ-ET-GaCl$_4$ and λ-STF-GaCl$_4$ in order to include them in Fig. 7.4 would provide a good test, whether the HT peak solely originates from electronic correlations or is also influenced by details of the crystal structure, such as the packing motif or disorder in the anion layers.

7.5.2 Low-temperature peak

Let us come to the LT peak, which was not observed in previous ambient pressure studies of κ-CuCN[31, 32, 34, 206]. Consistently in κ-CuCN and κ-AgCN, we see a growth of the LT peak with pressure and a shift in peak position (cf. Figs. 6.2,6.4,6.8 and 6.9). In κ-STF$_x$-CuCN, however, the LT peak remains weak up to $x = 0.10$ indicating that STF substitution has an additional effect besides tuning the bandwidth. At the moment, we can only speculate about this effect, but it might be related to the induced distortion of

the lattice upon increasing x, leading to some kind of Anderson localization suppressing the emergence of the LT peak upon approaching the IMT. However, the clearly distinct pressure evolution of the LT parameters compared to the HT peak in κ-CuCN and κ-AgCN indicates a different origin (Figs. 7.7 and 7.17).

In Ch. 8, we will provide conclusive evidence that the LT-peak emerges due to a small metallic filling fraction already on the insulating side of the phase diagram; as the phase transition is approach, it grows and eventually becomes the enhanced peak at the percolation threshold, as is documented in Figs. 6.2,6.4,6.8 and 6.9. As can be seen from Fig.7.9, in κ-CuCN the peak appears only for $T < T_{\mathrm{crit}}$ with a sharp contrast between the metallic inclusions and the insulating host. In κ-AgCN, the LT peak becomes apparent only for elevated pressures and at low temperatures (cf Fig. 7.15). This is in agreement with its assignment as an precursor feature of the phase coexistence while the IMT in this compound is located above our accessible pressure range. The detailed discussion of the polarization effects at the percolation threshold follows in the next chapter.

7.5.3 Anomaly

We identify the anomaly peak in κ-AgCN as the counterpart of the 6 K feature (cf. Ch.3.4) in κ-CuCN [31], which for the latter is below our experimental temperature range. Our assignment is corroborated by ^{13}C NMR measurements on κ-AgCN [30] observing the corresponding feature around 20 K, which fits our findings in $\varepsilon_1(T)$ quite well (cf. Fig.7.15).

The origin of this anomaly is still under debate while recent theoretical studies interpret it as the onset of a valence bond glass (VBG) at $T^* = 6$ K for κ-CuCN [128]. According to K. Riedl *et al.* [128], the pattern of frozen valence bonds in the VBG is influenced by disorder in the polar CN^- links, imposing a random electronic potential on the BEDT-TTF layers, and by charged defects due to chemical impurities. The latter is in accordance with thermal expansion measurements on κ-CuCN [211], which reveal a strong sample to sample variation of the anomaly and also suggest, that it is suppressed in crystals with a large amount of impurities. This could explain why the anomaly is also not observed in our ambient pressure measurements on κ-CuCN (cf Fig.7.1). Our pressure-dependent results on κ-AgCN indicate, that the anomaly becomes sharper upon applying pressure until it is masked by the growing LT peak (cf. Fig.6.8). However, it remains yet unclear in which way the formation of the VBG affects the dielectric properties of spin liquid compounds.

7.5.4 Mode 2

The high frequency mode 2 is observed in all investigated compounds and becomes apparent at low temperatures, when it sufficiently slowed down upon cooling to enter our experimental frequency window and when mode 1 is shifted towards lower frequencies. This and its small dielectric strength $\Delta\varepsilon_2$, which is usually one order of magnitude smaller then its counterpart of mode 1, is probably the reason why it was not reported before in literature [31–33]. Moreover, mode 2 clearly is subject to a pronounced sample-to-sample variation, as nicely demonstrated in our comparison of ambient pressure measurements on κ-CuCN in Fig. 7.1. It seems that mode 2 is less apparent for sample #2 which, compared to the other samples, exhibits a shift of the HT peak attributed to an increased number of defects in the anion layers. Interestingly, mode 2 is also less developed in κ-STF$_x$-CuCN.

For κ-CuCN at ambient and low pressures, $\tau_2(T)$ increases monotonically upon cooling whereas upon intensifying pressure a minimum is observed that shifts to lower temperatures and gets more pronounced (cf. Fig. 7.10). We note, that similar relaxation dynamics has been widely observed for confined systems as well as in the relaxor ferroelectric $KTa_{0.65}Nb_{0.35}O_3$ when doped with Cu by approximately 0.1% [212]. This non-monotonic behavior is most noticeable for sample #1 close to the IMT. Interestingly, $\tau_2(T)$ maintains its monotonicity upon cooling in κ-STF$_x$-CuCN, even for the compound with $x = 0.10$ which is already close to the IMT. In κ-AgCN, it is observed for intermediate pressures between 4.1 and 5.7 kbar, right where the anomaly peak in $\varepsilon_1(T)$ is most pronounced, and around 20 K, which also fits the position of the anomaly peak.

8

Phase coexistence at the Mott insulator-metal transition

In this chapter, we discuss the strong enhancement of ε_1 in vicinity of the Mott insulator-metal transition. We present a detailed analysis of our results obtained on κ-CuCN and κ-STF$_x$-CuCN, wherein the bandwidth tuned Mott transition is achieved by applying hydrostatic pressure and via chemical substitution, respectively. Our findings provide unambiguous evidence for a percolative phase coexistence around the first order Mott transition.

8.1 Phase coexistence in κ-(BEDT-TTF)$_2$Cu$_2$(CN)$_3$

The most surprising observation of our pressure-dependent measurements on κ-CuCN is the dramatic increase of the dielectric constant upon crossing the phase boundary (cf. Figs. 6.4 and 6.4). To articulate this more clearly, we plot $\varepsilon_1(T)$ and $\sigma_1(T)$ for sample #2 in Fig. 8.1 for various pressures as indicated. The enhancement in $\varepsilon_1(T)$ occurs simultaneously with the sudden increase of $\sigma_1(T)$, the latter marking the IMT (cf. Fig.6.1). Interestingly, the rise in ε_1 shifts up to 30 K upon increasing pressure up to 2.23 kbar, while at the same pressure and below 12 K a drop to negative values is observed, indicating the onset of purely metallic behavior. We emphasize that the latter is in accordance with the back-bended phase boundary and quantum Widom line (cf. Fig. 6.1).

To emphasize the pressure evolution of the dielectric properties, we plot in Fig. 8.2 the pressure dependence of $\varepsilon_1(p)$ and $\sigma_1(p)$ as obtained for a fixed frequency of $f = 100$ kHz for different temperatures as indicated. A pronounced peak in the permittivity appears around 1.8 kbar followed by a drop to negative values evidencing the onset of metallic conduction. Already at the lowest temperature, $T = 10$ K, the peak maximum occurs at a pressure slightly above p_{IMT}; it shifts to even higher pressure values as T rises. The peak in $\varepsilon_1(p)$ strongly diminishes upon heating and for $T >22$ K the anomaly is completely suppressed. Here a simple drop remains with a change in sign to large negative values of $\varepsilon_1(p = 43 \text{ kbar}) \approx -10^3$ to -10^4.

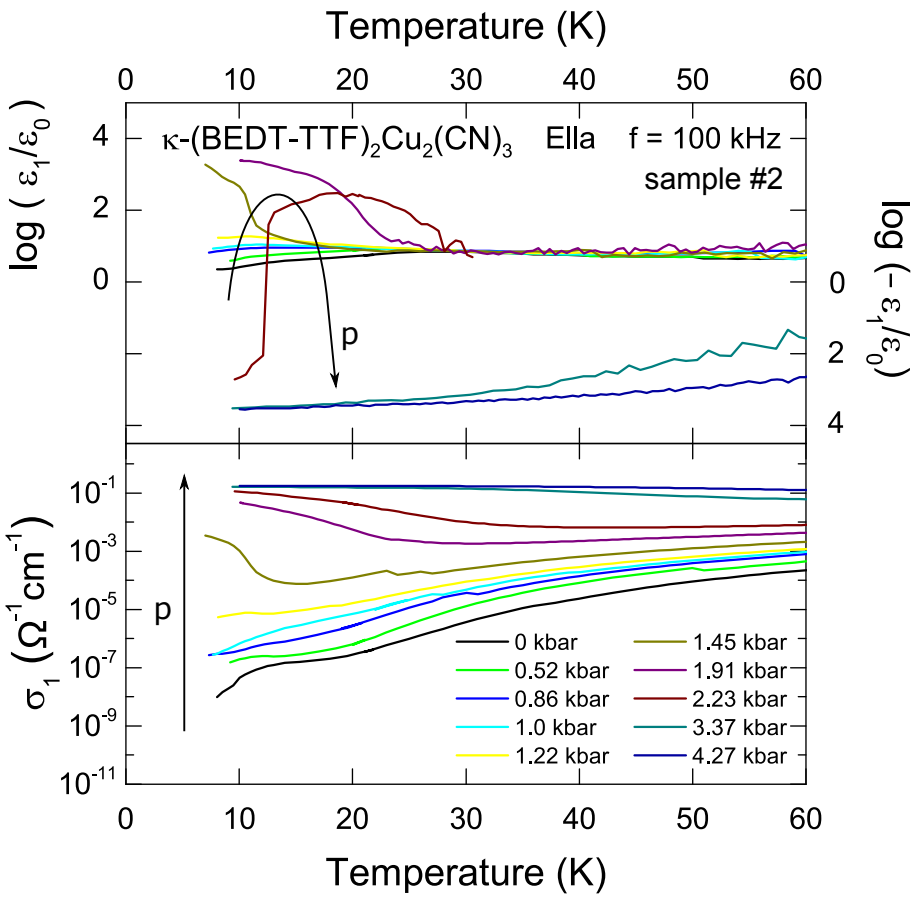

Figure 8.1: Temperature dependence of the dielectric properties of κ-(BEDT-TTF)$_2$-Cu$_2$(CN)$_3$ probed at $f = 100$ kHz and for various pressures as indicated. Upon intensifying pressure, a strong enhancement in $\varepsilon_1(T)$ is observed below 30 K, shifting to higher temperatures as pressure rises. Simultaneously, the conductivity increases by several orders of magnitude. For $p \leqslant 2.23$ kbar, a drop in $\varepsilon_1(T)$ indicates purely metallic behavior.

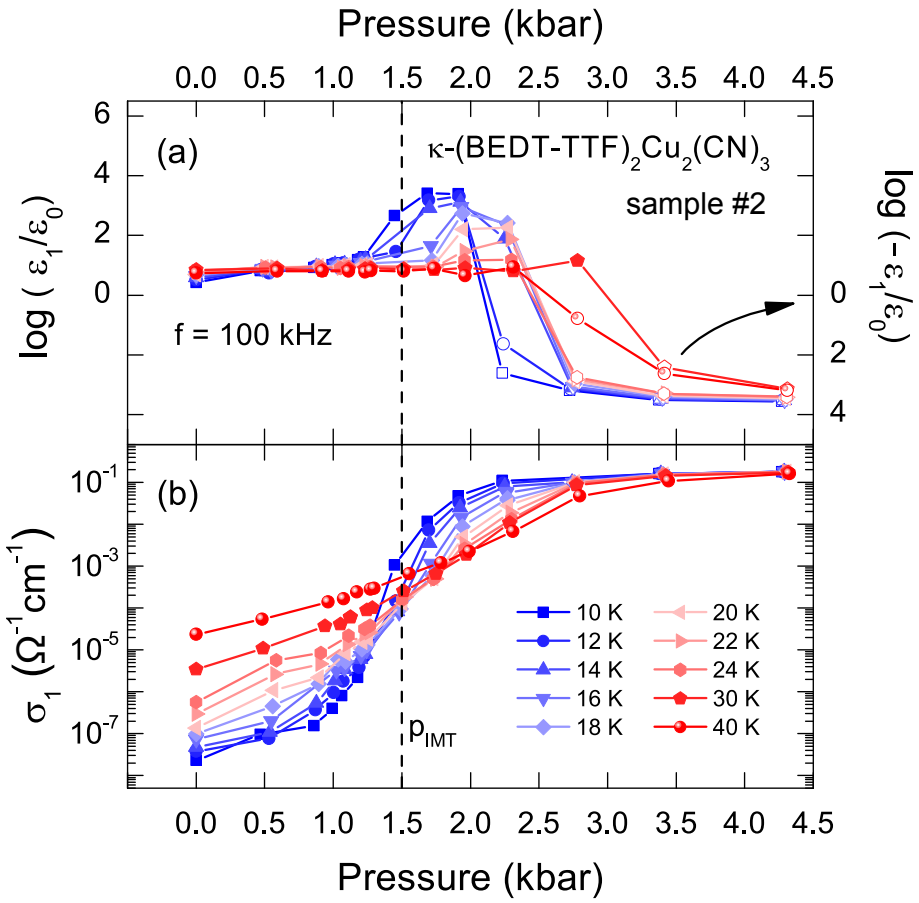

Figure 8.2: Pressure dependence of the dielectric properties of κ-(BEDT-TTF)$_2$-Cu$_2$(CN)$_3$ recorded for a fixed frequency f = 100 kHz at different temperatures as indicated. (a) The permittivity ε_1 forms a pronounced maximum followed by a rapid drop to negative values. (b) The conductivity σ_1 exhibits a step-like increase with an inflection point located right at the onset of the peak in ε_1. This percolating behavior stems from the nucleation and growth of metallic puddles spatially separated in an insulating matrix; the filling fraction increases by applying pressure. With rising temperature the features shift to higher pressures and diminish in amplitude or step size, respectively.

We explain this observation by percolation when the insulator-to-metal phase boundary is approached: metallic puddles develop and grow with increasing pressure. To our knowledge there is no systematic experimental study devoted to this coexistence region at the genuine Mott transition theoretically predicted by dynamical mean field theory [12, 25] and experimentally indicated in the sister compound κ-CuCl by a pronounced hysteresis in pressure-dependent dc-measurements in Ref. [69]. By applying pressure we can now vary and control the fraction of the metallic phase and thus investigate the percolating behavior in detail.

The enhancement of the dielectric constant is accompanied by a step-like feature in the conductivity, plotted in Fig. 8.2(b). With pressure, the metallic fraction grows; consequently $\sigma_1(p)$ rises continuously until a saturation is reached in the metallic phase. The inflection point p_{infl} at 10 K is located close to p_{IMT}. With increasing temperature, the step feature shifts to higher pressure values, smears out and becomes a more gradual increase consistent with the change from the first-order insulator-metal transition to the crossover region upon heating.

8.1.1 Effective medium approach

In a simple picture we could assume an increasing fraction of metallic puddles in an insulating matrix, as treated by Bruggeman's effective medium approximation (BEMA, cf. Ch. 4.4.2):

$$m\,\frac{\varepsilon_m - \varepsilon_{\mathrm{eff}}}{\varepsilon_{\mathrm{eff}} + L(\varepsilon_m - \varepsilon_{\mathrm{eff}})} + (1-m)\,\frac{\varepsilon_i - \varepsilon_{\mathrm{eff}}}{\varepsilon_{\mathrm{eff}} + L(\varepsilon_i - \varepsilon_{\mathrm{eff}})} = 0 \quad , \tag{8.1}$$

where m is the volume fraction of the metallic inclusions, L is their shape factor, ε_i and ε_{m} are the complex permittivities of the insulating and metallic phases, respectively, and $\varepsilon_{\mathrm{eff}}$ is the effective permittivity of the composite. Since the insulator-metal transition is observed at the same value for different crystal directions, we can restrict ourselves to the simplest case of spherical inclusions in three dimensions: $L = 1/3$.

With the help of Eq. (8.1), we can estimate the metallic filling fraction m for particular pressure values p, by assuming that for $p = 0$ the system is completely insulating and for $p = 4.3$ kbar the metallic state is fully established. The measured effective dielectric function, $\varepsilon_{\mathrm{eff}}(p, T, f)$ corresponds to a certain value of m.

In Fig. 8.3(a-d), the pressure dependences of $\varepsilon_1(p)$ and $\varepsilon_2(p)$ are plotted for different frequencies for $T = 10$ K and 30 K. The solid lines are obtained from simultaneously fitting $\varepsilon_1(p)$ and $\varepsilon_2(p)$ by the BEMA with a single value of m for all frequencies.

For $T = 10$ K, the BEMA model gives a reasonable fit for ε_1 (Fig. 8.3(a)) except for pressures from 1.5 kbar to 3 kbar, where the pronounced maximum is observed. The

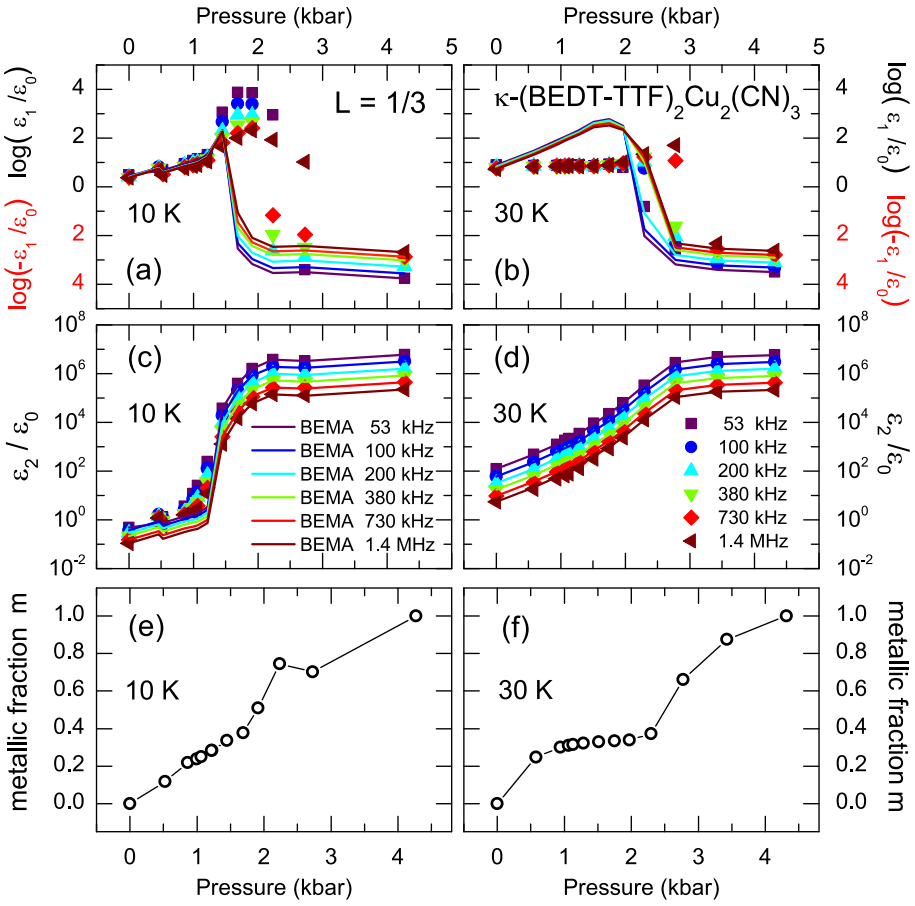

Figure 8.3: (a-d) Pressure dependence of the permittivity (full symbols) of κ-(BEDT--TTF)$_2$Cu$_2$(CN)$_3$ at 10 K and 30 K measured at different frequencies as indicated. The solid lines represent fits according to the Bruggeman's effective medium approximation (BEMA, Eq. (8.1)) with a fixed shape factor of $L = 1/3$ for spherical metallic inclusions and the metallic filling fraction m as free parameter. (e,f) The metallic filling fraction m in dependence of pressure as determined from the fits in panels (a-d).

shortcoming of the BEMA in ε_1 close to the percolation threshold is inherent to the model [176, 181], since it considers polarization of the inclusions with a simple dipole approximation, which does not hold anymore when the inclusions get closer to each other, i.e. with increasing filling fraction respectively pressure. Moreover, inclusions coalesce above the percolation threshold such that their shape is not spherical anymore. ε_2 (Fig. 8.3(c)) relates to the conductivity via $\varepsilon_2 = \sigma_1/\omega$ which is not subject to these limitations and hence is fitted well for all pressures. This allows us to determine the metallic filling fraction m in dependence of pressure, which is plotted in Fig. 8.3(e).

At higher temperatures $T > T_{\mathrm{crit}}$ the sharp first-order transition is converted to a continuous transition in the crossover region. Here, the BEMA model reproduces the gradual increase in ε_2 (Fig. 8.3(d)) and its saturation at high pressures while it fails by overestimating $\varepsilon_1(p)$ (Fig. 8.3(b)). The latter is not surprising due to the absence of well defined inclusions which are prerequisites for applying the effective-medium model as in Eq. (8.1). Consequently, the resulting filling fraction exhibits a broad plateau between 1 and 2 kbar with values close to the percolation threshold $m_c = 0.33$ defined by $L = 1/3$. This observation is another indication for the failure of the BEMA model for temperatures above the critical endpoint T_{crit}.

To find out, up to which temperature the BEMA model gives reasonable results, we fitted our data for $T < 30$ K and plot the resulting metallic filling fraction m in the pressure-temperature false-color plot in Fig. 8.4 together with the first-order phase transition (solid black line), the critical endpoint (T_{crit}, black circle). For $T < 16$ K, the filling fraction is $m = 0.33$ (dotted line) right at the first-order transition consistent with the BEMA model, while for $T > 16$ K, the area around $m = 0.33$ significantly broadens and does not coincide with the crossover. This gives us a critical point at $(1.8\ \mathrm{kbar}, 16\ \mathrm{K})$, which fits the findings of previous dc-measurements [17, 39].

8.1.2 Divergent dielectric constant

The dielectric properties of percolating systems have been subject of numerous investigations for half a century [176, 177]. As pointed out by Efros and Shklovskii [178], the static dielectric constant of a percolating system depends on the filling fraction m of the metallic phase and diverges at the percolation threshold m_c:

$$\varepsilon_1(\omega = 0, m) \propto (m_c - m)^{-q} \quad , \tag{8.2}$$

where the critical exponent q depends on the dimension of the system; in 3D we expect q ranging from 0.8 to 1 [174, 178–180, 213], while $q = 1.3$ is expected for 2D [178]. The

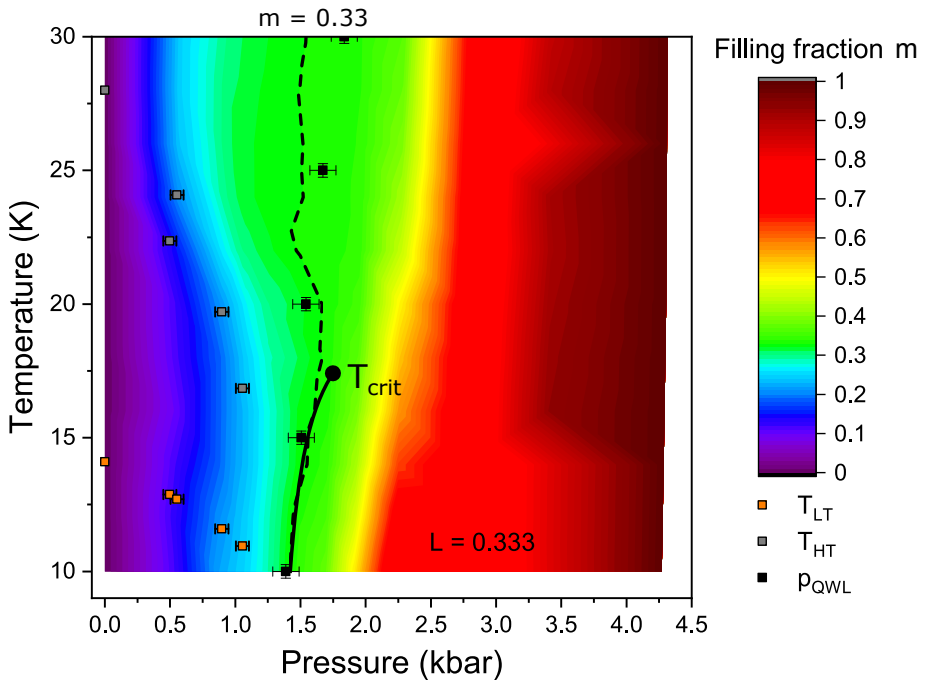

Figure 8.4: Metallic filling fraction m as obtained from Eq. (8.1) in a color pressure-temperature plot. p_{QWL} is the point of inflection in $\rho_1(p)$ (cf. Ch. 6.1) and indicates the first-order insulator-metal transition (black solid line) with the estimated position of the critical endpoint T_{crit} (black circle). Above T_{crit}, p_{QWL} marks the quantum Widom line. T_{LT} and T_{HT} are the positions of the LT and HT peak from Fig. 7.9. For temperatures below T_{crit}, the metallic fraction increases to $m = 0.33$ (dotted line) upon approaching the first-order transition from the insulating side, as expected for $L = 1/3$, and rises to $m = 1$ on the metallic side. At temperatures above T_{crit}, the sharp first-order transition becomes a gradual crossover such that the formation of metallic puddles is suppressed. Hence, applying Eq. (8.1) is not well defined anymore and such that the $m = 0.33$ line deviates from p_{QWL}.

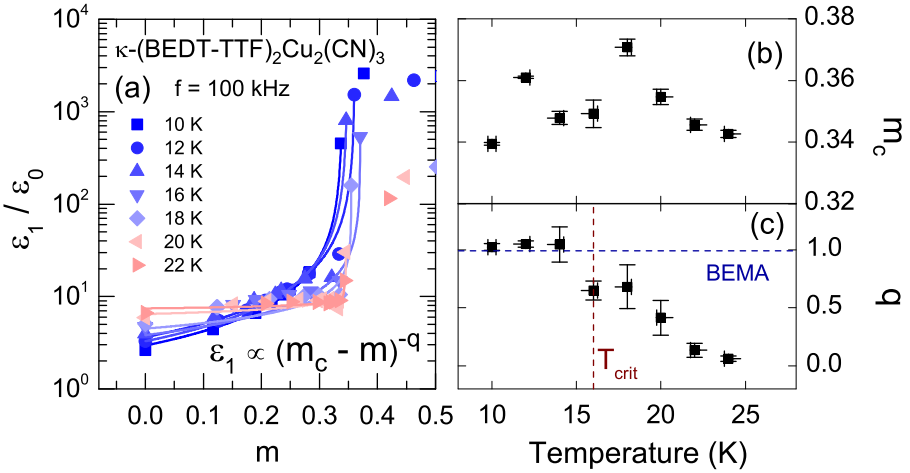

Figure 8.5: (a) Dielectric constant ε_1 of κ-(BEDT-TTF)$_2$Cu$_2$(CN)$_3$ measured at f = 100 kHz for several temperatures in dependence of the metallic filling fraction m. The solid lines represent fits according to Eg. (8.2). (b) Temperature dependence of the percolation threshold pressure m_c, as obtained from fits of $\varepsilon_1(p)$ according to Eg. (8.2). (c) Temperature dependence of the exponents q. We attribute the drop of q above T = 20 K to the change from the first-order insulator-metal transition to a crossover at higher temperatures. For clarity reasons, we also include T_{crit} (dashed red line) and the predictions for q of the BEMA model (dashed blue line).

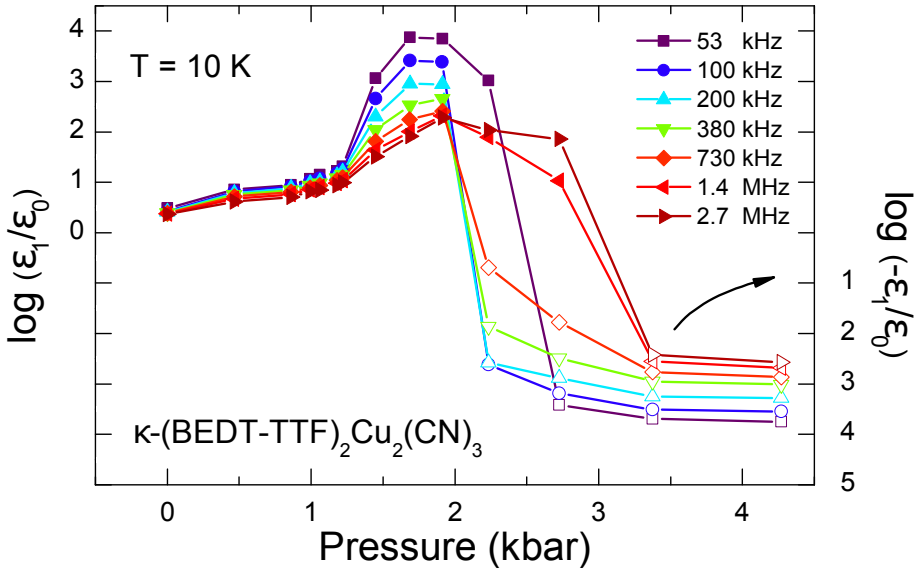

Figure 8.6: The pressure dependence of $\varepsilon_1(p)$ recorded at the lowest temperature T = 10 K by using different frequencies from 53 kHz to 2.7 MHz. The amplitude of the percolation peak diminishes with increasing frequency. The negative values of ε_1 above $p = 2.5$ kbar (open symbols) mark the onset of the metallic regime; note that for these data points the value -log($-\varepsilon_1/\varepsilon_0$) was taken.

BEMA model predicts $q = 1$ independent of the dimensionality of the percolating system [174].

In Fig. 8.5(a) the dependence of ε_1 on the metallic filling fraction m is plotted for the 100 kHz data together with the fit according to Eq. (8.2) shown by the solid lines. The temperature dependence of the percolation threshold m_c and the exponent q is plotted in Fig. 8.5(b) and (c), respectively. From our pressure-dependent dielectric measurements we find $q \approx 1$ up to $T = 16$ K as expected. For higher temperatures, q decreases to 0; this behavior is consistent with the suppression of the percolation for $T > T_{\mathrm{crit}}$ and agrees with the findings in Fig. 8.4.

8.1.3 Resonance effects

In a next step, we consider the frequency dependence of the percolation peak which is shown in Fig. 8.6 by plotting $\varepsilon_1(p)$ at $T = 10$ K and for various frequencies as indicated. The percolating behavior with a rise of $\varepsilon_1(p)$ upon crossing the IMT at $p_{\mathrm{IMT},\#2} = 1.45$ kbar and a drop to negative values at $p = 4.23$ kbar is observed for all frequencies. However for 2.23kbar $\leqslant p \leqslant$ 3.7 kbar, a change in the sign of ε_1 from positive to negative values occurs upon going from low to high frequencies. This peculiar frequency-dependent behavior is not expected within the framework of standard percolation theory.

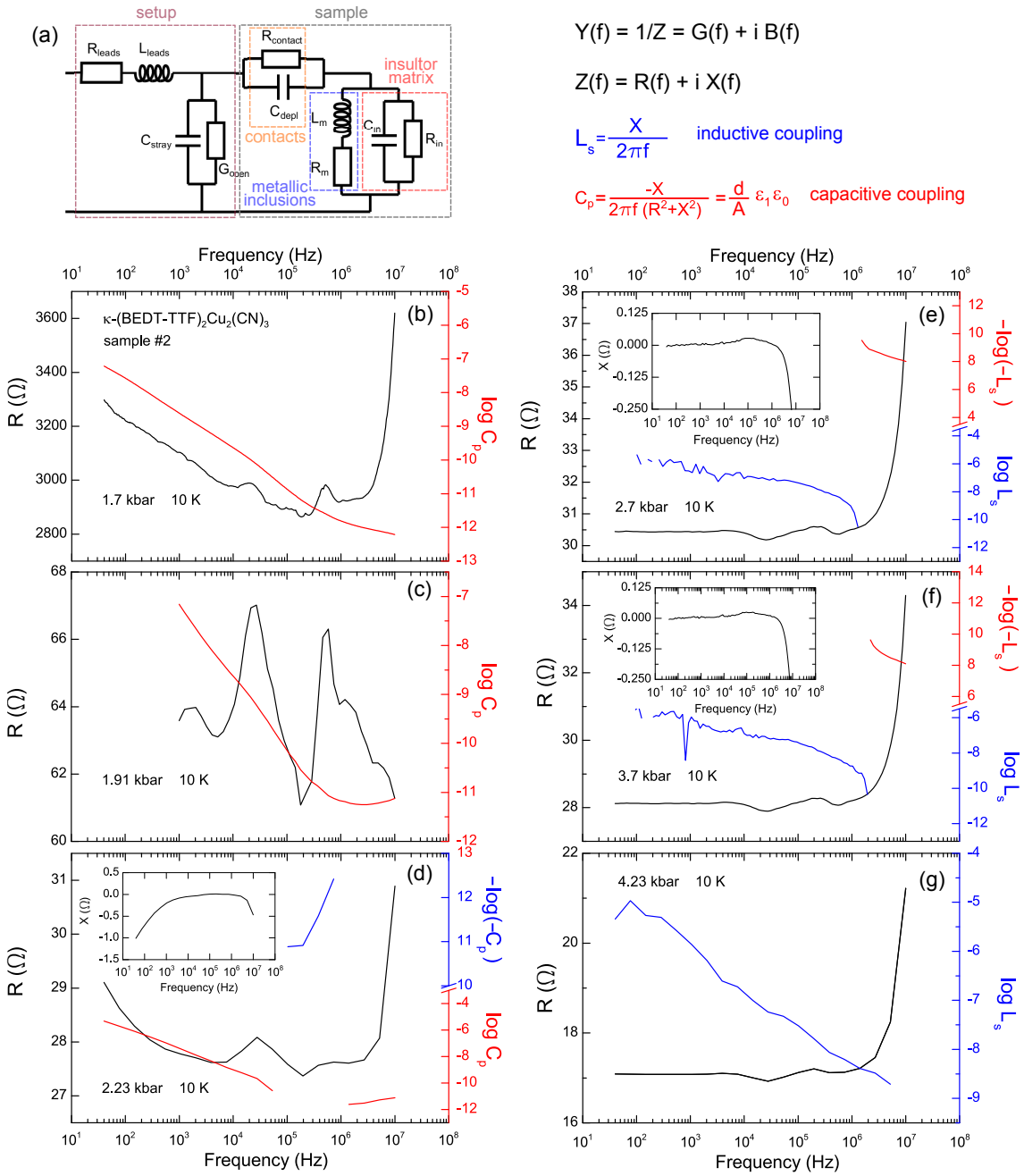

Figure 8.7: (a) Scheme of a simple equivalent circuit modeling the measurement system including contributions from the sample holder and test leads, the contacts and from the sample, which here is model with a typical insulating response in parallel to a tyical metallic response to account for the phase coexistence region. (b-g) Frequency dependence of the resistance $R(f)$ and the overall parallel capacitance C_p or the series inductance L_s of the system. For $p = 1.7$ kbar and 1.91 kbar (b,c), the system shows capacitive behavior as expected for the phase coexistence region. Although slight oscillations are present in $R(f)$, the resonant condition is obviously not fulfilled here. From 2.23 kbar to 3.7 kbar (d-f), oscillations in $R(f)$ and a change in sign in C_p are observed, the latter indicating the presence of resonance effects in the measurement circuit. At $p = 4.23$ kbar, the system is deep in the metallic region and, as expected, shows inductive response.

In dielectric spectroscopy, resonances in the measurement circuit may give rise to spurious features which erroneously might be attributed to the sample. In general, the measurement circuit includes the sample, the contacts, the sample holder as well as the test leads and can be modeled by a RLC circuit, which may become rather complex. For instance a simple scheme of the measurement circuit accounting for the major contributions is depicted in Fig. 8.7(a). For any kind of RLC circuit, however, the signature of a self-resonance is a zero crossing in the frequency dependence of the imaginary part of both the measured impedance $Z(f) = R(f)+iX(f)$ and the admittance $Y(f) = 1/Z = G(f)+iB(f)$. In order to check for the presence of resonance effects in our measurements, we plot in Fig.8.7 the frequency-dependence of the resistance $R(f)$ and the parallel capacitance C_p at $T = 10$ K and for various pressures as indicated, since the latter is more intuitive for an insulator and the capacitive coupling of spatially separated metallic puddles in the phase coexistence region, respectively. For $p = 1.7$ kbar and 1.91 kbar, $C_\mathrm{p}(f)$ monotonically deceases with rising frequency as expected fo a percolating system while small oscillations are observed in $R(f)$. At $p = 2.23$ kbar, $C_\mathrm{p}(f)$ flips to negative values at $f = 10^5$ Hz, indicating inductive behavior, and changes back again to positive values at $f = 10^6$ Hz. Since this change of sign occurs several times, we mark positive values of C_p, indicating a capacitive response, with red color and negative values, indicating an inductive response, with blue color. Concomitant to the changes of sign in $C_\mathrm{p}(f)$, we observe small oscillations of $R(f)$ as well. Similar behavior is observed for $p = 2.7$ kbar and 3.7 kbar whereas here, the overall behavior is inductive, such that it is more convenient to plot the inductance $L_\mathrm{s}(f)$, which flips to capacitive behavior at highest frequencies. At $p = 4.23$ kbar, a monotonic decrease of $L_\mathrm{s}(f)$ with rising frequency is observed, indicating purely inductive behavior without any interfering resonance effects.

The results plotted in Fig. 8.7 show, that spurious resonance effects are present in the pressure range from 2.23 kbar to 3.7 kbar and interfere with the percolating behavior, thus giving rise to a peculiar frequency dependence of the dielectric properties. In this region, the metallic fraction prevails upon to insulating and the capacitive behavior is expected to be weak, such that the resonance contribution to the measured response is not negligible anymore. However, for 0 kbar $\leqslant p \leqslant$ 1.7 kbar and 3.27 kabr $\leqslant p \leqslant$ 4.7 kbar, resonance effects are insignificant for frequencies below 1 MHz. We note, that the determination of the metallic filling fraction in Fig. 8.3 does not suffer from these resonances. First, because in the corresponding pressure range the BEMA model is not able to capture $\varepsilon_1(p)$ anyway and m is determined by fitting $\varepsilon_2(p)$. Second, because the fits of $\varepsilon_1(p)$ and $\varepsilon_2(p)$ are averaged in frequency over a many orders of magnitude.

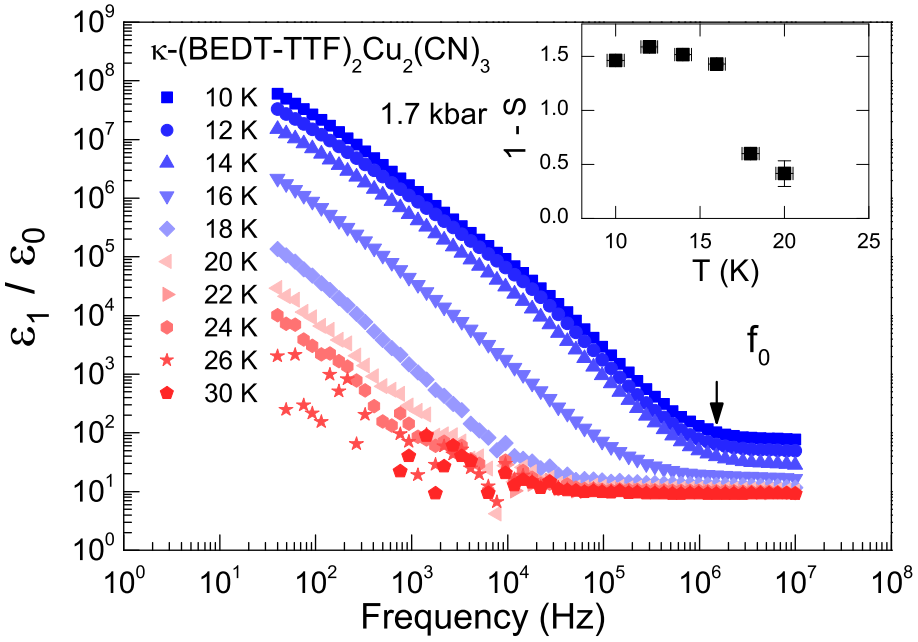

Figure 8.8: Double-logarithmic plot of $\varepsilon_1(f)$ at 1.7 kbar for various temperatures T, as indicated. For $T \leqslant 16$ K a power-law behavior is observed, which saturates above $f = 2$ MHz. The percolating behavior of κ-(BEDT-TTF)$_2$Cu$_2$(CN)$_3$ is suppressed for $T > 16$ K where the first-order transition becomes a gradual crossover. The inset shows the temperature dependence of the exponent $1-S$ obtained from fits by Eq. (8.3).

8.1.4 Frequency dependence at the percolation threshold

The results obtained at 1.7 kbar are not influenced by resonances. From the data recorded at various temperatures, the values of $\varepsilon_1(p = 1.7\ \text{kbar})(f)$ are plotted in Fig. 8.8 as a function of frequency in a double logarithmic fashion. For $T \leqslant 16$ K, we observe a strong reduction of $\varepsilon_1(f)$ with increasing frequency and a saturation for $f >2$ MHz. Surprisingly, rather high values remain for temperatures above $T_{\text{crit}} = 16$ K which could be attributed to the onset of phase segregation upon approaching the coexistence region from high temperatures. Another possible scenario would be the restrengthening of the contact contribution at the IMT, which is masked by the dominating percolation contribution below T_{crit} and becomes apparent upon leaving the coexistence region. However, the behavior in $\varepsilon_1(f)$ can not be modeled with the simple equivalent circuit shown in Fig. 8.9, wherein C_{depl} and C_{sample} are considered as frequency-independent. The application of a more complex model goes hand in hand with an increased number of unknown variables, which can not be determined with the available data set. At $T = 30$ K, the decline with rising frequency vanishes and merges into a frequency-independent response.

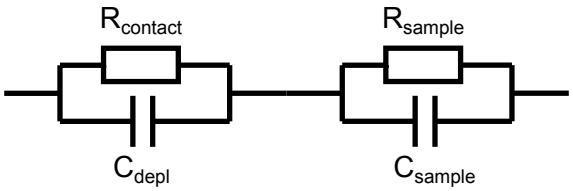

Figure 8.9: Most simple model considering contact contribution to the measured impedance.

Standard percolation theory [178] predicts a power law decrease of the permittivity upon rising frequency

$$\varepsilon_1(f, m_c) \approx \left(\frac{1}{f}\right)^{1-S} \quad , \tag{8.3}$$

with the critical exponent $S = 0.62$ for 3D and $S = 0.5$ for 2D.

For each temperature we have fitted the data in Fig. 8.8 according to Eq. (8.3), and plot the obtained parameter $1 - S$ in the inset. Obviously the observed frequency dependence deviates from standard percolation theory [178]. Sarychev and Brouers [37] extended these considerations by taking into account tunneling between finite metallic clusters in order to explain the low-frequency response of percolating systems [36, 214–216]. The strong rise of $\varepsilon_1(f)$ with decreasing frequencies we observe in our data resembles similar frequency dependence found in percolating granular metal films sputtered onto a SiO_2 substrate [36]. The kink in $\varepsilon_1(f)$ marks the cut-off frequency f_0 of phonon assisted tunneling processes and is estimated [36, 37] to

$$f_0 = f_{\mathrm{ph}} \exp[-2d_{\mathrm{t}}/a_{\mathrm{loc}}] \quad , \tag{8.4}$$

with the phonon frequency f_{ph}, the localization length a_{loc} and the upper limit for the tunneling distance d_{t}. In κ-(BEDT-TTF)$_2$Cu$_2$(CN)$_3$ the charge carriers are localized on dimers in a distance $a_{\mathrm{loc}} \approx 3.47$ Å and $f_{\mathrm{ph}} \approx 1$ THz is the frequency range of low-lying phonons that incorporate BEDT-TTF dimers and anion layers [60]. With $f_0 \approx 1.5$ MHz extracted from our data, we obtain $d_{\mathrm{t}} \approx 23$ Å at $T = 10$ K as an upper limit for the tunneling distance, which is only slightly larger then the spacing between BEDT-TTF layers with $a = 16.072$ Å. However, it remains unclear on which length scale metallic regions are clearly distinguishable from insulating regions, or in other words, how sharp the phase segregation occurs in spatial dimension. That this could happen on a length scale comparable to the lattice constants is hard to believe and challenges the tunneling scenario as a possible origin of the unexpected strong decrease in $\varepsilon_1(f)$ with rising frequency.

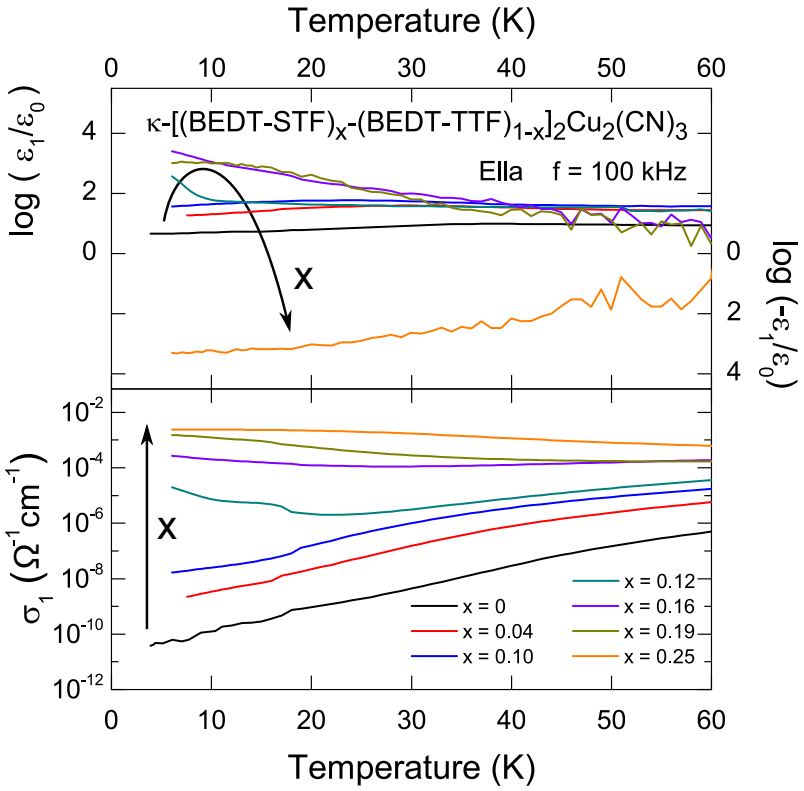

Figure 8.10: Temperature dependence of the dielectric properties of κ-[(BEDT-STF)$_x$-(BEDT-TTF)$_{1-x}$]$_2$Cu$_2$(CN)$_3$ probed at $f = 100$ kHz and for various substitution levels x as indicated. Upon increasing x, a strong enhancement in $\varepsilon_1(T)$ is observed below 30 K, shifting to higher temperatures as x rises. Simultaneously, the conductivity increases by several orders of magnitude. At $x = 0.25$ kbar, a drop in $\varepsilon_1(T)$ to negative values indicates purely metallic behavior.

8.2 Phase coexistence in κ-[(BEDT-STF)$_x$-(BEDT-TTF)$_{1-x}$]$_2$Cu$_2$(CN)$_3$

In Fig. 8.10, we plot $\varepsilon_1(T)$ and $\sigma_1(T)$ of κ-STF$_x$-CuCN for various substitution levels x as indicated. Rising the substitution up to $x = 0.19$ results in a strong enhancement of $\varepsilon_1(T)$ up to 10^3, whereas for $x = 0.25$ a drop to large negative values of the order of -10^3 is observed. Concurrently, $\sigma_1(T)$ increases by several orders of magnitude while the development of a minimum at $T = 22$ K for $x \leqslant 0.12$ indicates the crossing of the phase boundary into the metallic regime, as we already described in detail in chapter 6.2.

To highlight the dependence of the dielectric properties of κ-STF$_x$-CuCN on the substitution, we plot $\varepsilon_1(x)$ and $\sigma_1(x)$ in Fig. 8.10 for $f = 100$ kHz and at various fixed

temperatures as indicated. We observe a similar evolution of ε_1 and σ_1 upon increasing x as observed for intensifying pressure. In particular, the strong upturn in $\varepsilon_1(x)$ sets in right after the Mott IMT is crossed at $x_{\mathrm{IMT}} = 0.12$ (cf. Fig. 6.5) , followed by a drop to negative values for $x = 0.25$ evidencing the onset of metallic conduction. The peak in $\varepsilon_1(x)$ declines upon heating and is completely suppressed for $T >$30 K. Here a simple drop remains with a change in sign to large negative values of $\varepsilon_1(x = 0.25) \approx -10^3$. The enhancement of the permittivity occurs after the step-like increase in $\sigma_1(x)$ at the IMT. With rising x, $\sigma_1(x)$ increases continuously until a saturation is reached for $x = 0.25$. Upon heating, the step feature smears out and becomes a more gradual increase consistent with the change from the first-order IMT to the crossover region above T_{crit}.

Most importantly, the observed substitution dependence of the dielectric properties agrees with the expected signature of a phase coexistence region enveloping the first-order IMT and resembles the results from our pressure-dependent measurements (cf. Ch. 8.1). When the IMT phase boundary is approached with increasing x, metallic puddles nucleate and grow in number and size upon further advancing into the metallic phase. In contrast to the pressure-dependent analysis, however, the substitution-dependence is obtained by comparing various different samples, which besides the intentionally altered substitution x, are subject to sample-to-sample variations as discussed in Ch. 7.1. The latter is found most pronounced in the insulating region and explains the increased value of $\varepsilon_1(x)$ for $x = 0.04$ compared to the expected percolation behavior. Moreover, we also suffer from a limited number of available substitution levels x impeding a more detailed analysis of our results with percolation theory in analogy to the procedure for the pressure-dependent results on κ-CuCN.

8.2.1 Resonance effects

In Fig. 8.12, we plot $\varepsilon_1(x)$ of κ-STF$_x$-CuCN at $T = 10$ K and for various frequencies as indicated. The enhancement of $\varepsilon_1(x)$ upon approaching the IMT with increasing x and the subsequent drop to negative values is observed for all frequencies. The percolation peak around $x = 0.16$ exhibits a pronounced frequency dependence while at $x = 0.19$ a change of sign occurs in ε_1 for frequencies exceeding 100 kHz which is not expected for the percolation scenario and indicates the presence of resonance effects in the measurement circuit.

In order to determine to what extent and in which frequency range the resonances contribute to the measured impedance, we plot in Fig. 8.13 $R(f)$ and $C_{\mathrm{p}}(f)$ at $T = 10$ and for various substitution levels x as indicated. For $x = 0.12$ and 0.16, slight oscillations of $R(f)$ indicate the onset of resonance effects which, however, are not apparent in $C_{\mathrm{p}}(f)$,

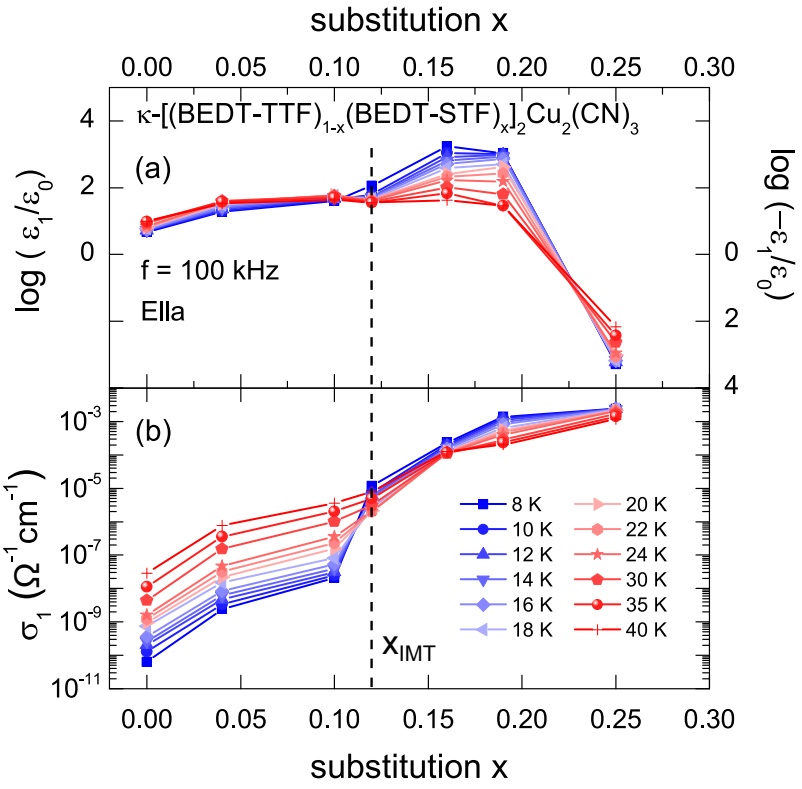

Figure 8.11: Dielectric properties of κ-[(BEDT-STF)$_x$-(BEDT-TTF)$_{1-x}$]$_2$Cu$_2$(CN)$_3$ in dependence of the substitution level x, recorded for a fixed frequency f = 100 kHz at different temperatures as indicated. (a) The permittivity $\varepsilon_1(x)$ forms a pronounced maximum followed by a rapid drop to negative values. (b) The conductivity $\sigma_1(x)$ exhibits a step-like increase at $x_{\mathrm{IMT}} = 0.12$, indicating the Mott IMT. The observed behavior matches the signature of a percolating system. At the IMT, the nucleation and growth of metallic puddles sets in which are spatially separated in an insulating matrix. Upon increasing x, the metallic filling fraction grows until the metallic state is completely established at $x = 0.25$. With rising temperature the features diminish in amplitude or step size, respectively, consistent with the change from the first-order IMT to the crossover region at elevated temperatures.

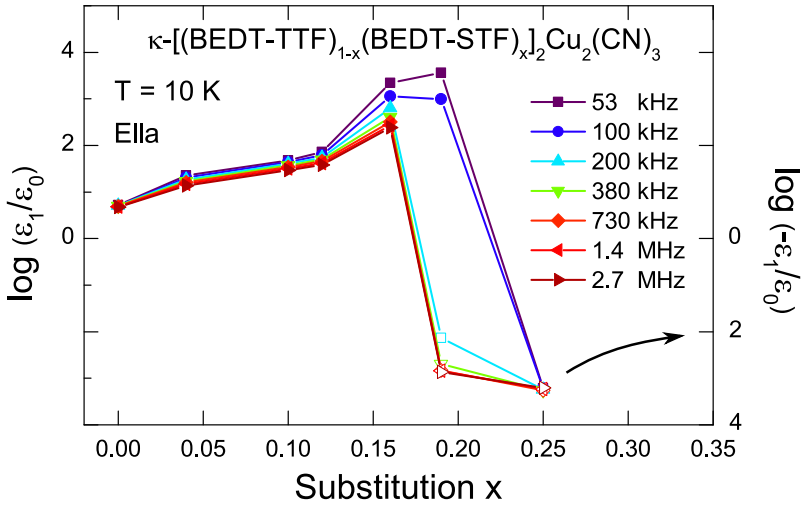

Figure 8.12: Substitution dependence of $\varepsilon_1(x)$ for κ-STF$_x$-CuCN recorded at $T = 10$ K by using different frequencies from 53 kHz to 2.7 MHz. The amplitude of the percolation peak diminishes with increasing frequency. The negative values of ε_1 at $x = 0.25$ (open symbols) mark the onset of the metallic regime; note that for these data points the value -log($-\varepsilon_1/\varepsilon_0$) was taken.

since here the monotonic decrease is in agreement with the expectations. It seems that the high resistance and the strong capacitive coupling between the metallic inclusions are prevailing upon the resonance contribution to $C_\mathrm{p}(f)$. At $x = 0.19$ and $f = 2 \cdot 10^5$ Hz, a change in sign to negative values is observed in $C_\mathrm{p}(f)$ evidencing a dominating resonance effect, which shifts to $f = 4 \cdot 10^4$ Hz upon increasing the substitution to $x = 0.25$. It seems that the resistance has to be low to fulfill the resonance condition and for the available substitution levels the systems remains subject to resonance effects. In order to check whether purely inductive behavior is achieved in κ-STF$_x$-CuCN samples with $x > 0.25$ have to be investigated.

8.2.2 Frequency dependence at the percolation threshold

The results shown in Fig. 8.13 confirm the absence of noticeable resonance effects for $0.12 \leqslant x \leqslant 0.16$ and allow for further analysis of the frequency-dependence. Fig. 8.14 shows double logarithmic plots of $\varepsilon_1(f)$ at $x = 0.12$ and $x = 0.16$ for various temperatures as indicated.

For $x = 0.12$, $\varepsilon_1(f)$ strongly diminishes with increasing frequency following a power law behavior with a saturation to a constant value for frequencies exceeding f_0. Upon heating, f_0 shifts to lower frequencies and $\varepsilon_1(f)$ is reduced by several orders of magnitude. Interestingly, for the latter rather high values remain for $T \geqslant 18$ K which is clearly above

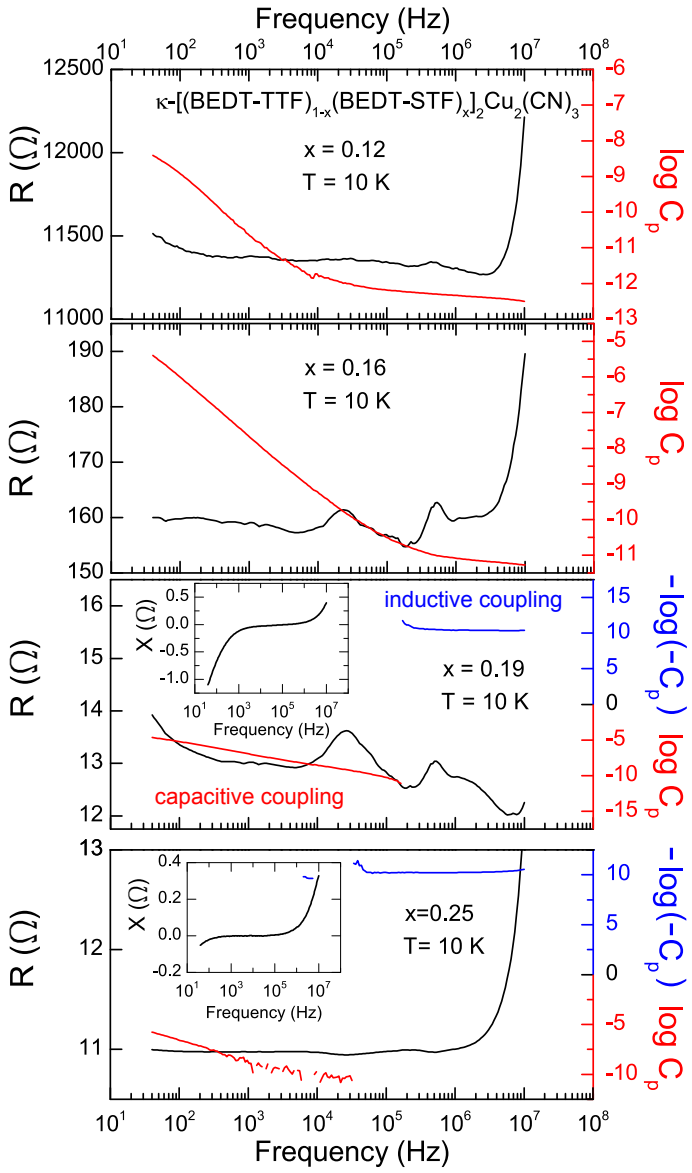

Figure 8.13: The frequency dependence of of the resistance R and the parallel capacitance C_p at $T = 10$ K and for various substitution levels as indicated.

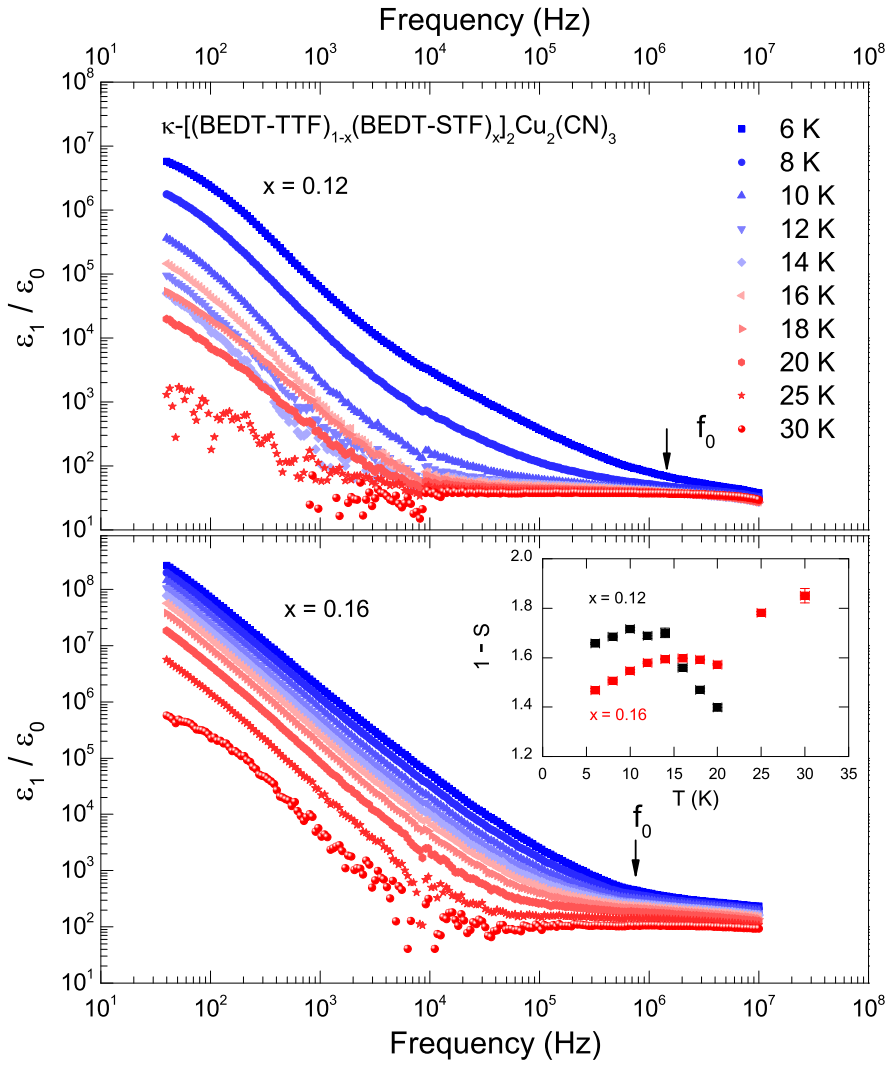

Figure 8.14: Double-logarithmic plot of $\varepsilon_1(f)$ for $x = 0.12$ and $x = 0.16$ for various temperatures T as indicated. The observed power-law behavior saturates at f_0, which clearly shifts to higher frequencies upon heating. The inset shows the temperature dependence of the exponent $1-S$ obtained from fits by Eq. (8.3).

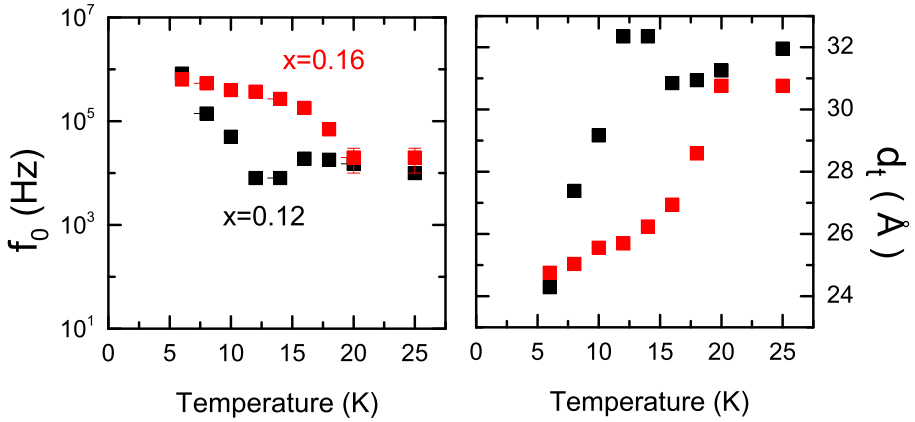

Figure 8.15: Temperature-dependence of the saturation frequency f_0 and the upper limit for the tunneling distance d_t, determined according to Eq. (8.4). For both substitutions, f_0 shifts to lower frequencies upon heating. Concomitantly, d_t increases from 24 Å to above 30 Å which is approximately the same length scale as determined for the pristine compound under pressure. The obtained values for d_t are rather small compared to the hopping distance usually obtained in semiconductors, up to 100 nm, and is only slightly larger than the lattice constant $a = 16.072$ Å along the measurement direction.

the first-order transition and hence not expected in the phase coexistence picture. For $f < 10^3$ Hz, ε_1 slightly increases upon rising temperature.

A similar shift of f_0 and a reduction of $\varepsilon_1(f)$ upon increasing T is observed for $x = 0.16$ as well while $\varepsilon_1(f)$ remains at even higher values for temperatures above $T_\mathrm{crit} = 16$ K. A possible origin of this behavior could be the additional contact contribution to the measured capacitance which becomes apparent upon leaving the coexistence region (cf. Ch. 5.3).

To compare the observed behavior with simple percolation theory, we fit $\varepsilon_1(f)$ with Eq. (8.3). The obtained exponent $1 - S$ is plotted over T in the inset of Fig. 8.13 and strongly deviates from the expectations, $1 - S = 0.38$ for 3D and $1 - S = 0.5$ for 2D. While for $x = 0.12$, $1 - S(T)$ resembles the behavior of the pressure-dependent investigations (cf. Fig. 8.8) with slightly higher values, the obtained values for $1 - S(T)$ increase upon heating, indicating a steeper decrease of $\varepsilon_1(f)$.

In analogy to the analysis for the pressure-dependent results, we test the phonon assisted tunneling approach and determine d_t according to Eq. (8.4) for κ-STF$_x$-CuCN as well. The temperature dependence of f_0 and d_t is plotted in Fig. 8.15. For both substitutions, d_t rises from 24 Å to above 30 Å which is approximately the same length scale as determined for the pristine compound under pressure.

8.3 Discussion

For both investigated systems, κ-CuCN under increasing pressure p and κ-STF$_x$-CuCN with rising the substitution x, the observed signature of ε_1 and σ_1 in the low temperature part of the phase diagram agrees very well with the expectations for a percolating system (cf. Ch. 4.5). Upon approaching the Mott IMT from the insulating side, metallic puddles start to nucleate and grow upon decreasing the interaction strength U/W. Right at the phase boundary, a part of the metallic clusters from a continuous path from one side of the specimen to the opposite, i.e. the infinite cluster, and the conductivity of the systems changes from insulating to conducting. In contrast to conventional dc-transport, our measurements of the complex dielectric permittivity are sensitive to polarization effects at the interface between finite metallic clusters in the insulting host fraction, which lead to the drastic enhancement of ε_1. We therefore unequivocally confirm the sharp first-order character of the Mott transition and the concomitant phase coexistence in the investigated organic spin liquid compounds.

In fact, the first-order nature of the Mott transition was already revealed by Limelette *et al.* in the antiferromagnetically ordered sister compound κ-CuCl, but this was not so clear for Mott insulators hosting a quantum spin liquid state. For the latter, the magnetic excitations are spinons obeying the Fermi-Dirac statistics, in contrast to magnons, the bosonic spin excitations in an AFM. Hence, the scenario was put forward of a smooth transformation of a spin Fermi surface to a conventional charge Fermi surface upon crossing the phase boundary [21], leading to a quasi-continuous Mott transition [17]. In contrast to that, DMFT predicts a phase coexistence in proximity to the phase boundary in accordance to a first-order scenario [12, 13, 25] while its extension with resonating valence bond theory negates a coherent merging of the two Fermi surfaces at the Mott transition [22]. In this framework, spinons are well defined only deep in the insulating state and are destroyed by charge fluctuations upon approaching the Mott transition [19].

The findings of this thesis provide conclusive evidence for the DMFT picture and finally settle this debate. In accord with our experiments, DMFT calculations [204] reveal that the permittivity varies only little as the transition is approached from the insulating side by reducing the Mott gap. The enhancement of $\varepsilon_1(U/W)$ – corresponding to $\varepsilon_1(p)$ – is sharply confined to the coexistence region, where it exceeds the values of the (homogeneous) Mott insulator by orders of magnitude. We show that dielectric spectroscopy as a bulk method is sensitive to phase segregation at IMTs and provides information on the formation and growth of metallic regions in vicinity to the phase boundary.

Moreover, it also reveals the occurrence of quasi-particles upon entering the metallic transport regime, as can be nicely seen in Fig. 8.16. Panels (a,d) show the phase diagrams

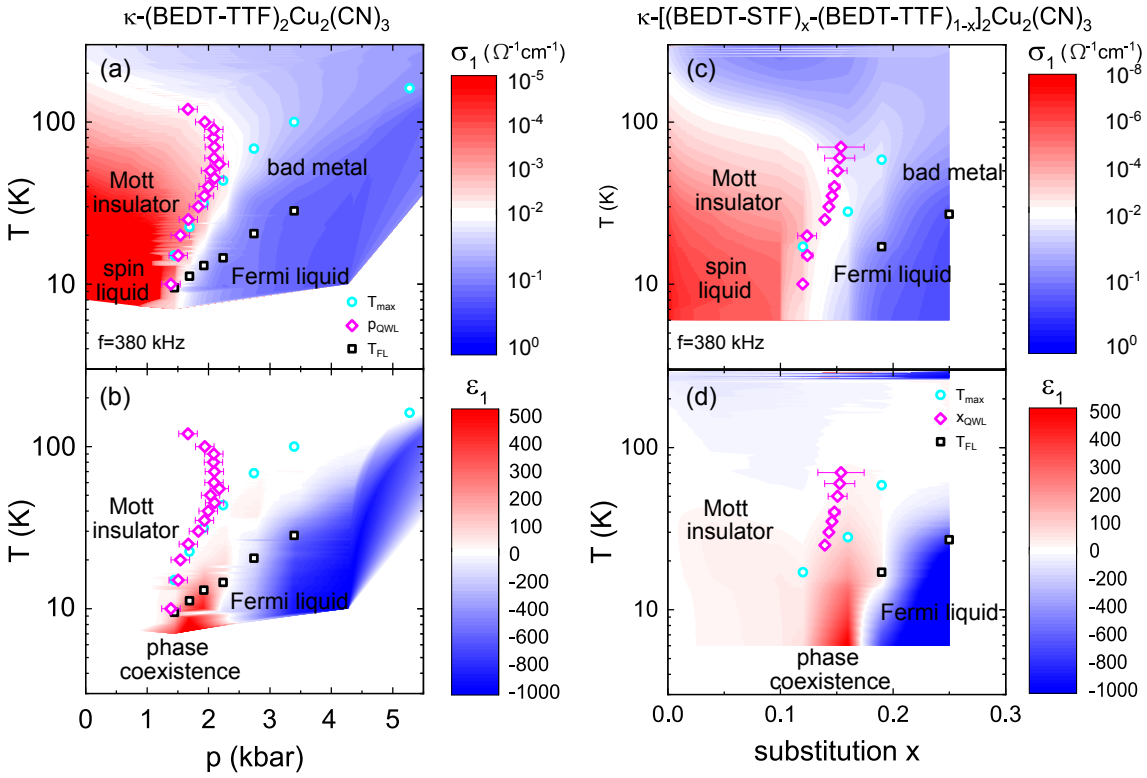

Figure 8.16: The phase diagrams of κ-(BEDT-TTF)$_2$Cu$_2$(CN)$_3$ and κ-[(BEDT-STF)$_x$-(BEDT-TTF)$_{1-x}$]$_2$Cu$_2$(CN)$_3$ are constructed on the values of ε_1 and σ_1 simultaneously measured at $f = 380$ kHz. Additionally, we include T_{max}, T_{FL} and the QWL as determined in Ch. 6. For the former (a,b) the correlation strength is experimentally varied with applying hydrostatic pressure p, while for the latter (c,d) the system is tuned across the Mott IMT upon changing the substitution x. For both compounds, the plots of σ_1 resemble corresponding dc-measurements. Upon approaching the IMT, a strong enhancement of ε_1 is clearly seen upon applying pressure as well as with varying the substitution, evidencing the percolating phase coexistence concomitant to the first order nature of the Mott transition. We also emphasize that the change in sign of ε_1 coincides with T_{max}, which indicates the Brinkman-Rice line, while an equivalent feature is missing in σ_1.

of κ-CuCN and κ-STF$_x$-CuCN based on contour plots of $\sigma_1(p,T)$ and $\sigma_1(x,T)$, respectively, wherein we include $T_{\max}$, T_{FL} and the QWL as determined in chapter 6. For both compounds, our results reproduce corresponding dc-measurements in minute detail [17]. Panels (b,d) show the corresponding plots of the simultaneously determined ε_1, wherein the contract contribution is subtracted as describe in detail in chapter 6.4. The strong enhancement of the permittivity in the phase coexistence region is clearly seen upon applying pressure as well as with varying the substitution. We also emphasize that the change in sign of ε_1 coincides with $T_{\max}$, which indicates the Brinkman-Rice line, while an equivalent feature is missing in σ_1. At the Brinkman-Rice line, so called resilient quasi-particles [11, 26] form upon cooling or increasing the correlation strength U/W which eventually become the well known Landau quasi-particles in ther Fermi liquid regime at even lower temperatures. This proofs dielectric spectroscopy as powerful technique combining the determination of complex conductivity/permittivity with detailed pressure and temperature tuning which is capable of distinguishing all relevant conduction regimes of correlated electron systems.

Let us now come back to the LT peak. As can be seen from Fig. 7.9, it appears only for $T < T_{\mathrm{crit}}$ with a sharp contrast between the metallic inclusions and the insulating host. For these temperatures, the pressure evolution of $\varepsilon_1(p)$ in κ-CuCN upon approaching the phase boundary includes the LT-peak and perfectly fits the expectations for a percolating system (Fig. 8.5). Applying the BEMA model to our results yields the metallic filling fraction m in dependence of pressure and a critical exponent of $q \sim 1$ upon approaching the threshold from the insulating side. A closer look on Fig. 8.4 also reveals a slightly enhanced metallic filling fraction m at the LT-peak position. The LT-peak emerges due to a small metallic filling fraction m already on the insulating side of the phase diagram, corroborating the previous suggestion of metallic quantum fluctuations drawn from optical spectroscopy studies at ambient pressure [20]. As the phase transition is approach, it grows and eventually becomes the dominant peak at the percolation threshold, as is documented in Figs. 6.2 and 6.4.

The energy Δ_{LT} corresponding to the LT peak stays constant up to the IMT, right where $\varepsilon_1(p)$ is reproduced very well by the BEMA model (Fig. 8.3), the latter is not considering a capacitive coupling of the metallic inclusions. Hence, we attribute the drop in Δ_{LT} close to the percolation threshold to an increased coupling between the metallic inclusions. With values of τ_{LT} decreasing from 10^{-6} to 10^{-8} s, the LT relaxation is clearly slower than the HT peak; it hardens upon increasing m. The origin of this intriguing behavior has yet to be clarified, i.e. whether this can be assigned to changes in size and/or shape of the metallic inclusions. Such a behavior was revealed by ellipsometric studies of VO_2 films [217]. At this point it is worthwhile to mention, that the LT peak is reminiscent of the

dielectric response in the sibling compound κ-CuCl, for which a pressure of 0.4 kbar is already sufficient to reach the IMT. In particular, the reported dielectric response in κ-CuCl [133] is less dispersive when compared to its siblings and rather resembles the signature of the LT peak. Hence κ-CuCl enables investigations of the LT peak and the nature of the metallic inclusions at ambient pressure via a broad spectrum of experimental techniques, such as scanning near-field infrared microscopy [77].

What remains puzzling is the unexpected frequency-dependence of $\varepsilon_1(f)$ in the coexistence phase which does not match standard percolation theory. In addition, the high values of $\varepsilon_1(f)$ at temperatures above T_{crit} and for frequencies $f < 10$ kHz are rather surprising and might either indicate fluctuations in the onsetting formation of metallic inclusions [20] or a restrengthening of the contact contribution concomitant to the increase in conductivity upon approaching the phase boundary. We also tested another approach [36, 37] ascribing the peculiar behavior in $\varepsilon_1(f)$ to phonon assisted tunneling of charge carriers between the metallic inclusions. Applying this framework ot our data yields $d_t \approx 23$ Å as an upper limit for the tunneling between adjacent metallic regions, which is rather small. Anyway, this poses the question on which length scale metallic regions are clearly distinguishable from insulating regions, or in other words, how sharp the phase segregation occurs in spatial dimension. This issue is beyond the scope of this thesis. We note, however, that the depletion zone can extend up to several hundreds of nm in semiconductor heterojunctions [218] as well as in Schottky diodes based on organic p-type semiconductor [219], which is clearly above our estimated tunneling distance and challenges this scenario.

Finally, we draw attention to recent dynamical mean-field-theory calculations [38] revealing a crossover (non-asymptotic) power law behavior in the spectral function $A(\omega)$ and the self-energy $-\mathfrak{Im}\Gamma(\omega)$ extending from low to elevated temperatures. Concomitantly, consistent scaling of the resistivity is found both above and below T_{crit} as well. Both are traced back to the metastable insulating phase in the coexistence region, suggesting local quantum criticality of the Mott transition below T_{crit}, which eventually is also responsible for its well-known counterpart at elevated temperatures. Besides these fundamental findings, this study reveals a peculiar low-frequency behavior of $A(\omega)$ in proximity to the Mott transition. Whether this can be connected to the intriguing dielectric response observed here has yet to be clarified, but might provide a route to place the various features in $\varepsilon_1(p, T, f)$ on the same footing, such as the pressure evolution of the HT peak and the anomalous power-law decrease of $\varepsilon_1(f)$ in the coexistence region.

9

Summary

The findings of this thesis unveil a percolating phase coexistence at the bandwidth-tuned Mott insulator-metal transition (IMT) of the organic spin liquid compound κ-(BEDT-TTF)$_2$Cu$_2$(CN)$_3$ (κ-CuCN) [14–16, 27–30] and thereby unequivocally proof the first oder nature of the genuine Mott transition, which is solely mediated by Coulomb interactions without breaking any symmetry [18–20]. Moreover, we shed light onto the anomalous dielectric response (ADR) observed in the insulating phase of many organic charge transfer salts subject to electronic correlations, which puzzled the community for a decade.

We performed comprehensive dielectric spectroscopy measurements on the organic dimer Mott insulators κ-CuCN, κ-[(BEDT-STF)$_x$-(BEDT-TTF)$_{1-x}$]$_2$Cu$_2$(CN)$_3$ (κ-STF$_x$-CuCN) and κ-(BEDT-TTF)$_2$Ag$_2$(CN)$_3$ (κ-AgCN). In addition to varying temperature and frequency as experimental parameters, we applied hydrostatic pressure to tune κ-CuCN across the Mott insulator-metal transition (IMT) and to scrutinize the dielectric response in the entire phase diagram. Additional pressure-dependent measurements of κ-AgCN extend our investigations further into the insulating state of the organic spin liquid compounds allowing us to thoroughly inspect the ADR. These investigations are complemented by measuring a set of κ-STF$_x$-CuCN crystals, wherein varying the substitution level x is used to tune the compound across the Mott IMT.

The first part ot this PhD project was dedicated to establishing a setup for dielectric spectroscopy measurements in dependence of temperature, pressure and frequency at our institute. A crucial point in achieving this was to design and manufacture a novel electrical feedtrough for a clamp type pressure cell. Our feedthrough provides outstanding high-frequency characteristics, such as low attenuation and high cut-off frequency, and a very low stray capacitance of $C_{\mathrm{stray}} = 40$ nF while withstanding pressures up to 10 kbar. Moreover, it provides the means for in-situ monitoring of the inherent pressure loss upon cooling, significantly improving the accuracy in analyzing our pressure-dependent results.

After a short overview of the experimental results (see chapter 6), the main findings are divided into the investigation of the dielectric response in the Mott insulating phase (see chapter 7) and the study of polarization effects due to the percolating phase coexistence at the Mott IMT (see chapter 8).

Dielectric response in the Mott insulating phase

The dielectric response $\varepsilon_1(T)$ in the insulating state of the investigated compounds contains two main dielectric contributions, a high-temperature (HT) peak, showing relaxor ferroelectric characteristics, and a low-temperature (LT) peak. The HT peak corresponds to the dielectric response of the Mott insulating fraction. In contrast, the LT peak emerges due to a small metallic filling fraction already on the insulating side of the phase diagram and is a precursor feature of the phase coexistence enveloping the IMT. Additionally, a high frequency mode (mode 2) is observed, whose characteristics show strong sample-to-sample variations.

We identify the HT peak with the ADR previously observed at ambient pressure in various organic charge transfer salts. The corresponding activation energy Δ_{HT} diminishes upon intensifying pressure while the relaxation time τ_{HT} in the high-temperature limit increases. In the framework of domain walls, the former indicates that domains are easier to move and the latter that their size increases upon approaching the IMT. Despite comprehensive considerations, however, the microscopic origin of the domain walls remains yet unclear while we only can discard quantum electric dipoles or disorder in the anion network as a possible origin, which were put forward previously in literature [31–34].

The ADR shifts towards lower temperature upon increasing pressure p or the substitution x, showing that it is sensitive to modifying the correlations strength W/U. An elaborate comparison of our findings with other organic dimer Mott insulators indicates, that the intriguing ADR is common to organics with correlated electrons. Thereby we also exclude a purely phononic origin of the ADR. However, we can not rule out a connection of the ADR to details of the crystal lattice yet, such as the packing motif or a structural degrees of freedom related to hydrogen atoms.

Phase coexistence at the Mott insulator-metal transition

For both investigated systems, κ-CuCN under increasing pressure p and κ-STF$_x$-CuCN with rising the substitution x, the observed signature of ε_1 and σ_1 in the low temperature part of the phase diagram agrees very well with the expectations for a percolating system (see chapter 4.5). Upon approaching the Mott IMT from the insulating side, metallic puddles start to nucleate and grow upon decreasing the interaction strength U/W. In contrast to conventional dc-transport, our measurements of the complex dielectric permittivity are sensitive to polarization effects at the interface between finite metallic clusters in the insulting host fraction, which lead to the drastic enhancement of ε_1 up to 10^5 for 7.5 kHz. The percolative behavior is strongly suppressed for higher temperatures where

the first-order Mott insulator-to-metal transition becomes a smooth crossover and the contrast in conductivity between metallic and insulating fraction diminishes. We therefore unequivocally confirm the sharp first-order character of the Mott transition and the concomitant phase coexistence in the investigated organic spin liquid compounds.

The findings of this thesis are in striking agreement with dynamical mean-field theory (DMFT) calculations, predicting the Mott IMT to be of first order with concomitant phase coexistence, and discard a smooth transformation of a spin Fermi surface to a conventional charge Fermi surface upon crossing the IMT, as recently put forward in literature. Moreover, we establish pressure-dependent dielectric spectroscopy as a powerful tool to scrutinize the whole phase diagram of correlated electron systems, revealing relevant physical regimes. Among them are the presence of phase coexistence or the Brinkman-Rice line, the latter separating incoherent conduction from bad metal behavior, besides the easily detectable insulating and metallic regimes.

We apply Bruggeman's effective medium approximation (BEMA) to determine the metallic filling fraction m and obtain the critical exponent $q \approx 1$ upon approaching the threshold from the insulating side. The LT-peak emerges due to a small metallic filling fraction already on the insulating side of the phase diagram. A drop of Δ_{LT} close to the IMT indicates an increased coupling between the metallic inclusions. τ_{LT} decreasing from 10^{-6} to 10^{-8} s upon increasing m. The origin of this intriguing behavior has yet to be clarified, i.e. whether this can be assigned to changes in size and/or shape of the metallic inclusions. Such a behavior was revealed by ellipsometric studies of VO_2 films [217].

In the coexistence phase, we observed an unexpected strong power-law decrease of $\varepsilon_1(f)$ with increasing frequency, which does not match standard percolation theory. Testing our data with theory [36, 37] ascribing the peculiar behavior to phonon assisted tunneling of charge carriers between the metallic inclusions yields rather unrealistic results. Very recent DMFT calculations [38] with particular emphasis on low frequencies reveal a peculiar frequency-dependence of the spectral function $A(\omega)$ in proximity to the Mott IMT. Whether this can be connected to the intriguing dielectric response observed here has yet to be clarified, but might provide a route to place the various features in $\varepsilon_1(p, T, f)$ on the same footing, such as the pressure evolution of the HT peak and the anomalous power-law decrease of $\varepsilon_1(f)$ in the coexistence region.

The main results of our pressure- and temperature-dependent dielectric spectroscopy on κ-CuCN are summarized in Fig. 9.1, where a three-dimensional plot of $\varepsilon_1(p, T)$ is produced from the data taken at $f = 380$ kHz. The bottom area contains a sketch of the phase diagram constructed on the projection of the $\varepsilon_1(p, T)$ values with the corresponding color code; the intense dark red area indicates the enhanced values in the coexistence phase when spatially separated metallic regions grow in the insulating matrix. The percolative

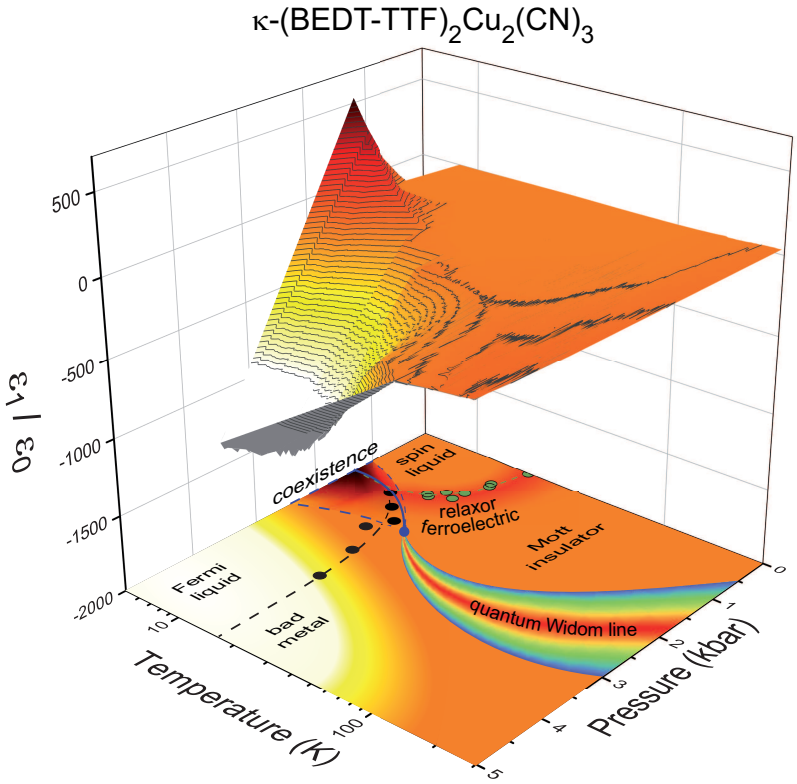

Figure 9.1: 3D plot of $\varepsilon_1(p,T)$ probed at 380 kHz and the phase diagram of κ-(BEDT--TTF)$_2$Cu$_2$(CN)$_3$. Most importantly, we observe a strong increase of ε_1 up to 500, centered around 1.8 kbar and below 20 K, close to the first-order Mott transition (blue line). We ascribe this to a coexistence phase hosting spatially separated metallic and insulating regions, as predicted by theory [25]. For temperatures above 16 K, the first-order insulator-to-metal transition becomes a gradual crossover which is indicated by the quantum Widom line [17, 20, 35]. The Mott insulating phase for $p < 1.5$ kbar reveals a relaxor ferroelectric response in $\varepsilon_1(T)$ wherein T_B (green circles) is the bifurcation temperature indicating a change in the relaxation mechanism.

behavior softens as temperature increases: the maximum diminishes and eventually a gradual crossover remains above T_{crit}. Additionally, we include the quantum Widom line reproduced after Ref. [39], the bifurcation temperature T_{B} marking the change from the HT to the LT peak and the concomitant change in the relaxation dynamics, and the Fermi-liquid temperature T_{FL}.

9.1 Outlook

We provided conclusive experimental proof for the phase coexistence at the genuine Mott transition in organic spin liquid compound κ-(BEDT-TTF)$_2$Cu$_2$(CN)$_3$, which in the future has to be considered in the interpretation of non-local probes. Some aspects of the phase coexistence remain unclear and require more investigations. First of all, the evolution of size and shape of the metallic inclusions upon approaching the IMT is still open and goes hand in hand with the question, on what length scale metallic regions can be clearly distinguished from insulating regions. Or more precisely, how sharp is the phase segregation in spatial dimension? Scanning near-field optical microscopy (SNOM) [77–79] as well as ellipsometry measurements in dependence of polarization and temperature [217, 220] turned out to be proper tools to shed light onto these questions. Thus, low-temperature SNOM and ellipsometry measurements on κ-[(BEDT-STF)$_x$-(BEDT-TTF)$_{1-x}$]$_2$Cu$_2$(CN)$_3$ for various substitutions levels would provide the unique opportunity to investigate and monitor the morphology of the phase segregation in dependence of the correlation length U/W.

Besides tuning the U/W, BEDT-STF substitution in κ-STF$_x$-CuCN introduces additional disorder which might give rise to Anderson localization, as indicated by an in-gap contribution in the optical conductivity for $x = 0.04$ and $x = 0.10$. Extending BEDT-STF substitution to other compounds, for instance κ-(BEDT-TTF)$_2$Ag$_2$(CN)$_3$, is a route to explore the interplay of electronic correlations and Anderson localization.

Moreover, our comprehensive analysis of the dielectric response observed in the insulating part of the phase diagram suggest electronic correlations as the driving force of the intriguing ADR with relaxor ferroelectric characteristics. We suggest pressure-dependent dielectric spectroscopy measurements on λ-type compounds, such as the newly synthesized λ-ET-GaCl$_4$ and λ-STF-GaCl$_4$, to test whether the ADR solely stems from electronic correlations or is also related to details in the crystal structure. To that end, also λ-ET-GaBr$_4$ or λ-ET-FeCl$_4$ should be investigated, the latter also features ferromagnetic ordering of Fe-atoms in the anion layer. It would be interesting to test, whether the signature of the ADR changes in this case or if an organic multi-ferroic system could be obtained. A

connection of the ADR to structural degrees of freedom of the hydrogen atoms in the BEDT-TTF molecules should be completely ruled out, which is best done by studying deuterated samples with dielectric spectroscopy and compare the results with their protonated counterparts. Finally, the ADR in organic charge transfer slats should be compared in detail with the dielectric properties in the Mott insulating state of other material classes, like transition metal oxides, to check for a common signature and oppose the dielectric response of single-band to multiple-band correlated electron systems.

A

Appendix A

A.1 Maxwell's equations

The interaction of electromagnetic fields with matter on an atomic scale is captured by the set of Maxwell's equations[1] in vacuum:

$$\nabla \cdot \mathbf{E} = \frac{\rho}{\varepsilon_0}, \tag{A.1}$$

$$\nabla \cdot \mathbf{B} = 0, \tag{A.2}$$

$$\nabla \times \mathbf{E} = \frac{\partial \mathbf{B}}{\partial t}, \tag{A.3}$$

$$\nabla \times \mathbf{B} = \mu_0 \mathbf{j} + \mu_0 \varepsilon_0 \frac{\partial \mathbf{E}}{\partial t} \tag{A.4}$$

with the electric field $\mathbf{E}$ and the magnetic flux density $\mathbf{B}$. The charge density ρ and the current density j used in the vacuum version of the MW equations refer to the total quantities.

In presence of a medium, the propagation of $\mathbf{E}$ and $\mathbf{B}$ is modified by the charges and magnetic moments constituting the medium while in return, $\mathbf{E}$ and $\mathbf{B}$ may induce currents, electric dipoles, magnetic moments and polarization charges. The number of charged particles embodying the medium and participating to ρ and j is usually huge ($N_\mathrm{A} \sim 10^{23}$), such that the above set of equations is unmanageable. This is circumvented in the version of Maxwell's equation in matter via building the response of the solid into the structure of the equations:

[1] Throughout this thesis, we will use the SI unit system.

$$\nabla \cdot \mathbf{D} = \rho_{cond}, \tag{A.5}$$

$$\nabla \cdot \mathbf{B} = 0, \tag{A.6}$$

$$\nabla \times \mathbf{E} = \frac{\partial \mathbf{B}}{\partial t}, \tag{A.7}$$

$$\nabla \times \mathbf{H} = \left(\mathbf{J}_{cond} + \frac{\partial \mathbf{D}}{\partial t} \right) \tag{A.8}$$

The modification of the electromagnetic fields by the solid is taken into account by the dielectric displacement $\mathbf{D}$ and the magnetic field $\mathbf{H}$. The induced entities are divided into two parts: the first due to the motion of free electrons in the presence of an electric field, with the charge density ρ_{cond} and current density $\mathbf{J}_{cond}$; the second due to the redistribution of bound charges on a microscopic scale, with the bound charge density ρ_{bound} and the bound current density $\mathbf{j}_{bound}$. In case there is no other additional external charge or current, the total charge density ρ_{total} and the total current density $\mathbf{j}_{total}$ in the medium follow

$$\rho_{total} = \rho_{cond} + \rho_{bound} \tag{A.9}$$

$$\mathbf{j}_{total} = \mathbf{j}_{cond} + \mathbf{j}_{bound}. \tag{A.10}$$

The dielectric displacement $\mathbf{D}$ and the magnetic field $\mathbf{H}$ are defined by

$$\mathbf{D} = \varepsilon_0 \mathbf{E} + \mathbf{P} \tag{A.11}$$

$$\mathbf{H} = \frac{1}{\mu_0} \mathbf{B} - \mathbf{M}, \tag{A.12}$$

and are therefore by definition related to the polarization $\mathbf{P}$ and the magnetization $\mathbf{M}$, which embody the response of the medium to the $\mathbf{E}$ and $\mathbf{B}$ field. By considering the set in vacuum (A.1-A.4) and subtracting the set in matter (A.5-A.8), we obtain the relations

$$\nabla \cdot \mathbf{P} = -\rho_{bound} \tag{A.13}$$

$$\nabla \times \mathbf{M} + \frac{\partial (\mathbf{P})}{\partial t} = \mathbf{j}_{bound} \tag{A.14}$$

which have to be fulfilled in order to keep both sets consistent.

The dependence of $\mathbf{P}(\mathbf{E}, \mathbf{B})$ and $\mathbf{M}(\mathbf{B}, \mathbf{E})$ on $\mathbf{E}$ and $\mathbf{B}$ has to be determined in experiment and gives a so called constitutional equation, which defines an experimental

observable, also called a material parameter. For instance, in case of a linear and isotropic dielectric material, the constitutional equation

$$\mathbf{P} = \varepsilon_0 \chi_{\text{elec}} \mathbf{E}, \tag{A.15}$$

defines the electric susceptibility χ_{elec}, which is a linear response function. In case of a non-linear and isotropic dielectric material, for instance, this constitutional equation would be

$$P = \varepsilon_0 \left(\chi^1_{\text{elec}} E + \chi^2_{\text{elec}} E^2 + \chi^3_{\text{elec}} E^3 + ... \right), \tag{A.16}$$

containing the coefficients χ^n_{elec} of the n-th-oder of the Taylor expansion in E and wherein we omitted the fact that in χ^n_{elec} is a tensor and the vector nature of P and E. In presence of a magnetoelectric effect, additional terms in dependence of an magnetic field would arise. So while the Maxwell equations describe the propagation of electromagnetic fields in a medium, the response of the medium to the **E** and **B** fields is contained in the constitutional equations defining experimental observables.

A.2 "+" or "-" in $\hat{\varepsilon}$

For a linear and isotropic medium, the permittivity $\hat{\varepsilon}$ is

$$\hat{\varepsilon} = \varepsilon_1 \pm i\varepsilon_2. \tag{A.17}$$

Whether a + or a − is used in Eq. A.17 is a matter of choice but has to be consistent with the definition of the harmonic electric field $\mathbf{E} = \mathbf{E}_0 \exp \mp i\omega t$ which goes into the Maxwell equations.

To show this explicitly, we first have to consider the total current density

$$\mathbf{j}_{\text{tot}} = \mathbf{j}_{\text{cond}} + \mathbf{j}_{\text{D}}, \tag{A.18}$$

which is split into a displacement current density $\mathbf{j}_{\text{D}}$, arising from a microscopic displacement of bound charge carries in an external **E**-field, and a conduction current density $\mathbf{j}_{\text{cond}}$ embodying the transport of mobile charge carriers in the medium in response to **E**. The former is given by

$$\mathbf{j}_{\text{D}} = \frac{\partial \mathbf{D}}{\partial t} = \mp i\omega \hat{\varepsilon} \mathbf{E}, \tag{A.19}$$

and the latter, in absence of any magnetoresistive effects and within the limit of linear response, is given by Ohm's law

$$\mathbf{j}_{\mathrm{cond}} = \sigma_1 \mathbf{E}, \tag{A.20}$$

with the conductivity σ_1 of the medium.

The time average over one period $T = 2\pi/\omega$ of the dissipated energy $\overline{W}_{\mathrm{diss}}$ per unit volume V in the medium is given by

$$\frac{\overline{W}_{\mathrm{loss}}}{V} = \frac{1}{2} Re\left[\mathbf{j}_{\mathrm{tot}} \cdot \mathbf{E}^*\right] = \frac{E_0^2}{2} Re\left[\sigma_1 + \mp i\omega\hat{\varepsilon}\right] = \frac{E_0^2}{2} Re\left[\sigma_1 + \mp i\omega(\varepsilon_1 \pm i\varepsilon_2)\right], \tag{A.21}$$

wherein Re takes the real part and $\mathbf{E}^*$ denotes the complex conjugate of the electric field. The term scaling with ε_1 does not contribute to $\overline{W}_{\mathrm{diss}}$ and represents the energy which is stored in the medium while the term quantified by σ_1 is the loss due free charge carries and the one proportional to ε_2 the loss due to bound charge carries, for instance arising from dipole relaxation. The losses add up as long as the sign in $\hat{\varepsilon} = \varepsilon_1 \pm i\varepsilon_2$ and in $\mathbf{E} = \mathbf{E}_0 \exp \mp i\omega t$ are set consistently. In both cases $\varepsilon_2 > 0$ corresponds to a lossy dielectric whereas $\varepsilon_2 < 0$ represents an active medium.

B

Achnowledgements

Finally, I would like to thank all the people who supported me during the last four and a half years at the 1. Physical Institute.

- First of all, I would like to thank my supervisor Prof. Dressel for his continuous support and encouragement. You always have an open door, give valuable advice and appreciate scientific discussions and new ideas. I had the freedom to make own decisions and pursue different projects while You managed to keep me on track with my PhD and all the things around it. Most importantly, I also want to thank you for the warm and familiar atmosphere at your institute.

- I also would like to thank Prof. Daghofer for kindly agreeing to be examination chairperson and Prof. Takagi for kindly agreeing to co-referee this thesis.

- Many thanks to Dr. Ece Uykur for all the usefull discussions and input. With you at PI1, things got a lot easier since we could discuss the details and shortcomings of dielectric spectroscopy. Most of all, however, I would like to thank you for your great attitude, drive and your wise and well-tempered character. It was a pleasure to work with you.

- I would be impossible to do research at our institute without the great technical support by the low temperature and the mechanical workshop. I also want to emphasize the outstanding assistance by Gabi Untereiner, thank you for your assistance in preparing the feedthrough and for contacting many samples.

- I also would like to thank Agnieszka Cienkowska-Schmidt for keeping the institute running and for her great kindness.

I also want to acknowledge all collaborators, people who provided samples and those who supported my work.

- I want to thank Dr. Andrej Pustogow for comprehensive discussions and input on our papers as well as for establishing the fruitful collaboration with Prof. Dobrosavljević

and Yuting Tan. Also for our good time at PI1; I appreciate your great drive and enthusiasm in doing research.

- Special thanks go to Dr. Yohei Saito for providing the κ-[(BEDT-STF)$_x$-(BEDT--TTF)$_{1-x}$]$_2$Cu$_2$(CN)$_3$ samples and the many discussion we had on organics. Also thank you for being a great gym buddy and the good time we had at PI1. I very much appreciate your humble and kind character.

- Prof. Schlueter for providing κ-(BEDT-TTF)$_2$Cu$_2$(CN)$_3$ samples. Dr. Ralph Hübner and Anja Löhle for their efforts which culminated in the synthesis of κ-(BEDT--TTF)$_2$Cu$_2$(CN)$_3$ and κ-(BEDT-TTF)$_2$Ag$_2$(CN)$_3$ crystals at PI1. Anja, also thank you for introducing me to the AC/DC lab and your cheerful and bright nature.

- Thanks to Prof. Dobrosavljević and Yuting Tan for the enlightening discussion, valuable theory input and the fruitful collaboration.

I had the privilege to spend my time at PI1 with amazing and inspiring people who made this an unforgettable and enriching part of my life for which I am very grateful.

- Dr. Bruno Gompf, Dr. Artem Pronin, Dr. Seulki Roh, Dr. Mark Scheffler and Dr. Ece Uykur for all the enlightening discussions, for sharing their knowledge and for contributing to the warm and familiar atmosphere at PI1.

- Weiwu for your positive and merry nature as well as our countless discussion on physics. Ievgen for your great humor and attitude as well as your help with python. Tobias for his good mood bringing a relaxed yet productive atmosphere. Mehmet for your good-humored and humble character. Sascha for being great and for kindly sharing your expertise and supplies in coffee. Guilherme for our good times inside and outside the gym. It was a great pleasure to have you guys as colleagues and friends at PI1.

- My PhD colleagues Andrea, Olga, Micha, Markus, Björn, Nikolaj, Andreas, David, Mojtaba, Uwe, Lucky and Yuk for the positive and friendly atmosphere.

- My bachelor students Annette and Maxim as well as my Master students Daniel and Vincent for their great attitude and their dedication to our projects.

- All other members of PI1. Olga, Di, Lena, Desiree, Alessandro, Karl, Diego as well as Dr. Helga Kumrić and Birgit Mann for the friendly and positive ambiance at PI1.

At its hear, life is about the people we meet and bond on our journey. At this occasion, I would like to express my gratitude to my friends and family for being an irreplaceable part of my life.

- Maldin and Suhaeel for being great and strong. You boys are amazing!

- The dedicated people at INSIDEOUT, Leila, Moema, Micha, Anja, Tilman and Alexej. Thank you for protecting our free democratic principles and for giving me the chance to contribute to that.

- The Moscow connection Thorsten, Johannes and Alexander for our rare but very fun and inspiring meetings.

- My friends from Austria, Clemens and Lukas, for being inspirational and extremely funny as well as for our eventful and exciting trips.

- My friends from Munich times. Frederik, Norbert, Konstantin, Moritz, Christoph, Philipp, Andrej, Martin, Klaus, Andi, Summer, Jochen and Sebi for being awesome, inspiring and amazing. I cannot put in words how happy and privileged I feel to have you as friends. Physics and life can be tough and it still is good to have somebody to talk to about all the difficulties; thank you for your support and encouragement. Even more, thank you for all the great and fun times, our awesome trips and for staying together in dear times. It is always a big highlight to see you guys.

- My family for unconditionally supporting me throughout my entire life. My parents for continuously encouraging me to go my own way and for their caring love. My sister Carla and my brothers Bertram and Lorenz for being inspiring and awesome persons, our good relation and for caring for each other.

- Hanna, thank you for your warm, considerate, active and merry nature. Thank you for listening, your commitment and your advice. Our lives were about to change when we met and will so in the future, still you became the a constant in my life and this makes me very happy. You are a wonderful person.

Bibliography

[1] H. Seo, C. Hotta, and H. Fukuyama, "Toward systematic understanding of diversity of electronic properties in low-dimensional molecular solids", *Chem. Rev.* **104**, 5005–5036 (2004).

[2] A. Lebed, ed., *The physics of organic superconductors and conductors*, vol. 110, Springer Series in Materials Science, Berlin: Springer-Verlag, (2008).

[3] Q. Si and F. Steglich, "Heavy fermions and quantum phase transitions", *Science* **329**, 1161–1166 (2010).

[4] I. G. Austin and N. F. Mott, "Metallic and nonmetallic behavior in transition metal oxides", *Science* **168**, 71–77 (1970).

[5] S. Maekawa, T. Tohyama, S. Barnes, S. Ishihara, W. Koshibae, and G. Khaliullin, *Physics of transition metal oxides*, Springer Series in Solid-State Sciences, Springer Berlin Heidelberg, (2013).

[6] J. Hubbard, "Electron correlations in narrow energy bands. III. An improved solution", *Proc. Roy. Soc. A* **281**, 401 – 419 (1964).

[7] N. F. Mott and E. A. Davis, *Electronic Processes in Non-Crystalline Materials*, 2nd ed., Oxford: Clarendon Press, (1979).

[8] N. F. Mott, *Metal-Insulator Transitions*, 2nd ed., Bristol: Taylor & Francis Ltd., (1990).

[9] M. Imada, A. Fujimori, and Y. Tokura, "Metal-insulator transitions", *Rev. Mod. Phys.* **70**, 1039–1263 (1998).

[10] V. Dobrosavljević, N. Trivedi, and J. Valles, Jr., eds., *Conductor Insulator Quantum Phase Transitions*, Oxford: Oxford University Press, (2012).

[11] X. Deng, J. Mravlje, R. Žitko, M. Ferrero, G. Kotliar, and A. Georges, "How bad metals turn good: spectroscopic signatures of resilient quasiparticles", *Phys. Rev. Lett.* **110**, 086401 (2013).

[12] A. Georges, G. Kotliar, W. Krauth, and M. J. Rozenberg, "Dynamical mean-field theory of strongly correlated fermion systems and the limit of infinite dimensions", *Rev. Mod. Phys.* **68**, 13–125 (1996).

[13] D. Vollhardt, "Dynamical mean-field theory for correlated electrons", *Ann. Phys. (Berl.)* **524**, 1–19 (2012).

[14] P. W. Anderson, "Resonating valence bonds: a new kind of insulator?", *Mate. Res. Bull.* **8**, 153 - 160 (1973).

[15] L. Balents, "Spin liquids in frustrated magnets", *Nature* **464**, 199 (2010).

[16] B. J. Powell and R. H. McKenzie, "Quantum frustration in organic Mott insulators: from spin liquids to unconventional superconductors", *Rep. Prog. Phys.* **74**, 56501 (2011).

[17] T. Furukawa, K. Kobashi, Y. Kurosaki, K. Miyagawa, and K. Kanoda, "Quasi-continous transition from a Fermi liquid to a spin liquid in κ-$(ET)_2Cu_2(CN)_3$", *Nat. Comm.* **9**, 307 (2018).

[18] M. Dressel and A. Pustogow, "Electrodynamics of quantum spin liquids", *J. Phys. Condens. Matter* **30**, 203001 (2018).

[19] A. Pustogow, Y. Saito, E. Zhukova, B. Gorshunov, R. Kato, T.-H. Lee, S. Fratini, V. Dobrosavljević, and M. Dressel, "Low-energy excitations in quantum spin liquids identified by optical spectroscopy", *Phys. Rev. Lett.* **121**, 056402 (2018).

[20] A. Pustogow, M. Bories, A. Löhle, R. Rösslhuber, E. Zhukova, B. Gorshunov, S. Tomić, J. A. Schlueter, R. Hübner, T. Hiramatsu, Y. Yoshida, G. Saito, R. Kato, T.-H. Lee, V. Dobrosavljević, S. Fratini, and M. Dressel, "Quantum spin liquids unveil the genuine Mott state", *Nat. Mat.* **17** (2018).

[21] T. Senthil, "Theory of a continuous Mott transition in two dimensions", *Phys. Rev. B* **78**, 045109 (2008).

[22] T.-H. Lee, S. Florens, and V. Dobrosavljević, "Fate of spinons at the Mott point", *Phys. Rev. Lett.* **117**, 136601 (2016).

[23] T. Senthil, "Critical Fermi surfaces and non-Fermi liquid metals", *Phys. Rev. B* **78**, 035103 (2008).

[24] H. Terletska, J. Vučičević, D. Tanasković, and V. Dobrosavljević, "Quantum critical transport near the Mott transition", *Phys. Rev. Lett.* **107**, 026401 (2011).

[25] J. Vučičević, H. Terletska, D. Tanasković, and V. Dobrosavljević, "Finite-temperature crossover and the quantum Widom line near the Mott transition", *Phys. Rev. B* **88**, 075143 (2013).

[26] J. Vučičević, D. Tanasković, M. J. Rozenberg, and V. Dobrosavljević, "Bad-metal behavior reveals Mott quantum criticality in doped Hubbard models", *Phys. Rev. Lett.* **114**, 246402 (2015).

[27] Y. Shimizu, K. Miyagawa, K. Kanoda, M. Maesato, and G. Saito, "Spin liquid state in an organic Mott insulator with a triangular lattice", *Phys. Rev. Lett.* **91**, 107001 (2003).

[28] Y. Kurosaki, Y. Shimizu, K. Miyagawa, K. Kanoda, and G. Saito, "Mott transition from a spin liquid to a Fermi liquid in the spin-frustrated organic conductor $\kappa-(ET)_2Cu_2(CN)_3$", *Phys. Rev. Lett.* **95**, 177001 (2005).

[29] K. Kanoda and R. Kato, "Mott physics in organic conductors with triangular lattices", *Annu. Rev. Condens. Matter Phys.* **2**, 167-188 (2011).

[30] Y. Shimizu, T. Hiramatsu, M. Maesato, A. Otsuka, H. Yamochi, A. Ono, M. Itoh, M. Yoshida, M. Takigawa, Y. Yoshida, and G. Saito, "Pressure-tuned exchange coupling of a quantum spin liquid in the molecular triangular lattice κ-$(ET)_2Ag_2(CN)_3$", *Phys. Rev. Lett.* **117**, 107203 (2016).

[31] M. Abdel-Jawad, I. Terasaki, T. Sasaki, N. Yoneyama, N. Kobayashi, Y. Uesu, and C. Hotta, "Anomalous dielectric response in the dimer Mott insulator κ-(BEDT-TTF)$_2$Cu$_2$(CN)$_3$", *Phys. Rev. B* **82**, 125119 (2010).

[32] M. Pinterić, M. Čulo, O. Milat, M. Basletić, B. Korin-Hamzić, E. Tafra, A. Hamzić, T. Ivek, T. Peterseim, K. Miyagawa, K. Kanoda, J. A. Schlueter, M. Dressel, and S. Tomić, "Anisotropic charge dynamics in the quantum spin-liquid candidate κ-(BEDT-TTF)$_2$Cu$_2$(CN)$_3$", *Phys. Rev. B* **90**, 195139 (2014).

[33] M. Pinterić, P. Lazić, A. Pustogow, T. Ivek, M. Kuveždić, O. Milat, B. Gumhalter, M. Basletić, M. Čulo, B. Korin-Hamzić, A. Löhle, R. Hübner, M. Sanz Alonso, T. Hiramatsu, Y. Yoshida, G. Saito, M. Dressel, and S. Tomić, "Anion effects on electronic structure and electrodynamic properties of the Mott insulator $\kappa - (BEDT - TTF)_2Ag_2(CN)_3$", *Phys. Rev. B* **94**, 161105 (2016).

[34] M. Pinterić, D. Rivas Góngora, Z. Rapljenović, T. Ivek, M. Čulo, B. Korin-Hamzić, O. Milat, B. Gumhalter, P. Lazić, M. Sanz Alonso, W. Li, A. Pustogow, G. Gorgen Lesseux, M. Dressel, and S. Tomić, "Electrodynamics in organic dimer insulators close to Mott critical point", *Crystals* **8**, 190 (2018).

[35] U. Geiser, H. H. Wang, K. D. Carlson, J. M. Williams, H. A. Charlier, J. E. Heindl, G. A. Yaconi, B. J. Love, and M. W. Lathrop, "Superconductivity at 2.8 K and 1.5 kbar in κ-(BEDT$-$TTF)$_2$Cu$_2$(CN)$_3$: the first organic superconductor containing a polymeric copper cyanide anion", *Inorg. Chem.* **30**, 2586-2588 (1991).

[36] A. B. Pakhomov, S. K. Wong, X. Yan, and X. X. Zhang, "Low-frequency divergence of the dielectric constant in metal-insulator nanocomposites with tunneling", *Phys. Rev. B* **58**, R13375–R13378 (1998).

[37] A. K. Sarychev and F. Brouers, "New scaling for ac properties of percolating composite materials", *Phys. Rev. Lett.* **73**, 2895–2898 (1994).

[38] H. Eisenlohr, S.-S. B. Lee, and M. Vojta, "Mott quantum criticality in the one-band Hubbard model: dynamical mean-field theory, power-law spectra, and scaling", *arXiv:1906.05293* (2019).

[39] T. Furukawa, K. Miyagawa, H. Tanigchi, R. Kato, and K. Kanoda, "Quantum criticality of Mott transition in organic materials", *Nat. Phys.* **11**, 221–224 (2015).

[40] P. Limelette, A. Georges, D. Jérome, P. Wzietek, P. Metcalf, and J. M. Honig, "Universality and critical behavior at the Mott transition", *Science* **302**, 89-92 (2003).

[41] F. Kagawa, T. Itou, K. Miyagawa, and K. Kanoda, "Transport criticality of the first-order Mott transition in the quasi-two-dimensional organic conductor $\kappa - (\mathrm{BEDT-TTF})_2\mathrm{Cu[N(CN)_2]Cl}$", *Phys. Rev. B* **69**, 064511 (2004).

[42] S. E. Brown, P. M. Chaikin, and M. J. Naughton, "La Tour des Sels de Bechgaard", *The physics of organic superconductors and conductors*, ed. by A. Lebed, Springer-Verlag, (2010).

[43] M. Dressel, "Spin-charge separation in quasi one-dimensional organic conductors", *Naturwissenschaften* **90**, 337–344 (2003).

[44] L. Savary and L. Balents, "Quantum spin liquids: a review", *Rep. Prog.Phys.* **80**, 016502 (2017).

[45] Y. Zhou, K. Kanoda, and T.-K. Ng, "Quantum spin liquid states", *Rev. Mod. Phys.* **89**, 025003 (2017).

[46] R. Rösslhuber, E. Uykur, and M. Dressel, "Pressure cell for radio-frequency dielectric measurements at low temperatures", *Rev. Scien. Inst.* **89**, 054708 (2018).

[47] F. Gebhard, *The Mott Metal-Insulator Transition: Models and Methods*, Springer Tracts in Modern Physics, Springer Berlin Heidelberg, (2003).

[48] Y. Shimizu, K. Miyagawa, K. Kanoda, M. Maesato, and G. Saito, "Emergence of inhomogeneous moments from spin liquid in the triangular-lattice Mott insulator κ-$(\mathrm{ET})_2\mathrm{Cu}_2(\mathrm{CN})_3$", *Phys. Rev. B* **73**, 140407 (2006).

[49] R. Kato, "Development of π-electron systems based on $[\mathrm{M(dmit)_2}]$ (M = Ni and Pd; dmit: 1,3-dithiole-2-thione-4,5-dithiolate) anion radicals", *Bull. Chem. Soc. Jpn.* **87**, 355-374 (2014).

[50] M. P. Shores, E. A. Nytko, B. M. Bartlett, and D. G. Nocera, "A structurally perfect S = 1/2 Kagomé antiferromagnet", *J. Am. Chem. Soc.* **127**, 13462-13463 (2005).

[51] J. S. Helton, K. Matan, M. P. Shores, E. A. Nytko, B. M. Bartlett, Y. Yoshida, Y. Takano, A. Suslov, Y. Qiu, J.-H. Chung, D. G. Nocera, and Y. S. Lee, "Spin dynamics of the spin-1/2 Kagome lattice antiferromagnet $ZnCu_3(OH)_6Cl_2$", *Phys. Rev. Lett.* **98**, 107204 (2007).

[52] F. Bert, A. Olariu, A. Zorko, P. Mendels, J. C. Trombe, F. Duc, M. A. de Vries, A. Harrison, A. D. Hillier, J. Lord, A. Amato, and C. Baines, "Frustrated magnetism in the quantum Kagome Herbertsmithite $ZnCu_3(OH)_6Cl_2$ antiferromagnet", *J. Phys. Conf.* **145**, 012004 (2009).

[53] P. Mendels and F. Bert, "Quantum kagome antiferromagnet : $ZnCu_3(OH)_6Cl_2$", *J. Phys. Conf.* **320**, 012004 (2011).

[54] M. J. Lawler, H.-Y. Kee, Y. B. Kim, and A. Vishwanath, "Topological spin liquid on the hyperkagome lattice of $Na_4Ir_3O_8$", *Phys. Rev. Lett.* **100**, 227201 (2008).

[55] D. A. Huse and V. Elser, "Simple variational wave functions for two-dimensional Heisenberg spin-$\frac{1}{2}$ antiferromagnets", *Phys. Rev. Lett.* **60**, 2531–2534 (1988).

[56] L. Capriotti, A. E. Trumper, and S. Sorella, "Long-range Néel order in the triangular Heisenberg model", *Phys. Rev. Lett.* **82**, 3899–3902 (1999).

[57] R. Kaneko, S. Morita, and M. Imada, "Gapless spin-liquid phase in an extended spin 1/2 triangular Heisenberg model", *J. Phys. Soc. Jpn.* **83**, 093707 (2014).

[58] T. Yamamoto, T. Fujimoto, T. Naito, Y. Nakazawa, M. Tamura, K. Yakushi, Y. Ikemoto, T. Moriwaki, and R. Kato, "Charge and lattice fluctuations in molecule-based spin liquids", *Sci. Rep.* **7**, 12930 ().

[59] T. Furukawa, K. Miyagawa, T. Itou, M. Ito, H. Taniguchi, M. Saito, S. Iguchi, T. Sasaki, and K. Kanoda, "Quantum spin liquid emerging from antiferromagnetic order by introducing disorder", *Phys. Rev. Lett.* **115**, 077001 (2015).

[60] M. Dressel, P. Lazić, A. Pustogow, E. Zhukova, B. Gorshunov, J. A. Schlueter, O. Milat, B. Gumhalter, and S. Tomić, "Lattice vibrations of the charge-transfer salt κ-(BEDT-$TTF_2Cu_2(CN)_3$: comprehensive explanation of the electrodynamic response in a spin-liquid compound", *Phys. Rev. B* **93**, 081201 (2016).

[61] P. Lazić, M. Pinterić, D. Rivas Góngora, A. Pustogow, K. Treptow, T. Ivek, O. Milat, B. Gumhalter, N. Došlić, M. Dressel, and S. Tomić, "Importance of van der Waals interactions and cation-anion coupling in an organic quantum spin liquid", *Phys. Rev. B* **97**, 245134 (2018).

[62] P. Foury-Leylekian, V. Ilakovac, V. Balédent, P. Fertey, A. Arakcheeva, O. Milat, D. Petermann, G. Guillier, K. Miyagawa, K. Kanoda, P. Alemany, E. Canadell, S. Tomić, and J.-P. Pouget, "$(BEDT\text{-}TTF)_2Cu_2(CN)_3$ spin liquid: beyond the average structure", *Crystals* **8**, 158 (2018).

[63] V. Kalmeyer and R. B. Laughlin, "Equivalence of the resonating-valence-bond and fractional quantum Hall states", *Phys. Rev. Lett.* **59**, 2095–2098 (1987).

[64] A. C. Potter, T. Senthil, and P. A. Lee, "Mechanisms for sub-gap optical conductivity in Herbertsmithite", *Phys. Rev. B* **87**, 245106 (2013).

[65] R. V. Mishmash, J. R. Garrison, S. Bieri, and C. Xu, "Theory of a competitive spin liquid state for weak Mott insulators on the triangular lattice", *Phys. Rev. Lett.* **111**, 157203 (2013).

[66] M. R. Norman, "Colloquium: Herbertsmithite and the search for the quantum spin liquid", *Rev. Mod. Phys.* **88**, 041002 (2016).

[67] T.-K. Ng and P. A. Lee, "Power-law conductivity inside the Mott gap: application to $\kappa-(BEDT-TTF)_2Cu_2(CN)_3$", *Phys. Rev. Lett.* **99**, 156402 (2007).

[68] J. Knolle and R. Moessner, "A field guide to spin liquids", *Annu. Rev. Condens. Matter Phys.* **10**, 451 (2019).

[69] P. Limelette, P. Wzietek, S. Florens, A. Georges, T. A. Costi, C. Pasquier, D. Jérome, C. Mézière, and P. Batail, "Mott transition and transport crossovers in the organic compound κ-$(BEDT\text{-}TTF)_2Cu[N(CN)_2]Cl$", *Phys. Rev. Lett.* **91**, 016401 (2003).

[70] T. Sasaki, N. Yoneyama, N. Kobayashi, Y. Ikemoto, and H. Kimura, "Imaging phase separation near the Mott boundary of the correlated organic superconductors $\kappa-(BEDT-TTF)_2X$", *Phys. Rev. Lett.* **92**, 227001 (2004).

[71] K. Wark and D. Richards, *Thermodynamics*, McGraw-Hill series in mechanical engineering, WCB/McGraw-Hill, (1999).

[72] S.-S. Lee and P. A. Lee, "Emergent U(1) gauge theory with fractionalized boson/fermion from the Bose condensation of excitons in a multiband insulator", *Phys. Rev. B* **72**, 235104 (2005).

[73] S.-S. Lee, P. A. Lee, and T. Senthil, "Amperean pairing instability in the U(1) spin liquid state with Fermi surface and application to κ-(BEDT-TTF)$_2$Cu$_2$(CN)$_3$", *Phys. Rev. Lett.* **98**, 067006 (2007).

[74] K. v. Klitzing, G. Dorda, and M. Pepper, "New method for high-accuracy determination of the fine-structure constant based on quantized Hall resistance", *Phys. Rev. Lett.* **45**, 494–497 (1980).

[75] V. Dobrosavljević and G. Kotliar, "Dynamical mean-field studies of metal-insulator transitions", *Phil. Trans. Math. Phys. Eng. Sci.* **356**, 57-74 (1998).

[76] G. Kotliar, E. Lange, and M. J. Rozenberg, "Landau theory of the finite temperature Mott transition", *Phys. Rev. Lett.* **84**, 5180–5183 (2000).

[77] M. M. Qazilbash, M. Brehm, B.-G. Chae, P.-C. Ho, G. O. Andreev, B.-J. Kim, S. J. Yun, A. V. Balatsky, M. B. Maple, F. Keilmann, H.-T. Kim, and D. N. Basov, "Mott transition in VO_2 revealed by infrared spectroscopy and nano-imaging", *Science* **318**, 1750–1753 (2007).

[78] A. McLeod, E. van Heuman, J. Ramirez, S. Wang, T. Saerbeck, S. Guenon, M. Goldflam, L. Anderegg, P. Kelly, A. Mueller, M. Liu, I. K. Schuller, and D. Basov, "Nanotextured phase coexistence in the correlated insulator V_2O_3", *Nat. Phys.* **13**, 80–86 (2017).

[79] K. Post, A. McLeod, M. Hepting, M. Bluschke, Y. Wang, G. Cristiani, G. Logvenov, A. Charnukha, G. X. Ni, P. Radhakrishnan, M. Minola, A. Pasupathy, A. Boris, E. Benckiser, K. Dahmen, E. Carlson, B. Keimer, and D. Basov, "Coexisting first- and second-order electronic phase transitions in a correlated oxide", *Nat. Phys.* **14**, 1056–1061 (2018).

[80] K. Takenaka, M. Tamura, N. Tajima, H. Takagi, J. Nohara, and S. Sugai, "Collapse of coherent quasiparticle states in $\theta-(\mathrm{BEDT-TTF})_2\mathrm{I}_3$ observed by optical spectroscopy", *Phys. Rev. Lett.* **95**, 227801 (2005).

[81] H. Takagi, B. Batlogg, H. L. Kao, J. Kwo, R. J. Cava, J. J. Krajewski, and W. F. Peck, "Systematic evolution of temperature-dependent resistivity in $La_{2-x}Sr_xCuO_4$", *Phys. Rev. Lett.* **69**, 2975–2978 (1992).

[82] Y. Sawaki, K. Takenaka, A. Osuka, R. Shiozaki, and S. Sugai, "Al-substitution effect on charge transport in $La_{1-x}Sr_xMnO_3$: incoherent metallic state in a double-exchange ferromagnet", *Phys. Rev. B* **61**, 11588–11593 (2000).

[83] P. B. Allen, R. M. Wentzcovitch, W. W. Schulz, and P. C. Canfield, "Resistivity of the high-temperature metallic phase of VO_2", *Phys. Rev. B* **48**, 4359–4363 (1993).

[84] N. E. Hussey, K. Takenaka, and H. Takagi, "Universality of the Mott-Ioffe-Regel limit in metals", *Philos. Mag.* **84**, 2847-2864 (2004).

[85] N. Toyota, M. Lang, and J. Müller, *Low-dimensional molecular metals*, vol. 154, Springer Series in Solid-State Sciences, Berlin: Springer-Verlag, (2007).

[86] T. Mori, *Electronic Properties of Organic Conductors*, Tokyo: Springer, (2016).

[87] R. S. Mulliken, "Molecular compounds and their spectra. II", *J. Am. Chem. Soc.* **74**, 811-824 (1952).

[88] H. Anzai, J. M. Delrieu, S. Takasaki, S. Nakatsuji, and J. Yamada, "Crystal growth of organic charge-transfer complexes by electrocrystallization with controlled applied current", *J. Cryst. Growth* **154**, 145 - 150 (1995).

[89] E. Scriven and B. J. Powell, "Effective coulomb interactions within BEDT-TTF dimers", *Phys. Rev. B* **80**, 205107 (2009).

[90] K. Sedlmeier, S. Elsässer, D. Neubauer, R. Beyer, D. Wu, T. Ivek, S. Tomć, J. A. Schlueter, and M. Dressel, "Absence of charge order in the dimerized κ-phase BEDT-TTF salts", *Phys. Rev. B* **86**, 245103 (2012).

[91] T. Mori, H. Mori, and S. Tanaka, "Structural genealogy of BEDT-TTF-based organic conductors II. inclined molecules: θ, α, and κ Phases", *Bull. Chem. Soc. Jpn.* **72**, 179-197 (1999).

[92] D. Faltermeier, J. Barz, M. Dumm, M. Dressel, N. Drichko, B. Petrov, V. Semkin, R. Vlasova, C. Meźière, and P. Batail, "Bandwidth-controlled Mott transition in κ-(BEDT-TTF)$_2$Cu[N(CN)$_2$]Br$_x$Cl$_{1-x}$: optical studies of localized charge excitations", *Phys. Rev. B* **76**, 165113 (2007).

[93] A. M. Kini, U. Geiser, H. H. Wang, K. D. Carlson, J. M. Williams, W. K. Kwok, K. G. Vandervoort, J. E. Thompson, and D. L. a. Stupka, "A new ambient-pressure organic superconductor, κ-(ET)$_2$Cu[N(CN)$_2$]Br , with the highest transition temperature yet observed (inductive onset T$_c$ = 11.6 K, resistive onset = 12.5 K)", *Inorg. Chem.* **29**, 2555-2557 (1990).

[94] J. M. Williams, A. M. Kini, H. H. Wang, K. D. Carlson, U. Geiser, L. K. Montgomery, G. J. Pyrka, D. M. Watkins, and J. M. Kommers, "From semiconductor-semiconductor transition (42 K) to the highest-T$_c$ organic superconductor, κ-(ET)$_2$-Cu[N(CN)$_2$]Cl (T$_c$ = 12.5 K)", *Inorg. Chem.* **29**, 3272-3274 (1990).

[95] K. Miyagawa, A. Kawamoto, Y. Nakazawa, and K. Kanoda, "Antiferromagnetic ordering and spin structure in the organic conductor, κ-(BEDT-TTF)$_2$Cu[N(CN)$_2$]Cl", *Phys. Rev. Lett.* **75**, 1174–1177 (1995).

[96] H. Ito, T. Ishiguro, M. Kubota, and G. Saito, "Metal-nonmetal transition and superconductivity localization in the two-dimensional conductor κ-(BEDT-TTF)$_2$-Cu[N(CN)$_2$]Cl under pressure", *J. Phys. Soc. Jpn.* **65**, 2987-2993 (1996).

[97] S. Lefebvre, P. Wzietek, S. Brown, C. Bourbonnais, D. Jérome, C. Mézière, M. Fourmigué, and P. Batail, "Mott transition, antiferromagnetism and unconventional superconductivity in layered organic superconductors", *Phys. Rev. Lett.* **85**, 5420-5423 (2000).

[98] M. Dumm, D. Faltermeier, N. Drichko, M. Dressel, C. Meźière, and P. Batail, "Bandwidth-controlled Mott transition in κ-(BEDT-TTF)$_2$Cu[N(CN)$_2$]Br$_x$Cl$_{1-x}$: optical studies of correlated carriers", *Phys. Rev. B* **79**, 195106 (2009).

[99] S. Yasin, M. Dumm, B. Salameh, P. Batail, C. Meźière, and M. Dressel, "Transport studies at the Mott transition of the two-dimensional organic metal κ-(BEDT-TTF)2Cu[N(CN)2]Br$_x$Cl$_{1-x}$", *Eur. Phys. J. B* **79**, 383–390 (2011).

[100] T. Hiramatsu, Y. Yoshida, G. Saito, A. Otsuka, H. Yamochi, M. Maesato, Y. Shimizu, H. Ito, Y. Nakamura, H. Kishida, M. Watanabe, and R. Kumai, "Design and preparation of a quantum spin liquid candidate κ-(ET)$_2$Ag$_2$(CN)$_3$ having a nearby superconductivity", *Bull. Chem. Soc. Jpn.* **90**, 1073-1082 (2017).

[101] T. Kobayashi and A. Kawamoto, "Evidence of antiferromagnetic fluctuation in the unconventional superconductor λ-(BETS)$_2$GaCl$_4$ by ^{13}C NMR", *Phys. Rev. B* **96**, 125115 (2017).

[102] Y. Saito, S. Fukuoka, T. Kobayashi, A. Kawamoto, and H. Mori, "Antiferromagnetic ordering in organic conductor λ-(BEDT-TTF)$_2$GaCl$_4$ probed by ^{13}C NMR", *J. Phys. Soc. Jpn.* **87**, 013707 (2018).

[103] T. Naito, A. Miyamoto, H. Kobayashi, R. Kato, and A. Kobayashi, "Superconducting transition temperature of the organic alloy system κ-[(BEDT-TTF)$_{1-x}$(BEDT-STF)$_x$]$_2$ Cu[N(CN)$_2$]Br", *Chem. Lett.* **21**, 119-122 (1992).

[104] T. Naito, H. Kobayashi, and A. Kobayashi, "The electrical behavior of charge-transfer salts based on an unsymmetrical donor bis(ethylenedithio)diselenadithiafulvalene (STF): disorder effect on the transport properties", *Bull. Chem. Soc. Jpn.* **70**, 107-114 (1997).

[105] H. Mori, T. Okano, M. Kamiya, M. Haemori, H. Suzuki, S. Tanaka, Y. Nishio, K. Kajita, and H. Moriyama, "Bandwidth and band filling control in organic conductors", *Physica C* **357-360**, 103 - 107 (2001).

[106] T. Kobayashi, Y. Ihara, and A. Kawamoto, "Modification of local electronic state by BEDT-STF doping to κ-(BEDT-TTF)$_2$Cu[N(CN)$_2$]Br salt studied by ^{13}C NMR spectroscopy", *Phys. Rev. B* **93**, 094515 (2016).

[107] W. Sherman and A. Stadtmuller, *Experimental techniques in high-pressure research*, John Wiley Sons Australia, Limited, (1987).

[108] M. Eremets, *High pressure experimental methods*, Oxford science publications, Oxford University Press, (1996).

[109] J.-P. Pouget, P. Alemany, and E. Canadell, "Donor-anion interactions in quarter-filled low-dimensional organic conductors", *Mater. Horiz.* **5**, 590-640 (2018).

[110] J. Müller, B. Hartmann, R. Rommel, J. Brandenburg, S. M. Winter, and J. A. Schlueter, "Origin of the glass-like dynamics in molecular metals κ-(BEDT-TTF)$_2$X: implications from fluctuation spectroscopy and ab initiocalculations", *New J. Phys.* **17**, 083057 (2015).

[111] J. Müller and T. Thomas, "Low-Frequency dynamics of strongly correlated electrons in (BEDT-TTF)$_2$X studied by fluctuation spectroscopy", *Crystals* **8**, 166 (2018).

[112] H. C. Kandpal, I. Opahle, Y.-Z. Zhang, H. O. Jeschke, and R. Valentí, "Revision of model parameters for κ-type charge transfer salts: an ab initio study", *Phys. Rev. Lett.* **103**, 067004 (2009).

[113] W. Li, "Optical studies on 2D organic conductors under high pressure", PhD Thesis, Universität Stuttgart, (2019).

[114] T. Isono, T. Terashima, K. Miyagawa, K. Kanoda, and S. Uji, "Quantum criticality in an organic spin-liquid insulator κ-(ET)$_2$Cu$_2$(CN)$_3$", *Nat. Comm.* **7** (2016).

[115] Y. Saito, T. Minamidate, A. Kawamoto, N. Matsunaga, and K. Nomura, "Site-specific ^{13}C NMR study on the locally distorted triangular lattice of the organic conductor $\kappa-(\mathrm{BEDT-TTF})_2\mathrm{Cu}_2(\mathrm{CN})_3$", *Phys. Rev. B* **98**, 205141 (2018).

[116] Y. Saito, R. Rösslhuber, A. Löhle, A. Pustogow, M. Sanz-Alonso, M. Wenzel, E. Uykur, and M. Dressel, "Pressure-dependent dc-transport measurements on the bandwidth-tuned organic conductor κ-[(BEDT–STF)$_x$-(BEDT–TTF)$_{1-x}$]$_2$Cu$_2$-(CN)$_3$", (2019).

[117] R. S. Manna, M. de Souza, A. Brühl, J. A. Schlueter, and M. Lang, "Lattice effects and entropy release at the low-temperature phase transition in the spin-liquid candidate $\kappa-(\mathrm{BEDT-TTF})_2\mathrm{Cu}_2(\mathrm{CN})_3$", *Phys. Rev. Lett.* **104**, 016403 (2010).

[118] S. Yamashita, Y. Nakazawa, M. Oguni, Y. Oshima, H. Nojiri, Y. Shimizu, K. Miyagawa, and K. Kanoda, "Thermodynamic properties of a spin-1/2 spin-liquid state in a κ-type organic salt", *Nat. Phys.* **4**, 459 (2008).

[119] M. Yamashita, N. Nakata, Y. Kasahara, T. Sasaki, N. Yoneyama, N. Kobayashi, S. Fujimoto, T. Shibauchi, and Y. Matsuda, "Thermal transport measurements in a quantum spin-liquid state of frustrated triangular magnet κ-(BEDT-TTF)$_2$Cu$_2$(CN)$_3$", *Nat. Phys.* **5**, 44 (2009).

[120] M. Poirier, M. de Lafontaine, K. Miyagawa, K. Kanoda, and Y. Shimizu, "Ultrasonic investigation of the transition at 6 K in the spin-liquid candidate κ-(BEDT-TTF)$_2$Cu$_2$(CN)$_3$", *Phys. Rev. B* **89**, 045138 (2014).

[121] F. L. Pratt, P. J. Baker, S. Blundel, T. Lancaster, S. Ohira-Kawamura, C. Baines, Y. Shimizu, K. Kanoda, I. Watanabe, and G. Saito, "Magnetic and non-magnetic phases of a quantum spin liquid", *Nature* **471**, 612-616 (2011).

[122] K. Padmalekha, M. Blankenhorn, T. Ivek, L. Bogani, J. A. Schlueter, and M. Dressel, "ESR studies on the spin-liquid candidate $\kappa-$(BEDT-TTF)$_2$Cu$_2$(CN)$_3$: anomalous response below T=8K", *Physica B* **460**, 211 - 213 (2015), Special Issue on Electronic Crystals (ECRYS-2014).

[123] M. Poirier, S. Parent, A. Côté, K. Miyagawa, K. Kanoda, and Y. Shimizu, "Magnetodielectric effects and spin-charge coupling in the spin-liquid candidate κ-(BEDT-TTF)$_2$Cu$_2$(CN)$_3$", *Phys. Rev. B* **85**, 134444 (2012).

[124] J. Liu, J. Schmalian, and N. Trivedi, "Pairing and superconductivity driven by strong quasiparticle renormalization in two-dimensional organic charge transfer salts", *Phys. Rev. Lett.* **94**, 127003 (2005).

[125] T. Grover, N. Trivedi, T. Senthil, and P. A. Lee, "Weak Mott insulators on the triangular lattice: possibility of a gapless nematic quantum spin liquid", *Phys. Rev. B* **81**, 245121 (2010).

[126] V. Galitski and Y. B. Kim, "Spin-triplet pairing instability of the spinon Fermi surface in a $U(1)$ spin liquid", *Phys. Rev. Lett.* **99**, 266403 (2007).

[127] Y. Qi and S. Sachdev, "Insulator-metal transition on the triangular lattice", *Phys. Rev. B* **77**, 165112 (2008).

[128] R. Kira, V. Roser, and W. Stephen M., "Critical spin liquid versus valence-bond glass in a triangular-lattic organic antiferromagnet", *Nat. Comm.* **10**, 2561 (2019).

[129] K. Gregor and O. I. Motrunich, "Nonmagnetic impurities in a $S = \frac{1}{2}$ frustrated triangular antiferromagnet: broadening of ^{13}C NMR lines in $\kappa-(ET)_2Cu_2(CN)_3$", *Phys. Rev. B* **79**, 024421 (2009).

[130] K. Watanabe, H. Kawamura, H. Nakano, and T. Sakai, "Quantum spin-liquid behavior in the spin-1/2 random Heisenberg antiferromagnet on the triangular lattice", *J. Phys. Soc. Jpn.* **83**, 034714 (2014).

[131] T. Shimokawa, K. Watanabe, and H. Kawamura, "Static and dynamical spin correlations of the $S = \frac{1}{2}$ random-bond antiferromagnetic Heisenberg model on the triangular and kagome lattices", *Phys. Rev. B* **92**, 134407 (2015).

[132] P. Lunkenheimer, J. Müller, S. Krohns, F. Schrettle, A. Loidl, B. Hartmann, R. Rommel, M. de Souza, C. Hotta, J. A. Schlueter, and M. Lang, "Multiferroicity in an organic charge-transfer salt that is suggestive of electric-dipole-driven magnetism", *Nat. Mater.* **11**, 755 (2012).

[133] P. Lunkenheimer and A. Loidl, "Dielectric spectroscopy on organic charge-transfer salts", *J. Phy. Condens. Matter* **27**, 373001 (2015).

[134] S. Iguchi, S. Sasaki, N. Yoneyama, H. Taniguchi, T. Nishizaki, and T. Sasaki, "Relaxor ferroelectricity induced by electron correlations in a molecular dimer Mott insulator", *Phys. Rev. B* **87**, 075107 (2013).

[135] T. Ivek, R. Beyer, S. Badalov, M. Čulo, S. Tomić, J. A. Schlueter, E. I. Zhilyaeva, R. N. Lyubovskaya, and M. Dressel, "Metal-insulator transition in the dimerized organic conductor $\kappa-(BEDT\text{-}TTF)_2Hg(SCN)_2Br$", *Phys. Rev. B* **96**, 085116 (2017).

[136] M. Abdel-Jawad, N. Tajima, R. Kato, and I. Terasaki, "Disordered conduction in single-crystalline dimer Mott compounds", *Phys. Rev. B* **88**, 075139 (2013).

[137] M. Pinterić, T. Ivek, M. Čulo, O. Milat, M. Basletić, B. Korin-Hamzić, E. Tafra, A. Hamzić, M. Dressel, and S. Tomić, "What is the origin of anomalous dielectric response in 2D organic dimer Mott insulators κ-(BEDT-TTF)2Cu[N(CN)2]Cl and κ-$(BEDT\text{-}TTF)_2Cu_2(CN)_3$", *Physica B* **460**, 202 - 207 (2015).

[138] C. Hotta, "Quantum electric dipoles in spin-liquid dimer Mott insulator κ-$(ET)_2Cu_2(CN)_3$", *Phys. Rev. B* **82**, 241104 (2010).

[139] C. Hotta, "Theories on frustrated electrons in two-dimensional organic solids", *Crystals* **2**, 1155–1200 (2012).

[140] M. Naka and S. Ishihara, "Electronic ferroelectricity in a dimer Mott insulator", *J. Phy. Soc. Jpn.* **79**, 063707 (2010).

[141] H. Li, R. T. Clay, and S. Mazumdar, *J. Phys.: Condens. Matter* **22**, 272201 (2010).

[142] S. Dayal, R. T. Clay, H. Li, and S. Mazumdar, "Paired electron crystal: order from frustration in the quarter-filled band", *Phys. Rev. B* **83**, 245106 (2011).

[143] R. T. Clay, S. Dayal, H. Li, and S. Mazumdar, "Beyond the quantum spin liquid concept in frustrated two dimensional organic superconductors", *Phys. Status Solidi B* **249**, 991-994 (2012).

[144] H. Gomi, M. Ikenaga, Y. Hiragi, D. Segawa, A. Takahashi, T. J. Inagaki, and M. Aihara, "Ferroelectric states induced by dimer lattice disorder in dimer Mott insulators", *Phys. Rev. B* **87**, 195126 (2013).

[145] K. Yakushi, K. Yamamoto, T. Yamamoto, Y. Saito, and A. Kawamoto, "Raman spectroscopy study of charge fluctuation in the spin-liquid candidate κ-$(ET)_2Cu_2(CN)_3$", *J. Phys. Soc. Jpn.* **84**, 084711 (2015).

[146] S. Tomić and M. Dressel, "Ferroelectricity in molecular solids: a review of electrodynamic properties", *Rep. Prog. Phys.* **78**, 096501 (2015).

[147] T. Ivek, B. Korin-Hamzić, O. Milat, S. Tomić, C. Clauss, N. Drichko, D. Schweitzer, and M. Dressel, "Collective excitations in the charge-ordered phase of α-$(BEDT\text{-}TTF)_2I_3$", *Phys. Rev. Lett.* **104**, 206406 (2010).

[148] P. Lunkenheimer and A. Loidl, "Response of disordered matter to electromagnetic fields", *Phys. Rev. Lett.* **91**, 207601 (2003).

[149] A. Schönhals and F. Kremer, "Theory of Dielectric Relaxation", *Broadband Dielectric Spectroscopy*, Berlin, Heidelberg: Springer Berlin Heidelberg, (2003).

[150] M. Dressel and G. Grüner, *Electrodynamics of solids*, Cambridge: Cambridge University Press, (2002).

[151] D. Vanderbilt and R. D. King-Smith, "Electric polarization as a bulk quantity and its relation to surface charge", *Phys. Rev. B* **48**, 4442–4455 (1993).

[152] R. Resta, "Macroscopic polarization in crystalline dielectrics: the geometric phase approach", *Rev. Mod. Phys.* **66**, 899–915 (1994).

[153] D. Vanderbilt, "Berry-phase theory of proper piezoelectric response", *J. Phys. Chem. Solids* **61**, 147 - 151 (2000).

[154] R. Resta and D. Vanderbilt, "Theory of Polarization: A Modern Approach", *Physics of Ferroelectrics: A Modern Perspective*, Berlin, Heidelberg: Springer Berlin Heidelberg, (2007).

[155] R. D. King-Smith and D. Vanderbilt, "Theory of polarization of crystalline solids", *Phys. Rev. B* **47**, 1651–1654 (1993).

[156] R. Raffaele, "Manifestations of Berry's phase in molecules and condensed matter", *J. Phys. Condens. Matter* **12**, R107–R143 (2000).

[157] N. A. Spaldin, "A beginner's guide to the modern theory of polarization", *J. Solid State Chem.* **195**, 2 - 10 (2012), Polar Inorganic Materials: Design Strategies and Functional Properties.

[158] R. Martin, R. Martin, and C. U. Press, *Electronic Structure: Basic Theory and Practical Methods*, Cambridge University Press, (2004).

[159] P. Lunkenheimer, U. Schneider, R. Brand, and A. Loid, "Glassy dynamics", *Contemp. Phys.* **41**, 15-36 (2000).

[160] P. Debye, *Polar Molecules*, Chemical Catalog Company, Incorporated, (1929).

[161] P. Flory and J. Jackson, *Statistical Mechanics of Chain Molecules*, Hanser, (1989).

[162] N. Havriliak and S. Negami, "A complex plane analysis of α-dispersion in some polymer systems", *J. Polym. Sci. Pol. Sym.* **14**, 99-117 (1966).

[163] W. Haase and S. Wróbel, *Relaxation Phenomena: Liquid Crystals, Magnetic Systems, Polymers, High-Tc Superconductors, Metallic Glasses*, Springer Berlin Heidelberg, (2013).

[164] L. E. Cross, "Relaxor Ferroelectrics", Berlin, Heidelberg: Springer-Verlag, (2008).

[165] F. Nad and P. Monceau, "Dielectric response of the charge ordered state in quasi-one-dimensional organic conductors", *J. Phy. Soc. Jpn* **75**, 1–12 (2006).

[166] D. Starešinić, P. Lunkenheimer, J. Hemberger, K. Biljaković, and A. Loidl, "Giant dielectric response in the one-dimensional charge-ordered semiconductor $(NbSe_4)_3I$", *Phys. Rev. Lett.* **96**, 046402 (2006).

[167] G. Grüner, "The dynamics of charge-density waves", *Rev. Mod. Phys.* **60**, 1129–1181 (1988).

[168] G. Grüner, "The dynamics of spin-density waves", *Rev. Mod. Phys.* **66**, 1–24 (1994).

[169] F. Alvarez, A. Alegra, and J. Colmenero, "Relationship between the time-domain Kohlrausch-Williams-Watts and frequency-domain Havriliak-Negami relaxation functions", *Phys. Rev. B* **44**, 7306–7312 (1991).

[170] S. A. Kivelson and G. Tarjus, "In search of a theory of supercooled liquids", *Nat. Mat.* **7**, 831 (2008).

[171] T. Bauer, P. Lunkenheimer, and A. Loidl, "Cooperativity and the freezing of molecular motion at the glass transition", *Phys. Rev. Lett.* **111**, 225702 (2013).

[172] J. C. M. Garnett, "Colours in metal glasses and in metallic films", *Phil. Trans. A* **203**, 385 (1904).

[173] C. J. F. Böttcher, *Theory of electric polarisation*, 2nd ed., Amsterdam: Elsevier, (1973).

[174] J. P. Clerc, G. Giraud, J. M. Laugier, and J. M. Luck, "The electrical conductivity of binary disordered systems, percolation clusters, fractals and related models", *Adv. Phys.* **39**, 191 (1990).

[175] D. Stauffer and A. Aharony, *Introduction to Percolation Theory*, 2nd ed., Boca Raton, Florida: CRC Press, (1994).

[176] S. Kirkpatrick, "Percolation and conduction", *Rev. Mod. Phys.* **45**, 574–588 (1973).

[177] B. I. Shklovskii and A. L. Efros, *Electronic properties of doped semiconductors*, Berlin: Springer-Verlag, (1984).

[178] A. L. Efros and B. I. Shklovskii, "Critical behavior of conductivity and dielectric constant near the metal-non-metal transition threshold", *Phys. Status Solidi B* **76**, 475 (1976).

[179] L. Benguigui, "Dielectric scaling near a percolation threshold", *J. Phys. Lett. (Paris)* **46**, L-1015 (1985).

[180] M. Hövel, B. Gompf, and M. Dressel, "Dielectric properties of ultrathin metal films around the percolation threshold", *Phys. Rev. B* **81**, 035402 (2010).

[181] T. C. Choy, *Effective Medium Theory: Principles and Applications*, 2nd ed., Oxford: Oxford University Press, (2015).

[182] D. J. Bergman and D. Stroud, "Physical Properties of Macroscopically Inhomogeneous Media", ed. by H. EHRENREICH and D. TURNBULL, vol. 46, Solid State Physics, Academic Press, 1992.

[183] *Impedance measurement handbook*, 6th ed., Keysight technologies, 2009.

[184] *4294A Precision Impedance Analyzer Operation Manual*, 7th ed., Keysight technologies, 2003.

[185] K. Zaman, *High-pressure physics*, Scitus Academics LLC, (2017).

[186] J. Loveday, *High-pressure physics*, Scottish Graduate Series, Taylor & Francis, (2012).

[187] M. Fujimoto, *The physics of structural phase transitions*, Springer, (1997).

[188] C. Poole, H. Farach, R. Creswick, and R. Prozorov, *Superconductivity*, Elsevier insights, Elsevier Science, (2014).

[189] P. Gegenwart, Q. Si, and F. Steglich, "Quantum criticality in heavy-fermion metals", *Nat. Phys.* **4**, 186-197 (2008).

[190] M. Dressel, "Quantum criticality in organic conductors? Fermi liquid versus non-Fermi-liquid behaviour", *J. Phys. Condens. Matter* **23**, 293201 (2011).

[191] R. Beyer and M. Dressel, "Piston pressure cell for low-temperature infrared investigations", *Rev. Sci. Instrum.* **86**, 053904 (2015).

[192] *RG 178 B/U coaxial cable, manufactured by Habia Cable*, https://www.arnotec.de, cable configuration and distribution by arnotec GmbH, Dunantstr. 7, D-76131 Karlsruhe, GERMANY.

[193] *Institut of High Pressure Physics*, https://www.unipress.waw.pl, Polish Academy of Science, ul. Sokolowska 29/37, 01-142 Warsaw, POLAND.

[194] *Rf subminiature cable MMK5001*, www.elpsec.de, el-spec GmbH, Lauterbachstr. 23C, D-82538 Geretsried-Gelting, GERMANY.

[195] D. Starešinić, K. Biljaković, P. Lunkenheimer, and A. Loidl, "Slowing down of the relaxational dynamics at the ferroelectric phase transition in one-dimensional $(TMTTF)_2AsF_6$", *Solid State Commun.* **137**, 241–245 (2006).

[196] N. McCrum, B. Read, and G. Williams, *Anelastic and dielectric effects in polymeric solids*, John Wiley, (1967).

[197] F. Tian and Y. Ohki, "Electric modulus powerful tool for analyzing dielectric behavior", *IEEE Trans. Dielectr. Electr. Insul.* **21**, 929-931 (2014).

[198] P. B. Macedo, C. T. Moynihan, and R. Bose, "The role of ionic diffusion in polarization in vitreous ionic conductors", *Phys. Chem. Glasses* **13**, 171–179 (1972).

[199] I. Hodge, M. Ingram, and A. West, "Impedance and modulus spectroscopy of polycrystalline solid electrolytes", *J. Electroanal. Chem.* **74**, 125 - 143 (1976).

[200] *Advanced frequency response analyzer for smart measurement applications*, Novocontrol technologies.

[201] R. Gross and A. Marx, *Festkörperphysik*, Oldenbourg Wissenschaftsverlag, (2012).

[202] T. Komatsu, N. Matsukawa, T. Inoue, and G. Saito, "Realization of superconductivity at ambient pressure by band-filling control in κ-$(BEDT-TTF)_2Cu_2(CN)_3$", *J. Phy. Soc. Jpn.* **65**, 1340-1354 (1996).

[203] M. Dressel and N. Drichko, "Optical properties of two-dimensional organic conductors: signatures of charge ordering and correlation effects", *Chem. Rev.* **104**, 5689–5716 (2004).

[204] A. Pustogow, R. Rösslhuber, Y. Tan, E. Uykur, A. Böhme, A. Löhle, R. Hübner, J. A. Schlueter, and V. Dressel M.and Dobrosavljević, "Parting the Fermi sea at the Mott point: dynamics of correlated electrons reveals the mechanism underpinning mottness", *arXiv:1907.04437* (2019).

[205] E. Gati, U. Tutsch, A. Naji, M. Garst, S. Köhler, H. Schubert, T. Sasaki, and M. Lang, "Effects of disorder on the pressure-induced Mott transition in κ-(BEDT-TTF)$_2$Cu[N(CN)$_2$]Cl", *Crystals* **8**, 38 (2018).

[206] S. Sasaki, S. Iguchi, N. Yoneyama, and T. Sasaki, "X-ray irradiation effect on the dielectric charge response in the dimer-Mott insulator κ-(BEDT-TTF)$_2$Cu$_2$(CN)$_3$", *J. Phy. Soc. Jpn.* **84**, 074709 (2015).

[207] K. Itoh, H. Itoh, M. Naka, S. Saito, I. Hosako, N. Yoneyama, S. Ishihara, T. Sasaki, and S. Iwai, "Collective excitation of an electric dipole on a molecular dimer in an organic dimer-Mott insulator", *Phys. Rev. Lett.* **110**, 106401 (2013).

[208] H. Fukuyama, J.-i. Kishine, and M. Ogata, "Energy landscape of charge excitations in the boundary region between dimer-Mott and charge ordered states in molecular solids", *J. Phy. Soc. Jpn.* **86**, 123706 (2017).

[209] M. Paluch, C. M. Roland, S. Pawlus, J. Zioło, and K. L. Ngai, "Does the arrhenius temperature dependence of the Johari-Goldstein relaxation persist above T_g?", *Phys. Rev. Lett.* **91**, 115701 (2003).

[210] K. Sedlmeier, S. Elsässer, D. Neubauer, R. Beyer, D. Wu, T. Ivek, S. Tomić, J. A. Schlueter, and M. Dressel, "Absence of charge order in the dimerized κ-phase BEDT-TTF salts", *Phys. Rev. B* **86**, 245103 (2012).

[211] R. S. Manna, S. Hartmann, E. Gati, J. A. Schlueter, M. de Souza, and M. Lang, "Low-temperature lattice effects in the spin-liquid candidate κ-(BEDT-TTF)$_2$Cu$_2$(CN)$_3$" ().

[212] Y. E. Ryabov, A. Puzenko, and Y. Feldman, "Nonmonotonic relaxation kinetics of confined systems", *Phys. Rev. B* **69**, 014204 (2004).

[213] M. Hövel, B. Gompf, and M. Dressel, "Electrodynamics of ultrathin gold films at the insulator-to-metal transition", *Thin Solid Films* **519**, 2955 - 2958 (2011).

[214] R. B. Laibowitz and Y. Gefen, "Dynamic scaling near the percolation threshold in thin Au films", *Phys. Rev. Lett.* **53**, 380–383 (1984).

[215] M. F. Hundley and A. Zettl, "Temperature-dependent ac conductivity of thin percolation films", *Phys. Rev. B* **38**, 10290–10296 (1988).

[216] C. S. Yoon and S.-I. Lee, "Measurements of the ac conductivity and dielectric constant in a two-dimensional lattice percolation system", *Phys. Rev. B* **42**, 4594–4597 (1990).

[217] I. Voloshenko, F. Kuhl, B. Gompf, A. Polity, G. Schnoering, A. Berrier, and M. Dressel, "Microscopic nature of the asymmetric hysteresis in the insulator-metal transition of VO2 revealed by spectroscopic ellipsometry", *Appl. Phys. Lett.* **113**, 201906 (2018).

[218] N. Ashcroft and D. Mermin, *Festkörperphysik*, Oldenbourg Wissenschaftsverlag, (2012).

[219] A. Takshi, A. Dimopoulos, and J. D. Madden, "Depletion width measurement in an organic Schottky contact using a metal-semiconductor field-effect transistor", *Appl. Phys. Lett.* **91**, 083513 (2007).

[220] I. Voloshenko, B. Gompf, A. Berrier, M. Dressel, G. Schnoering, M. Rommel, and J. Weis, "Mueller matrix metrology: depolarization reveals size distribution", *Appl. Phys. Lett.* **115**, 063106 (2019).

Curriculum Vitae

Education

09/1999 – 07/2007	Bundesgymnasium Zaunergasse, Salzburg
10/2008 – 08/2012	Technical University of Munich B. Sc. in Condensed Matter Physics
08/20011 – 06/2012	Lomonossov Moscow State University TUM-Exchange Program
10/2012 – 12/2014	Technical University of Munich M. Sc. in Condensed Matter Physics
since 05/2015	PhD project, Prof. M. Dressel, University of Stuttgart

Experience

11/2010 – 07/2011	Walther Schottky Institute, Prof. M. Stutzmann, Student research assistent and Bachelor thesis: "Optical and structural characterization of ZnO/ZnMgO single and multiple quantum wells"
08/20011 – 06/2012	Lomonossov Moscow State University, Prof. Y.V. Timoshenko, visiting student, photoluminescence spectroscopy on ZnOYb_2O_3 nanocomposite and por-Si:(Er,Yb)
10/2012 – 08/2013	SCHAEFER Patent, Trademark & Design, student assistant at a law firm for intellectual property
10/2012 – 12/2014	Walther Meißner Institute, Dr. Habil. S.T.B. Goennenwein, Master thesis: "Photoconductivity Measurements in Yttrium Iron Garnet Thin Films"
since 05/2015	University of Stuttgart, 1st Physical Institute, Prof. M. Dressel: establishing a laboratory for dielectric spectroscopy (DS) including: (i) setup for DS in dependence of pressure and temperature, (ii) a setup for DS in dependence of temperature and magnetic-field and (iii) a setup for temperature-dependent ferroelectric hysteresis measurements, dc-resistivity, teaching laboratory courses, supervision of two Bachelor and two Master students

Declaration of Originality

I hereby declare that this thesis and the work reported herein was composed by and originated entirely from me. Information derived from the published and unpublished work of others has been acknowledged in the text and references.

Roland Rösslhuber